UNIVERSITY OF Southampton

Exact Invariant Solutions for Grooved Couette and Channel Flows

Thesis for the degree of Doctor of Philosophy

by

Sabarish Bharadwaz Vadarevu

Under the supervision of
Dr. Ati Sharma
Prof. Bharathram Ganapathisubramani

Faculty of Engineering and the Environment
University of Southampton
United Kingdom
December 2017

University of Southampton

ABSTRACT

Faculty of Engineering and the Environment
Aerodynamics and Flight Mechanics group

Doctor of Philosophy

Exact invariant solutions for grooved Couette and channel flows

by Sabarish Bharadwaz Vadarevu

The dynamical systems approach to turbulence has gained a lot of traction since the turn of the century. A large set of exact invariant solutions for canonical wall-bounded flows such as Couette, channel, and pipe flows has been found by researchers. These solutions, and their connections, are thought to form a skeleton for trajectories of turbulent flow. However, this vision of turbulence has not been extended to rough-walled flows despite the practical significance of such flows in engineering applications. This thesis describes continuation, by numerical homotopy, of known equilibria from smooth-walled plane shear flows to grooved plane shear flows using a domain transformation method, with the hope that this exploratory work would inform later efforts to extend such solutions to rough-walled flows. As a precursor to computing non-laminar equilibria, laminar solutions are computed for grooved channel flows for transverse, longitudinal, and oblique grooves. In addition to the numerical solutions, analytical solutions are also derived for asymptotically long groove-wavelengths, employing the Stokes-flow approximation for transverse and oblique grooves.

Exact invariant solutions can indeed be continued from plane Couette flow (PCoF) with smooth walls to grooved PCoF with longitudinal grooves using a simple domain transformation method. However, smooth PCoF equilibria exist as continuous families of solutions that are identical up to a translational shift; the loss of spanwise homogeneity due to the grooves restricts such continuous families to discrete families due to symmetry-breaking. This phase-based restriction can also be expected to be reflected in turbulent statistics. Continuation of equilibria in grooves of different wavelengths shows a drag increasing tendency for grooves of the same wavelength as the vortex-streak structure, and a drag reducing tendency for grooves of significantly smaller wavelengths. This can relate the optimal spacing of riblets for maximal drag reduction to the spanwise spacing of the vortex-streak structures observed in the self-sustaining near-wall cycle.

Contents

Abstract 3

List of Figures 11

Declaration of Authorship 13

Acknowledgements 14

Nomenclature 15

1 Introduction 20

1.1 Overview . . . 20

1.2 Structural description of turbulence . . . 23

1.3 Exact coherent states . . . 25

1.3.1 Transition to turbulence . . . 25

1.3.2 Near-wall cycle . . . 28

1.3.3 Organization in state-space . . . 29

1.3.4 Coherent structures at high Reynolds numbers: Vortex-wave interactions . . . 30

1.4 Turbulence over rough walls . . . 32

1.4.1 Drag reduction due to riblets . . . 37

1.5 Laminar solutions for rough-walled internal flows . . . 38

1.6 Concluding remarks . . . 42

1.7 Outline of the thesis . . . 43

2 Methodology — Grooved plane shear flows 45

2.0.1 Overview . . . 46
2.1 Smooth-walled plane shear flows . . . 48
2.1.1 Types of ECS . . . 48
2.1.2 Governing equations . . . 49
2.2 Flow symmetries . . . 51
2.2.1 Continuous symmetries . . . 51
2.2.2 Discretization . . . 52
2.2.3 Discrete symmetries . . . 53
2.3 Flow geometry and domain transformation . . . 55
2.3.1 Discretization in the transformed domain . . . 58
2.3.2 Inter-modal interaction . . . 59
2.4 Governing equations for transverse grooves . . . 60
2.4.1 Pressure gradient . . . 60
2.4.2 Diffusion . . . 61
2.4.3 Advection . . . 61
2.4.4 Continuity equation . . . 61
2.4.5 Boundary conditions . . . 62
2.5 Discretized system for transverse grooves . . . 62
2.5.1 Iterative scheme . . . 63
2.5.2 Matrix representing linear terms . . . 64
2.5.3 Matrix operator for non-linear terms . . . 66
2.5.4 Boundary conditions . . . 69
2.6 Modifications for oblique grooves . . . 72
2.7 Non-laminar equilibria for grooved Couette flows . . . 72
2.7.1 Computational memory requirements . . . 74
2.7.2 Multiple Fourier modes to represent grooves . . . 77
2.7.3 Reducing state-space dimensionality . . . 79
2.8 Numerical continuation . . . 84
2.8.1 Convergence criteria . . . 84
2.8.2 Initial iterate . . . 84

2.8.3 Code verification . . . 85
2.8.4 Grid convergence . . . 87
2.9 Limitations of the steady-state solver . . . 89
2.9.1 Failure of matrix-free methods . . . 89
2.9.2 Considerations for building a DNS code . . . 92

3 Laminar solutions for grooved channel flows 95
3.1 Stokes-flow approximation for long wavelength grooves . . . 97
3.1.1 Analytical solution: Longitudinal grooves . . . 97
3.1.2 Analytical Stokes-flow solution: Transverse grooves . . . 98
3.1.3 Analytical Stokes-flow solution: Oblique grooves . . . 99
3.2 Longitudinal grooves . . . 101
3.2.1 Low wavenumber asymptote . . . 102
3.2.2 High wavenumber asymptote . . . 103
3.3 Transverse grooves . . . 104
3.3.1 Asymptotes . . . 105
3.3.2 Flow regimes based on separation . . . 109
3.3.3 Re-dependence of U_{bulk} . . . 110
3.4 Oblique grooves . . . 113
3.5 Summary . . . 115
3.5.1 Grooves as low-order representation of roughness . . . 117

4 Equilibria for grooved Couette flows 118
4.0.1 Residual norm and spatial accuracy . . . 119
4.1 Existence of solutions for grooved PCoF . . . 120
4.1.1 Kinetic energy and dissipation rate . . . 124
4.2 Spanwise anchoring of the vortex-streak structure . . . 126
4.2.1 Significance to turbulence . . . 130
4.3 Wavelength dependence . . . 131
4.3.1 Mean velocity . . . 134
4.3.2 Energy density and dissipation rate . . . 134

5 Conclusion and Outlook **142**

5.1 Outlook . . . 144

A Convergence properties **146**

A.1 Lipschitz continuity . . . 146

A.2 Assumptions on smoothness . . . 154

A.3 Lemmas used for proof of convergence . . . 156

A.4 Proof of convergence . . . 157

A.5 Increment in g . . . 158

A.5.1 g-derivative of F . . . 159

B Analytical laminar solutions for long wavelength grooves **161**

B.1 Channel flow with longitudinal grooves . . . 161

B.2 Channel flow with transverse grooves . . . 164

B.2.1 Flow Symmetry . . . 165

B.2.2 Exact governing equations for each Fourier mode . . . 167

B.2.3 Approximate equations . . . 168

B.2.4 Solution . . . 175

B.2.5 Pressure drag . . . 175

B.3 Channel flow with oblique grooves . . . 176

B.4 Pressure drag in terms of Fourier coefficients . . . 179

C Methodology — Smooth-walled plane shear flows **183**

C.0.1 Time-marching . . . 183

C.1 Generating approximate solutions . . . 186

C.1.1 Bisection . . . 187

C.1.2 Homotopy . . . 187

C.1.3 Filtering . . . 188

C.2 Iterative solvers . . . 188

C.2.1 The Newton method and its variants . . . 188

C.2.2 Jacobian-free Newton-Krylov methods (JFNK) . . . 190

C.2.3 Global convergence: Line search 192
C.2.4 Global convergence: Locally constrained optimal hook-step . . . 193

List of Figures

1.1 Subcritical transition to turbulence in Couette flow 27

1.2 Friction factor for transitionally rough pipe flow 34

2.1 Geometry for plane Couette flow 50

2.2 Illustration of domain transformation 56

2.3 Grooved channel geometries with transverse, longitudinal, and oblique grooves 57

2.4 Grooved PCoF with longitudinal grooves 73

2.5 Illustration of grid convergence for laminar solutions 88

2.6 Spectrum of the Jacobian without preconditioning 90

2.7 Convergence of GMRES for Newton correction step without preconditioner 90

2.8 Spectrum of the Jacobian with linear operator based preconditioning . 91

2.9 Convergence of GMRES for Newton correction step with linear operator based preconditioner 91

3.1 Laminar flow in channels with longitudinal grooves 101

3.2 Accuracy of the Stokes-flow analytical solution for longitudinal grooves: Bulk velocity 103

3.3 Illustration of width-adjusted channel for high wavenumber grooves . . 103

3.4 Channel with longitudinal grooves; asymptotes of bulk velocity 104

3.5 Accuracy of the Stokes-flow analytical solution for transverse grooves: Bulk velocity (1) 106

3.6 Accuracy of the Stokes-flow analytical solution for transverse grooves: Bulk velocity (2) 106

3.7 Accuracy of the Stokes-flow analytical solution for transverse grooves: Pressure drag (1) . . . 108
3.8 Accuracy of the Stokes-flow analytical solution for transverse grooves: Pressure drag (2) . . . 108
3.9 Channel with transverse grooves; asymptotes of bulk velocity . . . 109
3.10 Laminar flow in transverse grooves: Streamlines . . . 110
3.11 Laminar flow in transverse grooves: Velocity contours . . . 111
3.12 Re-dependence of bulk velocity for channel with transverse grooves . . . 112
3.13 Friction factor for channel with transverse grooves (log scale) . . . 113
3.14 Channel with oblique grooves: wall-parallel velocity (1) . . . 114
3.15 Channel with oblique grooves: wall-parallel velocity (2) . . . 115

4.1 Cross-stream slice of grooved PCoF geometry . . . 119
4.2 EQ1 and EQ2 for smooth and grooved PCoF on a cross-stream plane . 121
4.3 EQ1 and EQ2 for grooved PCoF: Isometric, top, and side views . . . 123
4.4 Mean velocity for grooved PCoF; EQ1 and EQ2. . . . 124
4.5 Kinetic energy density and bulk dissipation rate in grooved PCoF for laminar flow, EQ1, and EQ2. . . . 125
4.6 Spanwise inhomogeneity for EQ1 in grooved PCoF . . . 127
4.7 Convergence of translated versions of EQ1, EQ2, EQ7, and EQ8 in grooved PCoF . . . 129
4.8 EQ1 in grooved PCoF with one, two, and three grooves per box . . . 132
4.9 EQ2 in grooved PCoF with one, two, and three grooves per box . . . 133
4.10 Mean velocity for grooved PCoF with multiple grooves; EQ1 and EQ2. 135
4.11 Kinetic energy density and bulk dissipation rate in grooved PCoF with multiple grooves. . . . 137

Declaration of Authorship

I, Sabarish Bharadwaz Vadarevu, declare that this thesis and the work presented in it are my own and has been generated by me as the result of my own original research.

Exact invariant solutions for grooved Couette and channel flows

I confirm that:

- This work was done wholly or mainly while in candidature for a research degree at this University;
- Where any part of this thesis has previously been submitted for a degree or any other qualification at this University or any other institution, this has been clearly stated;
- Where I have consulted the published work of others, this is always clearly attributed;
- Where I have quoted from the work of others, the source is always given. With the exception of such quotations, this thesis is entirely my own work;
- I have acknowledged all main sources of help;
- Where the thesis is based on work done by myself jointly with others, I have made clear exactly what was done by others and what I have contributed myself;
- None of this work has been published before submission.

Signed: Sabarish Bharadwaz Vadarevu

Date: December 7, 2017

Acknowledgements

I am grateful for the guidance provided my supervisors, Dr. Ati Sharma and Prof. Bharathram Ganapathisubramani, which has helped me grow as a researcher during my time as a PhD student. I am especially thankful for their role in helping me make steady progress whenever I got side-tracked or overwhelmed. I thoroughly enjoyed all of our weekly meetings; particularly when their complementary perspectives led to an exploration of a broad range of topics, with my final thesis predominantly stemming from such discussions. Even writing up this thesis has, for most part, been enjoyable thanks to Ati's efforts in helping me refine my writing style.

I must thank my lunchmates, Rafa, Manan, Arslan, Jaime, and Jorge, for making my time at the university as enjoyable as it was. Our random ramblings over lunch were often the best parts of my day. I learnt a lot of useless yet amusing things. Even as I meet different lunchmates through the years, I'll never forget our impassioned debates or recounting of strange stories.

I also owe my thanks to the volleyball club, the men's volleyball team, and the "Accies" volleyball team at the university. It was a pleasure to meet and play with lots of wonderful people from lots of different backgrounds. The early-morning trainings, the away games, and the crazy socials were all delightful, and it pains me to realize that I'm not a part of that now.

I acknowledge the use of the IRIDIS High Performance Computing Facility, and associated support services at the University of Southampton, in the completion of this work.

Finally, I owe a debt of gratitude to my parents for being there for me through everything.

Nomenclature

Latin Symbols

A Amplitude of grooves

D Differentiation matrix for wall-normal derivative, also bulk dissipation rate

E Kinetic energy density

$\mathbf{F}$ Time-derivative (partial) of the velocity field

$\mathbf{f}^t$ Time-t map for the flow

$\mathbf{f}$ Forcing term in the NSE

$\mathcal{F}_{lm}$ Projection on the the Fourier mode $e^{i(l\alpha x+m\beta z)}$

$\mathbf{g}$ Right hand side of the Pressure Poisson equation

g Semi-slope (see S)

$\mathcal{G}$ Jacobian of the non-linear part of the NSE

h Channel half-height

I Power input

J Jacobian of the dynamics matrix

L Largest harmonic of streamwise Fourier modes

$\mathfrak{L}_\zeta$ Reflection about the $Z = \zeta$ plane

$\mathcal{L}$ Operator for the linear terms of the NSE (excluding time-derivative)

L_x Streamwise size of periodic domain

L_z Spanwise size of periodic domain

M Largest harmonic of spanwise Fourier modes

N Number of Chebyshev collocation nodes (wall-normal)

$\boldsymbol{\mathcal{N}}$ Operator for the non-linear terms of the NSE

p Fluctuating pressure

$\mathfrak{P}_{\xi,\zeta}$ Point-wise inversion about $(X, Z) = (\xi, \zeta)$

$\frac{dP}{dx}$ Mean streamwise pressure gradient

$\mathfrak{R}_{\xi}$ Rotation by π about the Z axis at $X = \xi$

S Maximum slope of grooves (absolute value at phase $\pi/2$)

T Time period for periodic orbits

t Temporal coordinate

$\mathcal{T}$ Transformation function mapping a grooved geometry to a smooth geometry

U Laminar velocity profile

U_{CL} Average centerline velocity

$\mathbf{u}$ Velocity vector

(u, v, w) Components of non-dimensional velocity, ordered as streamwise, wall-normal, and spanwise

(x, y, z) Non-dimensional spatial Cartesian coordinates, ordered as streamwise, wall-normal, and spanwise

(X, Y, Z) Cartesian coordinates in a transformed domain with smooth walls

Greek Symbols

α Wavenumber for the fundamental streamwise Fourier mode

β Wavenumber for the fundamental spanwise Fourier mode

$\boldsymbol{\chi}$ State-vector

$\delta\boldsymbol{\chi}$ Correction (during iterations) to the state-vector

δt Time-step in a time-marching scheme

ϵ Semi-amplitude of grooves

γ Amplitude of wavenumber vector

ν Kinematic viscosity

ρ Density

σ_x Rotation about the z-axis

σ_z Reflection across the $z = 0$ plane

σ_{xz} Point-wise inversion about the origin

s_1 Shift-reflect operator

s_2 Shift-rotate operator

s_3 Shift-invert operator

τ_{l_x,l_z} Translation by l_x and l_z in the streamwise and spanwise directions

Abbreviations

DMD Dynamic mode decomposition

DNS Direct numerical simulation

ECS Exact coherent state

IBM Immersed boundary method

MMS Method of Manufactured Solutions

NSE Navier-Stokes equations

PCoF Plane Couette flow

PDE Partial differential equations

POD Proper orthogonal decomposition

Re Reynolds number

SSP Self sustaining process

SSP Self-sustaining process

SVD Singular value decomposition

SVD Singular value decomposition

TWS Travelling wave solution

Subscripts & Superscripts

$\hat{\boldsymbol{e}}_x$ Unit-vector along the x-axis

$\hat{u}$ Dimensional counterpart of u

$u_{l,m}$ Fourier coefficient of u for the mode $e^{i(l\alpha x+m\beta z)}$

$\mathbf{u}^n$ Velocity field, $\mathbf{u}$, at the n^{th} iteration or time-step

$u'_{l,m}$ Wall-normal derivative of the Fourier coefficient $u_{l,m}$

$\boldsymbol{\chi}^*$ State-vector representing an exact invariant solution of the NSE

A^T Transpose of a matrix A

u^j j^{th} velocity component in (u, v, w)

x_j j^{th} coordinate (non-dimesional)

Symbols & Operators

δ_{ij} Kronecker delta

Δ Laplacian

∇ Nabla operator (for gradient, divergence, and curl)

∂_{x_j} Partial derivative with respect to x_j

Chapter 1

Introduction

The scientist does not study nature because it is useful to do so. He studies it because he takes pleasure in it, and he takes pleasure in it because it is beautiful. If nature were not beautiful it would not be worth knowing, and life would not be worth living.

Henri Poincaré

1.1 Overview

The status of turbulence as being one of the greatest unsolved problems of classical physics naturally provokes our desire to understand the mechanisms of its sustenance. Furthermore, a strong motivation to understand turbulence dynamics comes from the prevalence of turbulent flows in applications related to combustion, flight dynamics, climate modelling, and the myriad of other fields of engineering involving fluid flows.

In spite of the existence of an adequate mathematical model to describe fluid flows — the Navier-Stokes equations (NSE) — only a limited class of flows can be solved analytically owing to the non-linearity of the equations. Direct numerical simulation (DNS) of turbulent flows are limited to low Reynolds number cases. Simulations of high Reynolds number flows must resort to modelling finer scales; such modelling

must have a basis in the physics of the problem: the dynamics of turbulence which cannot be completely resolved in coarse computations.

In the last three decades, we have seen great strides in our understanding of wall-bounded turbulence. Thanks to rapid advances in computing, direct numerical simulation (DNS) has allowed isolation of coherent structures that were observed more than fifty years ago in experiments. DNS solvers are being developed to handle larger and more complex flow cases, and high precision experimental techniques are making it possible to acquire highly resolved flow measurements.

This thesis, however, relates to a different vision of turbulence — the marriage of ergodic theory to turbulence theory that has opened up new avenues that were previously speculated but never realized. Since the pioneering work of Henri Poincaré, ergodic theory has seen rapid progress; and the dynamical systems approach to turbulence has made use of these advances to produce insight into turbulence dynamics that might not be possible with the statistical approach — the favoured approach in the last century.

Rough-walled turbulence, despite its pervasiveness in engineering applications, has not been subject to the dynamical systems approach in any significant manner. For smooth-walled turbulence, however, a large set of solutions are available in the literature for canonical flows; equilibria, relative equilibria, periodic orbits, and relative periodic orbits have been computed, and their connections in phase-space have been mapped. These exact recurring structures do remarkably well in describing features of turbulent flow — some replicate the near-wall cycle, some lie close to the laminar flow (excursions to these solutions through the connections to others resemble hibernating turbulence) and regulate transition to turbulence, while some others help in nucleating turbulent spots. These solutions are currently available only for low Reynolds numbers (~ 1000), but, asymptotic studies of high Re flows show the existence of vortex-streak structures that are similar to the ones seen in exact invariant solutions computed at low-Re, both in terms of spatial organization and energy scaling. In addition to aiding our understanding of turbulence, these solutions also provide low-dimensional bases

that can be used in modelling and control.

The original contributions of the current work are the following. A numerical homotopy method to continue the exact invariant solutions from smooth-walled canonical flows to corresponding grooved geometries is introduced, and is found to be robust. The homotopy method has been used to obtain such solutions earlier for smooth-walled flows, including the early solutions of Nagata (1990). Homotopy allows us to see how these structures morph from smooth-walled to grooved flows. A shift-reflect symmetry of plane Couette flow is found to be responsible for anchoring coherent structures in the near-wall region. When the grooves are smaller than the characteristic size of the coherent structure, the structure is squeezed out of the grooves, and is accompanied by a reduction in drag. As a precursor to computing non-laminar equilibria for plane Couette flow, laminar flows in grooved channels are investigated. Numerical solutions are obtained for longitudinal, transverse, and oblique grooves over a range of amplitudes and wavenumber. Analytical solutions are also derived for all three cases for asymptotically low wavenumbers.

A brief review of the literature on turbulence dynamics is now presented to motivate the study of exact invariant solutions for grooved Couette and channel flows. We start with the current state of understanding of turbulence dynamics, with focus on coherent structures; these are structures that advect through the flow without dissipating for significant times so that flow statistics are affected by them in good measure. Then, we move on to a discussion of turbulence over rough walls. We find that large gaps exist in our understanding of how walls influence turbulence. The curious case of drag reduction due to longitudinal riblets is also included; this thesis uses longitudinal riblets to serve as a launch-pad for studying wall-bounded turbulence owing to this intriguing behaviour. We also explore laminar flows over rough walls, because of their significance to applications such as heat exchange, lubrication, and biological flows, and also because of the low resolution requirements for computing laminar solutions.

An outline of the remaining chapters in this thesis is included at the end of this

chapter.

1.2 Structural description of turbulence

For a long time, turbulence has been known to consist of structures called eddies, which go from flow scales down to viscous scales. These eddies are split into families of self-similar attached and detached structures (Townsend, 1976; Perry et al., 1986). The mean velocity profile in the near-wall region and the inertial sublayer observed in experiments (Marusic et al., 2013) affirm this scaling. Perry and Marusic (1995) attempted to construct turbulent flow fields by adding ad-hoc vortical structures; but these structures have no basis in the governing equations, and their coefficients have to be fixed using experimental data.

Common techniques to extract dynamical information from numerical or experimental data are modal analysis methods such as Principal Orthogonal Decomposition (POD) or Dynamic Mode Decomposition (DMD) to obtain flow structures with the largest energy content (Taira et al., 2017). POD (sometimes referred to as PCA, principal component analysis) involves subjecting a collection of snapshots of a flowfield, say $X = [x_0, x_1, \cdots, x_N]$ for a column vector x_n representing the flowfield at a time t_n, to a singular value decomposition (SVD), $X = U\Sigma V^H$; here, V^H represents the conjugate transpose of the matrix V. Columns of the matrix U, the left singular vectors, are orthogonal and produce a complete basis for the space spanned by the state-vectors x_n. The columns of U are arranged such that the first column captures the most energetic structure in the snapshots (provided the induced norm used in the SVD is defined to be the energy of the flowfield), the second column captures the most energetic structure in the subspace orthogonal to the first column, and so on. A low-order representation of the flow can be obtained by keeping only the leading, say m, singular vectors.

Dynamic mode decomposition (DMD) also acts on snapshots of data to produce a complete basis. Unlike the basis vectors from POD, these vectors are not necessarily orthogonal; however, each mode evolves with a fixed oscillation frequency and

growth/decay rate. This is accomplished by finding a linear operator $A(\delta t)$, where $\delta t = t_n - t_{n-1}$ for the simple case of constant time intervals in the recorded data, in a least-squares sense such that the state-vector for any time t_n is given by $x_n = A\delta t x_{n-1}$. Eigenvectors of A produce a complete basis for the space spanned by $\{x_0, .., x_N\}$ and evolve according to their corresponding eigenvectors. Thus, DMD produces a linear operator that approximates the evolution of the flow directly from snapshots of the flow without prior knowledge of the governing equations. However, as we shall see in the next section, the dynamics of coherent structures in turbulence involve both a linear amplification about a base flow as well as a non-linear interaction that reinforces the base flow. Modal analyses such as POD and DMD cannot capture the non-linear feedback loop, and are hence inadequate in obtaining a complete dynamical description of turbulence.

The bursting process involving meandering, low-speed, streamwise streaks and streamwise vortices, observed in 1967 by Kline et al. (1967), was speculated to have a critical role in the production of wall-bounded turbulence. The minimal span computations of Jiménez and Moin (1991) showed that turbulence is indeed sensitive to the existence of these structures. They found that turbulence could be sustained only for periodic geometries with spanwize domain sizes larger than about 100 wall units. Whenever turbulence was sustained (in domains larger than 100 wall units), the domain contained the vortex-streak structure, and the mean velocity profiles from these minimal span computations showed good agreement with the empirical velocity profile from experiments up to a wall-normal height of about 40 wall units.

Waleffe (1997) isolated these structures in a periodic cycles, dubbed the self-sustaining process (SSP), and found these structures to be insensitive to the boundary condition; the cycle was isolated for a range of conditions from slip to no-slip in a flow between infinite flat plates, and for sinusoidal shear flow. The SSP involves the generation of streaks and vortices from mean shear; the interaction and instabilities of these structures lead to a breakdown that causes turbulence.

These vortex-streak structures are also obtained from modal analyses involving

linearization about a turbulent mean velocity profile (McKeon and Sharma, 2010; Cossu et al., 2009; Zare et al., 2016, for instance).

1.3 Exact coherent states

The pervasiveness of the vortex-streak structure in wall-bounded flows suggests that it has special significance to the NSE. Aside from the laminar solution (i.e., the linear streamwise velocity profile for plane Couette flow and the quadratic streamwise velocity profile for plane channel flow), exact coherent states (ECS) of the NSE are dominated by these structures (Nagata, 1990; Clever and Busse, 1997; Itano and Toh, 2001; Gibson et al., 2008). ECS of the NSE are useful in not just providing a theoretical basis for the vortex-streak building blocks of turbulence, but have also been envisioned to provide a quantitative description of turbulence dynamics following the investigations of Christiansen et al. (1997) of the simpler Kuramoto-Sivashinsky system highlighting the significance of time-periodic orbits to chaotic flows. A brief review of the literature in relation to the significance of simple, exact, invariant solutions of the NSE is now presented. A comprehensive review has been published by Kawahara et al. (2012).

1.3.1 Transition to turbulence

Transition from laminar to turbulent flow is a classical problem of fluid mechanics. Early investigations of laminar-turbulent transition had been restricted to a linear analysis of the evolution of infinitesimal modal perturbations (usually Fourier modes in time and one or two spatial dimensions) introduced to the laminar solution (Schmid and Henningson, 2001; Drazin and Reid, 2004). An eigenvalue analysis of the evolution of such modal perturbations can tell us if a particular perturbation decays or grows, i.e., if the flow returns to the laminar state or departs from it. This approach predicts that plane Poiseuille flow, for instance, is stable under all perturbations for Reynolds numbers less than ≈ 5772; however, transition to turbulence occurs at much lower Reynolds numbers.

Non-normality of the linearized Navier-Stokes operator means that small perturbations can see significant transient growth even when the linearized NSE are asymptotically stable (i.e., all perturbations decay to zero for sufficiently large times). This happens because the sum of individually decaying eigenmodes of the linear operator can show a short-term increase in energy if the eigenmodes are not orthogonal to each other, even though the evolution of each eigenmode is independent of the others. Such transient growth can then lead to non-linear evolution of the perturbations and eventually to turbulence. Such transition to turbulence is facilitated by the existence of finite-amplitude, exact solutions of the Navier-Stokes equation which lie close to the laminar solution (Waleffe, 1995).

A major obstacle to finding non-laminar exact solutions of the NSE is that there appear to be no such stable solutions, so that they are not easily realized in experiment or in DNS. Nagata (1990) worked around this problem using homotopy from the circular Taylor-Couette system to plane Couette flow (PCoF). The laminar solution in Taylor-Couette flow bifurcates into (stable) Taylor-vortex flow involving axial vortices, which further bifurcates into a three-dimensional wavy-vortex flow. The Newton-Raphson method was used to continue the solutions between the geometries; the Newton-Raphson method, or its variants, are used in most works involving finding exact invariant solutions of the NSE. The instabilities of these equilibria lead to time-periodic solutions, as well as travelling wave solutions asymmetric about the centerline (Clever and Busse, 1997). All of these solutions prominently feature the vortex-streak structure. The longitudinal vortex structure observed in these solutions was stabilized in experiments by Bottin et al. (1998).

Studies of the lifetimes of finite-amplitude, three-dimensional perturbations suggest that a boundary (or edge) seems to exist in (an appropriately identified) state-space which separates initial conditions that decay to the laminar state and initial conditions that support long-lived turbulence. The boundary itself seems to be formed by some of the exact invariant solutions and their stable manifolds (Schmiegel and Eckhardt, 1997; Skufca et al., 2006; Wang et al., 2007; Eckhardt et al., 2008), produc-

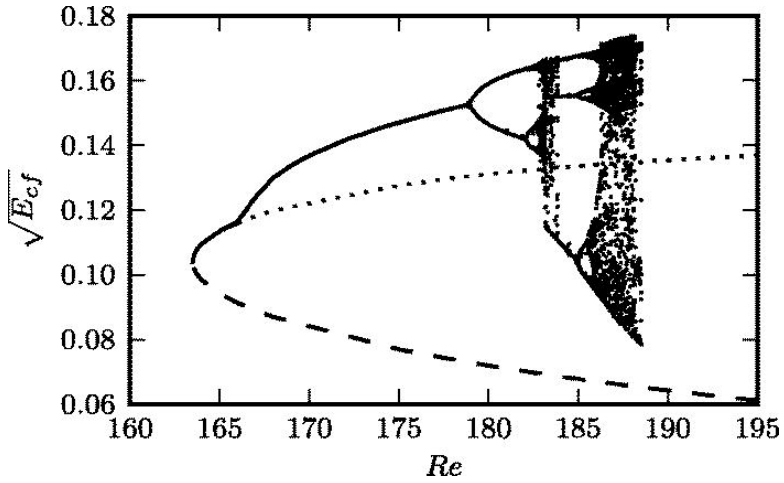

Figure 1.1: Emergence of equilibria and limit cycles in the linearly stable regime of plane Couette flow. The square-root of cross-flow energy $\sqrt{E_{cf}}$ is plotted. The lower branch (dashed) and upper branch (solid when stable, then dotted) equilibria appear in a saddle node bifurcation. The upper branch loses stability in a Hopf bifurcation producing a limit cycle that undergoes a period doubling cascade. Reproduced with permission from Kreilos and Eckhardt (2012)

ing a chaotic repeller that results in decay (to laminar solution) of initial conditions on one side, and "breakdown to turbulence" on the other. Stable (unstable) manifolds of an exact invariant solution are sets of initial conditions that converge to the solution in positive (negative) time. The invariant solutions which separate state-space into initial conditions that breakdown to turbulence and those that decay to laminar flow are called edge-states, and their stable manifolds make up the edge.

Evidence for this basin boundary, as well as embedded saddle-node edge-states, for boundary layer flows has also been found (Kreilos et al., 2016; Khapko et al., 2016). In the evolution of finite-amplitude, three-dimensional initial conditions, a large network of connections emerges between some of the equilibria, with the number of equilibria and their connections increasing with Reynolds number (see fig. 5 in Eckhardt et al., 2008). This suggests that the breakdown to turbulence could also be guided by these connected equilibria.

These results provide a strong link between transition to turbulence and the appearance and organization of exact invariant solutions of the NSE.

1.3.2 Near-wall cycle

Turbulent flows have hairpin-like vortex structures embedded in them, distributed most prominently in the buffer and log layers, with some evidence for their existence even in the wake layer (Adrian, 2007). These hairpin structures are found to be generated by interactions of long, weak streamwise vortices and low speed streamwise streaks (Zhou et al., 1999), suggesting that these vortex-streak structures could be a basic building block of wall-turbulence. Minimal channel DNS of Jiménez and Moin (1991), where the periodic domain of channel flow simulations was reduced until turbulence could no longer be sustained, revealed that the existence of turbulent flow was sensitive to the presence of these vortex-streak structures. When the domain size was too small for these structures to persist, turbulence could not be sustained.

The interactions between low-speed streamwise streaks and streamwise vortices leading to a regeneration cycle of near-wall turbulence was found in similar minimal channel DNS (Hamilton et al., 1995). A recurring flow pattern, labelled the "self sustaining process" (SSP), was isolated in minimal channel DNS by Waleffe (1997) to better illustrate the dynamics of turbulence. The SSP was found to be insensitive to the boundary conditions imposed, suggesting that it is generic to wall-turbulence.

In addition to exact recurring solutions (time-periodic solutions), spatially invariant solutions such as equilibria and travelling wave solutions (TWS) were also found for a sinusoidal shear flow, plane Couette, and channel flows (Waleffe, 2003); the solutions could be smoothly continued amongst plane shear flows with different boundary conditions, suggesting universality of their structure. These exact invariant solutions (equilibria and TWS), along with their stable and unstable manifolds, can describe dynamically important turbulence processes such as bursting (Itano and Toh, 2001), and capture the main structural and statistical features of turbulent flows (Waleffe, 2002). Exact invariant solutions have also been computed in relatively higher Reynolds number channel flow ($Re_\tau \lessapprox 1000$) by Hwang et al. (2016); the upper branch equilibrium is found to be a good proxy for turbulent flow at this Reynolds number.

Travelling wave solutions for pipe flows were computed by Faisst and Eckhardt (2003); Wedin and Kerswell (2004), obtaining solutions of different rotational symmetries. As with channel flows, turbulence trajectories were found to often visit neighbourhoods of these solutions. These solutions appear at Reynolds numbers that are about half as small as the Reynolds numbers where turbulence is sustained, and are immediately unstable.

The exact solutions mentioned so far are global (periodic) solutions. Solutions localized in the spanwise and streamwise solutions have also been found (Willis and Kerswell, 2008; Duguet et al., 2009; Schneider et al., 2010b; Gibson and Brand, 2014). These localized solutions lie between the laminar state and the region of turbulent states, and appear to primarily serve to nucleate turbulence. These solutions emerge in symmetry-breaking bifurcations from global, periodic solutions Chantry et al. (2014) or through the contamination of long wavelength solutions by $\mathcal{O}(1)$ wavelength solutions leading to snaking (Schneider et al., 2010a).

1.3.3 Organization in state-space

Nagata (1990) found two finite-amplitude, three-dimensional equilibria of NSE for PCoF, and classified them as upper branch and lower branch solutions which appear abruptly as a pair at a Reynolds number ≈ 500; the upper branch solutions have a greater strain-rate at the wall than the lower branch solutions. Jiménez et al. (2005) compiled a larger set of such equilibria and classified them into vortex-dominated and streak-dominated solutions based on the maxima of the fluctuating wall-normal velocity and streamwise velocity; the upper branch solutions correspond to vortex-dominated solutions, and lower branch to streak-dominated solutions.

The upper and lower branch solutions appear in a saddle-node bifurcation (Kreilos and Eckhardt, 2012) at a Reynolds number ~ 168. Lower branch solutions are immediately unstable upon appearance, and often lie on the laminar-turbulent basin of separation. Upper branch solutions, on the other hand, can sometimes start off being linearly stable, and become unstable in a Hopf bifurcation, producing limit cycles

that quickly undergo period-doubling with increasing Reynolds number. The upper branch solutions themselves are embedded in the regions that are densely visited by turbulent flow. Excursions to lower branch solutions have been found to represent hibernating turbulence (Park and Graham, 2015).

Equilibria and TWS resemble quiescent periods of turbulence, while their stable and unstable manifolds correspond to the bursting process (Itano and Toh, 2001; Jiménez et al., 2005). A more comprehensive picture of the dynamics is provided by time-periodic and relative time-periodic solutions (Kawahara et al., 2006; Viswanath, 2007). Relative periodic solutions are time-periodic solutions with a drift in the streamwise and/or spanwise directions.

A phase-portrait of trajectories starting close to equilibria reveals an elegant visualization of turbulence. Heteroclinic orbits exist: starting close to one equilibrium, their unstable manifolds lead away from this solution towards another equilibrium. Turbulent flow can then be visualized as a set of trajectories often visiting the neighbourhoods of equilibria, TWS, and unstable time-periodic orbits (Gibson et al., 2008; Chandler and Kerswell, 2013; Cvitanović, 2013). Thus, the role of these solutions is to partition the infinite dimensional state-space into a finite set of neighbourhoods that are visited by long-time turbulence. Recent experimental evidence due to Suri et al. (2017) reinforces this description of the role of exact solutions.

1.3.4 Coherent structures at high Reynolds numbers: Vortex-wave interactions

The exact invariant solutions, also referred to in more general terms as exact coherent structures, discussed so far are at low Reynolds numbers (~ 1000). Wang et al. (2007) extended a lower branch equilibrium of PCoF to higher Reynolds numbers ($\sim 50,000$) to study the asymptotic Re-scaling of lower branch states; for $Re > 6168$, only the fundamental streamwise Fourier mode was retained. The lower branch state is composed of $O(1)$ streamwise streaks and $O(Re^{-1})$ streamwise rolls, both of which are streamwise-homogeneous, and the streamwise-varying fundamental mode ($e^{i\alpha x}$,

where $2\pi/\alpha$ is the streamwise periodicity) whose energy scales as $O(Re^{-0.9})$. Higher harmonics decay faster than Re^{-1}, making their contributions insignificant at higher Re. The spatial structure of the (streamwise) homogeneous and fundamental modes also collapse when scaled by Re.

High Re simulations are expensive due to the resolution required to capture the smallest scales. The results of Wang et al. (2007) suggest that, at least where lower branch states are concerned, it is reasonable to seek asymptotic solutions at high Re by truncating higher harmonics in the streamwise direction. In this context, Hall and Sherwin (2010) revisited the vortex-wave interaction mechanism formalised by Hall and Smith (1991), where a neutrally-stable travelling wave exists as an eigenmode of the streamwise-homogeneous streaks based in a narrow critical layer of $O(Re^{-1/3})$. For symmetrical (about the centerline) streaks in PCoF, the appropriate critical layer is that of zero wave-speed. These critical-layer-based waves feed energy into the streamwise rolls, which in turn sustain the streamwise streaks in the presence of a mean shear; this mechanism is not unlike the self-sustaining process of Waleffe (1997).

The existence of the neutrally-stable wave is crucial, because in the absence of forcing, the streamwise-homogeneous streak-roll system decays to the laminar state. Indeed, the significance of forcing is not unexpected. Early approaches to finding exact coherent structures in low Re flows involved introducing a forcing to the NSE that stabilize the solutions; the homotopy of Nagata (1990) from Taylor-Couette flow can be seen as including a centrifugal body force, while the first solutions found by Waleffe and co-workers (Waleffe, 1997, 2002, 2003) were arrived at by including sinusoidal body forcing. Exact coherent states stabilized in "forced" flows are then continued to the flow of interest, plane Couette flow or channel flow, by slowly turning off the forcing terms and using the Newton-Raphson method (or its variants). However, the neutrally-stable wave of the vortex-wave interaction described by Hall and Sherwin (2010) evolves at a smaller time scale and is concentrated in a thin critical layer due to the high Re at which asymptotic solutions are sought.

In the past several years, VWI theory (Vortex-Wave Interaction theory) has seen

significant improvements to allow dealing with asymptotic behaviour of upper branch states, coherent states in arbitrary shear flows, and localization of exact coherent structures (e.g. Blackburn et al., 2013; Deguchi and Hall, 2014; Dempsey et al., 2016). Existence of long streamwise wavelength structures with multiple-scale dynamics has been reported (Deguchi and Hall, 2014, 2017), which are speculated to represent outer-layer and free-stream coherent structures in wall-bounded turbulence, unlike the low-Re exact solutions in the literature, which are limited to descriptions of the near-wall cycle.

1.4 Turbulence over rough walls

The classical view of roughness effects has been that it acts by changing only the friction velocity (the stress at the wall), and that the mean velocity, turbulent kinetic energy (TKE), and Reynolds shear stress (RSS) profiles collapse when scaled with the new friction velocity. The mean velocity of the turbulent flow over a smooth walled flat plate (or in a fully developed channel or a pipe) is given as (Townsend, 1956; Jiménez, 2004):

$$\frac{U}{u^*} = \kappa^{-1} log(y^+) + A + \Pi\kappa^{-1} W(y/\delta) \tag{1.4.1}$$

where the last term in the right-hand-side represents a wake function which reflect the outer-layer dynamics. The first term is the log-law for the inertial sublayer, and the second term represents a net-effect of the viscous sublayer and the buffer layer. This equation is held to be valid for the log-layer and beyond. $\kappa \approx 0.4$ is the Kaŕmań constant, and the value of the constant A is given as 5.1 (Jiménez, 2004; Pope, 2000).

Several studies have shown the validity of Townsend's outer layer similarity hypothesis (for instance Schultz and Flack, 2005; Allen et al., 2007; Flack et al., 2005). In this case, it must be possible to express the mean velocity for flow over a rough wall in a form similar to that of a smooth wall, provided the near-wall effects of roughness are properly accounted for. From his early experimental studies of flows in rough pipes, with carefully graded, closely packed sand, Nikuradse (1950) found that the

log-law for the mean velocity is valid even for flows over rough walls, with the same value for the Kármán constant. He gave the following equation for the mean velocity of rough-walled flows (for the fully rough case):

$$\frac{U}{u^*} = \kappa^{-1} log(y/k_s) + 8.1 + \Pi\kappa^{-1} W(y/\delta) \tag{1.4.2}$$

Here, the value of the constant A is changed to 8.1 from the smooth wall value of 5.1. The wall-normal distance is not scaled in the inner units, but instead by a roughness parameter, k_s, the height of the sand-grain roughness. The same equation is used today for other types of roughness, and the parameter k_s that gives the shift in the velocity profile is called the 'equivalent' or 'effective' sand roughness. Jiménez (2004) discusses variations of this equation to highlight different aspects of the roughness and its effects.

Before further discussing the effects of surface-roughness, it is essential to identify if and when the effects of roughness merit consideration. Hutchings (1992) reported that the RMS roughness of industrial surfaces ranges from $0.05\mu m$ to $25\mu m$. In eq. (1.4.2), it is clear that the scaling for the mean velocity is not dependent on the viscosity (or Re). The regime in which such an equation holds for flows over rough surfaces is referred to as the fully rough regime. The flow over a rough wall becomes fully rough when the (average) height of the roughness elements is more than ~ 100 wall-units. When the size of the roughness elements is smaller than one wall-unit, the flow may be considered to be aerodynamically smooth; and the regime between aerodynamically smooth and fully rough-flows is referred to as transitionally rough (Jiménez, 2004).

Nikuradse (1950) found from his experiments that as a flow became transitionally rough, the friction factor (defined below) became larger than that for a smooth-walled flow at the same Reynolds number. This increase is explained by the increased dissipation caused by the flow over roughness elements compared to the dissipation in flow over smooth walls. As the size of roughness elements relative to the viscous

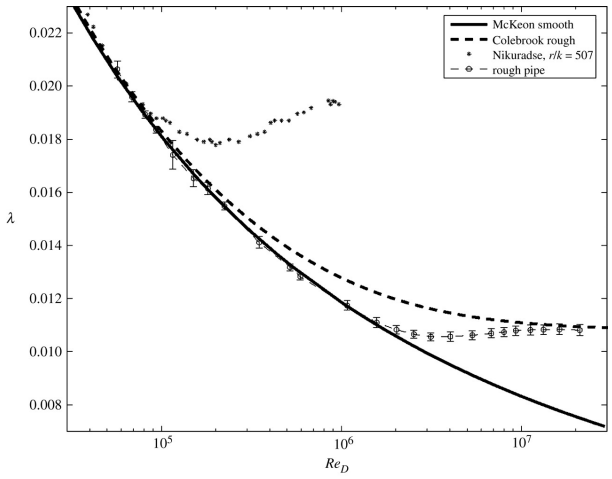

Figure 1.2: Friction factor λ in the transitionally rough regime from Allen et al. (2007). Curves shown are for the experimental data of Allen et al. (2007), Colebrook's curve for the same k_s, the smooth-wall relation of McKeon et al. (2005), and the results for the smallest sand-grain roughness used by Nikuradse (1930)

length increases, the form drag dominates the viscous friction, until the viscous friction becomes negligible compared to the form drag (Jiménez, 2004). Colebrook (1939) gave an empirical curve fit to relate the friction factor of a pipe to the roughness parameters, based on experimental data available at the time:

$$\frac{1}{\sqrt{\lambda}} = 1.74 - 2log(\frac{k_s}{R} + \frac{18.6}{Re_D\sqrt{\lambda}}) \tag{1.4.3}$$

where, k_s is the equivalent Nikuradse sand-grain roughness value for the surface, and λ is the friction factor, defined as:

$$\lambda = \frac{-\frac{dp}{dx}D}{\frac{1}{2}\rho\bar{U}^2} \tag{1.4.4}$$

where, dp/dx represents the mean pressure gradient in the pipe, D is the diameter, ρ is the density, and $\bar{U}$ is the average bulk velocity.

Colebrook's curve describes a monotonic decrease of the friction factor as Re increases, with the flow going from aerodynamically smooth to transitionally rough to fully rough. For any specific rough surface, the lowest friction factor is reached in the fully rough regime (this friction factor is still higher than the friction factor for smooth-walled flows at the same Re), where Re becomes irrelevant. Allen et al. (2007)

reported that this is not the case, as shown in fig. 1.2. The friction factor does not show a monotonic decrease. The point of departure of the friction factor from the curve for a smooth-walled flow is at a much higher Re than what is predicted by the Colebrook curve. At the actual point of departure, Colebrook's curve overestimates the friction factor by approximately 10%. They attribute this discrepancy to the difficulties involved in accurately measuring the friction factor (or the wall-stress) in high Re flows. They also report that the critical k_s^+, the effective roughness at which the flow goes from aerodynamically smooth to transitionally rough, is about 3.5, whereas Colebrook's equation predicts that the critical roughness can be as low as 0.05.

The equation for the mean velocity for flow over a rough wall (Nikuradse, 1950; Jiménez, 2004),

$$\frac{U}{u^*} = \kappa^{-1} log(y/k_s) + 8.1 + \Pi\kappa^{-1} W(y/\delta) \tag{1.4.5}$$

is also written in a velocity-shift form:

$$\frac{U}{u^*} = \kappa^{-1} log(y^+) + 5.1 + \Pi\kappa^{-1} W(y/\delta) - \Delta U^+ \tag{1.4.6}$$

where ΔU^+ is the downward velocity-shift due to roughness-effects. This form is more meaningful in cases of transitionally rough flows, where there is still some Re-dependence. The velocity shift is given by a roughness function which takes as its argument the equivalent sand roughness, i.e., $\Delta U^+ = f(k_s^+)$. The existence of such roughness functions was demonstrated by Granville (1958), where he considered similarity laws for logarithmic profiles in inner and outer scaling to develop a general relation for the friction coefficient of flat plates with arbitrary roughness in boundary layers. However, he showed, the equivalent sand roughness cannot be based on a single length scale of the roughness, and multiple scales must be considered to account for effects of geometry, texture, etc.. Notable works related to the identification the set of relevant scales, and their effects on the flow, include those by, but not limited to, Schultz and Flack (2005); Townsin and Dey (1990); Ligrani and Moffat (1986); Bandyopadhyay (1987); Gioia and Chakraborty (2006); Gioia and Bombardelli (2001);

Placidi and Ganapathisubramani (2012).

Jiménez (2004) discusses the distinction between two classes of roughness: k-type and d-type. k-type roughness refers to “normal surfaces", for which the effective sand roughness is proportional to the physical dimensions of roughness elements. For these surfaces, an important parameter is the frontal solidity, defined as the ratio of the total projected frontal area of roughness elements to the planform area of the surface. A plan solidity can similarly be defined as the area of projected planform area of roughness elements to total planform area of the surface. Placidi and Ganapathisubramani (2012) stress the importance of frontal solidity over plan solidity, and found that as the frontal solidity increases, the friction coefficient increases and then decreases. Both highly sparse and highly dense surfaces have lower friction coefficients compared to moderately sparsely (or densely) distributed roughness.

For d-type surfaces, first mentioned by Perry et al. (1969), the effective sand roughness (and consequently the friction coefficient) apparently scales with the flow dimensions, instead of just the roughness dimensions. However, it must be noted that the flows considered had a high k/δ, in which case outer layer similarity may not hold. Despite such uncertainties, d-type roughness has received considerable attention, with researchers citing the existence of stable recirculation vortices near the wall that isolate the outer flow from the vortices (Perry et al., 1969; Djenidi et al., 1999; Liou et al., 1990) to explain the apparent anomaly in scaling. Jiménez (2004) speculates that this effect could also be related to the interaction between the near-wall cycle and the LSMs, although such an interaction is yet to be demonstrated.

We have noted that well-resolved flow field data, either experimental or computational, is not easily obtained (Jiménez, 2004), except at low Re, because of a vast separation of scales in turbulent flows. Computational data from low Re simulations, partial flow field data from high Re experiments, linear stability analyses at transitional Re, and asymptotic approximations at very high Re have helped explain and model turbulence statistics. However, a comprehensive understanding of the dynamics of turbulence still eludes us. A relatively young approach to understand turbulence

dynamics is through exact solutions — stationary, travelling, and recurring — of the Navier-Stokes equations. Since the NSE are known to be an excellent physical model for fluid flows, accurate solutions of the equations may be expected to be much more representative of flow dynamics than, say, POD modes of experimental and computational data.

Dynamics of rough-walled turbulence is much less understood compared to smooth-walled turbulence, because scaling laws used in smooth-walled turbulence are inapplicable in the near-wall region of rough-walled flows; and velocity fields in the near-wall region are hard to obtain in experiments, while computational solutions are constrained to low Re. Researchers have attempted to replace the roughness of the wall with velocity boundary conditions at the wall (for instance Choi et al., 1993; Luchini, 2013). Such modelling of surface-roughness can be very useful in engineering applications because of the cost reduction afforded by them. However, these models are designed to replicate the effects of rough-walls only on some average quantities such as the mean velocity at some finite distance from the walls; so, they are of limited use in investigations of the fundamental dynamics of rough-walled turbulence where the resolution of near-wall dynamics is an important consideration.

1.4.1 Drag reduction due to riblets

An interesting, special case of ordered roughness is that of riblets. Riblets are parallel, streamwise grooves on wing-surfaces, and are known for passive drag-reduction (Walsh, 1982) of up to 10%. Numerical studies of flow over riblets are available (such as Walsh, 1983; Choi et al., 1993; Dean and Bhushan, 2010). Tani (1988) considered riblets as a form of roughness, and compared them with Nikuradse's sand roughness. They reported that there is a small range of roughness height relative to viscous length where drag over a rough wall is lower than that over a smooth wall. Bio-inspired herringbone riblets have also been investigated. They show greater drag reduction than streamwise-homogeneous riblets (Chen et al., 2013, 2014). This drag reduction is explained as being due to the displacement of the near-wall vortex-streak structure by

the grooves (Lee and Lee, 2001; Dean and Bhushan, 2010) to sit above the grooves, leading to lower streamwise velocities within the grooves, and consequently lower shear stresses.

1.5 Laminar solutions for rough-walled internal flows

While research has proceeded far enough for time-periodic orbits to be computed at moderate Reynolds numbers in Couette and Poiseuille flows, this holds true only for smooth-walled flows. Exact solutions for rough-walled flows are available only as laminar solutions.

Several researchers used the approximation of Stokes flow to solve for laminar flows over rough walls. The reasoning is that, for infinitesimal roughness, velocities near the wall would be low enough for inertial effects to be negligible (compared to viscous terms). The resulting linear system is then solved with the appropriate boundary conditions. If steady solutions are sought, the Navier-Stokes equation for incompressible flow reduces to a Poisson equation

$$\nabla p = \nu \nabla^2 \boldsymbol{u} \tag{1.5.1}$$

along with the divergence-free condition on the velocity field:

$$\nabla \cdot \boldsymbol{u} = 0 \tag{1.5.2}$$

The Poisson equation can be simplified further to a Laplace equation by invoking symmetries of the flow. For instance, for flow over longitudinal riblets with no mean pressure gradient, a solution can be sought whose streamwise-derivative of pressure (along the riblets) is zero. For flows with a mean pressure gradient, the velocity field may be split into 1) a base field that satisfies the Poisson equation for flat-walled flows, and 2) a correction for the rough wall; then, the correction field is governed by the Laplace equation.

Bechert and Bartenwerfer (1989) solved the Laplace equation, $\partial_{zz}u + \partial_{yy}u = 0$ for the streamwise velocity, for a riblet-mounted boundary layer flow. They compared the velocity fields for (spanwise) periodic riblets to the velocity field for a flat wall. The velocity field for flat-walled flows may be appropriately normalized so that the shear stress at the wall is 1, or that the velocity is given by $u = y$. Their solutions for riblet flows showed that at locations sufficiently far from the wall, the velocity profile becomes linear as $u = y - c$, for some constant c. They argued that the flow sufficiently far away from the wall experiences the riblet-mounted wall simply as a virtual flat wall that is present at $y = c$; hence, riblet-mounted flows may be dealt with by replacing the physical boundary with a virtual plane located at a new origin.

The height for which the riblets extend above this virtual plane is referred to as the *protrusion height*. Drag reduction in riblet-mounted turbulent flows is attributed to protrusion height. The authors postulated that the protruding surface interfered with the near-wall cycle, which seems to be essential for producing wall-turbulence. It is known (Jiménez and Moin, 1991) that the low-speed streaks are crucial for the sustenance of the near-wall cycle, and that imposing external spanwise length scales could work against the cycle. They further advised that riblets with sharper tips are likely to produce better drag reduction than those with rounded tips, since sharper profiles have higher protrusion heights than smoother profiles of the same height. Sharper profiles produce greater protrusion heights since the fluid flowing in the grooves is retarded by lesser surface area (per unit volume of fluid flowing in the groove).

Luchini et al. (1991) compared the protrusion heights, as defined by Bechert and Bartenwerfer (1989), for longitudinal and cross flows. Their results showed that the virtual plane is located higher (closer to tip of corrugations) for flows normal to the corrugations than for flows parallel to corrugations. This is interpreted, for riblet-mounted flows, as secondary cross flows experiencing a greater retardation. The authors pointed out that while the origin itself may be arbitrarily chosen for different cases, the difference in the protrusion heights is not arbitrary, and hence served as a

reliable measure to quantify boundary layer flows.

Sarkar and Prosperetti (1996) solved the Laplace equation for stochastic roughness, modelled by randomly distributed bosses on a smooth surface. Despite the qualitative difference in the surface corrugations from the previous work, they also concluded that for certain forms of roughness, the flow sufficiently far from the wall can be obtained simply by considering a smooth surface displaced into the flow from the location of the rough wall. For other classes of roughness, however, they found that a shifted virtual plane was not sufficient. Surface corrugations could also produce a spanwise force, even when uniformly distributed, provided the profiles of corrugations were asymmetric. They presented a model to substitute the rough wall with (localized) slip boundary conditions on a smooth wall.

Luchini (2013) computed linearized boundary conditions for roughness elements of different profiles and aspect ratios, both in isolation and in periodic arrays. Charts were provided for two non-dimensional coefficients- the protrusion coefficient defined above, and a proximity coefficient to account for interference with surrounding elements- for profiles considered, along with estimates of the influence of aspect ratio on the accuracy of linearized boundary conditions.

Mohammadi and Floryan (2013) used sinusoidal grooves as a first-order approximation for roughness; they found that sinusoidal grooves adequately represent other periodic groove-shapes as well. Three groove configurations are identified: the general case of oblique grooves (grooves not aligned with the mean pressure gradient), and special cases of longitudinal and transverse grooves. The transverse and oblique cases lead to flow separation within the grooves, and for high depth-to-length aspect ratio of the grooves, a "lift-up" of the streamlines is observed so that the flow can be considered to be constricted to a channel or a reduced height; this is not unlike the protrusion height of Bechert and Bartenwerfer (1989); Luchini et al. (1991). Oblique grooves also produce spanwise currents due to the asymmetrical alignment, and these currents are greatest when the grooves are aligned at an angle of $\approx 42\,\mathrm{deg}$ with the mean pressure gradient.

Islam et al. (2015) computed full non-linear laminar solutions for axisymmetric pipe flow with periodically varying diameter, for different profiles of diametric variation. Onset of separation was noted for different profiles, along with the appearance of a second recirculation vortex for large diametric variations. However, only a limited range of parameters was explored in the work.

Laminar flow in channels with streamwise corrugations (furrows) has two routes to turbulence that are directly influenced by the near-wall flow (Nishimura et al. (1990); Gschwind et al. (1995); Blancher et al. (2015):

1. Kelvin-Helmholtz instability of the shear layer formed in the separated flow inside furrows. The flow remains 2-D during the initial growth of disturbances.

2. Centrifugal instability on concave surfaces, resulting in Taylor-Goertler vortices (Saric, 1994). This instability makes the flow 3-D. Gschwind et al. (1995) indicated that this instability enhanced mixing and heat-transfer for small pressure-drop flows where turbulence could not be completely sustained.

There is significant interest in understanding the stability of laminar solutions of riblet-mounted flows, because of the drag reduction reported in the literature for turbulent flows in such geometries. Chu and Karniadakis (1993) performed DNS to compute solutions for riblet flows in the laminar, transitional, and turbulent regimes. They reported no drag reduction for the laminar case, but reported about 6% drag reduction for the turbulent case. However, Moradi and Floryan (2014) reported drag reduction for the laminar case as well, when the wavelength of the (sinusoidal) riblets was large enough compared to channel half-height. This is explained as a result of increased local mass flux in streamtubes in wider sections of the channels compared to the mean.

Moradi and Floryan (2014) also performed a linear stability analysis of their laminar solutions. They used the appearance of linear instability as an indicator for an increase in drag. Riblet-geometries with critical Reynolds number greater than that for smooth channels were considered to be drag-reducing. For riblets with wavenum-

bers less than 4.22 (non-dimensionalized by channel half-height), the critical Reynolds number was found to increase with increasing groove-amplitude . Kasliwal et al. (2012) used a similar geometry, with similar motivations, and reported a reduction in wall shear stress; however, if the total drag decreases when integrated over the surface area of the riblet is not clear.

1.6 Concluding remarks

For smooth-walled flows, the vortex-streak structures that are ever-present in turbulent flow have a special relation to the NSE; they resemble exact invariant solutions. We can expect exact invariant solutions of the NSE in rough-walled geometries to contain structures that are dynamically important to rough-walled turbulence. Finding such structures is not a trivial task.

In fact, finding exact invariant solutions of the NSE in rough-walled geometries is a natural extension to the literature, considering the increasing success of the dynamical systems approach to turbulence. The primary obstacle to finding exact invariant solutions stems from the instability of most of these solutions in flows of interest. Iterative schemes for solving non-linear systems such as the Newton-Raphson method need good initial guesses to achieve convergence. Fortunately, a large database of exact invariant solutions is available for smooth-walled flows. Presumably, a major hurdle has already been overcome.

The vast set of possible roughness geometries means that the solutions of one class of geometries may not provide a reliable description of the near-wall dynamics of another class. A good starting point to systematically investigate the effect of surface-roughness is the simple case of longitudinal grooves (riblets). The observed drag reduction due to riblets provides additional motivation to undertake this study. Earlier work indicates that the drag reduction in such geometries is due to a displacement of the vortex-streak structure out of the grooves. It will be interesting to see if this displacement can be captured in the continuation of exact invariant solutions from smooth-walled flows to flows with longitudinal grooves (riblets).

It is in this context that the present author has found it appealing to develop a solver to compute exact invariant solutions for grooved plane shear flows. As a first step, the even simpler case of laminar solutions for grooved channel flows are computed, and then we move on to non-laminar equilibria of grooved plane Couette flow.

1.7 Outline of the thesis

The numerical method used in this thesis to compute exact invariant solutions for plane shear flows with grooved walls is described in chapter 2. The steady state Navier-Stokes equations are solved, with the divergence-free constraint, using a domain transformation method for a particular class of grooved walls — "in-phase grooves" — and an exact Newton method using full-rank inversion for solving the linear equation. A brief discussion of the symmetries of plane Couette flow is included. This method is illustrated for the case of laminar solutions in channels with transverse grooves. All of the related exact invariant solutions found in the literature have been computed using a time-stepping DNS solver, as opposed to the steady-state solver used in this thesis. The reasons for using the steady-state solver are given at the end of the chapter, along with a brief discussion of the failure of matrix-free methods when used with the steady-state solver. Convergence properties of the numerical method for laminar flows are briefly discussed in appendix A.

Appendix C, is included in the appendix to discuss DNS solvers and matrix-free methods. A significant part of the chapter is devoted to a discussion of "Channel Flow" by Gibson (2014), an open-source solver for finding these solutions in Couette and channel flows. This appended chapter complements the review of the literature on ECS and provides context to the discussion on the limitations of the steady-state solver described in the thesis.

Chapter 3 presents solutions for laminar flows in grooved channels, including analytical solutions obtained for long wavenumber grooves under the Stokes flow approximation. These solutions complement those available in the literature for grooved

channel flows. In particular, the analytical solution is accurate to second order in the wavenumber, as opposed to the first order accuracy that is common in such solutions. The steady-state solver can also compute at high Reynolds numbers (~ 5000) where the laminar solution is unstable, which could be used to produce base flows for studies of transition.

Three-dimensional exact invariant solutions for plane Couette flow with longitudinal grooves are discussed in chapter 4. Owing to the computational expense of the matrix-based method, the number of solutions that could be found was rather low. However, the few solutions that were continued demonstrate a drag reduction associated with grooves smaller than the characteristic size of the vortex-streak structure, and a symmetry based anchoring of the structure.

The final chapter, chapter 5, summarizes the main conclusions of the present work, includes pointers to more grooved flow cases that could be run with the present solver, and highlights some of the important questions raised in this thesis. The author also indulges in some speculation regarding drag reduction in geometries that could not be investigated in the present work.

Chapter 2

Methodology — Grooved plane shear flows

> *In judging policies, we should consider the results that have been achieved through them, rather than the means by which they have been executed.*
>
> Niccoló Machiavelli

Plane shear flows are often used to investigate the dynamics of turbulence and transition to turbulence; this is because of their lower computational expense which springs from their compatibility with spectral methods. The non-homogeneity produced by grooved (and rough) walls precludes direct application of the Fourier spectral method for discretization in the streamwise and spanwise directions. The present work employs a domain transformation method to map the grooved plane shear flow geometry to a smooth-walled geometry, so that the Fourier spectral method can be used to discretize the mapped domain.

This thesis deals with two classes of steady-state solutions, investigated in the next two chapters. The first, termed "laminar solution" in this thesis, is the highly symmetric quasi-1d steady solution: $U(x, y, z) = 1 - y^2$ for channel flow, and $U(x, y, z) = y$ for Couette flow (assuming appropriate non-dimensionalization and coordinate frame). This solution is sometimes called the "base flow". Continuation of this solution to

grooved channel flow is the subject of chapter 3. In channels with longitudinal grooves, the velocity field for this solution has the form $[u, v, w] = [u(y, z), 0, 0]$. In channels with transverse grooves, the velocity field takes the form $[u, v, w] = [u(x, y), v(x, y), 0]$. The laminar solution is identified as the one with the most number of symmetries, and as the one continuing from the smooth-walled laminar solutions mentioned earlier.

The second class of solutions is the more complex 3-dimensional equilibria discussed in § 1.3. These solutions are also laminar because of the "smoothness" of the velocity field (and the fact that they are not actually turbulent). However, to avoid confusing these with the quasi-1d or quasi-2d laminar solutions mentioned above, these 3d steady solutions are exclusively referred to as "equilibria".

The aim of the present work is to see **if** existing exact invariant solutions can be continued from smooth to rough walled flows. The most direct way to explore this question is to solve the steady-state NSE, using the Newton method to allow continuation of solutions. One could be sceptical about the numerical stability and feasibility of such an approach. The symmetries and smoothness of the laminar solution, and the associated low dimensionality of state-space, makes laminar flows a good choice for exploring such questions.

2.0.1 Overview

This chapter is organized as follows. The basics of computing exact invariant solutions for smooth-walled plane shear flows is outlined in § 2.1; the discussion on DNS solvers and matrix-free methods is pushed to appendix C. The symmetries of plane Couette flow (PCoF) are important to computing and interpreting equilibria of PCoF; these are discussed in § 2.2 for smooth PCoF. Geometries for grooved channel flows and grooved PCoF investigated in this thesis are described in § 2.3. The domain transformation method and the accompanying spectral discretization are also outlined in this section. In § 2.4, modifications to each of the terms in the governing equations due to the domain transformation are shown, and in § 2.5, the discretized system along with the iterative scheme are described. To keep the equations short, they are

presented for only the special case of laminar solution in channels with transverse grooves.

The modifications to be made to the numerical method to compute laminar solutions for oblique grooves are outlined in § 2.6. Similarly, the changes needed to accommodate the equilibria of grooved PCoF are described in § 2.7. Details of the iterative scheme such as parametric continuation and convergence criteria are given in § 2.8.

Exact invariant solutions for smooth-walled plane shear flows known in the literature have all been found using a DNS engine (Kawahara et al. (2012)) that produced a time-t map of initial conditions as defined in § 2.1.1. These methods are briefly discussed in appendix C. The solver used in the present work is a steady-state solver, and involves storing and inverting the Jacobians. The reasons for using such a solver, and its limitations, are presented in § 2.9.

An alternative to the domain transformation method, which is used in this thesis, is the immersed boundary method (IBM). In IBM, a larger flow domain that extends beyond the contours of the wall is defined so that the full domain resembles that of smooth-walled plane shear flows. The boundary conditions of eq. (2.3.4) are imposed by modifying the boundary conditions at the edges of the enclosing domain. The present work does not contrast between the efficiency of the two methods for solving grooved plane shear flows; see Mohammadi and Floryan (2013) for comments on the suitability of each method to grooved plane shear flows.

2.1 Smooth-walled plane shear flows

2.1.1 Types of ECS

Several types of exact coherent states (ECS) are discussed in the literature. To define these, we first define the evolution of the flow in terms of time-t map, $\mathbf{f}^t(\mathbf{u})$ (following the notation of Gibson et al. (2008)) as

$$\mathbf{f}^t(\mathbf{u}) = \mathbf{u} + \int_0^t \mathbf{F}(\mathbf{u}) \quad d\tau, \qquad \text{where } \mathbf{F}(\mathbf{u}) := \frac{\partial \mathbf{u}}{\partial t}, \tag{2.1.1}$$

and $\mathbf{u}$ is the state-vector (discretized velocity field).

Different types of ECS can be defined for these maps.

1. Equilibria: $\mathbf{F}(\mathbf{u}_{EQ}) = 0$, or $\mathbf{f}^t(\mathbf{u}_{EQ}) = \mathbf{u}_{EQ}$ for all time, $t \in \mathbb{R}$.

2. Travelling wave (or relative equilibria) propagating at a phase velocity of $\mathbf{c} = (c_x, 0, c_z)$: $\mathbf{F}(\mathbf{u}_{TW}) = (-\mathbf{c} \cdot \nabla)\mathbf{u}_{TW}$, or $\mathbf{f}^t(\mathbf{u}_{TW}) = \tau(c_x t, c_z t)\mathbf{u}_{TW}$ for all time, $t \in \mathbb{R}$.

3. Periodic orbit with period T_p: $\mathbf{f}^{T_p}(\mathbf{u}_p) = \mathbf{u}_p$.

4. Periodic orbit with period T_p and shift $\tau_p = (l_x, l_z)$: $\mathbf{f}^{T_p}(\mathbf{u}_p) = \tau_p \mathbf{u}_p$.

The time-t map, $\mathbf{f}^t$, is often generated through a DNS solver. In this thesis, we do not generate time-t maps. Instead, a steady-state solver is used, and the instantaneous time derivative is used as the criterion for identifying equilibria (or laminar solutions). So far, we have used two terms, exact invariant solutions and exact coherent states. The former is often used in the literature to refer to equilibria and travelling wave solutions to highlight their time-invariance of their evolution. The latter refers to any solution of the NSE that contains a coherent structure (the vortex-streak structure in all known solutions); the most prominent solution of the NSE for wall-bounded shear flows that is not considered an ECS is the laminar solution.

2.1.2 Governing equations

The plane shear flows investigated in this thesis are restricted to low-speed Newtonian flows with no temperature gradients. For such flows, the Navier-Stokes equations, along with the continuity equation, can be written in Cartesian coordinates in non-dimensional form, using ∂_s to represent partial derivatives with respect to a scalar s, as

$$\begin{aligned} \partial_t u^j + (u^k \partial_{x_k}) u^j &= -\frac{dP}{dx_1}\delta_{1j} - \partial_{x_j} p + \frac{1}{Re}\Delta u^j, \qquad j = 1,2,3 \\ \partial_{x_k} u^k &= 0, \end{aligned} \tag{2.1.2}$$

using Einstein summation notation, with $(x_1, x_2, x_3) = (x, y, z)$, the streamwise, wall-normal, and spanwise coordinates, and $(u^1, u^2, u^3) = (u, v, w)$, the streamwise, wall-normal, and spanwise velocity components respectively. The origin is located on a plane located half-way between the two walls. The mean pressure gradient, $\frac{dP}{dx}$ is explicitly accounted for so that the fluctuating pressure, p, remains homogeneous for flows with a mean pressure gradient. The factor δ_{1j} in the mean pressure gradient term represents the Kronecker delta. The lengths, velocities, and pressure are non-dimensionalized as

$$u^k = \frac{\hat{u}^k}{\hat{U_{CL}}}, \quad x_k = \frac{\hat{x}_k}{\hat{h}}, p = \frac{\hat{p}}{\hat{\rho}\hat{U}_{CL}^2}, \quad t = \frac{\hat{t}\hat{U}_{CL}}{\hat{h}}, \tag{2.1.3}$$

where hatted symbols represent dimensional quantities; $\hat{h}$ is half the distance between the walls in channel and Couette flows; $\hat{U}_{CL}$ is the centerline velocity in channel flows, and half the relative speed of the walls in Couette flows; $\hat{\rho}$ is the density of the flow. The Reynolds number Re in eq. (2.1.2) is defined as

$$Re = \frac{\hat{U}_{CL}\hat{h}}{\hat{\nu}}, \tag{2.1.4}$$

where $\hat{\nu}$ is the kinematic viscosity of the fluid.

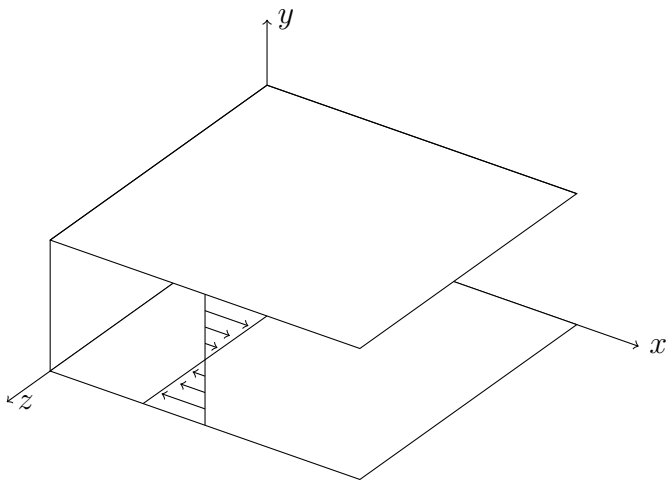

Figure 2.1: Plane Couette flow: fluid flow between two infinite parallel walls moving in-plane in opposite directions. The coordinate frame is chosen such that the (non-dimensional) speed of the walls is ± 1 in the x-axis, and the walls are at $y = \pm 1$.

The boundary conditions are

$$u(y=\pm 1) = \begin{cases} 0, \text{ channel flow,} \\ \pm 1, \text{ Couette flow,} \end{cases} \qquad v(y=\pm 1) = 0$$
$$w(y=\pm 1) = 0, \qquad \nabla \cdot \mathbf{u}(y=\pm 1) = 0 \tag{2.1.5}$$

2.2 Flow symmetries

2.2.1 Continuous symmetries

The present work is focused on finding equilibria in plane Couette flows (PCoF) with longitudinal grooves. The continuous symmetries discussed here apply to both Couette flows and channel flows, while the discrete symmetries discussed later apply only to Couette flows; however, similar symmetry transformations can be identified for channel flows too. Smooth-walled plane Couette flow (illustrated in fig. 2.1) involves infinite, parallel plates moving in opposite directions. This allows for solutions that are invariant under certain symmetry transformations; we follow the notation of Gibson et al. (2009) to represent these symmetries. Homogeneity in the streamwise and spanwise directions leads to admission of solutions that are invariant under continuous translation in the $x-z$ plane; the symmetry transformations for these translations become the continuous two-parameter group $SO(2)_x \times SO(2)_z$, denoted by

$$\tau(l_x, l_z)[u, v, w](x, y, z) = [u, v, w](x + l_x, y, z + l_z). \tag{2.2.1}$$

This homogeneity also means that spatially periodic solutions can be sought, so that computations can be carried out over small domain sizes using the Fourier spectral method for discretization. Different box sizes produce different solutions; however, provided that the box-sizes are within certain ranges — of the order of the channel half-height — these solutions all seem to contain the vortex-streak structure.

While the homogeneity allows for relatively inexpensive, spatially periodic solutions, it also produces vast families of solutions that are dynamically similar. That is, every solution field $[u^*, v^*, w^*]$ is part of a continuous family of solutions spanned by $\tau(l_x, l_z)[u^*, v^*, w^*]$ for arbitrary l_x, l_z. Presence of such families could obscure our view of turbulent flows. Willis et al. (2013) developed a projection method called the "method of slices" to identify families of dynamically similar solutions with one repre-

sentative solution for each family, thus reducing the number of solutions that would have to be considered, say, when developing low-order models for control. Specifically, smooth-walled plane shear flows admit travelling wave solutions and relative periodic orbits, and the method of slices relates such solutions to dynamically similar equilibria and periodic orbits by projecting the former onto a hyperplane using a pre-defined template. Grooved flows, however, are inhomogeneous in the direction transverse to the grooves. We explore the consequences of this loss of homogeneity in § 4.2.

2.2.2 Discretization

Owing to the existence of spatially periodic solutions for channel flows and PCoF, the flowfield can be discretized using the Fourier spectral method in the wall-parallel directions. A periodic field $\phi(x, y, z, t)$ for a periodic box of streamwise and spanwise lengths L_x and L_z is written as a sum of Fourier modes,

$$\phi(x, y, z, t) = \sum_{k\in\mathbb{Z}} \sum_{l\in\mathbb{Z}} \sum_{m\in\mathbb{Z}} \hat{\phi}_{k,l,m}(y, t) e^{i(l\alpha x + m\beta z)}, \tag{2.2.2}$$

where $\alpha, \beta = 2\pi/L_x, 2\pi/L_z$. The Fourier modes are truncated to some $|l| \leq L$ and $|m| \leq M$ to obtain a finite-dimensional representation of the field variable in x and z. Henceforth, we drop the hats on the coefficients of Fourier modes for convenience, with the understanding that integer-subscripted symbols represent Fourier coefficients.

The Fourier coefficients are functions of the wall-normal coordinate and time. An appropriate basis for the wall-bounded wall-normal direction is the set of Chebyshev polynomials — orthogonal polynomials of increasing order, whose roots are the Chebyshev nodes — which can also be truncated to obtain a finite-dimensional representation in the wall-normal direction. A collocation method for the Chebyshev spectral method can also be used so that state-vectors contain entries for values taken by the field variables at the Chebyshev nodes instead of the coefficients of Chebyshev polynomials. In the present work, the collocation method is used, but the two methods are equivalent in terms of their accuracy. The time dependence is usually

accounted for by marching forward from an initial condition; but in the steady-state solver used in this work, this dependence is dropped.

2.2.3 Discrete symmetries

Smooth PCoF also admits discrete symmetries, which are restricted by the counter-moving walls to reflection across $x-y$ planes (σ_z), rotation about the z-axis (σ_x), and point-wise inversion about the origin (σ_{xz}), which is the product of the reflection and rotation. These symmetry transformations generate a discrete dihedral group $D_1 \times D_1 = \{e, \sigma_x, \sigma_z, \sigma_{xz}\}$, where

$$\begin{aligned} \sigma_x[u,v,w](x,y,z) &= [-u,-v,w](-x,-y,z), \\ \sigma_z[u,v,w](x,y,z) &= [u,v,-w](x,y,-z), \\ \sigma_{xz}[u,v,w](x,y,z) &= [-u,-v,-w](-x,-y,-z), \end{aligned} \tag{2.2.3}$$

and e is the identity transformation. The equations of smooth PCoF are invariant under the group $\Gamma = D_{1,x} \ltimes SO(2)_x \times D_{1,z} \ltimes SO(2)_z$, where $\ltimes$ stands for a semi-direct product, x subscripts indicate translations along x and sign changes in x and y, and y subscripts indicate translations along z and sign changes in z.

The laminar solution for the smooth PCoF system is invariant under every symmetry transformation in Γ. Equilibria, such as those of Nagata (1990), are invariant under fewer symmetries. Streamwise travelling waves cannot exist when σ_x is imposed, spanwise travelling waves cannot exist when σ_z is imposed, and neither can exist when σ_{xz} is imposed. More complex solutions appear as these symmetries are relaxed, with the fully turbulent state unlikely to satisfy any of the symmetries in Γ (although discrete translational symmetries are imposed in simulations in the form of periodic boxes). The reader is referred to Gibson et al. (2009); Halcrow (2008) for a comprehensive treatment of invariance under discrete symmetry groups. They identify one particular order-4 group, $S = \{e, s_1, s_2, s_3\}$, to be important to finding

equilibria of smooth PCoF, where

$$\begin{aligned} s_1 &= \tau(L_x/2, 0)\sigma_z, \\ s_2 &= \tau(L_x/2, L_z/2)\sigma_x, \\ s_3 &= \tau(0, L_z/2)\sigma_{xz}, \end{aligned} \tag{2.2.4}$$

are products of half-cell shifts and the discrete symmetries of $D_{1,x} \times D_{1,z}$. All the solutions used in the present work are invariant under the symmetries of S, while a few highly symmetric solutions are invariant under an order-8 group, $S \times \{e, \tau_{xz}\}$.

Due to the high-dimensionality of the state-space of smooth PCoF, and fluid flows in general, a large number of exact invariant solutions exist; in fact, an infinite number of solutions exist due to the continuous translational invariance of the governing equations. A small set of dynamically important solutions has to be identified in order to realistically describe and predict turbulence. The symmetry groups S, $S \times \{e, \sigma_{xz}\}$, and other specific subgroups of Γ offer one way of reducing the infinite stationary points of the NSE to a small set, while the method of slices described earlier offers a complementary way to constraining continuous symmetries.

2.3 Flow geometry and domain transformation

The governing equations laid out earlier for smooth-walled plane shear flows are now extended to the case of grooved plane shear flows, using non-dimensional coordinates (x, y, z) along the streamwise, wall-normal, and spanwise directions respectively, non-dimensionalized by half of the distance between the walls. A general case of wall roughness periodic in $(L_x, L_z) = (2\pi/\alpha, 2\pi/\beta)$, where L_x is the streamwise size of the periodic box and L_z is its spanwise size, can be represented by

$$y_{top} = 1+\sum_{l,m} \frac{A^t_{l,m}}{2} e^{i(l\alpha x+m\beta z+\phi^t_{l,m})}, \quad y_{bottom} = -1+\sum_{l,m} \frac{A^b_{l,m}}{2} e^{i(l\alpha x+m\beta z+\phi^b_{l,m})}, \quad l, m \in \mathbb{Z}, \tag{2.3.1}$$

with the constraints

$$A_{l,m} = A_{-l,-m}, \qquad \phi_{l,m} = -\phi_{-l,-m}, \tag{2.3.2}$$

so that the sum of the two modes produces $A_{l,m}\cos(l\alpha x + m\beta z + \phi_{l,m})$. $A/2$ is used instead of A in eq. (2.3.1) so that the amplitude of each sinusoidal mode of the wall is A instead of $2A$.

This geometry may be mapped to a flat-walled geometry using a domain transformation,

$$Y = -1 + 2(y - y_{bottom})/(y_{top} - y_{bottom}). \tag{2.3.3}$$

Domain transformation is a common method used to discretize flow geometries; for usage involving sinusoidal walls, see, for instance, Kasliwal et al. (2012); Moradi and Floryan (2013). A consequence of this transformation is that the boundary conditions become

$$\begin{gathered} u(Y=\pm1)=0 \qquad \text{(channel)}, \qquad u(Y=\pm1)=\pm1 \qquad \text{(Couette)}, \\ v(Y=\pm1)=0, \qquad w(Y=\pm1)=0, \qquad \nabla\cdot\mathbf{u}(Y=\pm1)=0 \end{gathered} \tag{2.3.4}$$

The motivation for this domain transformation is that the Fourier spectral method

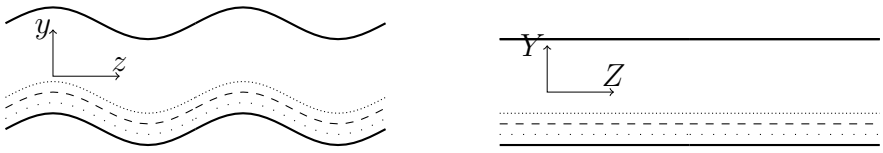

(a) (b)

Figure 2.2: Illustration of the domain transformation: fig. 2.2a- the grooved channel geometry, and fig. 2.2b- the transformed domain

is easily applied in the transformed domain; the boundary conditions are that all Fourier mode coefficients of all velocity components and divergence take a value of zero at the walls (except for the $(0,0)$ mode for u in the case of Couette flow). However, mapping partial derivatives from the transformed domain to the physical domain of eq. (2.3.1) is rather cumbersome. However, when $A^t_{l,m} = A^b_{l,m}$ and $\phi^t_{l,m} = \phi^b_{l,m}$, i.e., when the width between the top and bottom walls remains constant, the required domain transformation is

$$Y = y - \sum_{l,m} A_{l,m} e^{i(l\alpha x + m\beta z + \phi_{l,m})}, \tag{2.3.5}$$

which produces simpler relations between the partial derivatives in the physical domain of eq. (2.3.1) and the transformed domain. This is illustrated in fig. 2.2.

The additional simplification of $\phi_m = 0$, and $A_{|m|\neq 1} = 0$ is used here for laminar solutions, while the second constraint is relaxed to include multiple groove-modes when computing grooved PCoF equilibria. The walls for this simple class of grooved channels are given by

$$y_{walls} = \pm 1 + A\cos(\alpha x + \beta z). \tag{2.3.6}$$

Such geometries can be distinguished into three classes: 1) Longitudinal grooves: $\alpha = 0$, 2) Transverse grooves: $\beta = 0$, and 3) Oblique grooves: $\alpha\beta \neq 0$; they are illustrated in fig. 2.3. This classification is important because of distinctive flow features of each class; longitudinal grooves admit solutions with zero wall-normal and spanwise velocity and produce no flow separation; transverse grooves produce flow separation but still have zero spanwise velocity; and oblique grooves may produce flow separation as well as currents in the spanwise direction (and along the homogeneous direction of

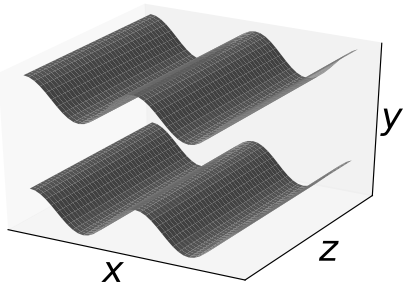

(a) Transverse grooves: $\beta = 0$

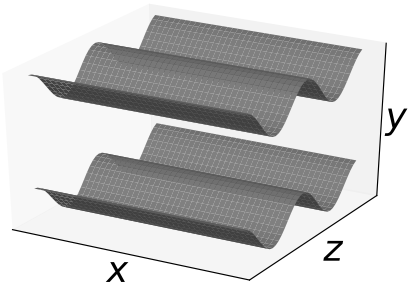

(b) Longitudinal grooves: $\alpha = 0$

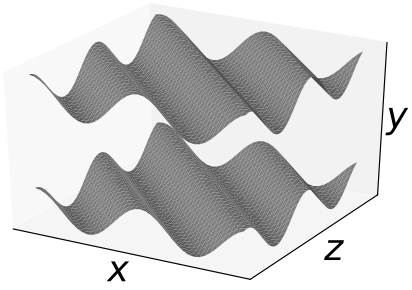

(c) Oblique grooves: $\alpha\beta \neq 0$

Figure 2.3: Grooved channel flow illustrating (a) Transverse, (b) Longitudinal, and (c) Oblique grooves.

the grooves).

The domain transformation method is now outlined for the case of transverse grooves, whose geometry is given by

$$y_{walls} = \pm 1 + \frac{A}{2}\cos(\alpha x), \tag{2.3.7}$$

and the grooved geometry is mapped to a smooth geometry as

$$X = x, \qquad Y = \mathcal{T}(x, y) = y - \frac{A}{2}\cos(\alpha x), \qquad Z = z. \tag{2.3.8}$$

The partial derivatives in the two domains relate as

$$\begin{aligned} \partial_x &= \partial_X + \mathcal{T}_x \partial_Y = \partial_X - i\alpha\frac{A}{2}(e^{i\alpha x} - e^{-i\alpha x})\partial_Y, \\ \partial_y &= \partial_Y, \end{aligned} \tag{2.3.9}$$

$$\partial_z = \partial_Z.$$

The original $x-y-z$ coordinate system is henceforth referred to as the "physical system" or "physical domain", while the $X-Y-Z$ coordinate system is referred to as the "transformed system" or "transformed domain". For laminar flow in a channel with transverse grooves, a solution with zero spanwise derivatives and zero spanwise velocity is sought. The numerical method is now outlined for this case; the modifications for longitudinal and oblique grooves in channels are discussed towards the end.

2.3.1 Discretization in the transformed domain

In the smooth-walled transformed domain, the flow can be discretized using the Fourier spectral method in the streamwise direction the Chebyshev pseudo-spectral method (Chebyshev collocation method) in the wall-normal direction as

$$\big[u,v,p\big](X,Y) = \sum_{l\in\mathbb{R}} \big[u_l(Y), v_l(Y), p_l(Y)\big] e^{il\alpha_{discr}X}. \tag{2.3.10}$$

The fundamental discretization wavenumber, α_{discr}, of the periodic domain is set to be equal to the wavenumber α of the transverse grooves, so that exactly one groove is included in each periodic domain. This condition is relaxed later when studying equilibria, but for now, the two wavenumbers are not distinguished.

Conventionally, Fourier coefficients of a field are distinguished from the field using a tilde or a hat. In this thesis, no such distinction is made, with the understanding that field-symbols with subscripts represent Fourier coefficients of the corresponding field.

In the equations to follow, the streamwise Fourier transform of a spanwise-homogeneous field $f(X,Y)$ is denoted by

$$\{f\}_k(Y) = \mathcal{F}_l\{f\}(Y) = \frac{\alpha}{2\pi} \int_0^{2\pi/\alpha} f(X,Y) e^{-il\alpha X} \quad dX. \tag{2.3.11}$$

2.3.2 Inter-modal interaction

The grooves, and the accompanying domain transformation, introduce a coupling between Fourier modes even for linear terms, which is absent in smooth-walled plane shear flows. This can be seen from the Fourier coefficients of the partial derivatives of the streamwise velocity, u. For a general, three-dimensional, periodic field in a periodic box of size $(L_x = 2\pi/\alpha, L_z = 2\pi/\beta)$, the derivatives in y and z,

$$\begin{aligned} \mathcal{F}_{l,m}(\partial_y u) &= \partial_y \mathcal{F}_{l,m}(u), \\ \mathcal{F}_{l,m}(\partial_z u) &= im\beta \mathcal{F}_{l,m}(u), \end{aligned} \tag{2.3.12}$$

remain decoupled amongst Fourier modes, as they do for smooth-walled geometries. Mode coupling appears in the x-derivative,

$$\mathcal{F}_{l,m}(\partial_x u) = il\alpha \mathcal{F}_{l,m}(u) - i\alpha \frac{A}{2} \Big\{ \partial_Y \mathcal{F}_{l-1,m}(u) - \partial_Y \mathcal{F}_{l+1,m}(u) \Big\}, \tag{2.3.13}$$

where modes $(l \pm 1, m)$ contribute to the x-derivative of mode (l, m). The last two terms on the right hand side are zero whenever A or α are zero, and the usual equations for the smooth-walled channel are recovered.

2.4 Governing equations for transverse grooves

The governing equations (steady-state NSE) in the Cartesian coordinate system of $x-y-z$ are, using index notation,

$$\begin{aligned}(u^k\partial_{x_k})u^j &= -\frac{dP}{dx_1}\delta_{1j} - \partial_{x_j}p + \frac{1}{Re}\Delta u^j, \qquad j,k \in \{1,2,3\}\\ \partial_{x_k}u^k &= 0.\end{aligned} \tag{2.4.1}$$

For laminar flow in channels with transverse grooves, $u^3 = \partial_{x_3}u^k = 0, \forall k \in \{1,2,3\}$. The discretization (in the transformed domain) of eq. (2.3.10) introduces streamwise-varying coefficients to the equations. Two new quantities are defined: the semi-amplitude $\epsilon = A/2$, and the semi-slope $g = A\alpha/2$. $A\alpha$ is the absolute value of the slope of the sinusoidal grooves at $\alpha x = (2k+1)\pi/2, k \in \mathbb{Z}$, and also quantifies the depth-to-height aspect ratio (AR) of the grooves, $AR = A\alpha/\pi$. The semi-slope and semi-amplitude appear more often in the equations than the slope or the amplitude.

Fourier coefficients for each term in the governing equations are now presented.

2.4.1 Pressure gradient

The pressure term is written $P+p$, where $P = \frac{dP}{dx}x$ is due to the mean pressure gradient, and p is the fluctuating pressure.

$$\begin{aligned}\{\partial_x(P+p)\}_l &= \{(\partial_X + \mathcal{T}_x\partial_Y)(P+p)\}_l = \frac{dP}{dx}\delta_{l,0} + il\alpha p_l - \epsilon i\alpha(\frac{dp_{l-1}}{dY} - \frac{dp_{l+1}}{dY})\\ \{\partial_y(P+p)\}_l &= \{\partial_Y p\}_l = \frac{dp_l}{dY}\end{aligned}$$

Re-arranging the terms,

$$\begin{aligned}\{\partial_x p\}_l &= \{-igD\}p_{l-1} + \{il\alpha\}p_l + \{igD\}p_{l+1} + \frac{dP}{dx}\delta_{l,0},\\ \{\partial_y p\}_l &= \{D\}p_l,\end{aligned} \tag{2.4.2}$$

where D is a linear operator representing differentiation with respect to Y. The discretization along the wall-normal direction allows the linear operator D to be replaced by a matrix.

2.4.2 Diffusion

The Fourier coefficients of the Laplacian of the velocity can similarly be expressed in terms of Fourier coefficients of the velocity field. The diffusion term is $\frac{1}{Re}\Delta u^i$; the Fourier coefficients of the Laplacian are

$$\begin{aligned}\{\partial_{x_j x_j} u^i\}_l =&\{-g^2 D^2\} u^i_{l-2} + \{g\alpha(2k-1)D\} u^i_{l-1} \\ &+\{(-l^2\alpha^2 + 2g^2D^2 + D^2\} u^i_l \\ &+\{g\alpha(-2k-1)D\} u^i_{l+1} + \{-g^2D^2\} u^i_{l+2}.\end{aligned} \tag{2.4.3}$$

2.4.3 Advection

The advection term is non-linear. In this thesis, the velocity is not decomposed into a base-flow and fluctuations. The Fourier coefficients of the advection term are expressed using sums of products of Fourier coefficients of the velocity field as

$$\begin{aligned}\{u^j \partial_{x_j} u^i\}_l =& \sum_n \{in\alpha u_{l-n} - ig(u_{l-n-1} - u_{l-n+1})\frac{d}{dY}\} u^i_n \\ &+ \sum_n \{v_{l-n}\frac{d}{dY}\} u^i_n\} u^i_n\end{aligned} \tag{2.4.4}$$

When discretized in the transformed domain $(X-Y)$, the advection term produces additional terms in the "triadic interaction" where interactions between modes are restricted to triads of the form $(l\alpha, l'\alpha, (l+l')\alpha)$.

2.4.4 Continuity equation

$$0 = \{\partial_{x_i} u^i\}_l = (-igD)u_{l-1} + il\alpha u_l + (igD)u_{l+1} + Dv_l \tag{2.4.5}$$

2.4.5 Boundary conditions

In the transformed system, the walls are at $Y = \pm 1$. Zero Dirichlet conditions are imposed on each Fourier coefficient for u and v as

$$u_l(Y = \pm 1) = 0, \qquad v_l(Y = \pm 1) = 0, \qquad \left[\{\partial_x u\}_l + D v_l\right](Y = \pm 1) = 0. \quad (2.4.6)$$

2.5 Discretized system for transverse grooves

The governing equations of eq. (2.4.1) are discretized using the Fourier spectral method in the streamwise direction and the Chebyshev collocation method in the wall-normal direction (for the spanwise-homogeneous case of transverse grooves) to produce a discretized form of the steady-state equations as

$$\boldsymbol{F}(\boldsymbol{\chi}) := \mathcal{L}\boldsymbol{\chi} + \boldsymbol{\mathcal{N}}(\boldsymbol{\chi}) - \boldsymbol{f} = 0, \quad (2.5.1)$$

where $\boldsymbol{\chi}$ is the state-vector containing the Fourier coefficients of u, v, and p, $\mathcal{L}$ is a matrix representing the action of the linear terms, $\boldsymbol{\mathcal{N}}(\boldsymbol{\chi})$ represents the non-linear term (advection term), and $\boldsymbol{f}$ represents a forcing.

The state-vector $\boldsymbol{\chi}$ is built as

$$\boldsymbol{\chi} = \begin{bmatrix} \chi_{-L} \\ \chi_{-L+1} \\ \vdots \\ \chi_{-1} \\ \chi_0 \\ \vdots \\ \chi_L \end{bmatrix}, \qquad \text{where, } \chi_l = \begin{bmatrix} u_l(Y) \\ v_l(Y) \\ p_l(Y) \end{bmatrix}, \quad (2.5.2)$$

where L is a positive integer representing the streamwise resolution, and χ_l is used to represent the coefficients for a particular Fourier mode.

2.5.1 Iterative scheme

The matrix $\mathcal{L}$ and a simple matrix representation of $\boldsymbol{\mathcal{N}}(\boldsymbol{\chi})$ are presented shortly. The discretized equation is solved using the exact Newton method, which iteratively refines a given estimate $\boldsymbol{\chi}^0$ of an exact solution $\boldsymbol{\chi}^*$ as

$$\begin{aligned}\boldsymbol{\chi}^{m+1} &= \boldsymbol{\chi}^m - \left\{\boldsymbol{F}'(\boldsymbol{\chi}^m)\right\}^{-1}\boldsymbol{F}(\boldsymbol{\chi}^m) \\ &= \boldsymbol{\chi}^m - \left\{\mathcal{L} + \mathcal{G}(\boldsymbol{\chi}^m)\right\}^{-1}\boldsymbol{F}(\boldsymbol{\chi}^m).\end{aligned} \tag{2.5.3}$$

until a convergence criterion is satisfied. Here, $\boldsymbol{F}'$ denotes the Jacobian of $\boldsymbol{F}$ and the state-dependent matrix $\mathcal{G}(\boldsymbol{\chi})$ is the Jacobian of the non-linear term $\boldsymbol{\mathcal{N}}(\boldsymbol{\chi})$; $\mathcal{G}(\boldsymbol{\chi})$ relates to the non-linear term as

$$\boldsymbol{\mathcal{N}}(\boldsymbol{\chi}) = \frac{1}{2}\mathcal{G}(\boldsymbol{\chi})\boldsymbol{\chi}, \tag{2.5.4}$$

as shall be shown soon. The superscript m on $\boldsymbol{\chi}$ relates to iterations of the numerical method, while subscripts in eq. (2.5.2) represent Fourier coefficients of the fields at a particular iteration.

To improve convergence of the Newton iterations, a line search method is used at the end of each iteration (see appendix C.2.3). If $\delta\boldsymbol{\chi}^+ = -\boldsymbol{F}'^{-1}(\chi)\boldsymbol{F}(\boldsymbol{\chi})$ is the solution to the matrix equation, then an optimal correction, $\delta\boldsymbol{\chi}^*$ along $\delta\boldsymbol{\chi}^+$, is found using a binary search over d_f as

$$\delta\boldsymbol{\chi}^* = \{\arg\min_{d_f\in\mathbb{R}}||\boldsymbol{F}(\boldsymbol{\chi}^+ + d_f\delta\boldsymbol{\chi}^+)||\}\,\delta\boldsymbol{\chi}^+, \text{ with } \delta\boldsymbol{\chi}^+ = -\{\boldsymbol{F}'\}^{-1}\boldsymbol{F}(\boldsymbol{\chi}). \tag{2.5.5}$$

The convergence criterion used in this thesis is that the residual norm (see § 2.8.1 for more details),

$$r = \sqrt{\sum_{l=-L}^{L}\frac{1}{2}\int_{Y=-1}^{1}|\partial_t u_l|^2 + |\partial_t v_l|^2 + |(\nabla\cdot\boldsymbol{u})|_l^2 \quad dY} \tag{2.5.6}$$

goes below a prescribed tolerance (usually 10^{-12}). To ensure that the steady solutions

are grid-independent, an accuracy (r_{2x}) is defined as the residual obtained when the state-vector is interpolated to a grid of twice the number of nodes(/modes) in each coordinate direction.

2.5.2 Matrix representing linear terms

From Eq. 2.4.2, 2.4.3, and 2.4.5, it may be seen that, although the grooves introduce a coupling among different Fourier modes, the interaction still remains linear in Fourier coefficients. These three equations are represented by a single matrix in the current formulation $\mathcal{L}$, while the non-linear advection terms are represented as a matrix operator $\boldsymbol{\mathcal{N}}(\boldsymbol{\chi})$. The mean pressure gradient in Eq. 2.4.2 is a constant, and is accounted for separately as a forcing term ($\boldsymbol{f}$ in Eq. 2.5.1).

The linear interactions due to the pressure-gradient and diffusion, and the continuity equation, are all represented by matrices of the form $g^{|k|}\Lambda_k^l$, where l represents the wavenumber for which the equation is solved, k represents modes neighbouring mode l, and $g = \epsilon\alpha$ is the semi-slope of the grooves. For sinusoidal walls, k is limited to the set {-2,-1,0,1,2}, i.e., linear interaction among modes is restricted to just two modes each on either side.

The interactions contributing to the advection term, on the other hand, are not limited to just a few on either side, but span the entire set of integers (although all but a few are neglected following the discretization). The treatment for this term is described in § 2.5.3.

From Eq. 2.4.2, 2.4.3, and 2.4.5, matrices Λ_k^l are defined as :

$$g^2\Lambda_{-2} = \begin{bmatrix} \frac{g^2}{Re}D^2 & Z & Z \\ Z & \frac{g^2}{Re}D^2 & Z \\ Z & Z & Z \end{bmatrix}$$

$$g\Lambda_{-1}^l = \begin{bmatrix} \frac{-g\alpha}{Re}(2l-1)D & Z & -igD \\ Z & \frac{-g\alpha}{Re}(2l-1)D & Z \\ -igD & Z & Z \end{bmatrix}$$

$$\Lambda_0^l = \begin{bmatrix} \frac{1}{Re}(l^2\alpha^2 - D^2 - 2\epsilon^2\alpha^2 D^2) & Z & il\alpha I \\ Z & \frac{1}{Re}(l^2\alpha^2 - D^2 - 2\epsilon^2\alpha^2 D^2) & D \\ il\alpha I & D & Z \end{bmatrix} \tag{2.5.7}$$

$$g\Lambda_1^l = \begin{bmatrix} \frac{g\alpha}{Re}(2l+1)D & Z & igD \\ Z & \frac{g\alpha}{Re}(2l+1)D & Z \\ igD & Z & Z \end{bmatrix}$$

$$g^2\Lambda_2 = \begin{bmatrix} \frac{g^2}{Re}D^2 & Z & Z \\ Z & \frac{g^2}{Re}D^2 & Z \\ Z & Z & Z \end{bmatrix}$$

where Z is a zero matrix of size $N \times N$, N being the number of Chebyshev collocation nodes for wall-normal resolution, and I is an identity matrix of the same size. The first row-block in each of the matrices corresponds to the (linear part of the) streamwise momentum equation, the second row corresponds to the wall-normal momentum equation, and the third row to the continuity equation.

The matrix equation for the l^{th} mode is:

$$\begin{bmatrix} g^2\Lambda_{-2} & g\Lambda_{-1}^l & \Lambda_0^l & g\Lambda_1^l & g^2\Lambda_2 \end{bmatrix}_{3N\times 15N} \begin{bmatrix} \boldsymbol{\chi}_{l-2} \\ \boldsymbol{\chi}_{l-1} \\ \boldsymbol{\chi}_{l} \\ \boldsymbol{\chi}_{l+1} \\ \boldsymbol{\chi}_{l+2} \end{bmatrix}_{15N\times 1} + \{\boldsymbol{\mathcal{N}}(\boldsymbol{\chi})_l\}_{3N\times 1} = \begin{bmatrix} |\frac{dP}{dx}|\delta_{l,0} \\ Z_{N\times 1} \\ Z_{N\times 1} \end{bmatrix}_{3N\times 1}$$

The complete matrix $\mathcal{L}$ is organized into $3N \times 3N$ sub-matrices, $\mathcal{L}_{l,l+k}$ as

$$\mathcal{L} = \begin{bmatrix} \mathcal{L}_{-L,-L} & \mathcal{L}_{-L,-L+1} & \cdots & \mathcal{L}_{-L,L} \\ \mathcal{L}_{-L+1,-L} & \mathcal{L}_{-L+1,-L+1} & \cdots & \mathcal{L}_{-L+1,L} \\ \vdots & \ddots & \ddots & \vdots \\ \mathcal{L}_{L,-L} & \mathcal{L}_{L,-L+1} & \cdots & \mathcal{L}_{L,L} \end{bmatrix}. \tag{2.5.8}$$

The sub-matrices $\mathcal{L}_{l,l+k}$ relate to Λ_k^l as

$$\begin{aligned} \mathcal{L}_{l,k} &= g^{|l-k|}\Lambda_{k-l}^l, \\ &\text{where, } m \notin \{-2,-1,0,1,2\} \implies \Lambda_m^k = Z_{3N\times 3N}. \end{aligned} \tag{2.5.9}$$

2.5.3 Matrix operator for non-linear terms

As shall shortly be shown, the vector function representing the non-linear terms, $\boldsymbol{\mathcal{N}}(\boldsymbol{\chi})$ can be expressed as a product of its Jacobian $\mathcal{G}(\boldsymbol{\chi}) = \boldsymbol{\mathcal{N}}'()$ and the state-vector $\boldsymbol{\chi}$ (times half). In this section, the advection term for the i^{th} momentum at the k^{th} Fourier mode is denoted by ϕ_k^i. From Eq. 2.4.4

$$\begin{aligned} \phi_k^i = \{u^j \partial_{\tilde{x}_j} u^i\}_k = &\sum_n \{in\alpha u_{k-n} - ig(u_{k-n-1} - u_{k-n+1})D\}u_n^i \\ &+ \sum_n \{v_{k-n}D\}u_n^i \end{aligned} \tag{2.5.10}$$

The non-linear function $\boldsymbol{\mathcal{N}}(\boldsymbol{\chi})$ in Eq. 2.5.1 has entries ordered as

$$\boldsymbol{\mathcal{N}}(\boldsymbol{\chi}) = \begin{bmatrix} \phi_{-n}^1(\boldsymbol{\chi}) \\ \phi_{-n}^2(\boldsymbol{\chi}) \\ 0 \\ \vdots \\ \phi_0^1 \\ \phi_0^2 \\ 0 \\ \vdots \\ \phi_n^2 \\ 0 \end{bmatrix} \tag{2.5.11}$$

where the zeros that take the place of ϕ_k^3 follow from the absence of non-linear terms in the continuity equation.

Its Jacobian $\mathcal{G}(\boldsymbol{\chi})$ is defined as

$$\mathcal{G}(\boldsymbol{\chi}) = \begin{bmatrix} \frac{\partial \phi^1_{-n}}{\partial u^1_{-n}} & \frac{\partial \phi^1_{-n}}{\partial u^2_{-n}} & \frac{\partial \phi^1_{-n}}{\partial p_{-n}} & \frac{\partial \phi^1_{-n}}{\partial u^1_{-n+1}} & \cdots & \frac{\partial \phi^1_{-n}}{\partial u^1_0} & \frac{\partial \phi^1_{-n}}{\partial u^2_0} & \cdots & \frac{\partial \phi^1_{-n}}{\partial u^2_n} & \frac{\partial \phi^1_{-n}}{\partial p_n} \\ \frac{\partial \phi^2_{-n}}{\partial u^1_{-n}} & \frac{\partial \phi^2_{-n}}{\partial u^2_{-n}} & \frac{\partial \phi^2_{-n}}{\partial p_{-n}} & \frac{\partial \phi^2_{-n}}{\partial u^1_{-n+1}} & \cdots & \frac{\partial \phi^2_{-n}}{\partial u^1_0} & \frac{\partial \phi^2_{-n}}{\partial u^2_0} & \cdots & \frac{\partial \phi^2_{-n}}{\partial u^2_n} & \frac{\partial \phi^2_{-n}}{\partial p_n} \\ 0 & 0 & 0 & 0 & \cdots & 0 & 0 & \cdots & 0 & 0 \\ \frac{\partial \phi^1_{-n+1}}{\partial u^1_{-n}} & \frac{\partial \phi^1_{-n+1}}{\partial u^2_{-n}} & \frac{\partial \phi^1_{-n+1}}{\partial p_{-n}} & \frac{\partial \phi^1_{-n+1}}{\partial u^1_{-n+1}} & \cdots & \frac{\partial \phi^1_{-n+1}}{\partial u^1_0} & \frac{\partial \phi^1_{-n+1}}{\partial u^2_0} & \cdots & \frac{\partial \phi^1_{-n+1}}{\partial u^2_n} & \frac{\partial \phi^1_{-n+1}}{\partial p_n} \\ \vdots & \vdots & \vdots & \vdots & \ddots & \vdots & \vdots & \ddots & \vdots & \vdots \\ \frac{\partial \phi^1_0}{\partial u^1_{-n}} & \frac{\partial \phi^1_0}{\partial u^2_{-n}} & \frac{\partial \phi^1_0}{\partial p_{-n}} & \frac{\partial \phi^1_0}{\partial u^1_{-n+1}} & \cdots & \frac{\partial \phi^1_0}{\partial u^1_0} & \frac{\partial \phi^1_0}{\partial u^2_0} & \cdots & \frac{\partial \phi^1_0}{\partial u^2_n} & \frac{\partial \phi^1_0}{\partial p_n} \\ \vdots & \vdots & \vdots & \vdots & \ddots & \vdots & \vdots & \ddots & \vdots & \vdots \\ \frac{\partial \phi^2_n}{\partial u^1_{-n}} & \frac{\partial \phi^2_n}{\partial u^2_{-n}} & \frac{\partial \phi^2_n}{\partial p_{-n}} & \frac{\partial \phi^2_n}{\partial u^1_{-n+1}} & \cdots & \frac{\partial \phi^2_n}{\partial u^1_0} & \frac{\partial \phi^2_n}{\partial u^2_0} & \cdots & \frac{\partial \phi^2_n}{\partial u^2_n} & \frac{\partial \phi^2_n}{\partial p_n} \\ 0 & 0 & 0 & 0 & \cdots & 0 & 0 & \cdots & 0 & 0 \end{bmatrix} \tag{2.5.12}$$

where, it must be noted, $\frac{\partial \phi^i_k}{\partial p_l}$ is zero for any k, l ($i \in \{1, 2\}$).

The entries of the Jacobian $\mathcal{G}(\boldsymbol{\chi})$ can be calculated from Eq. 2.5.10. The way the derivatives in Eq. 2.5.12 are expressed in the context of discretized domains is now briefly discussed. When calculating the partial derivative of ϕ^i_k (for some k) with respect to u^i_l, only those terms in the expansion of ϕ^i_k that contain either u^i_l or u'^i_l need to be considered (where u'^i_l denotes the wall-normal derivative of u^i_l). The partial derivatives $\frac{\partial \phi^i_k}{\partial u^i_l}$ must be $N \times N$ matrices that multiply a vector u^i_l of size $N \times 1$ to give a vector of size $N \times 1$, where N is the number of collocation nodes used for wall-normal resolution.

u^j_l can appear in several kinds of terms. The treatment for each of these kinds is given below. The partial derivatives are $N \times N$matrices. $\mathrm{diag}(u^i_k)$ represents a diagonal matrix with the elements of the vector u^i_k on its principal diagonal, D is a dense $N \times N$ matrix that represents the wall-normal derivative operator, $(i, k) \neq (j, l)$, and repeated indices do not represent summation over the indices:

$$\frac{\partial}{\partial u^j_l}(C u^i_k u^j_l) = C\,\mathrm{diag}(u^i_k)$$
$$\frac{\partial}{\partial u^j_l}(C u^i_k u'^j_l) = C\,\mathrm{diag}(u^i_k) D$$

$$\frac{\partial}{\partial u_l^j}(Cu_k'^i u_l^j) = C\mathrm{diag}(Du_k^i) \tag{2.5.13}$$
$$\frac{\partial}{\partial u_l^j}(Cu_l^j u_l^j) = C\mathrm{diag}(u_l^j) + C\mathrm{diag}(u_l^j)$$
$$\frac{\partial}{\partial u_l^j}(Cu_l'^j u_l^j) = C\mathrm{diag}(Du_l^j) + C\mathrm{diag}(u_l^j D)$$

For instance, all the terms in which u_l appears in ϕ_k^1 are

$$il\alpha u_{k-l}u_l + i(k-l)\alpha u_l u_{k-l} + v_{k-l}Du_l + v_l Du_{k-l}$$
$$-ig\{u_{k-l-1}Du_l + u_l Du_{k-l-1} - u_{k-l+1}Du_l - u_l Du_{k-l+1}\}$$

The Jacobian $\mathcal{G}(\boldsymbol{\chi})$ can be constructed by collecting the terms as above from ϕ_k^1, ϕ_k^2 for u_l^1, u_l^2 and then adding up the matrices corresponding to the partial derivatives of each term as given in Eq. 2.5.13: (here, diag() is truncated to d())

$$\begin{aligned}
\frac{\partial}{\partial u_l}(\phi_k^1) =& \frac{\partial}{\partial u_l}[il\alpha u_{k-l}u_l + i(k-l)\alpha u_l u_{k-l} + v_{k-l}Du_l + v_l Du_{k-l} \\
&- ig\{u_{k-l-1}Du_l + u_l Du_{k-l-1} - u_{k-l+1}Du_l - u_l Du_{k-l+1}\}] \\
=& ik\alpha \mathrm{d}(u_{k-l}) - ig\{\mathrm{d}(u_{k-l-1})D + \mathrm{d}(Du_{k-l-1})\} \\
&+ ig\{\mathrm{d}(u_{k-l+1})D + \mathrm{d}(Du_{k-l+1})\} + \mathrm{d}(v_{k-l})D \\
\frac{\partial}{\partial u_l}(\phi_k^2) =& \frac{\partial}{\partial u_l}[i(k-l)\alpha u_l v_{k-l} - igu_l Dv_{k-l-1} + igu_l Dv_{k-l+1}] \\
=& i(k-l)\alpha \mathrm{d}(v_{k-l}) - ig\mathrm{d}(Dv_{k-l-1}) + ig\mathrm{d}(Dv_{k-l+1}) \\
\frac{\partial}{\partial v_l}(\phi_k^1) =& \frac{\partial}{\partial v_l}[v_l Du_{k-l}] \\
=& \mathrm{d}(Du_{k-l}) \\
\frac{\partial}{\partial v_l}(\phi_k^2) =& \frac{\partial}{\partial v_l}[il\alpha u_{k-l}v_l - igu_{k-l-1}Dv_l + igu_{k-l+1}Dv_l + v_{k-l}Dv_l + v_l Dv_{k-l}] \\
=& il\alpha \mathrm{d}(u_{k-l}) - ig\mathrm{d}(u_{k-l-1})D + ig\mathrm{d}(u_{k-l+1})D + \mathrm{d}(v_{k-l})D + \mathrm{d}(Dv_{k-l})
\end{aligned} \tag{2.5.14}$$

From Eq. 2.5.12 and Eq. 2.5.14, it can be seen that

$$\mathcal{G} \text{ is linear in } \boldsymbol{\chi} \tag{2.5.15}$$

It has been remarked earlier that the elements of $\boldsymbol{\mathcal{N}}(\boldsymbol{\chi})$ can be calculated from $\boldsymbol{\mathcal{G}}(\boldsymbol{\chi})$. Or specifically, we have

$$\boldsymbol{\mathcal{N}}(\boldsymbol{\chi}) = 0.5\boldsymbol{\mathcal{G}}(\boldsymbol{\chi})\boldsymbol{\chi} \tag{2.5.16}$$

This is shown by again considering the five forms of terms in Eq. 2.5.13:

$$\begin{aligned}
Cu_k^i u_l^j &= 0.5\{C\mathrm{diag}(u_k^i)u_l^j + C\mathrm{diag}(u_l^j)u_k^i)\} &&= 0.5\{\frac{\partial(Cu_k^i u_l^j)}{\partial u_l^j}u_l^j + \frac{\partial(Cu_k^i u_l^j)}{\partial u_l^j}u_k^i\}\\
Cu_k^i u_l'^j &= 0.5\{C\mathrm{diag}(u_k^i)D(u_l^j) + C\mathrm{diag}(Du_l^j)u_k^i\} &&= 0.5\{\frac{\partial(Cu_k^i u_l'^j)}{\partial u_l^j}u_l^j + \frac{\partial(Cu_k^i u_l'^j)}{\partial u_l^j}u_k^i\}\\
Cu_k'^i u_l^j &= 0.5\{C\mathrm{diag}(Du_k^i)u_l^j + C\mathrm{diag}(u_l^j)Du_k^i\} &&= 0.5\{\frac{\partial(Cu_k'^i u_l^j)}{\partial u_l^j}u_l^j + \frac{\partial(Cu_k'^i u_l^j)}{\partial u_l^j}u_k^i\}\\
Cu_l^j u_l^j &= C\mathrm{diag}(u_l^j)u_l^j &&= 0.5\frac{\partial(Cu_l^j u_l^j)}{\partial u_l^j}u_l^j\\
Cu_l^j u_l'^j &= 0.5\{C\mathrm{diag}(u_l^j)D(u_l^j) + C\mathrm{diag}(Du_l^j)u_l^j\} &&= 0.5\frac{\partial(Cu_l^j u_l'^j)}{\partial u_l^j}u_l^j
\end{aligned}$$

Since ϕ_k^i is made up of sums of terms of the kind on the left hand side, and $\boldsymbol{\mathcal{G}}(\boldsymbol{\chi})\boldsymbol{\chi}$ contains sums of the kind on the right hand side, it may be concluded that Eq. 2.5.16 is valid.

2.5.4 Boundary conditions

The boundary conditions in the transformed domain are

$$u = v = 0, \qquad \text{at } Y = \pm 1 \tag{2.5.17}$$

When the velocities are Fourier-decomposed, the same zero-Dirichlet-conditions apply on each Fourier mode. The conditions are imposed by including the velocities at the walls in the state-vectors, and including a pair of equations for each velocity that sets the wall-velocities to zero. With the way that the variables are ordered (eq. (2.5.2)), for N Chebyshev nodes used in discretizing the domain, the boundary conditions for the k^{th} Fourier mode are imposed through rows $\{(k+n)3N+1, (k+$

$n)3N+N, (k+n)3N+N+1, (k+n)3N+2N\}$ of the matrix $L+N()$, corresponding to the four conditions in eq. (2.5.17). To impose the boundary conditions, all elements except the ones on the principal diagonal are set to zero in these rows. Consequently, the equations formed by these rows would be

$$u_k^i(Y=\pm 1) = f_k^i(Y=\pm 1), \qquad \text{for } i=1,2$$

The zero Dirichlet conditions are then imposed by setting the corresponding elements in the forcing vector to zero.

There are other ways to impose boundary conditions. Some schemes solve for the flow only on internal nodes (nodes except the ones at the wall), and use differentiation matrices that implicitly account for boundary conditions. The approach used in the present work is easily imposed and is versatile, i.e., it allows for specification of a wider variety of boundary conditions without having to modify the differentiation matrices. However, it follows from the inclusion of wall nodes in the equations that 6 additional singular values and vectors (2 each for u, v, p) appear as compared to an SVD of a matrix defined only over the internal nodes. Preliminary runs showed that these additional singular vectors result in spikes at the walls for all the other modes. The two approaches, the one involving wall-nodes and the one without wall-nodes in the equations, have been compared for linear stability analysis of smooth-walled laminar channel flow. Both approaches produce identical results in terms of the dominant eigenvalues and eigenvectors. The present formulation also works without issue for continuing solutions to grooved flows. There are other approaches that use ghost cells that extend outside the domain of the flow, but these have not been considered.

A more relevant question is in relation to the treatment of pressure. Pressure appears in the governing equations only in terms of its gradients. eq. (2.4.2):

$$\{\partial_{\tilde{x}} p\}_k = \{-igD\}p_{k-1} + \{ik\alpha\}p_k + \{igD\}p_{k+1} + \frac{dP}{dx}\delta_{k,0}$$

$$\{\partial_{\tilde{y}} p\}_k = \{D\}p_k$$

The coefficients $p_0(y)$ and $K + p_0(y)$ produce the same pressure gradient terms for any constant K. The same cannot be said of other wavenumbers because of the $ik\alpha p_k$ term (which is zero for $k = 0$). It follows that a unique solution does not exist for the governing equations and that they must be rank deficient by at least 1, i.e., the matrix $L + N()$ is not invertible. Resolving this would involve modifying the pressure gradient term such that only a unique solution for $p_0(y)$ exists. Two ways of dealing with this have been considered:

- A pseudo-inverse is used instead of an inverse of $\mathcal{L} + \boldsymbol{\mathcal{N}}()$; to be precise, the singular values and vectors corresponding to a constant pressure for the zeroth Fourier mode are dropped.
- A boundary condition $p_0 = 0$ is imposed, replacing the continuity equation at one of the walls.

Both approaches have produced identical results.

Thus far, a Poisson equation for pressure has not been discussed. This is because the divergence-free condition is used directly as an equation in $F(\chi) = 0$, and the iterations converge without issue. Since the algorithm does not involve time-marching, the present author believes there is no reason to use a pressure Poisson equation instead of the divergence equation for velocity.

2.6 Modifications for oblique grooves

For geometries with oblique grooves, a periodic solution is sought with homogeneity along the homogeneous direction of the grooves with the discretization

$$\big[u, v, w, p\big](X, Y, Z) = \sum_{k\in\mathbb{R}} \big[u_k(Y), v_k(Y), w_k(Y), p_k(Y)\big] e^{ik(\alpha X+\beta Z)}. \tag{2.6.1}$$

For longitudinal grooves, α is set to zero. The formulation for oblique grooves is similar to that described in §§ 2.4 and 2.5, except that the velocity field must now include the spanwise component w, and the derivatives of the domain transformation function are non-zero for both x and z:

$$X = x, \qquad Y = T(x, y, z) = y - \frac{A}{2}\cos(\alpha x + \beta z), \qquad Z = z. \tag{2.6.2}$$

$$\begin{aligned} \partial_x &= \partial_X - i\alpha\frac{A}{2}(e^{i(\alpha x+\beta z)} - e^{-i(\alpha x+\beta z)})\partial_Y, \\ \partial_y &= \partial_Y, \\ \partial_z &= \partial_Z - i\beta\frac{A}{2}(e^{i(\alpha x+\beta z)} - e^{-i(\alpha x+\beta z)})\partial_Y. \end{aligned} \tag{2.6.3}$$

The discretized equations remain much the same as the transverse groove case; the state-vector now contains Fourier coefficients for modes $(k\alpha, k\beta)$ instead of $(k\alpha, 0)$.

2.7 Non-laminar equilibria for grooved Couette flows

Plane Couette flow has been chosen because of its simplicity and the historical interest in PCoF in relation to finding non-laminar equilibria. Henceforth, we shall use "equilibria" to exclusively refer to non-laminar equilibria. The top and bottom walls of the grooved PCoF geometry are given by

$$y_{walls} = \pm 1 + A\cos(\beta z). \tag{2.7.1}$$

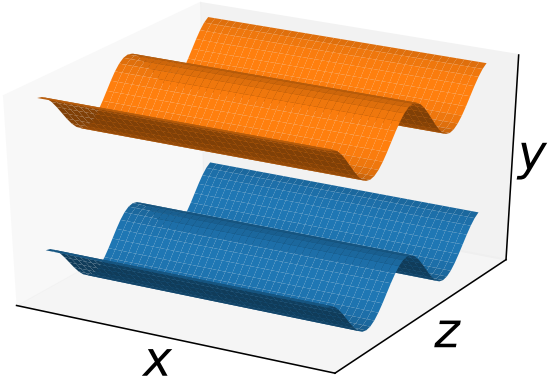

Figure 2.4: Couette flow between infinite plates with longitudinal grooves. The grooves are arranged "in-phase" so that the distance between the plates remains constant.

This geometry is illustrated in fig. 4.1. The grooved PCoF is mapped to a smooth PCoF geometry as

$$X = x, \qquad Y = T(y,z) = y - A\cos(\beta z), \qquad Z = z. \tag{2.7.2}$$

The partial derivatives in the two domains relate as

$$\partial_x = \partial_X, \qquad \partial_y = \partial_Y, \qquad \partial_z = \partial_Z - \left\{ i\beta\frac{A}{2}(e^{i\beta z} - e^{-i\beta z}) \right\}\partial_Y. \tag{2.7.3}$$

This domain transformation produces a mode coupling in the z-derivative,

$$\mathcal{F}_{l,m}(\partial_z u) = \mathcal{F}_{l,m}(u) - i\beta\left\{ \sum_{m'} m' \frac{A_{|m'|}}{2} \partial_Y \mathcal{F}_{l,m-m'}(u) \right\}, \tag{2.7.4}$$

where mode $(l, m \pm 1)$ contributes to the z-derivative of mode (l, m). This is how the topology of the roughness enters the formulation. The consequences of this mode coupling is discussed later in this chapter, as well as in chapter 5 with regards to developing a DNS engine for grooved plane shear flows. This formulation is extended to multiple grooves per box later in this chapter.

2.7.1 Computational memory requirements

The laminar solution for smooth channel flow is $\big[u, v, w\big] = \big[1 - y^2, 0, 0\big]$. These solutions, when extended to grooved flows, are homogeneous along the homogeneous direction of the grooves. Even for the case of oblique grooves, the flow field variables could be expanded in a Fourier basis as

$$\big[u, v, w, p\big](X, Y, Z) = \big[u_k(Y), v_k(Y), w_k(Y), p_k(Y)\big] e^{ik(\alpha X + \beta Z)}$$

for oblique grooves given by $y_{walls} = \pm 1 + A\cos(\alpha x + \beta z)$.

However, known equilibria for smooth channel and Couette flows vary in both the streamwise and spanwise directions (or along any pair of orthogonal vectors in the wall-parallel plane). The consequence of this 3-dimensionality is that a Fourier expansion for the velocity and pressure fields must incorporate two orthogonal axes,

$$\big[u, v, w, p\big](X, Y, Z) = \big[u_{l,m}(Y), v_{l,m}(Y), w_{l,m}(Y), p_{l,m}(Y)\big] e^{i(l\alpha X + m\beta Z)}, \qquad (2.7.5)$$

for a solution periodic in a box of streamwise length $L_x = 2\pi/\alpha$ and spanwise length $L_z = 2\pi/\beta$. The discretization of the NSE and matrix-formulation of the Newton iteration step remain similar to what was done for the laminar case, except that the matrices are significantly larger. Henceforth, we refer to the Fourier mode $e^{i(l\alpha X + m\beta Z)}$ simply as the mode (l, m).

The large size of the state-vector, and the Jacobian in eq. (2.5.3), make computation of equilibria rather expensive. The storage required for these problems is easily estimated. The equilibria used in the present work are taken from the online database provided at www.channelflow.org. The nominal resolution used for these solutions is $L = 16$, $M = 16$, and $N = 35$, where the Fourier modes used in the streamwise and spanwise directions are $|l| \leq L$ and $|m| \leq M$, and N is the number of Chebyshev polynomials (number of Chebyshev nodes for the collocation method). For this resolution, with a naive implementation that does not exploit the symmetries of the

problem, the state-vector has 152,460 complex elements. Using double precision, the size of the Jacobian matrix comes to about 350 Gigabytes. This is without considering the memory needed to solve the iteration step of eq. (2.5.3). If this is also taken into account, the required memory would be about 600 Gigabytes (for the algorithm used in the present work to solve the iterative step). Clearly, such computations are not practical.

The alternatives to carrying out such computations are, 1) to use a matrix-free method for the steady-state equations, or 2) to use a matrix-free method with a DNS engine as has been done in all earlier works. These are not easy tasks, and the associated challenges are listed in a later chapter. In the present work, the equations are instead solved by exploiting the symmetries of the flow where possible, or solving them at lower resolutions to achieve what insight we can from the limited resolution. The computations have been limited to run on a computational node with 64GB of RAM without using any additional swap space.

Imposing real-valuedness

The variables, $[u, v, w, p]$, are all real-valued fields. While their Fourier coefficients are complex-valued, the real-valuedness means that the following constraint applies:

$$\big[u_{-l,-m}, v_{-l,-m}, w_{-l,-m}, p_{-l,-m}\big] = \big[u_{l,m}, v_{l,m}, w_{l,m}, p_{l,m}\big]. \tag{2.7.6}$$

This can be shown by taking a complex conjugate of the Fourier transform, illustrated below for the streamwise velocity:

$$\begin{aligned}
\overline{u_{l,m}}(Y) &= \mathrm{CC}\left\{ \frac{\alpha}{2\pi}\frac{\beta}{2\pi} \int_0^{2\pi/\alpha}\int_0^{2\pi/\beta} u(X,Y,Z) e^{-i(l\alpha X + m\beta Z)} \quad dX \quad dZ \right\} \\
&= \frac{\alpha}{2\pi}\frac{\beta}{2\pi} \int_0^{2\pi/\alpha}\int_0^{2\pi/\beta} u(X,Y,Z) e^{i(l\alpha X + m\beta Z)} \quad dX \quad dZ \\
&= u_{-l,-m}(Y),
\end{aligned} \tag{2.7.7}$$

where CC{} and the overline represent complex conjugates. Since half of the Fourier coefficients are complex conjugates of the other half, the flowfield is completely determined from the Fourier coefficients of just one half of the modes. Hence, in the Newton correction step ($J\delta\boldsymbol{\chi} = -\boldsymbol{F}(\chi)$), we discard equations (i.e, rows of J and $\boldsymbol{F}$) that correspond to a half of the modes, $l > 0$. Similarly, we drop the Fourier coefficients for modes $l > 0$ from the state-vector as well. However, equations for modes $l \leq 0$ contain terms involving coefficients of modes $l > 0$ (arising from the triadic interactions of the advection term). Since the $l > 0$ coefficients are dropped from the state-vector, these terms must be computed from their complex conjugate counterparts. This is done by splitting the Fourier coefficients for $l \leq 0$ into real and imaginary parts as follows.

We consider an equation that has both $u_{l,m}$ and $u_{-l,-m}$. We abuse notation yet again to represent these two coefficients simply as u and $\bar{u}$, collecting all terms in any specific equation as

$$Au + B\bar{u}.$$

Each factor in each term can be split into its real and imaginary parts,

$$\begin{aligned} Au + B\bar{u} &= (A_r + iA_i)(u_r + iu_i) + (B_r + iB_i)(u_r - iu_i) \\ &= A_r u_r - A_i u_i + B_r u_r + B_i u_i + i\{A_i u_r + A_r u_i + B_r u_r - B_r u_i\} \\ &= (A_r + B_r)u_r + (B_i - A_i)u_i + i\{(A_i + B_r)u_r + (A_r - B_r)u_i\} \end{aligned}$$

Thus, two complex-valued coefficients, $u(Y), \bar{u}(Y)$, can be replaced by two real-valued coefficients, $u_r(Y), u_i(Y)$. In the full state-vector containing complex-valued Fourier coefficients for modes (l, m), $|l| \leq L, |m| \leq M$, all coefficients for modes with $l > 0$ can be dropped in favour of real-valued coefficients of their conjugate modes with $l \leq 0$. All equations are split into an equation for the real part and an equation for the imaginary part. The factor matrices for u_r, u_i are also real. The number of equations, and the number of elements in the state-vector, remain about the same. However, all entries are now real-valued, thus halving the size of the Jacobian matrix

(in memory).

Before moving to symmetry imposition, we revisit the governing equations to show how the domain transformation can be used for geometries with multiple grooves within the periodic domain.

2.7.2 Multiple Fourier modes to represent grooves

Since equilibria require finer resolution than laminar solutions, it is possible to include a few more Fourier modes into the grooves until the highest wavenumber of the groove can be adequately resolved. The equation for the wall is extended to a more general form as

$$y_{walls} = \pm 1 + S(z) = \pm 1 + \sum_{q \in \mathbb{Z}} A_q \cos(q\beta z - \phi_q \pi). \tag{2.7.8}$$

The phases, $\phi_q \pi$, provide a handle to break the discrete symmetries of PCoF outlined in § 2.2.3. When ϕ_q are all zero, then all Fourier modes peak at $z = 0$.

The domain transformation involves the coordinate mapping

$$Y = T(y, z) = y - S(z) = y - \sum_q A_q \cos(q\beta z - \phi_q \pi) = y - \sum_q \epsilon_q e^{i(q\beta z - \phi_q \pi)}, \tag{2.7.9}$$

where $\phi_{-|q|} = -\phi_{|q|}$ and $\epsilon_{-|q|} = \epsilon_{|q|} = A_{|q|}/2$.

The partial derivatives in x, y, z are expressed in terms of partial derivatives in X, Y, Z as

$$\begin{aligned} \partial_x &= \partial_X, \\ \partial_y &= \partial_Y, \\ \partial_z &= \partial_Z + T_z \partial_Y, \\ \partial_{xx} &= \partial_{XX}, \end{aligned} \tag{2.7.10}$$

$$\partial_{yy} = \partial_{YY},$$
$$\partial_{zz} = \partial_{ZZ} + T_{zz}\partial_Y + T_z^2\partial_{YY} + 2T_z\partial_{YZ},$$

and the governing equations in the transformed domain are

$$\begin{aligned}
u\partial_X u + v(\partial_y T)\partial_Y u + w\{(\partial_z T)\partial_Y + \partial_Z\}u &= -\partial_X p \\
&\quad + \frac{\tilde{\Delta}(\partial_{zz}T)\partial_Y + (\partial_z T)^2\partial_{YY} + 2(\partial_z T)\partial_{YZ}}{Re}u, \\
u\partial_X v + v(\partial_y T)\partial_Y v + w\{(\partial_z T)\partial_Y + \partial_Z\}v &= -(\partial_y T)\partial_Y p \\
&\quad + \frac{\tilde{\Delta} + (\partial_{zz}T)\partial_Y + (\partial_z T)^2\partial_{YY} + 2(\partial_z T)\partial_{YZ}}{Re}v, \\
u\partial_X w + v(\partial_y T)\partial_Y w + w\{(\partial_z T)\partial_Y + \partial_Z\}w &= -\{(\partial_z T)\partial_Y + \partial_Z\}p \\
&\quad + \frac{\tilde{\Delta} + (\partial_{zz}T)\partial_Y + (\partial_z T)^2\partial_{YY} + 2(\partial_z T)\partial_{YZ}}{Re}w, \\
\partial_X u + (\partial_y T)\partial_Y v + \{(\partial_z T)\partial_Y + \partial_Z\}w &= 0,
\end{aligned} \tag{2.7.11}$$

where $\tilde{\Delta} = \partial_{XX} + (\partial_y T)^2\partial_{YY} + \partial_{ZZ}$. The boundary conditions are those given in eq. (2.3.4).

The partial derivatives of T with respect to z are z-dependent and can be calculated as below.

$$\begin{aligned}
\sum_q T_{z,q}e^{qi\beta Z} = T_z(Z) = \sum_q -iq\beta\epsilon_q e^{i(q\beta z - \phi_q\pi)} \\
\implies \boxed{T_{z,q} = -i\beta q\epsilon_q e^{-i\phi_q\pi}} \\
\sum_q T_{zz,q}e^{qi\beta Z} = T_{zz}(Z) = \sum_q -(iq\beta)^2\epsilon_q e^{i(q\beta z - \phi_q\pi)} \\
\implies \boxed{T_{zz,q} = \beta^2 q^2\epsilon_q e^{-i\phi_q\pi}}
\end{aligned} \tag{2.7.12}$$

$T_{z,q}^2$ is a tricky one since it involves a product. Writing an explicit expression gets cumbersome; however, it is easily obtained by doing an inverse Fourier transform of $T_{z,q}$ to get $T_z(z)$ on a grid of appropriate size, squaring it, and taking the Fourier transform of the result.

2.7.3 Reducing state-space dimensionality

Section 2.2 discussed the symmetries of PCoF, along with some remarks on their significance to studying turbulence dynamics. It was also mentioned that these symmetries can be exploited to reduce the dimensionality of state-space. We have already used the wall-parallel homogeneity of the flow to restrict solutions to periodic boxes, allowing the usage of discrete Fourier modes. Now, we exploit a few more symmetries to further reduce the number of Fourier and Chebyshev modes that need to be used. The implementation in code of this reduction is fairly involved, and is omitted here for the sake of brevity. The symmetry transformations mentioned in § 2.2.3 are now described in terms of relations between Fourier coefficients. These relations are first obtained for generic translation, rotation, reflection, and pointwise inversion, and then composed to obtain the Fourier mode relations for the specific symmetries of s_1, s_2, and s_3.

Symmetry transformations are denoted as follows:

$au_{\xi,\zeta}$	Translation in X and Z by ξ and ζ respectively
$\mathfrak{L}_\zeta$	Reflection about the $Z = \zeta$ plane
$\mathfrak{R}_\xi$	Rotation by π about the Z axis at $X = \xi$
$\mathfrak{P}_{\xi,\zeta}$	Point-wise inversion about $(X, Z) = (\xi, \zeta)$

Translation

The translated field $\tau_{\xi,\zeta}u$ relates to the original field u as

$$u(x - \xi, Y, z - \zeta) = (\tau_{\xi,\zeta}u)(X, Y, Z).$$

Fourier coefficients of the translated field, $(\tau)_{l,m}(Y)$, can be related to those of the original field by expanding the functions as Fourier series, and matching coefficients for individual modes. This gives

$$(\tau_{\xi,\zeta}u)_{l,m}(Y) = e^{-i(l\alpha\xi + m\beta\zeta)}u_{lm}(Y). \tag{2.7.13}$$

The coefficients for variables v, w, and p also transform similarly.

If the flow field is invariant under translations by (ξ, ζ), i.e. when $\tau_{\xi,\zeta} u = u$, then the modes on the left hand side can be replaced by the original modes $u_{l,m}(Y)$,

$$u_{l,m}(Y) = e^{-i(l\alpha\xi + m\beta\zeta)} u_{lm}(Y).$$

The flow field is invariant under $\tau_{2n_1\pi\alpha, 2n_2\pi\beta}$ for integers n_1 and n_2, which follows from the assumed periodicity of the solution. The translation operator commutes with itself.

The special cases that we are interested in are of half-cell shifts, i.e. $\tau_{\pi/\alpha,0}, \tau_{0,\pi/\beta}, \tau_{\pi/\alpha,\pi/\beta}$. These induce a change in sign in some of the Fourier coefficients. For instance,

$$\big[\tau_{\pi/\alpha,\pi/\beta} u_{l,m}, \tau_{\pi/\alpha,\pi/\beta} v_{l,m}, \tau_{\pi/\alpha,\pi/\beta} w_{l,m}, \tau_{\pi/\alpha,\pi/\beta} p_{l,m}\big](Y) = (-1)^{l+m} \big[u_{l,m}, v_{l,m}, w_{l,m}, p_{l,m}\big](Y).$$

$\tau_{\xi,\zeta} u_{l,m}$ refers to $\big(\tau_{\xi,\zeta} u\big)_{l,m}$, the Fourier coefficients of the transformed field. The braces are dropped for convenience here and in later expressions.

Reflections about $Z = \zeta$ planes, $\mathfrak{L}_\zeta$

A reflection about any $Z = \zeta$ plane can be decomposed in terms of translations as $\mathfrak{L}_\zeta = \tau_{0,\zeta} \mathfrak{L}_0 \tau_{0,-\zeta}$, where the transformations are applied from right to left. Hence, it is sufficient to describe $\mathfrak{L}_0$, and reflections about all other planes follow. $(\mathfrak{L}_0 u)$, relates to the original field as

$$\big(\mathfrak{L}_0 \big[u, v, w, p\big]\big)(X, Y, Z) = \big[u, v, -w, p\big](X, Y, -Z).$$

Expanding the fields in a Fourier series and matching coefficients for individual modes produces

$$\big[\mathfrak{L}_0 u_{l,m}, \mathfrak{L}_0 v_{l,m}, \mathfrak{L}_0 w_{l,m}, \mathfrak{L}_0 p_{l,m}\big](Y) = \big[u_{l,-m}, v_{l,-m}, -w_{l,-m}, p_{l,-m}\big](Y). \qquad (2.7.14)$$

Unlike the translational case where the shift resulted in an extra factor, the reflection simply maps one Fourier mode (l,m) to another mode (l,-m), with a -1 factor for the spanwise velocity.

Rotations about $X = \xi$ axes, $\mathfrak{R}_\xi$

Similar to the reflections about different $Z = \zeta$ planes, rotations about $X = \xi$ axes can be decomposed in terms of translations as $\mathfrak{R}_\xi = \tau_{\xi,0}\mathfrak{R}_0\tau_{-\xi,0}$. Rotations about the x-axis are given by the transformation

$$\big(\mathfrak{R}_0\big[u,v,w,p\big]\big)(X,Y,Z) = \big[-u,-v,w,p\big](-X,-Y,Z),$$

and the Fourier coefficients of $(\mathfrak{R}_0 u)$ relate to those of the original field as

$$\big[\mathfrak{R}_0 u_{l,m}, \mathfrak{R}_0 v_{l,m}, \mathfrak{R}_0 w_{l,m}, \mathfrak{R}_0 p_{l,m}\big](Y) = \big[-u_{-l,m}, -v_{-l,m}, w_{-l,m}, p_{-l,m}\big](-Y). \quad (2.7.15)$$

Note the change in sign of the parameter Y for each Fourier coefficient.

Pointwise inversion, $\mathfrak{P}_{\xi,\zeta}$

Pointwise inversion about any point (ξ,ζ) can also be decomposed into translations and pointwise inversion about the origin as $\mathfrak{P}_{\xi,\zeta} = \tau_{\xi,\zeta}\mathfrak{P}_0\tau_{-\xi,-\zeta}$. Pointwise inversion about the origin,

$$\big(\mathfrak{P}_{0,0}\big[u,v,w,p\big]\big)(X,Y,Z) = \big[-u,-v,-w,p\big](-X,-Y,-Z) = (\mathfrak{R}_0\mathfrak{L}_0\big[u,v,w,p\big])(X,Y,Z),$$

is a composition of the rotation and reflection about the x-axis and the $z = 0$ plane respectively. The transformation of individual Fourier coefficients due to pointwise inversion can then be written as

$$\big[\mathfrak{P}_{0,0}u_{l,m}, \mathfrak{P}_{0,0}v_{l,m}, \mathfrak{P}_{0,0}w_{l,m}, \mathfrak{P}_{0,0}p_{l,m}\big](Y) = \big[-u_{-l,-m}, -v_{-l,-m}, -w_{-l,-m}, p_{-l,-m}\big](-Y). \quad (2.7.16)$$

We note here that $\mathfrak{L}_0, \mathfrak{R}_0$, and $\mathfrak{P}_0$ are the same as σ_z, σ_x, and σ_{xz} from § 2.2.3 respectively.

The symmetries s_1, s_2, and s_3 from § 2.2.3 can now be written in terms of how they transform Fourier coefficients. It must be noted that, in this section, we have deviated from the notation used in § 2.2.3 to accommodate an expansive definition for the discrete symmetries. In the notation used in this section, these symmetries are decomposed as $s_1 = \tau_{\pi/\alpha,0}\mathfrak{L}_0$, $s_2 = \tau_{\pi/\alpha,\pi/\beta}\mathfrak{R}_0$, and $s_3 = \tau_{0,\pi/\beta}\mathfrak{P}_0$. The symmetry s_3 is a product of s_1 and s_2.

$$\begin{aligned}
\big[s_1 u_{l,m}, s_1 v_{l,m}, s_1 w_{l,m}, s_1 p_{l,m}\big](Y) &= (-1)^l \big[u_{l,-m}, v_{l,-m}, -w_{l,-m}, p_{l,-m}\big](Y) \\
\big[s_2 u_{l,m}, s_2 v_{l,m}, s_2 w_{l,m}, s_2 p_{l,m}\big](Y) &= (-1)^{l+m} \big[-u_{-l,m}, -v_{-l,m}, w_{-l,m}, p_{-l,m}\big](-Y) \\
\big[s_3 u_{l,m}, s_3 v_{l,m}, s_3 w_{l,m}, s_3 p_{l,m}\big](Y) &= (-1)^m \big[-u_{-l,-m}, -v_{-l,-m}, -w_{-l,-m}, p_{-l,-m}\big](-Y)
\end{aligned} \tag{2.7.17}$$

Memory requirements with symmetries imposed

We now return to the estimate for the size of the Jacobian given in § 2.7.1. This estimate was based on a complex-valued state-vector with $\big[u_{l,m}, v_{l,m}, w_{l,m}, p_{l,m}\big](Y)$ for Fourier modes $-16 \leq l \leq 16$ and $-16 \leq m \leq 16$, and for 35 wall-normal Chebyshev nodes. Imposing the real-valuedness trims streamwise Fourier modes to $-16 \leq l \leq 0$ and replaces the complex-valued entries of the state-vector and the Jacobian with real-valued entries; however, the Fourier coefficient for each mode (l, m) now has 70 entries due to the real and imaginary parts of $u_{l,m}$. This brings down the required memory for storing the Jacobian to about 184 GB. Imposing s_1-invariance allows trimming spanwise Fourier modes to $-16 \leq m \leq 0$, and brings down the required memory to 50 GB. Finally, imposing s_3 in addition to s_1 allows dropping all $Y > 0$ nodes, reducing the number of Chebyshev nodes to 18. This brings down the required memory to 13 GB. If the memory needed to solve the linear equation in the iteration step is also accounted for, the total memory needed is still likely to remain under 32 GB, which can be handled by high performance computers.

It is important to note that the state-space dimensionality can be reduced as above only when seeking solutions that are invariant under these symmetries. In grooved PCoF, however, the geometry may not admit solutions that are invariant under these symmetries in some cases, or admit only a subset or superset of these symmetries. Even when the geometry admits any/all of these symmetries, they can only be exploited when we seek symmetric solutions. In § 4.2, we look at continuation of smooth-walled solutions that are shifted along the spanwise direction with respect to the grooves, so that the planes of (shift-)reflectional symmetry of the grooves do not coincide with those planes of the initial iterate. For these cases, the above dimensionality reduction is not possible.

2.8 Numerical continuation

2.8.1 Convergence criteria

Two quantities are defined to ascertain stationarity and grid independence of solutions, the residual norm ($||\mathbf{r}|| = ||\mathbf{F}(\boldsymbol{\chi})||$) and the spatial accuracy ($||\boldsymbol{F}(\boldsymbol{\chi}_{2\times})||$), as follows.

$$||\mathbf{r}|| = \left[\int_{x=0}^{2\pi/\alpha}\int_{z=0}^{2\pi/\beta}\int_{y=y_{bottom}}^{y_{top}} (\dot{u}^2 + \dot{v}^2 + \dot{w}^2 + (\nabla\cdot\boldsymbol{u})^2 \mathrm{d}y\mathrm{d}z\mathrm{d}x\right]^{1/2}. \tag{2.8.1}$$

The divergence term is included in the definition of the residual norm to reflect the inclusion of the divergence-free condition as an equation in the solver. In practice, any non-zero divergence introduced into the initial iterate (due to the domain transformation) is corrected in the first Newton iteration. This follows from the linearity of the divergence-free condition and the full-rank inversion of the Jacobian. Thus, the residual norm (squared) for all subsequent iterates is essentially an integral of the instantaneous time derivative over the periodic domain.

The spatial accuracy, ($||\boldsymbol{F}(\boldsymbol{\chi}_{2\times})||$), is the same as the residual norm except with the state-vector χ interpolated to a grid of twice the resolution along each direction. This interpolation is done by padding the state-vector with L and M additional, zero Fourier modes in X and Z respectively. In Y, the collocation over N Chebyshev nodes is interpolated to $2N$ Chebyshev nodes. The spatial accuracy is obtained simply by evaluating the NSE for padded and interpolated state-vector; no additional computations are performed.

In this thesis, solutions are deemed to have converged when the residual norm goes below 10^{-12} and the spatial accuracy is below 10^{-4}.

2.8.2 Initial iterate

Appendix A outlines a proof of convergence for the Newton iteration of eq. (2.5.3) for laminar channel flow with transverse grooves, along with an upper bound on a

continuation parameter ($g := A\alpha/2$) which ensures super-linear convergence (i.e., the ratio of successive errors $\boldsymbol{e}^{m+1}$ and $\boldsymbol{e}^{m}$ approaches zero as m increases). In practice, the iterative scheme shows convergence whenever the resolution is adequate and the initial iterate is "reasonably" close to the solution. In fact, the numerical continuation that is used in the present work does not involve any form of arc-length continuation; instead, an existing smooth-wall solution is used as the initial iterate even when the amplitudes of the grooves are as high as 20%. This is because the residual norm decreases fast enough in the first few iterations so that usage of continuation methods does not provide any computational advantage.

The initial iterate for obtaining laminar solutions in grooved channels, for all grooved geometries, is

$$u_{l,m} = (1 - Y^2)\delta_{l,0}\delta_{m,0}, \qquad v_{l,m} = 0, \qquad w_{l,m} = 0, \qquad p_{l,m} = 0. \tag{2.8.2}$$

For 3d equilibria in PCoF, solutions from the online database of www.channelflow.org are used; the solver hosted on the website includes a utility to solve for the pressure field for the velocity fields provided in the database. These solutions are introduced into the transformed domain of (X, Y, Z) coordinates. The phase of the solutions with respect to the grooves is set such that the discrete symmetries of the flow can be exploited. This may be achieved by setting the origin of the solutions from the database to coincide with the origin of the grooved geometry. For some geometries, multiple, dissimilar configurations are possible that allow symmetry exploitation. In § 4.2, the differences between these symmetry preserving configurations, as well as the consequences of breaking these symmetries is addressed in detail.

2.8.3 Code verification

The numerical method, and the code for its implementation, has two components: the evaluator for the steady-state NSE, $\boldsymbol{\mathcal{F}}(\boldsymbol{\chi})$), and the iterative scheme that minimizes $\boldsymbol{\mathcal{F}}(\boldsymbol{\chi})$. For validation, only the evaluator is considered. While the properties

of the iterative scheme are important from a computational standpoint, it is only the final result — the converged solution — that is important to the present work. The flow field of interest is only the steady-state solution, and not the intermediate iterates. As such, as long as we are confident that the evaluation of the steady-state NSE, that is sufficient to establish the validity of the numerical method. Its efficiency is a secondary issue that is not pursued in this thesis.

Method of Manufactured Solutions (MMS)

The Method of Manufactured Solutions (MMS) uses analytical solutions to verify the accuracy of CFD codes (Roache (2002)). The basic principle is to use evaluate the governing equations for an appropriate analytical field which is simple enough to be evaluated, while complex enough to reflect the physical problem. The residual is then introduced as a source term to the governing equations. The modified governing equations are then solved using the code in question, with the analytical solution used to generate the source terms as input. The error (residual for the modified equations) produced by this computation must, if the code is accurate, then be of the same order as the discretization error due to the scheme used.

The code used in the present work is verified in two steps. First, the accuracy of the evaluator of the steady-state NSE is established for smooth-walled geometries. This is done by setting the amplitude of the grooves to zero for any wavenumber pair (α, β), and verifying that laminar solutions (quadratic streamwise velocity for channel flow and linear streamwise velocity for PCoF) evaluate to zero. In addition, a set of solutions from the online database of smooth PCoF equilibria hosted at www.channelflow.org are evaluated with the present code. The residual norm for these solutions are $\sim 10^{-6}$, which is considered to be adequate considering the difference in the definition of the residuals; the solutions given in the database are obtained using a time-stepping algorithm, while we directly evaluate the steady-state NSE. This verifies the accuracy of the code for zero groove amplitude cases.

The second step is to verify the accuracy of the evaluator when the groove ampli-

tude is non-zero. This is done by evaluating the NSE for trial fields of the following kind

$$u_{l,m} = \frac{1}{(l^2+1)(m^2+1)}(1-Y^2),$$
$$v_{l,m} = \frac{A}{2}\frac{1}{(l^2+1)(m^4+1)}(1-Y^4),$$
$$w_{l,m} = \frac{A}{2}\frac{1}{(l^2+2)(m^2+2)}(1-Y^6),$$

for different grid sizes and amplitudes. All of the partial derivatives are easily calculated for the above trial flow fields, and so are the individual terms of the NSE. The partial derivatives, individual terms, and the full NSE evaluated from the code for the trial flow fields are compared to the expressions obtained analytically for different Fourier coefficients; the error in these terms is close to the precision of double floats ($\lesssim 10^{-15}$). This is also repeated with some higher order polynomials (greater than the number of collocation nodes used along the wall-normal direction) added to the Fourier coefficients, and the error reflects the amplitude of the higher order polynomials.

2.8.4 Grid convergence

Peformance of the solver for different grid resolutions is now illustrated for the simple case of laminar solutions in channel flows with longitudinal grooves. The groove amplitude chosen here is 1% and the wavenumber is 4; the solution is independent of Re. Figure 2.5 shows the spatial accuracy and the error in the converged solution plotted against the number of wall-normal nodes N for a set of spanwise grid points nz. The finest resolution used is $(nz, N) = (30, 70)$. Since a true solution that is devoid of discretization errors is not available, the error in the converged solution obtained at a resolution (nz, N) is defined as the norm of the difference in the velocity fields of the solution at the finest resolution, $(nz = 30, N = 70)$, and the solution at any other (nz, N) interpolated to $(nz = 30, N = 70)$.

For the geometry used in this illustration, $(A, \beta) = (0.01, 4)$, the spatial accuracy rapidly decreases as N increases from 10 and saturates at $N = 15$ for the $nz = 6$ case,

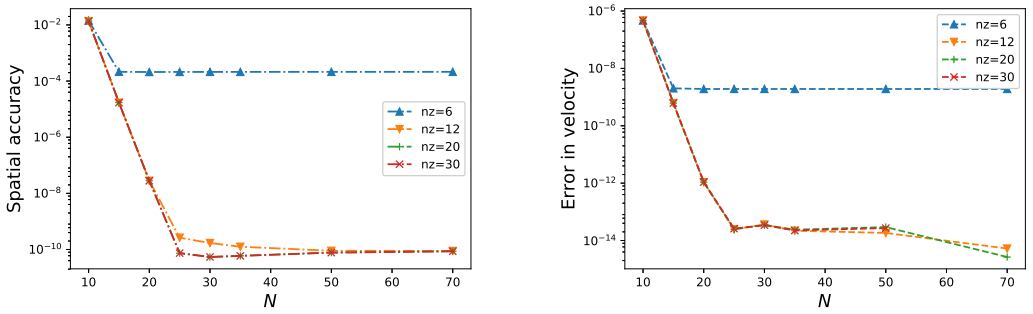

(a) Spatial accuracy (b) Error in solution

Figure 2.5: Spatial accuracy (left) and error in the converged solution (right) for longitudinal grooves with $A = 1\%$ and $\beta = 4$. The resolution is represented by N, the number of wall-normal nodes, and nz the number of spanwise grid points. The error in the solution is computed as the norm of the difference from the solution with the largest resolution.

and at $N = 25$ for the greater nz cases. The spatial accuracy faithfully represents the error in the solution. Clearly, a resolution of $(nz, N) = (12, 25)$ is adequate for the present case, where spatial accuracy goes below $\sim 10^{-9}$. Geometries with larger (A, β) cannot go to such low spatial accuracies at such resolutions. In present computations, iterations are initiated with coarse grids (decided based on iterations for cases at lower groove slopes), and the resolution is increased whenever the spatial accuracy is greater than 10^{-4}.

2.9 Limitations of the steady-state solver

2.9.1 Failure of matrix-free methods

Matrix equations such as the correction step of the Newton method, eq. (2.5.3), are often solved using matrix-free methods such as GMRES or LGMRES. This was attempted in the present work using finite differences of the residual $F(\chi)$ to estimate the action of the Jacobian on trial vectors; the residual function $F(\chi)$ can be evaluated without building the Jacobian matrices by looping over Fourier coefficients for the linear terms, and using the convolution theorem for the non-linear term. However, convergence could not be achieved unless GMRES proceeded to build a basis incorporating the full rank of the Jacobian, as discussed below.

We now investigate the convergence of GMRES for the present solver for a smooth channel and a transverse-grooved channel (amplitude and slope of 2% and 0.2 respectively). The Jacobian, $J = \boldsymbol{F}'(\boldsymbol{\chi})$, has contributions from the linear and non-linear parts of the NSE, and is a matrix-valued function of the state-vector $\boldsymbol{\chi}$. For the grooved case, the Jacobian is defined based on the laminar velocity for the smooth channel, $[u, v, w] = [1 - Y^2, 0, 0]$. For the smooth case, the same velocity field is used, except with a perturbation introduced so that the state-vector is not a solution. The perturbed flowfield used in this case is $[u, v, w] = [0.998(1 - y^2), 2\cos(\alpha x)\{0.01(1 - y^2) + 0.001(1 - y^4)\}, 0]$; their is no specific reason for using this particular velocity field except that it satisfies the velocity boundary conditions and is close to the laminar solution.

Convergence of GMRES-like methods depends on the spread of eigenvalues of the matrix A in $Ax = b$. If they are clustured close to some non-zero value, then a polynomial that goes to zero near this clustured value would rapidly reduce the residual. If the eigenvalues have a wide-spread, then convergence is harder since higher order polynomials (i.e., greater n, where n is the number of Arnoldi vectors) would be needed to have zeros at each of these eigenvalues. The eigenvalue spectra for the Jacobian matrices for the smooth and grooved channel flows are shown in fig. 2.6.

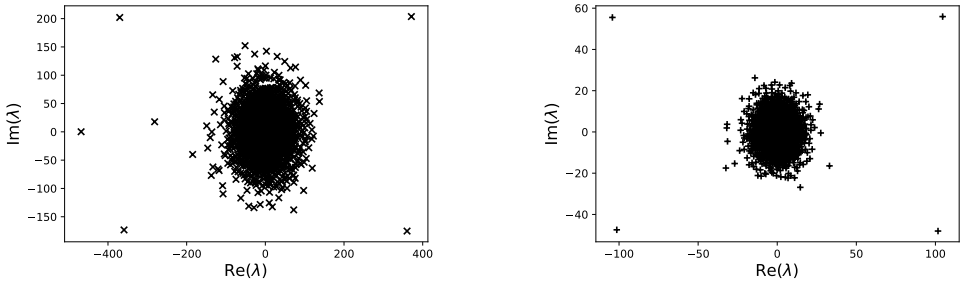

(a) Flat channel (b) $A = 0.02$, $S = 0.2$

Figure 2.6: Eigenvalues of the Jacobian without a preconditioner for a flat and grooved channel

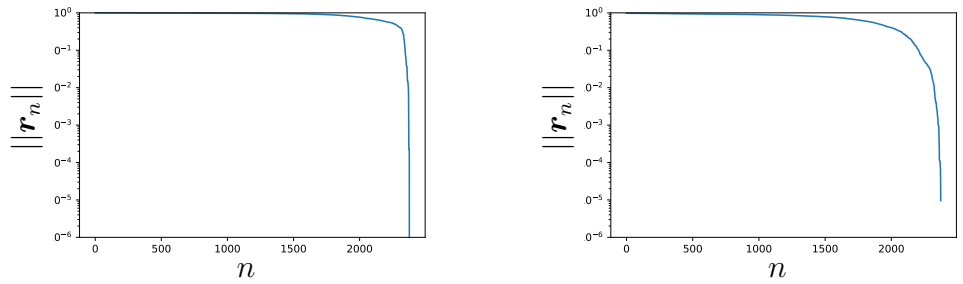

(a) Flat channel (b) $A = 0.02$, $S = 0.2$

Figure 2.7: Residual norm ($||\boldsymbol{r}||$) with iteration number (n) for GMRES (no restarting) without preconditioning. The Jacobian is based on the initial iterate $\left[u, v, w, p\right] = \left[1 - Y^2, 0, 0, 0\right]$.

The eigenvalues have a large spread in the complex plane. Matrices with eigenvalue spectra such as these are not suitable for use with Arnoldi-based methods such as GMRES.

Indeed, when a GMRES is used to solve the Newton correction step, $J\delta\boldsymbol{\chi} = -\boldsymbol{F}(\boldsymbol{\chi})$, the convergence is very slow. This is seen from fig. 2.7, where the residual in the linear equation is plotted against the size of the subspace constructed in GMRES.

Preconditioners are often used to improve convergence of matrix-free methods. A preconditioner is some matrix P, which must be easily invertible, so that $P^{-1}Ax = P^{-1}b$ is cheaper to solve than the original system $Ax = b$. For dense matrix solvers such as LU decomposition or QR decomposition based solvers, the requirement is for the condition number of $P^{-1}A$ to be significantly smaller than the condition number of A. For matrix-free solvers such as GMRES, the eigenvalue spectrum of $P^{-1}A$ must

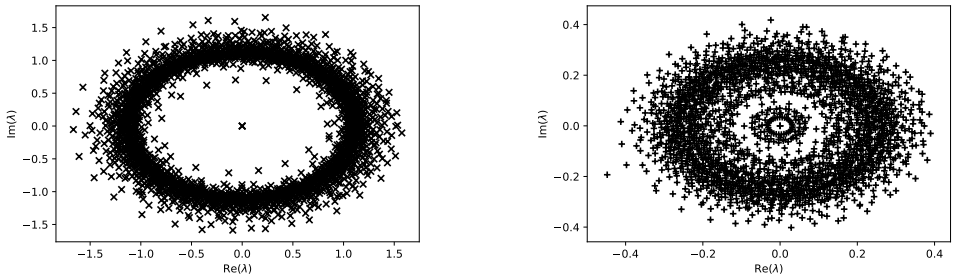

(a) Flat channel (b) $A = 0.02$, $S = 0.2$

Figure 2.8: Eigenvalues of the Jacobian with a preconditioner based on the linear operator for a flat and grooved channel

have more eigenvalues near zero and/or more eigenvalues that are clustered at fewer points in complex space than the eigenvalue spectrum of A.

Figure 2.8 shows the eigenvalue spectrum for the Jacobian (left-)multiplied with a preconditioner; the preconditioner here is the inverse of the linear operator (reference). While the eigenvalues are now closer than without the preconditioner, they are still spread out in the complex plane, and very few eigenvalues are near zero. This is true for the smooth and the grooved cases. A look at the convergence of GMRES in fig. 2.9b shows that including the preconditioner does not provide adequate improvement in convergence.

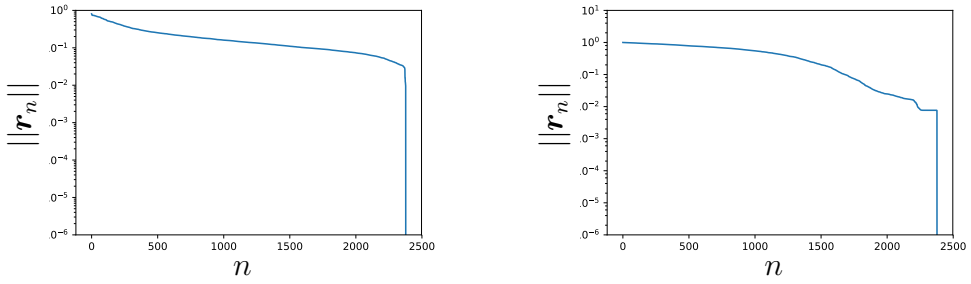

(a) Flat channel (b) $A = 0.02$, $\alpha = 10$.

Figure 2.9: Residual norm ($||\boldsymbol{r}||$) with iteration number (n) for GMRES (no restarting) with linear operator based preconditioning. The Jacobian is based on the initial iterate $\left[u, v, w, p\right] = \left[1 - Y^2, 0, 0, 0\right]$.

The poor performance of GMRES must be related to the Jacobian matrix being dense. Matrix-free methods work best for sparse matrices in which the number of non-zero elements scale as $\mathcal{O}(N \log N)$, where N is the number of rows or columns,

while the Jacobian from the steady-state NSE has about $\sim 0.7N^2$ non-zero elements due to the non-linear interactions and the dense wall-normal differentiation matrices. Indeed, there is no reason to believe that such a dense matrix would perform well with matrix-free methods. Variants of the Newton method employing trust-region method, using implementations in Scipy (Python library for computing), have also been used to see if other matrix-free methods could help obtain solutions based on the steady-state NSE. Unsurprisingly, such methods also have a slow rate of convergence, significantly slower than the full-rank inversion that has been used to obtain the results in this thesis. The slow convergence for the smooth channel case suggests that the slow convergence is not related to the grooves, but is caused by the steady-state solver itself.

2.9.2 Considerations for building a DNS code

Minimization of the residual from the steady-state NSE is unsuitable for matrix-free methods because of the Jacobian matrix being dense; this formulation can be extended to periodic orbits by using temporal Fourier modes, but the problem of dense matrices persists. The DNS-based solver of Gibson (2014) shows a good rate of convergence to equilibria, suggesting that time-t maps produce a sparse Jacobian. The challenges with extending the DNS engine of this solver to grooved geometries employing the domain transformation method are now outlined.

Spectral DNS codes for plane shear flows in periodic boxes are computationally cheap because the Fourier spectral method produces modes that are decoupled. As outlined in § C.0.1, this allows the time-marching step

$$\begin{aligned}\left[\frac{1}{\Delta t}-\frac{1}{2}\mathcal{L}\right]\boldsymbol{u}^{n+1}+\frac{1}{2}\nabla p^{n+1} = \\ \left[\frac{1}{\Delta t}+\frac{1}{2}\mathcal{L}\right]\boldsymbol{u}^{n}-\frac{1}{2}\nabla p^{n+1}+\frac{3}{2}\boldsymbol{\mathcal{N}}(\boldsymbol{u}^{n})-\frac{1}{2}\boldsymbol{\mathcal{N}}(\boldsymbol{u}^{n-1})+\boldsymbol{f},\end{aligned} \tag{2.9.1}$$

to be decomposed into equations for each Fourier coefficient as

$$\begin{aligned} c_1 \boldsymbol{u}''^{n+1}_{l,m} + c_2 \boldsymbol{u}^{n+1}_{l,m} + c_3 \nabla p^{n+1}_{l,m} &= \boldsymbol{g}_{l,m}, \\ il\alpha u_{l,m} + v'_{l,m} + im\beta w_{l,m} &= 0, \\ (u_{l,m} - U) = v_{l,m} = w_{l,m} = v'_{l,m} &= 0 \qquad \text{at y} = \pm 1, \end{aligned} \tag{2.9.2}$$

where $u'_{l,m} = \frac{du_{l,m}}{dy}$ and $u''_{l,m} = \frac{d^2 u_{l,m}}{dy^2}$

For grooved PCoF, when the domain transformation is used to obtain the equations in eq. (2.7.11), Z-dependent coefficients appear as factors for the linear terms. The decoupling of Fourier modes is now replaced by interactions with adjacent Fourier modes, i.e. z-derivatives of the coefficient $u_{l,m}$ now involve $u_{l,m+q}$ for each Fourier mode q that has a non-zero amplitude in the Fourier expansion of the groove geometry in eq. (2.7.9). If the linear term, $\boldsymbol{\mathcal{L}u}$, is to be treated implicitly, then collections of Fourier coefficients, $(l, -M \leq m \leq M)$ have to be solved simultaneously. This becomes rather expensive, especially when several hundreds or thousands of time-steps are needed to produce the time-t map for each trial velocity field.

An influence matrix technique is described in appendix C.0.1 to account for the coupling between wall-normal velocity and pressure for each Fourier coefficient; this is briefly outlined now. This technique is used to tackle the issue of unknown boundary conditions for pressure when solving the pressure Poisson equation when advancing the flowfield in time; the boundary condition on the pressure Poisson equation is the divergence-free condition, which is $v'_{l,m} = 0$ for flat walls. In this technique, the pressure Poisson equation and the equation for the wall-normal velocity for each Fourier coefficient are solved by splittin the solution into three parts. The first part is for the "forced" equations with zero Dirichlet boundary conditions on pressure and wall-normal velocity. The second pair is for equations with zero forcing and zero Dirichlet boundary conditions on wall-normal velocity, but with pressure being 0 at the bottom wall and 1 at the top wall for one solution, and being 1 at the bottom wall and zero at the top wall for the other. This pair of solutions, which produce

$v'l, m \neq 0$ at the walls, are then scaled and added to the first solution such that the sum of v' for the first part and the second pair becomes zero at both walls.

Even if one were to solve for a set of modes $(l, -M \leq m \leq M)$ simultaneously, application of the influence matrix technique is not so straight-forward. While the A problem described in appendix C.0.1 is easily solved, if at a significant computational expense (in terms of memory usage), framing the B-problem is not as simple. This is because the problem now involves a set of Fourier modes; instead of two problems, B_+ and B_- where the pressure BCs are alternated, a large number of permutations of different $p_{l,m}$ have to be incorporated to adequately solve this system. Furthermore, the divergence of the velocity at the walls, $\nabla \cdot \boldsymbol{u}(Y = \pm 1)$, is not equal to $v'(Y = \pm 1)$ because $\{\partial_z w\}(Y = \pm 1) \neq 0$ at most locations on the wall. This leads to additional coupling with the spanwise velocity in the influence matrix method.

A fully implicit scheme for the linear terms becomes rather cumbersome. One might envisage using a semi-implicit scheme for discretizing the linear terms in eq. (2.9.1), where contributions to $\mathcal{F}(\mathcal{L}\boldsymbol{u})_{l,m}$, a Fourier coefficient of the linear term, due to all adjacent modes is treated explicitly. However, if such a scheme will be stable is not known for this domain transformation method, and has hence not been pursued in the present work.

Chapter 3

Laminar solutions for grooved channel flows

The difficult problems in life always start off being simple. Great affairs always start off being small.

Lao Tzu

Laminar solutions are useful in learning the effectiveness of the present approach to continuing exact invariant solutions, because of the relatively small dimensionality of the laminar solution. Channel flows are investigated here because a steady laminar solution can be found for longitudinal, transverse, and oblique grooves in channel flows; in Couette flows, the streamwise motion of streamwise-inhomogeneous walls leads to the disappearance of steady solutions when the grooves are not longitudinal.

The most relevant work in the literature for our laminar investigations is the one by Mohammadi and Floryan (2013), where they investigated channel geometries with a flat wall at the top and a grooved wall at the bottom, unlike the ones in this thesis with two grooved walls. They used an immersed boundary method (IBM) to compute solutions for laminar flows in channels with transverse, longitudinal, and oblique grooves (on the bottom wall), focusing on the relative contributions to the total drag from the pressure drag and the shear stresses at the wall. A stream lift-up is reported for channel flows with transverse grooves when the depth-to-wavelength aspect ratio is

sufficiently high ($\gtrsim 1$); this is consistent with the "protrusion height" used previously by Bechert and Bartenwerfer (1989); Luchini et al. (1991), and relates to separation of flow within the grooves. Flow turning is observed for oblique grooves due to the spanwise asymmetry, and the bulk spanwise velocity depends on the orientation angle of the grooves.

These phenomena are related to in this thesis for the channel flow geometry with two grooved walls, as opposed to the geometries of Mohammadi and Floryan (2013) which involve a flat wall and a grooved wall. The grooved walls are arranged in-phase to allow for a simple domain transformation method, as outlined in § 2.3. This can be contrasted to the out-of-phase arrangement of longitudinal grooves in Moradi and Floryan (2014), who report a drag reduction for low wavenumbers ($\lessapprox 1$) due to the disproportional lowering of shear stress in locations of the largest channel height (compared to locations of the smallest channel height). The in-phase arrangement of grooves produces a constant channel height at every (x, z), and, as we shall see later in this chapter, does not produce any drag reduction for the laminar solution.

The chapter is organized as follows. In § 3.1, analytical solutions are presented for longitudinal, transverse, and oblique grooves for the long wavelength asymptote; Stokes-flow approximation is used for the cases of transverse and oblique grooves to reduce the NSE to a linear equation. Numerical results are discussed for each class of groove geometries — longitudinal grooves in § 3.2, transverse grooves in § 3.3, and oblique grooves in § 3.4.

For longitudinal grooves, numerical solutions are compared against analytical solutions for low and high wavenumber asymptotes. As in the methodology chapter (chapter 2), the discussion of numerical results is mostly focused on the case of transverse grooves. Section 3.3.1 compares numerical results to low and high wavenumber asymptotes, § 3.3.2 identifies three flow regimes based on flow separation in the grooves: attached flow, weakly separated flow, and strongly separated flow, and § 3.3.3 discusses changes in the bulk velocity and friction factor with changing groove amplitude and slope. For oblique grooves, we look only at flow turning due to the breaking

of spanwise symmetry.

3.1 Stokes-flow approximation for long wavelength grooves

The simplest case of grooved channel flows is that of long wavelength sinusoidal grooves. Analytical solutions can be derived for such cases. The laminar solution is identified as the solution that satisfies the largest number of symmetries. This is reflected in the derivations where we assume homogeneity of the flow along the homogeneous direction of the grooves.

3.1.1 Analytical solution: Longitudinal grooves

For the case of longitudinal grooves, long wavelength or not, a laminar solution can be sought with zero wall-normal and spanwise velocities and streamwise-homogeneous streamwise velocity, reducing the (non-dimensionalized) streamwise momentum equation in eq. (2.1.2) to the linear equation

$$\Delta u = -2, \tag{3.1.1}$$

with boundary conditions

$$u\big(y = \pm 1 + 2\epsilon\cos(\beta z)\big) = 0, \tag{3.1.2}$$

where $\epsilon = A/2$ is half the amplitude of the groove. Such a solution does exist:

$$\begin{aligned} u(Y,Z) = {} & (1 - 2\epsilon^2\beta^2)(1 - Y^2) \\ & + \frac{2\epsilon\beta^2}{3}(Y^3 - Y)\cos(\beta Z) + 2\epsilon^2\beta^2(1 - Y^2)\cos(2\beta Z). \end{aligned} \tag{3.1.3}$$

The derivation is shown in appendix B. Similar laminar solutions for streamwise homogeneous flows are known in the literature (see Mohammadi and Floryan, 2013, for a similar derivation). Traditionally, such solutions are derived by expanding the flow

field variables about a base state and ignoring terms of order 2 and higher in the quantity about which the expansion is sought. The present derivation in appendix B does not use such an expansion, but instead, makes some weak assumptions regarding the smoothness of the solution. The solution is also accurate to $\mathcal{O}(\beta^2)$, unlike similar solutions that are often only accurate to $\mathcal{O}(\beta)$. This is possible because of the in-phase arrangement of the top and bottom walls of the channel.

3.1.2 Analytical Stokes-flow solution: Transverse grooves

Transverse grooves produce a non-zero streamwise derivative for the streamwise velocity, which forces the wall-normal velocity to be non-zero to impose incompressibility. Due to the spanwise homogeneity, solutions can still be sought with zero spanwise velocity. Unlike the longitudinal case, the non-linear terms are not zero. However, the non-linear terms may be considered to be negligible when the Reynolds number is small enough; the analytical solution is later compared to a numerical solution without this restriction to find the limit for which this assumption is valid. A discrete symmetry of the flow due to the grooves has to be used to obtain the solution, which suggests that other, less symmetric solutions may exist. However, this is not explored in the present work.

The Stokes-flow equations are solved. In the physical system of $x-y$ coordinates, these are

$$\begin{aligned} -\partial_x \tilde{p} + \Delta u &= -2, \\ -\partial_y \tilde{p} + \Delta v &= 0, \\ \partial_x u + \partial_y v &= 0, \end{aligned} \tag{3.1.4}$$

with boundary conditions

$$\begin{aligned} u\big(y = \pm 1 + 2\epsilon\cos(\alpha x)\big) &= 0, \\ v\big(y = \pm 1 + 2\epsilon\cos(\alpha x)\big) &= 0, \\ (\partial_x u + \partial_y v)\big(y = \pm 1 + 2\epsilon\cos(\alpha x)\big) &= 0. \end{aligned} \tag{3.1.5}$$

The pressure $\tilde{p}$ above includes the Reynolds number Re: $\tilde{p} = pRe$. The Reynolds

number, Re, is defined based on the driving mean pressure gradient; this way, a smooth-walled channel flow is driven by the same pressure gradient as a grooved channel flow, and the difference in the velocity is due to the geometries only.

The solution in the $X-Y$ coordinates, accurate to $\mathcal{O}(\alpha^2)$, is

$$\begin{aligned} u(X,Y) &= (1-4\epsilon^2\alpha^2)(1-Y^2) + \frac{4\epsilon\alpha^2}{3}(Y^3-Y)\cos(\alpha X), \\ v(X,Y) &= -2\epsilon\alpha(1-Y^2)\sin(\alpha X), \\ \tilde{p}(X,Y) &= 4\epsilon\alpha Y\sin(\alpha X) + 4\epsilon^2\alpha\sin(2\alpha X). \end{aligned} \tag{3.1.6}$$

The pressure drag, as a fraction of total drag, is expressed in terms of the Fourier coefficients of the fluctuating pressure at the wall as

$$\frac{D_{pres}}{D_{total}} = -\epsilon\alpha \mathrm{Im}(p_{-1,bw})Re. \tag{3.1.7}$$

See appendix B.4 for derivation. Here, $\mathrm{Im}(p_{-1,bw})$ is the imaginary part of the Fourier coefficient of mode -1 at the bottom wall. The above expression involves the pressure p and not $\tilde{p} = pRe$, and is not subject to the assumptions of Stokes flow or the long wavelength asymptote. For the analytical solution of eq. (B.2.24) with $p_{-1,bw} = -2i\epsilon\alpha/Re$, this reduces to

$$\frac{D_{pres}}{D_{total}} = 2\epsilon^2\alpha^2. \tag{3.1.8}$$

3.1.3 Analytical Stokes-flow solution: Oblique grooves

Under the Stokes-flow approximation, the flow due to oblique grooves can be decomposed into a flow along the homogeneous direction of the grooves and the flow normal to this direction (in the wall-parallel plane). The driving mean pressure gradient is split amongst the two directions. A detailed derivation employing this decomposition is shown in appendix B.3; this derivation uses the solutions from the longitudinal

and transverse groove cases given earlier. The solution for the oblique groove case is

$$
\begin{aligned}
u &= (1-2\epsilon^2(\alpha^2+\gamma^2))(1-Y^2) + \frac{2\epsilon(\alpha^2+\gamma^2)}{3}(Y^3-Y)\cos(\gamma\xi) + 2\epsilon^2\beta^2(1-Y^2)\cos(2\gamma\xi),\\
v &= -2\epsilon\alpha(1-Y^2)\sin(\gamma\xi),\\
w &= -2\epsilon^2\alpha\beta(1-Y^2) + \frac{2\epsilon\alpha\beta}{3}(Y^3-Y)\cos(\gamma\xi) - 2\epsilon^2\alpha\beta(1-Y^2)\cos(2\gamma\xi),\\
\tilde{p} &= 4\epsilon\alpha Y\sin(\gamma\xi) + 4\epsilon^2\alpha\sin(2\gamma\xi).
\end{aligned}
\tag{3.1.9}
$$

where $\gamma\xi = \alpha x + \beta z$, and $\gamma = \sqrt{\alpha^2+\beta^2}$.

For the present case of $\gamma \ll 1, Re \ll 1$, the pressure drag along x and z as a fraction of the driving force (due to the mean pressure gradient is

$$
\begin{aligned}
\frac{F_{p,x}}{F_{driving}} &= 2\epsilon^2\alpha^2,\\
\frac{F_{p,z}}{F_{driving}} &= 2\epsilon^2\alpha\beta.
\end{aligned}
\tag{3.1.10}
$$

During the derivation, velocity components u_ξ and u_η are defined, with ξ and η being the coordinates along the directions

$$
\begin{aligned}
\hat{\boldsymbol{e}}_\xi &= \frac{\alpha}{\gamma}\hat{\boldsymbol{e}}_x + \frac{\beta}{\gamma}\hat{\boldsymbol{e}}_z,\\
\hat{\boldsymbol{e}}_\eta &= \frac{-\beta}{\gamma}\hat{\boldsymbol{e}}_x + \frac{\alpha}{\gamma}\hat{\boldsymbol{e}}_z,
\end{aligned}
\tag{3.1.11}
$$

so that η is the homogeneous direction of the grooves, and ξ is the direction normal to η. The velocities along these directions are

$$
\begin{aligned}
u_\xi &= (\frac{\alpha}{\gamma} - 4\epsilon^2\alpha\gamma)(1-Y^2) + \frac{4\epsilon\alpha\gamma}{3}(Y^3-Y)\cos(\gamma\xi),\\
u_\eta &= -(\frac{\beta}{\gamma} - 2\epsilon^2\beta\gamma)(1-Y^2) + \frac{-2\epsilon\beta\gamma}{3}(Y^3-Y)\cos(\gamma\xi) - 2\epsilon^2\beta\gamma(1-Y^2)\cos(2\gamma\xi).
\end{aligned}
\tag{3.1.12}
$$

The non-zero u_η is what distinguishes the oblique groove case from transverse case.

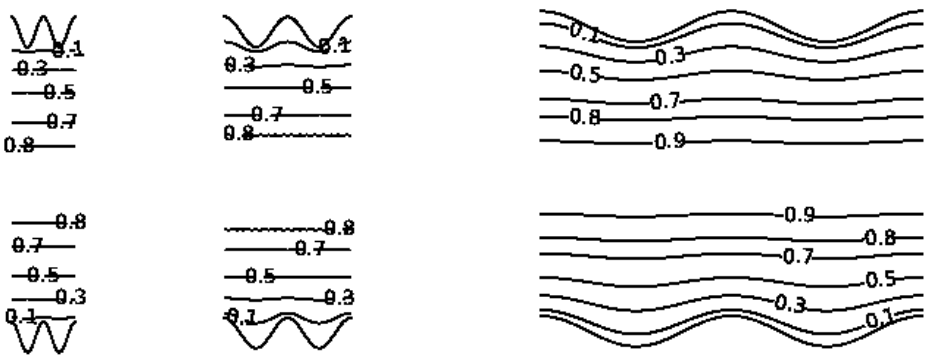

(a) $S_z = 3.0$ (b) $S_z = 1.5$ (c) $S_z = 0.5$

Figure 3.1: Streamwise velocity contours on the $x = 0$ section for channel flows with longitudinal grooves at an amplitude and Re of 0.1 and 100 respectively, with spanwise slopes ($S_z := A\beta$) of 3.0, 1.5, and 0.5. Wall-normal and spanwise velocities are zero everywhere for these flows.

3.2 Longitudinal grooves

For laminar flows in channels with longitudinal grooves, we expect laminar solutions with zero spanwise and wall-normal velocities, and with streamwise-homogeneous streamwise velocity. The advection term is zero everywhere in the flow, which is a consequence of the conditions

$$\partial_x u = 0, \qquad \partial_x p = 0, \qquad v = 0, \qquad w = 0.$$

The velocity fields are then independent of Re, and the Stokes approximation we earlier used for the low wavenumber asymptote of furrowed channels is valid for all Re for grooved channels. The exact governing equation is

$$\Delta u(y, z) = -2. \tag{3.2.1}$$

The -2 term represents the mean pressure gradient.

Numerical solutions have been computed without imposing zero spanwise and wall-normal velocities; only streamwise homogeneity and spanwise periodicity are imposed. When the Newton iterations are initialized with the smooth channel laminar solution ($u(Y) = 1 - Y^2$) under these restrictions, they converge to fields with zero wall-normal

and oblique velocities.

We now compare these numerical solutions to the analytical solutions given in § 3.1 to find out the upper limits for Re and groove amplitude and slope where the analytical solutions are no longer valid.

3.2.1 Low wavenumber asymptote

An asymptotic solution for low wavenumbers, $\beta \ll 1$, has been derived accurate to $O(\beta^2)$ as

$$u(Y,Z) = (1-\frac{S_z^2}{2})(1-Y^2) + \frac{S_z\beta}{3}(Y^3-Y)\cos(\beta Z) + \frac{S_z^2}{2}(1-Y^2)\cos(2\beta Z), \quad (3.2.2)$$

where S_z is the maximum slope of the longitudinal grooves, defined as $S_z = A\beta$. The bulk velocity for this asymptotic solution is

$$U_{bulk} = \frac{2}{3}(1-\frac{S_z^2}{2}). \quad (3.2.3)$$

The bulk velocity itself does not change significantly from flat channels to grooved channels. To compare the analytical approximation with computational results, a relative deficit in bulk velocity (relative to the flat channel case) as

$$\psi = 1 - \frac{U_{bulk,wavy}}{U_{bulk,flat}} = 1 - \frac{3}{2}U_{bulk,wavy}. \quad (3.2.4)$$

From eq. (3.2.3), $\psi_{analytical} = S_z^2/2$. We compare this with the relative deficit from computational results ($\psi_{computational}$) by defining a relative error in ψ as

$$\psi_{rel-err} = \frac{\psi_{analytical}}{\psi_{computational}} - 1 = \frac{S_z^2}{2\psi_{computational}} - 1. \quad (3.2.5)$$

Figure 3.2 shows ψ and $\psi_{rel-err}$ for several amplitudes plotted for β up to 100. The bulk velocity from the analytical and computational solutions match up to $\beta = 1$. Although we assumed that $\beta \ll 1$ when deriving the analytical solution, the

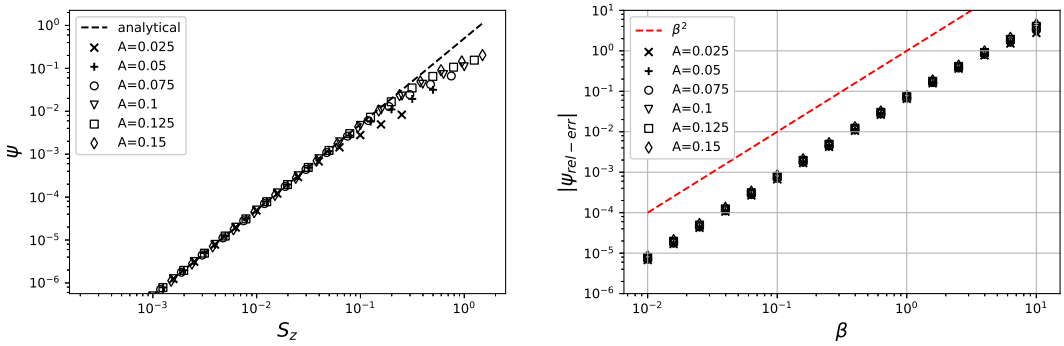

(a) ψ from computations

(b) Relative error in ψ for the asymptotic solution

Figure 3.2: Relative deficit in bulk velocity, ψ, and its relative error, $\psi_{rel-err}$, for the low wavenumber asymptote compared to computational results at β up to 100.

asymptotic limit seems to predict the bulk velocity even for $\beta \lessapprox 1$, with a relative error in ψ of 10% at $\beta = 1$ for amplitudes up to 15%. At higher wavenumbers, the asymptotic solution is invalid because higher order terms in β become much larger than β, β^2 terms.

3.2.2 High wavenumber asymptote

For large slopes $S \to \infty$, we speculate that the grooves are narrow enough for them to influence the flow as if their crests (points closest to the core of the flow) form a continuous surface. Figure 3.3 illustrates this for a finite but large slope; the dashed lines show the continuous surface formed by the crests of the grooves. With this assumption, we can calculate the bulk velocity of the grooved channel flow as the bulk velocity of a virtual flat channel flow with a reduced half-height, $h_{adjusted} = 1 - A$. Mohammadi and Floryan (2013) refer to this as a 'stream lift-up', and to the reduced half-height as an equivalent channel half-height.

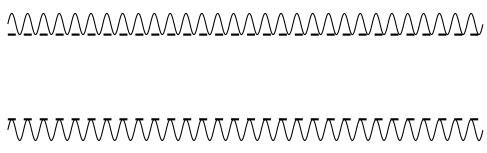

Figure 3.3: Illustration of a grooved channel with a large wavenumber for grooves. Dashed line indicates the walls for the flat channel that gives an approximation for the grooved channel flow

We now obtain the bulk velocity for this virtual flat channel flow, which we shall henceforth refer to as the *width-adjusted flat channel*. The dimensional volumetric flow rate (per unit spanwise length) for this flat channel flow is $4\hat{H}\hat{U}_{CL}/3$, where $\hat{H}$ and $\hat{U}_{CL}$ are the dimensional channel height and dimensional centerline velocity respectively. Since we use the half-height of the grooved channel (and not the virtual flat channel) for non-dimensionalization, the non-dimensional bulk velocity for the virtual flat channel with a reduced (non-dimensional) half-height of $1 - A$ becomes

$$U_{bulk} = \frac{2}{3}(1 - A)^3. \tag{3.2.6}$$

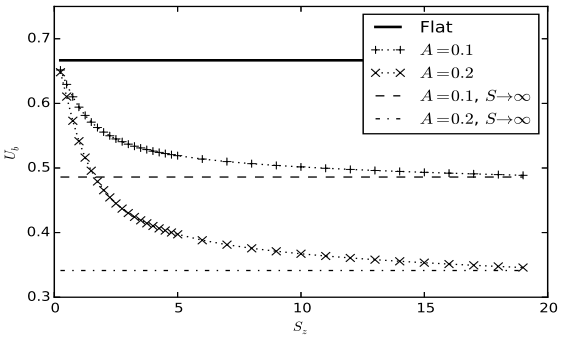

Figure 3.4: Variation of bulk velocity with slope at amplitudes of 10% and 20 %, along with bulk velocities for a flat channel and width-adjusted flat channels for both amplitudes.

Figure 3.4 shows contours of bulk velocity with increasing slopes of up to $S_z = 20$ for two different amplitudes. The bulk velocities asymptote to the limit of eq. (3.2.6).

3.3 Transverse grooves

The residual norm for the solutions presented here is below 10^{-12}, with an accuracy of 10^{-4} or better (see § 4.0.1 for definitions); for cases with large "slopes", defined as the product of the wavenumber and amplitude, higher resolution is needed to achieve this accuracy. Low slope ($\lessapprox 0.4$) cases have a nominal grid of 16x50 (streamwise Fourier modes from -7 to 8, and 50 wall-normal collocation nodes), while high slope (≈ 2.5) cases require grids of 60x100 nodes to achieve an accuracy of 10^{-4}.

Laminar flow in grooved channels has been comprehensively studied in Mohammadi and Floryan (2013). Their channel geometry has a flat top wall and a grooved bottom wall, so a direct comparison of the present results with theirs is not possible. However, our results show good qualitative agreement with those reported in the paper. This chapter presents some of the results computed with the present solver.

3.3.1 Asymptotes

Low wavenumber approximation

For transverse grooves with low wavenumbers, $\alpha \ll 1$, under the Stokes-flow approximation, the following analytical solution (accurate to α^2)can be obtained:

$$\begin{aligned} u(X,Y) &= (1-S^2)(1-Y^2) + \frac{2S\alpha}{3}(Y^3 - Y)\cos(\alpha X), \\ v(X,Y) &= -S(1-Y^2)\sin(\alpha X), \\ \tilde{p}(X,Y) &= 2SY\sin(\alpha X) + AS\sin(2\alpha X), \end{aligned} \tag{3.3.1}$$

where $\tilde{p} = pRe$, and $S = A\alpha$ is the maximum slope of the grooves.

The bulk velocity for this solution is

$$U_{bulk} = \frac{2}{3}(1-S^2). \tag{3.3.2}$$

The relative deficit in bulk velocity, $\psi = 1 - \frac{\psi_{grooved}}{\psi_{smooth}}$, for this profile is $\psi(S) = S^2$.

Figure 3.5 shows a comparison of the analytical solution to numerical solutions. The data points show ψ for A ranging from 2.5% to 15% for $0.01 \leq \alpha \leq 10$ at $Re \in \{0.1, 100\}$, while the dashed line represents the analytical profile, $\psi(S) = S^2$. The exact computational solutions deviate from the analytical approximation at higher slopes (> 0.2 in the figure).

For better comparison, we plot the relative error in ψ, defined as $\psi_{rel-error} = (\psi_{analytical} - \psi_{computational})/\psi_{computational}$. The relative error in ψ is plotted in fig. 3.6 against the wavenumber α (instead of the slope, which was used for the previous

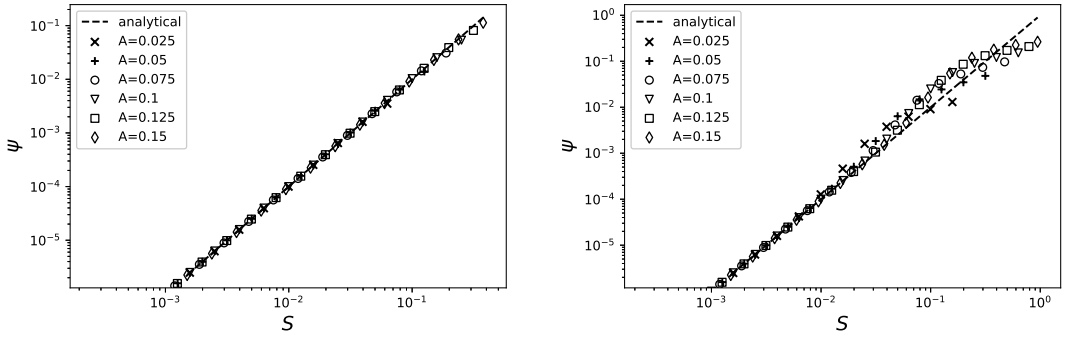

(a) $Re = 0.1$ (b) $Re = 100.0$

Figure 3.5: Relative deficit in bulk velocity compared to flat channel, $\psi = (U_{b,flat} - U_{b,grooved})/U_{b,flat}$. . Markers show ψ from computations, dashed line plots the analytical result of $\psi_{analytical} = S^2$

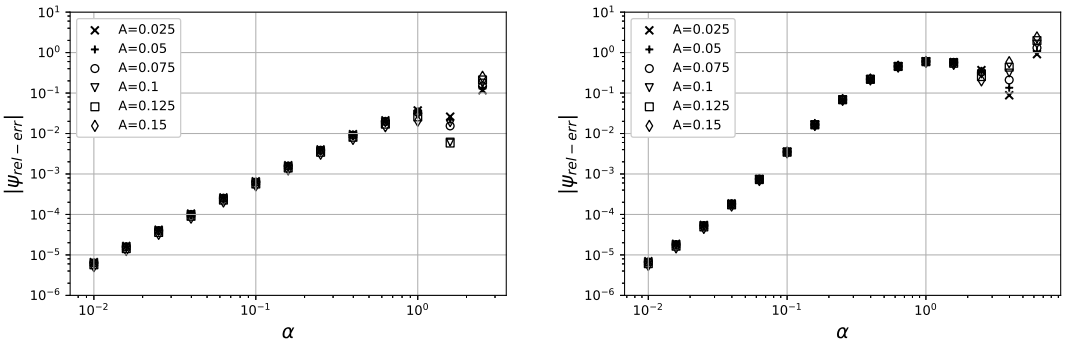

(a) $Re = 0.1$ (b) $Re = 100.0$

Figure 3.6: Relative error in $\psi_{analytical}$, $\psi_{rel-err} = (\psi_{analytical} - \psi_{computational})/\psi_{computational}$

plots). At $Re = 0.1$, the relative error remains within 10% for $\alpha \lessapprox 1$, and beyond $\alpha = 1$, the error increases sharply for larger amplitudes of the grooves. At $Re = 100$, the relative error goes above 10% for lower wavenumbers. This is to be expected, because the Stokes-flow approximation made in the derivation is no longer valid at this Re. The agreement at lower α is a consequence of weaker streamwise gradients in the flow, which make the advection term smaller compared to the high α cases. The asymptotic solution over-predicts the relative velocity deficit, which is not surprising since eq. (3.3.2) says that the bulk velocity decreases without bound as the slope increases; in reality, the bulk velocity asymptotes to a positive value ($U_{bulk} = 2(1 - A)^3/3$) for $S \to \infty$ as we see later in this section.

A second scalar that we shall use for comparison is the pressure drag, which is calculated by integrating the x-component of the pressure force acting on the walls. The pressure drag, as a fraction of the total drag (which must equal the driving force due to the mean pressure gradient) is given in eq. (B.2.26) as

$$\frac{D_{pres}}{D_{total}} = 2\epsilon^2\alpha^2 = \frac{S^2}{2}. \tag{3.3.3}$$

Consequently, drag due to the shear stress, as a fraction of the total drag, is

$$\frac{D_{skin}}{D_{total}} = 1 - \frac{S^2}{2}. \tag{3.3.4}$$

As with ψ, we plot relative error in the pressure drag (as a fraction of total drag) to compare the approximate analytical solutions to exact computational solutions. Figure 3.7 shows the pressure drag plotted against groove slope for several amplitudes at two different Reynolds numbers in log-log scale; the dashed curve shows the drag from the analytical solution, $D_{pres}/D_{total} = S^2/2$. Figure 3.8 shows the relative error for the analytical solution. As expected, the error increases with increasing wavenumber and is greater for $Re = 100$ than it is for $Re = 0.1$. The relative error seems to go as α^2, but remaining below the curve for $Re = 0.1$. At $Re = 100$, the relative error

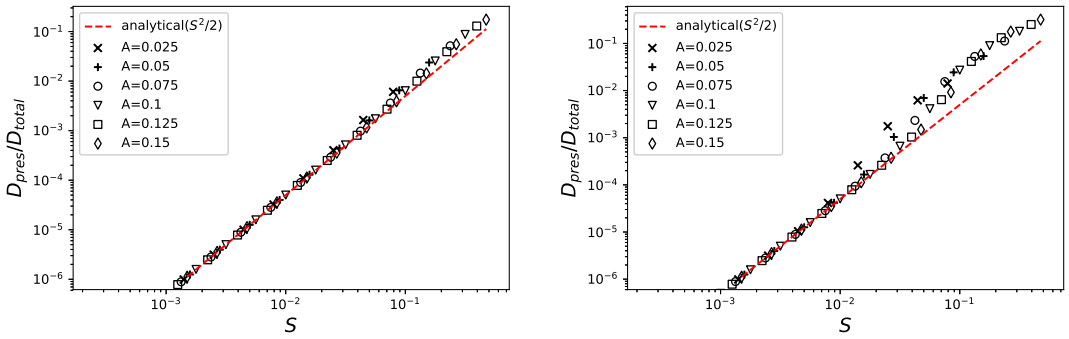

(a) $Re = 0.1$ (b) $Re = 100.0$

Figure 3.7: Pressure drag as a fraction of the total drag. Markers are used to distinguish groove amplitude. The dashed curve shows the pressure drag from the analytical solution.

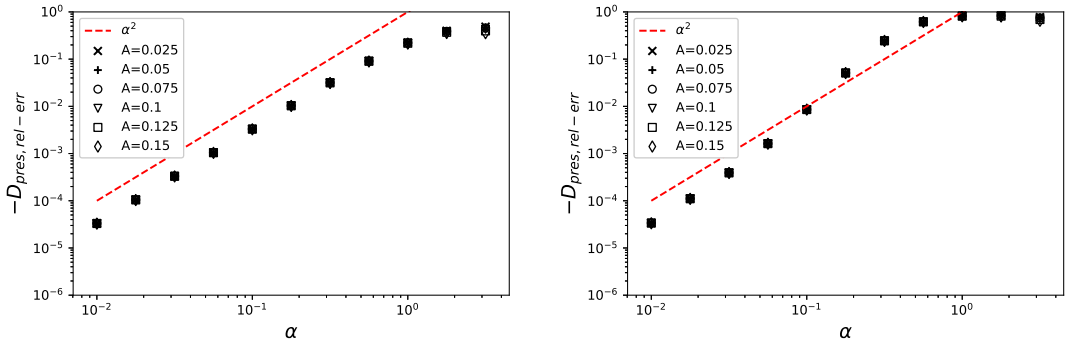

(a) $Re = 0.1$ (b) $Re = 100.0$

Figure 3.8: Relative error in $D_{pressure}/D_{total}$ for the same data show in fig. 3.7. The dashed curve, α^2, is shown to highlight the trend in the error.

also seems to start off similarly, but then goes beyond the α^2 curve.

High wavenumber asymptote

As we have done for channels with longitudinal grooves, we suppose that as $S_z \to \infty$, the flow in the channel outside the grooves becomes identical to the flow in a flat channel with an adjusted half-height $1 - A$. The bulk velocity for the width-adjusted flat channel is, as before,

$$U_{bulk} = \frac{2}{3}(1 - A)^3. \tag{3.3.5}$$

Figure 3.9 shows the bulk velocity for slopes up to 3.0 at $Re = 100$ and two different amplitudes. The bulk velocity for a flat channel and the width-adjusted channels for

the two amplitudes (given by eq. (3.2.6)) are plotted for reference. The maximum slope is limited to 3.0 because resolving the fine structures of the separated region in the grooves becomes expensive as the slope is increased further. Mohammadi and Floryan (2013) encounter the same problem, but they compute solutions up to a slope of 5.0. The plot is indicative of a high-slope asymptote close to eq. (3.2.6), but it does not conclusively show if the limit is exactly given by this equation.

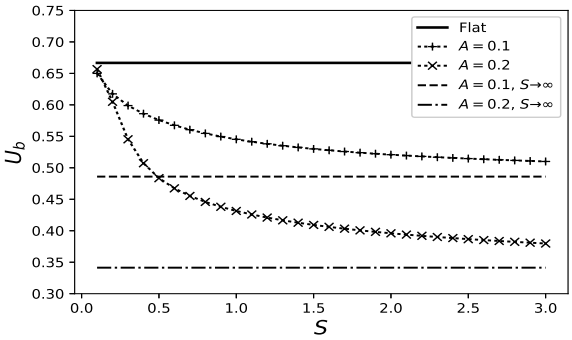

Figure 3.9: Variation of bulk velocity with slope at amplitudes of 10% and 20% and Re of 100. The expected upper and lower limits (width-adjusted flat channel) for the bulk velocity are also shown.

3.3.2 Flow regimes based on separation

Laminar solutions for three different cases are now presented to illustrate three regimes of laminar flows that can be identified in channels with transverse grooves.

Figure 3.10 shows velocity contours for three grooved channels with transverse grooves; the three geometries represent three flow regimes. The three geometries have the same amplitude and Reynolds number, $(A, Re) = (0.2, 100)$, and have slopes $(S := A\alpha)$ of 2.4, 0.8, and 0.3. At low slopes ($S = A\alpha \lessapprox 0.5$), we see meandering flows, where the core-flow is not parallel. Geometries with moderate slopes ($0.5 \lessapprox S \lessapprox 1$) have a separation bubble whose size increases with increasing slope. For slopes beyond $S = 1$, separation bubbles almost completely fill the furrows so that further increase in slope does not significantly affect the flow. Velocity contours for the same geometries are plotted in fig. 3.11. The lower slope case has higher streamwise velocity in the core region, but it also has stronger wall-normal velocity contours that extend farther

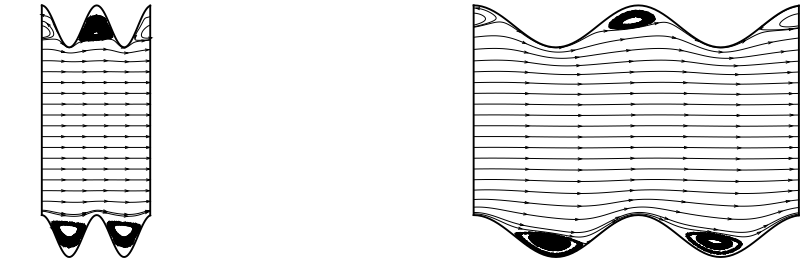

(a) $S = 2.4$ (b) $S = 0.8$

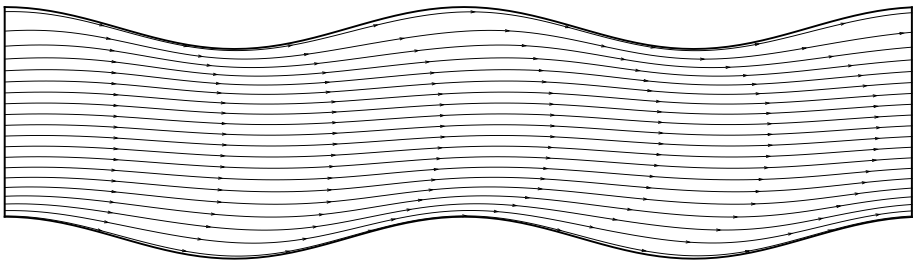

(c) $S = 0.3$

Figure 3.10: Streamlines illustrating three different flow regimes for channels with transverse grooves, with slopes, $S = A\alpha$, of 2.4, 0.8, and 0.3. The $S = 2.4$ (strongly separated) and $S = 0.8$ (weakly separated) cases have near-parallel core flow along with separation bubbles. The meandering flow case of $S = 0.3$ shows no separation, and the core flow is not parallel. All three cases are at $(A, Re) = (0.2, 100)$.

into the core from the walls. The higher slope cases have weaker penetration of wall-normal velocity contours into the core, however, they lead to greater reduction in the streamwise velocity.

3.3.3 Re-dependence of U_{bulk}

Figure 3.12 shows variation in bulk velocity with Re for several slopes at two amplitudes. Reynolds number is plotted in log scale to show the trend over three orders of magnitude. The upper and lower limits for bulk velocity for each amplitude are also shown, the upper limit being the bulk velocity for a flat channel, and the lower limit the bulk velocity for a width-adjusted flat channel representing $S \to \infty$. The convex (upward) appearance of the curves is only an artefact of the log scale used for Re; a linear Re-scale produces concave (upward) curves. Lower slope cases, i.e. meandering and weakly separated flows, show significant variation with Re for bulk

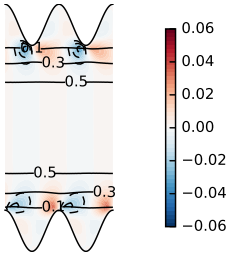

(a) $S = 2.4$

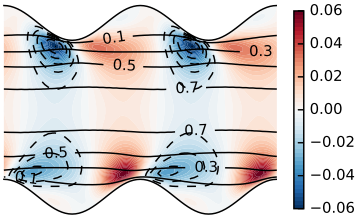

(b) $S = 0.8$

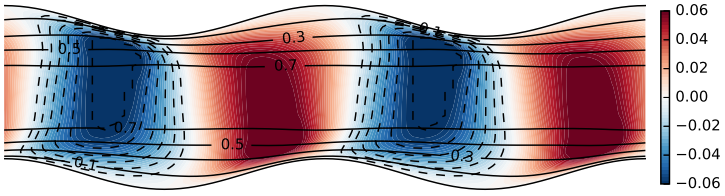

(c) $S = 0.3$

Figure 3.11: Velocity contours illustrating three different flow regimes: Strongly separated flow at slope $(S) = 2.4$, weakly separated flow at $S = 0.8$, and meandering flow at $S = 0.3$. All three cases are for an amplitude (A) of 0.2 and Reynolds number (Re) of 100. Filled contours (red and blue) show wall-normal velocity, with dashed line contours indicating negative velocities; the solid line contours are for streamwise velocity, and are plotted for four levels: $0.1, 0.3, 0.5, 0.7$.

velocity.

Bulk velocity plotted in fig. 3.12 is non-dimensionalized by the centerline velocity in a flat channel $(\hat{U}_{ref})$ arising from the same mean pressure gradient. While this helps in comparing flows for different corrugation geometries, the influence of Reynolds number on drag for a particular geometry is not easily expressed by plots of U_{bulk}. A better way to interpret the Re-dependence of bulk velocity is in terms of the friction factor (λ).

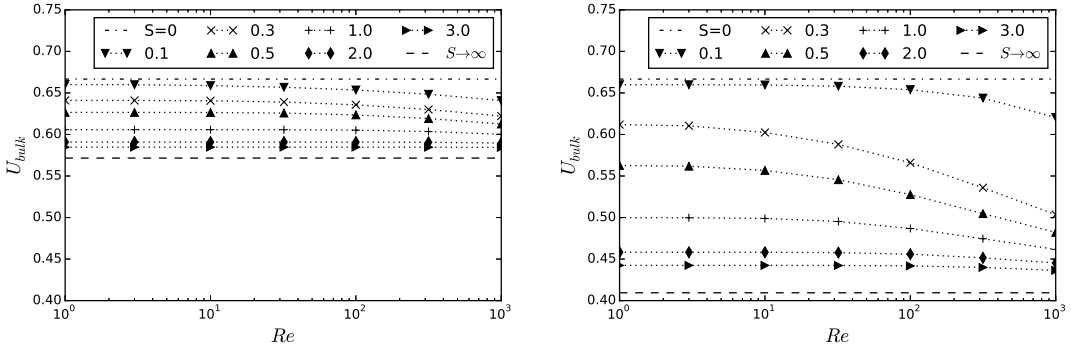

(a) $A = 0.05$ (b) $A = 0.15$

Figure 3.12: Re-dependence of bulk velocity for amplitudes of 5% and 15% at 6 different slopes, along with upper and lower limits at each amplitude.

Friction factor

For channel flows, (the Darcy-Weisbach) friction factor is defined as

$$\lambda = \frac{\hat{P}_{\hat{x}}(4\hat{h})}{\frac{\hat{\rho}\hat{U}_{bulk}^2}{2}}. \tag{3.3.6}$$

The $4\hat{h}$ factor corresponds to the hydraulic diameter ($D_{hydraulic}$) of the channel. The above equation can be rewritten in terms of Re and non-dimensional bulk velocity as

$$\lambda = \frac{16}{ReU_{bulk}^2} = \frac{16}{Re_{bulk}U_{bulk}}. \tag{3.3.7}$$

For flat channels, $U_{bulk} = 2/3$, which produces $\lambda = \frac{24}{Re_{bulk}}$.

For the low wavenumber asymptote, the friction factor is (from eqs. (3.3.2) and (3.3.6))

$$\lambda = \frac{24(1+S^2)}{Re_{bulk}}. \tag{3.3.8}$$

And for the high wavenumber asymptote, it is (from eq. (3.2.6))

$$\lambda = \frac{24}{Re_{bulk}(1-A)^3}. \tag{3.3.9}$$

Figure 3.13 shows the variation of friction factor with bulk Reynolds number.

Figure 3.13 shows curves for the friction factor plotted against Re_{bulk} for several

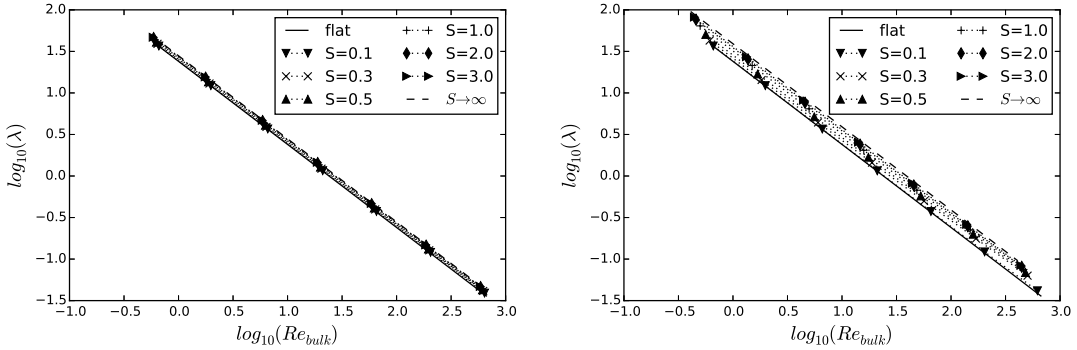

(a) $A = 0.05$ (b) $A = 0.15$

Figure 3.13: Log-log plots of friction factor against bulk Reynolds number for amplitudes of 5% and 15% at 6 different slopes, along with upper and lower limits for $S \to \infty$ and $S = 0$ at each amplitude.

slopes, shown in log-log scale to highlight the inverse relation between λ and Re_{bulk}. The upper and lower bounds due to the flat channel for $S = 0$ and the width-adjusted flat channel for $S \to \infty$ are included. These bounds have a constant slope of -1, with y-axis intercepts of $log_{10}(24)$ and $log_{10}(24/(1-A)^3)$ for $S = 0$ and $S \to \infty$ respectively.

3.4 Oblique grooves

The general case of grooved channels involves grooves aligned at an angle $0 < \theta < \pi/2$ to the mean pressure gradient. The walls for these cases are given by

$$y_{walls} = \pm 1 + A\cos(\alpha x + \beta z), \tag{3.4.1}$$

where (α, β) is the streamwise-spanwise wavenumber vector of the sinusoidal grooves. We also define a second set of coordinates

$$\xi = \frac{\alpha}{\gamma}x + \frac{\beta}{\gamma}z; \qquad \zeta = -\frac{\alpha}{\gamma}x + \frac{\beta}{\gamma}z, \tag{3.4.2}$$

where $\gamma^2 = \alpha^2 + \beta^2$. The walls of the channel can then be written as

$$y_{walls} = \pm 1 + A\cos(\gamma\xi). \tag{3.4.3}$$

We define streamwise and spanwise slopes, $S_x = A\alpha$ and $S_z = A\beta$, and an 'alignment angle' θ as the angle of the wavenumber vector (α, β) relative to the streamwise direction,

$$\theta = \tan^{-1}\left(\frac{\beta}{\alpha}\right). \tag{3.4.4}$$

For channels with transverse grooves, the alignment angle is zero, while for channels with longitudinal grooves, the alignment angle is $\pi/2$. For channels with any alignment angle, $0 \leq \theta \leq \pi/2$, we seek solutions that are periodic along $\boldsymbol{e}_\xi$ and homogeneous along $\boldsymbol{e}_\zeta$. For transverse grooves, $\boldsymbol{e}_\xi$ coincides with $\boldsymbol{e}_x$, and for longitudinal grooves, it coincides with $\boldsymbol{e}_z$. The velocities and pressure (fluctuating) are written as Fourier series of the form $\sum_{k\in\mathbb{Z}} f_k(Y)e^{ik\gamma\xi}$ (where Y is the wall-normal coordinate in the transformed domain).

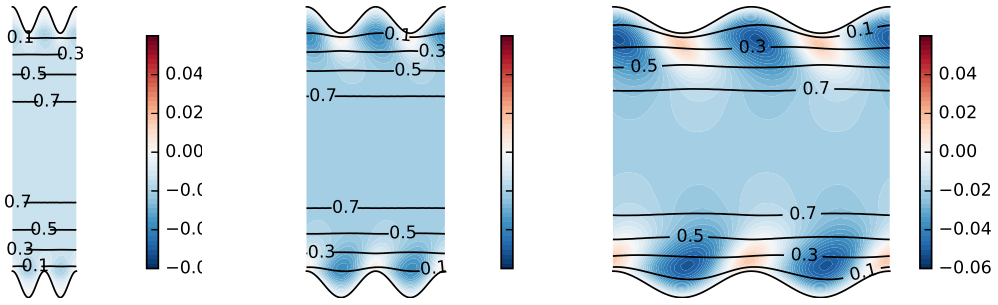

(a) $S_x = 2.6$ (b) $S_x = 1.2$ (c) $S_x = 0.6$

Figure 3.14: Wall-parallel velocity contours on the $z = 0$ section for oblique grooves with alignment angle $\theta = \pi/6$ at $Re = 100$ and $A = 0.1$ for three different streamwise slopes. Filled contours show spanwise velocity, and line contours show streamwise velocity. Wall-normal velocity is omitted.

Figures 3.14 and 3.15 show velocity contours (streamwise and spanwise) for two alignment angles, $\pi/3$ and $\pi/6$, and three different streamwise slopes $S_x \in \{0.6, 1.2, 2.6\}$ with $A = 0.1$ and $Re = 100$. The contours are plotted for the plane $z = 0$ from $x = 0$ to $x = 2\pi/\alpha$. Streamwise velocity contours for oblique grooves look similar to those for channels with grooves (as seen in fig. 3.11). Spanwise velocity is predominantly negative in the channel for positive β. This is because the non-zero alignment forward facing side of the grooves (the high pressure side) pushes the flow in the negative z direction. Interestingly, the low slope cases also produce a small positive spanwise

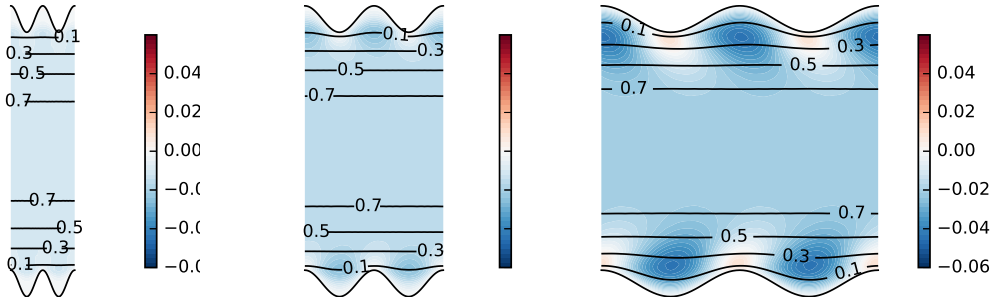

(a) $S_x = 2.6$ (b) $S_x = 1.2$ (c) $S_x = 0.6$

Figure 3.15: Wall-parallel velocity contours on the $z = 0$ section for oblique grooves with alignment angle $\theta = \pi/3$ at $Re = 100$. Filled contours show spanwise velocity, and line contours show streamwise velocity. Wall-normal velocity is omitted.

velocity region near the inner edge of the grooves. This is a consequence of the fact that the direction along the wall-parallel vector $\alpha\hat{\boldsymbol{e}}_x + \beta\hat{\boldsymbol{e}}_z$ is the direction of the steepest descent of the corrugation, which offers least resistance to the flow. Whether the flow actually moves along the positive z direction depends on the balance between the decrease in resistance at the backward facing side, which turns the flow towards $+z$, and the increase in resistance at the forward facing side, which turns the flow towards $-z$. Our results show that the flow turning due to the backward facing side is much weaker and are only important at small slopes (large wavelengths). The lower θ cases show stronger $-z$ currents than the higher θ cases, as can be expected.

3.5 Summary

Three cases of grooves in channels are investigated: transverse, longitudinal, and oblique. Longitudinal grooves are the simplest case, with the governing equations being reduced to a Poisson equation for velocity. They do not produce any flow separation or spanwise currents. Transverse grooves produce flow separation due to the adverse pressure gradient created in the grooves. Oblique grooves, in addition to flow separation, also produce a spanwise current.

The in-phase arrangement of the grooves allows for a simple derivation of analytical solutions for the long wavelength asymptote (low slopes); these derivations require

the Stokes-flow approximation for transverse and oblique grooves. These solutions are valid, at low Reynolds numbers, even when the wavenumbers are close to 1.

From the computations, we see that as the (streamwise) slope increases from a low value ≈ 0.1, a separation bubble fills the grooves, resulting in a 'lift-up' of the flow out of the grooves. A width-adjusted channel also seems to adequately describe the flow in channels with sufficiently low wavelengths; however, this could not be conclusively shown because the resolution requirements make computations prohibitively expensive for slopes beyond ≈ 5.

Finally, the steady-state solver described in this thesis can compute laminar solutions at high Reynolds numbers, which could be interesting in the context of transition to turbulence.

In conclusion, the investigations of this chapter serve two purposes. Firstly, continuation of laminar solutions serve as a testing ground for a similar continuation of non-laminar equilibria to grooved plane shear flows. The main takeaway is that the domain transformation method, in conjunction with the full-rank inversion for the Newton iterations, produces convergence. The laminar case is also used to test for the suitability of Jacobian-free methods using the domain transformation method, as outlined in § 2.9.1.

Secondly, the solutions found here complement the results of Mohammadi and Floryan (2013), who used a combination of a flat wall and a grooved wall in their channel geometry, as opposed to the two grooved wall configuration used in this work. While the physics of the flow does not change significantly, quantities such as bulk velocity and pressure drag are sensitive to the configuration; an extreme example is the apparent drag reduction observed in Moradi and Floryan (2014) for channels with out-of-phase longitudinal grooves. The analytical solution is particularly important in this context, since it serves as a good approximation in the meandering flow regime, and is of much simpler form than that of Mohammadi and Floryan (2013). The present configuration of two in-phase grooved walls also allows an unambiguous choice of

channel half-height, resolving one of the key issues associated with the configurations of Mohammadi and Floryan (2013).

3.5.1 Grooves as low-order representation of roughness

Squire's theorem discusses the prominence of two-dimensional disturbances with regards to linear stability. In the context of wall-roughness, Hamed et al. (2016) have shown that 2-d roughness leads to earlier transition to turbulence than their 3-d counterparts. In these cases, the disturbances and roughness are spanwise-homogeneous. Another interesting case is that of drag reduction in boundary layer flows due to longitudinal riblets, which are streamwise-homogeneous. Mohammadi and Floryan (2013) have investigated laminar flows in (2-d) grooved channels with different groove geometries, and concluded that the leading projection on a Fourier basis — sinusoidal grooves — adequately represents the flow in sharp-edged grooves such as triangular, trapezoidal, and rectangular grooves. In light of these observations, it is reasonable to use geometries with sinusoidal grooves, either longitudinal or transverse, as a starting point for understanding the dynamics of rough-walled flows.

Chapter 4

Equilibria for grooved Couette flows

The most exciting phrase to hear in science, the one that heralds new discoveries, is not, "Eureka! I've found it," but, "That's funny!"

Isaac Asimov

The primary aim of this thesis is to investigate if exact invariant solutions of smooth-walled plane Couette flows can be extended to rough-walled plane Couette flows. If this is possible, the secondary goal is to elucidate the role of grooved-walls in turbulence, with particular emphasis on explaining the drag reduction observed in riblet-mounted boundary layers.

In the previous chapter, the grooves in the channel geometry were allowed to be be longitudinal, transverse, or oblique. This chapter deals with equilibria of plane Couette flow, since a large set of these solutions are available for the flat walled case. When continuing these solutions to grooved geometries, the alignment of the grooves must be restricted to be longitudinal. For transverse or oblique geometries, equilibria cannot exist because of the relative motion of the walls. The inadmissibility of equilibria for transverse and oblique grooves can be argued for by noting that no reference frame exists where the boundary conditions are independent of time; the time dependence of boundary conditions inevitably leads to time-dependence of the solution. In order to allow continuation of equilibria, the geometries investigated are

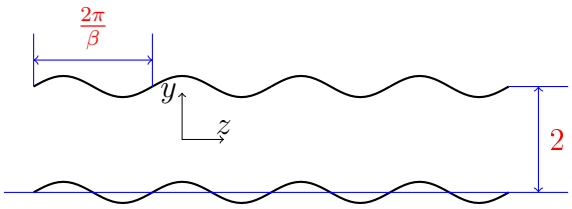

Figure 4.1: Cross-stream slice of grooved PCoF geometry; "One groove per box": $A_1 = 0.1$

restricted to the case of longitudinal grooves, whose boundary conditions are time invariant.

Equilibria of plane Couette flow (PCoF) available in the literature for the smooth-walled case are now extended to grooved PCoF (with longitudinal grooves) to answer these questions. The top and bottom walls of the grooved PCoF are given by

$$y_{walls} = \pm 1 + \sum_m A_m \cos(m\beta z). \tag{4.0.1}$$

In the remainder of the chapter, geometries are often identified as "k-grooves-per-box" to refer to a case with walls given by

$$y_{walls} = \pm 1 + \frac{A_k}{5}\cos(\beta z) + A_k \cos(k\beta z). \tag{4.0.2}$$

The small but significant amplitude in the first Fourier mode is included to ensure that the smallest spanwise length of the periodic box remains the same for geometries with different dominant groove wavelengths. The "one-groove-per-box" case is just $y_{walls} = \pm 1 + A_1 \cos(\beta z)$, and is illustrated in fig. 4.1.

4.0.1 Residual norm and spatial accuracy

The solver used in this work defines instantaneous time-derivatives of the velocity fields as the residual ($\mathbf{r}$), and the residual norm is defined as the integral

$$||\mathbf{r}|| = \left[\int_{x=0}^{2\pi/\alpha} \int_{z=0}^{2\pi/\beta} \int_{y=y_{bottom}}^{y_{top}} (\dot{u}^2 + \dot{v}^2 + \dot{w}^2) \mathrm{d}y\mathrm{d}z\mathrm{d}x \right]^{1/2}. \tag{4.0.3}$$

Solutions for grooved PCoF are computed with varying resolutions, depending on the imposition of discrete symmetries of the flow (see § 2.7.3) so that each flow case can run on a computational node with 64 Gigabytes of RAM. Grid-convergence of a computation is quantified by its spatial accuracy (following Gibson et al. (2009)), defined as the residual norm of the solution when extrapolated on a grid with double the number of modes along each direction.

Grooved PCoF solutions are computed to varying residual norms. Gibson et al. (2009) report a residual norm of $\sim 10^{-14}$ for their EQ1 and EQ2 solutions, with a spatial accuracy of $\sim 10^{-6}$ for EQ1 and $\sim 10^{-4}$ for EQ2. When these equilibria for smooth PCoF are evaluated by the present solver, the residual norms are $\sim 10^{-7}$ for EQ1 and $\sim 10^{-6}$ for EQ2, with accuracies of $\sim 10^{-6}$ for EQ1 and $\sim 10^{-4}$ for EQ2. This discrepancy arises from the difference in the definitions of the residuals. The present solver uses instantaneous time-derivatives as the residual, while the solver of Gibson (2014) involves differences in velocity fields over a finite time-interval. When EQ1 and EQ2 are refined with the present solver for smooth PCoF until the residual norm went below 10^{-10}, the refined solutions differ from the original solutions by $\lesssim 10^{-12}$, and the spatial accuracy of the solutions does not change significantly.

In the present work, any flow field with a residual norm below 10^{-7} for grooved PCoF is considered to have converged. Although this tolerance is not strictly of the order of precision of the arithmetic used, the residual norm represents the (non-dimensional) instantaneous time-derivative; for residual norms of 10^{-7}, the flow field is presumed to be sufficiently close to an exact equilibrium and is designated in this thesis as one.

4.1 Existence of solutions for grooved PCoF

Figure 4.2 shows velocity fields on the cross-stream plane $x = 0$ for four flow cases: EQ1 and EQ2 of Nagata (1990) for smooth PCoF, taken from the online database at www.channelflow.org, and their continued counterparts for the one-groove-per-box case at an amplitude $A_1 = 0.1$. The wavelength of the grooves is set to coincide with

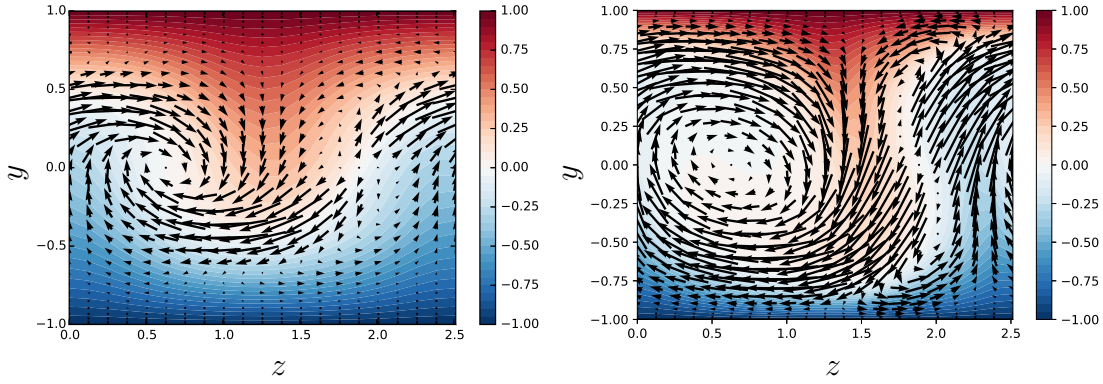

(a) EQ1; smooth PCoF

(b) EQ2; smooth PCoF

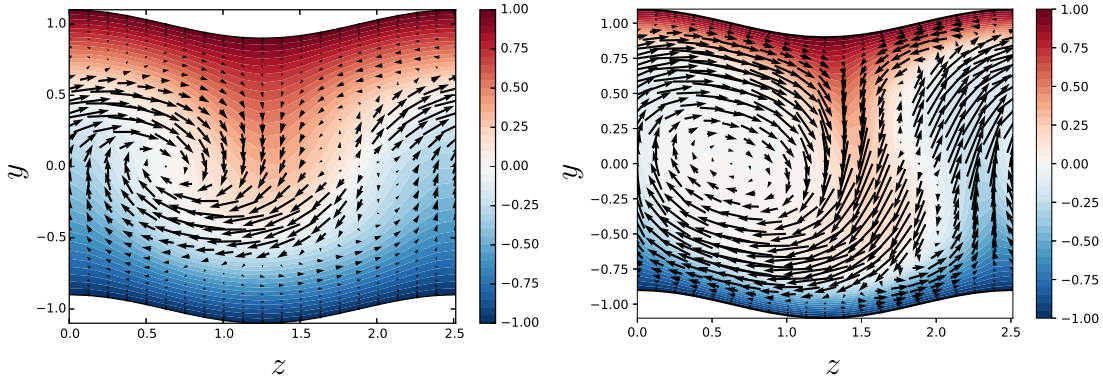

(c) EQ1; grooved PCoF with $A_1 = 10\%$

(d) EQ2; grooved PCoF with $A_1 = 10\%$

Figure 4.2: Velocity on a cross-stream plane ($x = 0$) for smooth PCoF (a-b) and grooved PCoF (c-d). Contours show streamwise velocity and quiver arrows show cross-stream velocities.

the spanwise periodic length of the original solutions, $\beta = 2.5$. The streamwise length of the periodic box is also set according to the solutions to be continued, $\alpha = 1.14$. The solutions are for $Re = 400$, and are computed with $(L, M, N) = (16, 16, 35)$ (a grid of 32x35x32 points). The discrete symmetries s_1 and s_2 are exploited to allow this resolution (see § 2.2.3); the phase of the smooth-walled solutions had to be restricted such that the $z = 0$ plane of the solutions coincide with the $z = 0$ plane of the grooves. EQ1 for grooved PCoF is computed to a residual norm and spatial accuracy of $\sim 10^{-12}$ and $\sim 10^{-5}$ respectively, while for EQ2 they are $\sim 10^{-8}$ and $\sim 10^{-4}$.

Lower branch solutions such as EQ1 are streak-dominated. They have a larger streamwise velocity fluctuation and a smaller wall-normal velocity fluctuation than their vortex-dominated counterparts — the upper branch solutions such as EQ2 (Kawahara et al. (2012)). The lower branch solutions regulate transition to tur-

bulence in the presence of a stable laminar flow, while the upper branch solutions produce coherent structures and velocity fluctuations comparable to the near-wall cycle. Figure 4.2 shows that the nature of these solutions does not change when they are continued to a grooved geometry with a significant groove amplitude. In fact, the structures seem very similar except for some large-scale distortion due to the geometry of the wall; the flow fields for grooved PCoF solutions have $\approx 99\%$ energy in the smooth PCoF solution-structure when projected on the latter in the transformed domain (X, Y, Z) (see eq. (2.7.9)).

Figure 4.3 illustrates the full vortex-streak structure of EQ1 and EQ2 in the periodic domain. The meandering vortices based on the low-speed streak are characteristic of all exact invariant solutions known for wall-bounded flows (Kawahara et al. (2012)), and this does not change for grooved PCoF. This is not surprising; the interaction of streamwise streaks and vortices is known to be a hallmark of wall-turbulence and has been shown to exist irrespective of the kind of wall-bounded flow Waleffe (1997); Blackburn et al. (2013). So, the action of the grooves on the structure of EQ1 and EQ2 shown in figs. 4.2a and 4.2b is to distort the cross-stream flow. However, this raises the question: how is the flow field distorted when the wavelength of the grooves does not coincide with the size of the periodic domain of the original solution? This is addressed in § 4.3.

The mean velocity profiles for EQ1 and EQ2 are shown in fig. 4.4; the mean velocity for grooved cases is shown as a difference from the smooth case. The mean velocity for grooved PCoF is defined as an average along the streamwise and spanwise directions and is defined only for wall-normal locations outside the grooves; this is why the difference, $U - U_{sm}$, does not extend to the walls and does not go to zero for the grooved cases. EQ1 and EQ2 show a velocity deficit compared to the laminar case — the magnitude of the mean velocity is smaller than it is for laminar — with EQ2 showing a greater deficit. Increasing groove amplitude further increases this deficit. This also produces stronger shear stresses at the wall for grooved PCoF.

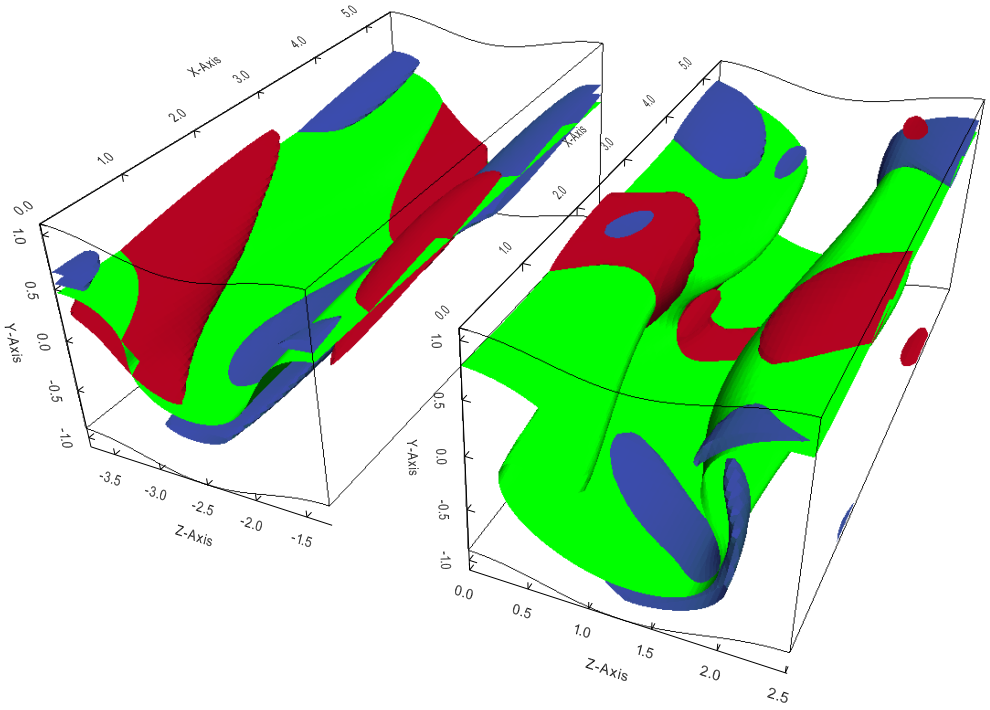

(a) EQ1 (left) and EQ2 (right) at $A = 0.1$

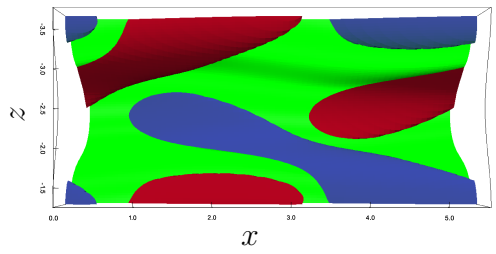

(b) EQ1 (top view)

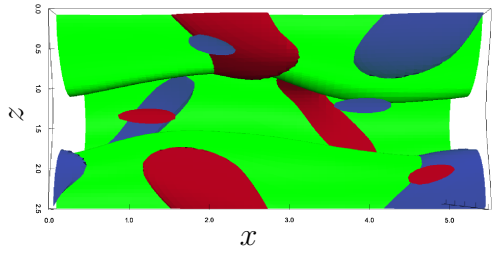

(c) EQ2 (top view)

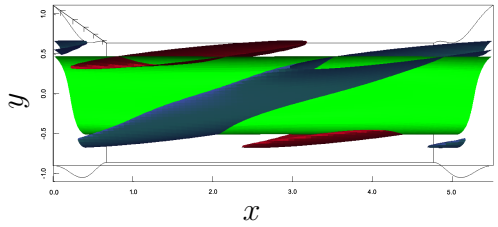

(d) EQ1 (side view)

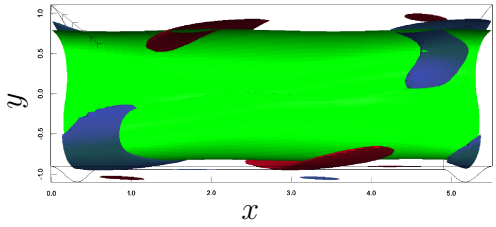

(e) EQ2 (side view)

Figure 4.3: Lower (EQ1) and upper (EQ2) branch equilibria for grooved PCoF at $A = 0.1$ showing isosurfaces for zero streamwise velocity (green) and streamwise vortices for $\omega_x = 0.7\max(\omega_x)$ (red) and $-0.7\max(\omega_x)$ (blue).

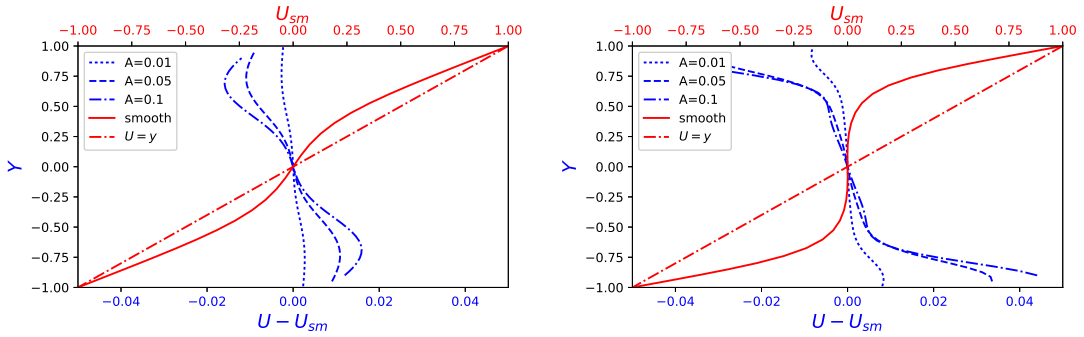

(a) EQ1 (b) EQ2

Figure 4.4: Mean velocity profiles for EQ1 and EQ2 in grooved PCoF, shown as differences from the smooth case. The laminar mean velocity, $U = y$, is included for comparison.

	Turb. Mean	Laminar	EQ1 (lower)	EQ2 (upper)
E	0.087	0.1667	0.1363	0.0780
D	2.926	1	1.429	3.044

Table 4.1: Kinetic energy density (E) and bulk dissipation rate (D) for smooth PCoF.

4.1.1 Kinetic energy and dissipation rate

The kinetic energy density E, bulk dissipation rate D, and power input I of a velocity field of plane Couette flow are given as

$$\begin{aligned} E(t) &= \frac{1}{V}\int_\Omega \frac{1}{2}|\mathbf{u}|^2 d\mathbf{x}, \\ D(t) &= \frac{1}{V}\int_\Omega |\nabla\times\mathbf{u}|^2 d\mathbf{x}, \\ I(t) &= \frac{1}{2\mathcal{A}}\int_{\mathcal{A}}\left(\left.\frac{\partial u}{\partial y}\right|_{y=1} + \left.\frac{\partial u}{\partial y}\right|_{y=-1}\right) dx d\zeta, \end{aligned} \tag{4.1.1}$$

where $V = 2L_xL_z$ is the volume of the periodic domain, $d\zeta$ is an infinitesimal arc-length along the wall in the spanwise direction, and $\mathcal{A}$ is the wetted surface area of each wall. These quantities are normalized so that $E = D = 1$ for laminar flow in smooth PCoF, and $\dot{E} = I - D$. For equilibria, E, I, and D are not time-dependent, and $I = D$.

The kinetic energy density and the bulk dissipation rate for smooth PCoF are showin in table 4.1. The second row, E_{vw}, shows the energy in the cross-strem velocity

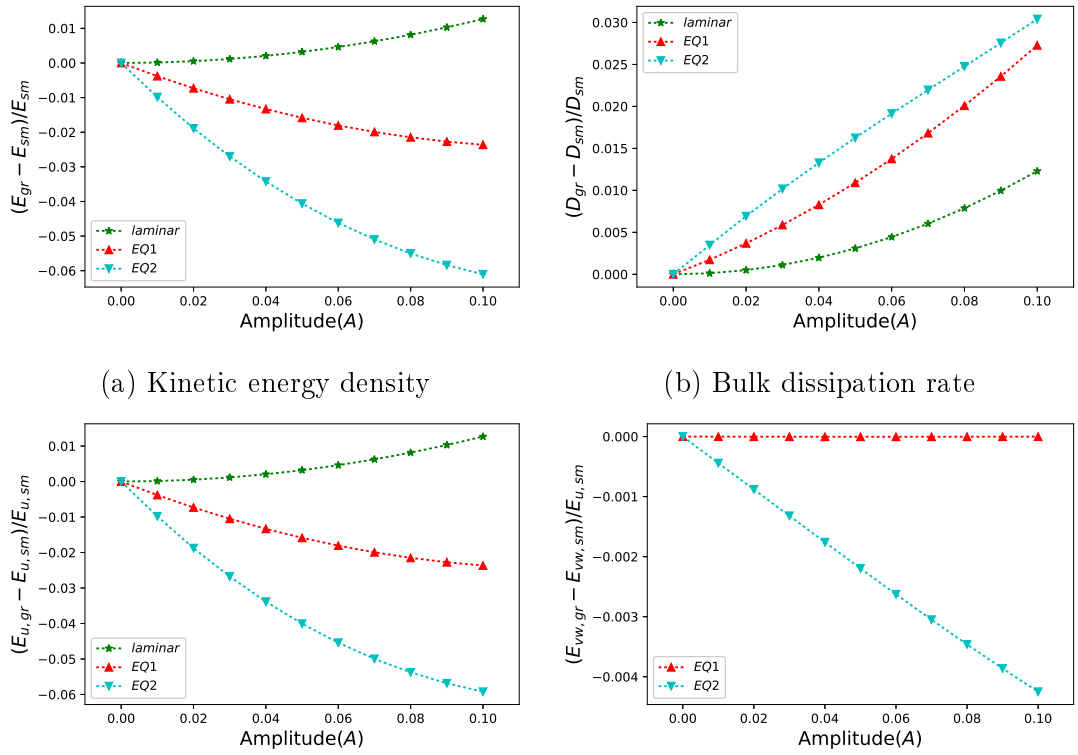

(a) Kinetic energy density

(b) Bulk dissipation rate

(c) Streamwise energy density

(d) Cross-stream energy density

Figure 4.5: Change in kinetic energy density and bulk dissipation rate in grooved PCoF for laminar flow and upper and lower branch equilibria.

components; this is zero for the turbulent mean and the laminar flow and negligible for EQ1, but significant for EQ2. The laminar case has the largest energy density and the smallest dissipation rate; the upper branch solution, EQ2, has the smallest energy density and the largest dissipation rate; and the lower branch solution, EQ1, lies between the two.

The effect of groove-amplitude on these the energy density and dissipation rate is shown in fig. 4.5. For laminar flow, increasing groove amplitude results in an increase in both the energy density and the dissipation rate. However, for EQ1 and EQ2, only the dissipation rate increases, while the energy density decreases. It is not surprising that EQ2 is more strongly affected than EQ1 by the grooves, because the streamwise vortex is concentrated in the core region for EQ1, while it extends to the walls in EQ2. For laminar flows, the increase in power input (which equals dissipation rate) accompanies an increase in energy density. For EQ1 and EQ2, however, increasing groove-amplitude increases power input while reducing energy density (to maintain

the same wall velocity). This can be considered to be a drag increasing tendency; a drag coefficient has not been used because the bulk velocity itself is zero.

4.2 Spanwise anchoring of the vortex-streak structure

The flow field shown in fig. 4.2a is just one member of a continuous family of solutions that arise due to spanwise homogeneity of smooth PCoF. Let this particular member be called χ^*. A flow field that is obtained by translating χ^* along z by some shift ζ is $\mathcal{T}_{0,\zeta}\chi^*$ (see § 2.7.3). The continuous family of flow fields obtained by translating χ^* along z is denoted as $\tilde{\mathcal{F}}(\chi^*) = \{\mathcal{T}_{0,\zeta}\chi^* : \zeta \in \mathbb{R}\}$, and the discrete family of flow fields obtained by translating χ^* along z through integral multiples of L_z/n as $\mathcal{F}_n(\chi^*) = \{\mathcal{T}_{0,qL_z/n}\chi^* : q \in \mathbb{Z}\}$. The argument χ^* for $\mathcal{F}$ is now dropped for convenience. Every $\mathcal{F}_n$ is a subset of $\tilde{\mathcal{F}}$. The members of $\mathcal{F}_1$ are identical to each other due to the periodicity of χ^*.

For smooth PCoF, because of its spanwise homogeneity, every member of $\tilde{\mathcal{F}}$ is an equilibrium of the NSE. Since the presence of grooves destroys spanwise homogeneity in grooved PCoF, we expect the continuous family of solutions in smooth PCoF to break down into discrete families in grooved PCoF. The remainder of this section explores two questions to elucidate on this symmetry breakdown: 1) How sensitive are solutions of grooved PCoF to spanwise translation? 2) Can every solution of smooth PCoF in the continuous family $\tilde{\mathcal{F}}(\chi^*)$ be continued to grooved PCoF (with a specific phase with respect to χ^*)?

Answering these questions requires that a reference phase of the solutions with respect to the grooves be identified. In the earlier discussion on discrete symmetries of PCoF in § 2.2.3, a shift-reflect symmetry, s_1, was identified; the reflection is about the $z = 0$ plane. When the solution χ^*, which satisfies s_1, is translated along z by ζ, the plane(s) about which s_1 holds is also translated by ζ. A plane(s) of reflectional symmetry can also be identified for the geometry of grooved PCoF. Since the walls

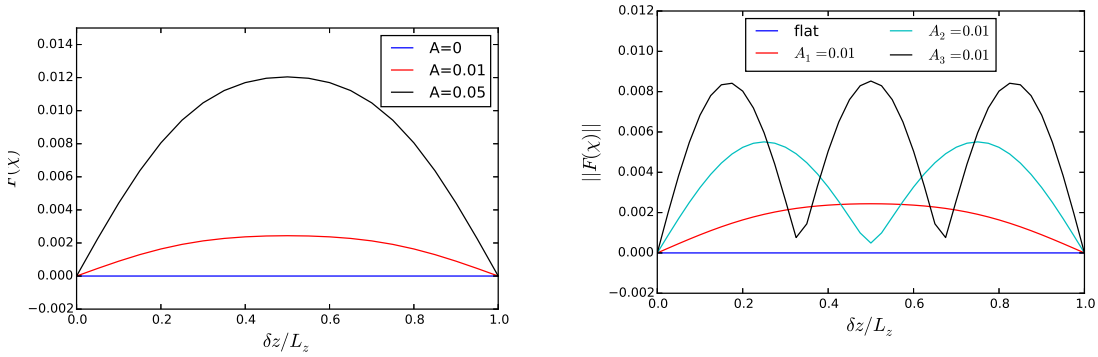

(a) One groove per box (b) One, two, and three grooves per box

Figure 4.6: Residual norm when continued EQ1 ($\chi^*_{A_k}$) is translated along a grooved PCoF. Smaller residual indicates proximity to an equilibrium for grooved PCoF.

are given as $y_{walls} = \pm 1 + A_1 \cos(\beta z) + A_2 \cos(2\beta z) + A_3 \cos(3\beta z)$, they are invariant under reflections about the $z = 0$ plane (or any $z = 2m\pi/\beta$ plane for integral m). The relative location of the planes of reflectional symmetry are used to specify the phase.

We use $\chi^*_{A_k}$ to denote zero-phase solutions for grooved PCoF of amplitude A_k obtained from continuation of χ^*, where $k = 1, 2, 3$ represent one, two, and three groove cases respectively. The fields in fig. 4.3 show $\chi^*_{A_1=0.1}$. The first question, the sensitivity of $\chi^*_{A_k}$ to spanwise translations, is represented graphically in fig. 4.6b for EQ1. The spanwise shift, δz, is with respect to the zero phase solution $\chi^*_{A_k}$, and this is normalized by the spanwise size of the periodic box, L_z. No Newton-iterations are performed to produce this plot. The zero-phase solutions, $\chi^*_{A_k}$ are simply translated along Z in the (X, Y, Z) domain, and the resulting residual norm is plotted. The spanwise-varying part of EQ1 is concentrated in the core of the PCoF, and yet, we see a significant change in the residual norm for $\chi^*_{A_k}$ under spanwise translation. This suggests that solutions of non-zero phase, if they exist, would look significantly different than $\chi^*_{A_k}$.

This brings us to the next question of continuing solutions of non-zero phase from smooth PCoF ($\tilde{\mathcal{F}}(\chi^*)$) to grooved PCoF? We explore this by running the iterative method with four different initial iterates, χ^*, $\mathcal{T}_{0,0.01\pi/\alpha}\chi^*$, $\mathcal{T}_{0,0.8\pi/\alpha}\chi^*$, and $\mathcal{T}_{0,\pi/\alpha}\chi^*$. However, the spatial resolution that can be afforded for these iterations is significantly

lower than what was used to produce the solutions discussed in the rest of this chapter. This relates to exploiting discrete symmetries of PCoF.

EQ1 and EQ2 are invariant under the symmetry transformations s_1, s_2, and s_3 described in § 2.2.3, and these can be exploited to reduce the dimensionality of state-space as discussed in § 2.7.3. While the "one-groove-per-box" geometry admits all three symmetries, the initial iterates $\mathcal{T}_{0,0.01\pi/\alpha}\chi^*$ and $\mathcal{T}_{0,0.8\pi/\alpha}\chi^*$ are not invariant under these symmetries. They have reflectional symmetries about different constant-z planes than the geometry; the discrete symmetries of PCoF cannot be exploited when continuing $\mathcal{T}_{0,0.01\pi/\alpha}\chi^*$ and $\mathcal{T}_{0,0.8\pi/\alpha}\chi^*$. This means that the size of the Jacobian becomes too large when run at a resolution of $(L, M, N) = (16, 16, 35)$. In this case when symmetries cannot be imposed, the iterations are run at a much lower resolution of $(L, M, N) = (7, 12, 30)$; finer resolution is allowed in the spanwise direction than the streamwise direction because EQ1 and EQ2 have greater energy in higher spanwise modes than streamwise modes. To facilitate a fair comparison, all four initial fields, χ^*, $\mathcal{T}_{0,0.01\pi/\alpha}\chi^*$, $\mathcal{T}_{0,0.8\pi/\alpha}\chi^*$, and $\mathcal{T}_{0,\pi/\alpha}\chi^*$, are run at the same resolution.

The residual norms and accuracies for three initial iterates, χ^*, $\mathcal{T}_{0,0.01\pi/\alpha}\chi^*$, and $\mathcal{T}_{0,0.8\pi/\alpha}\chi^*$, are plotted in fig. 4.7 after each Newton iteration. This is done for EQ1, EQ2, EQ7, and EQ8 of Gibson et al. (2008). The translated versions quickly saturate at a relatively high residual norm, while the original versions which have reflectional symmetry about $z = 0$ go down at least a few orders of magnitude for the same number of iterations. Due to the low resolutions, the residual norm does not go much lower. This allows us to speculate that the continuous families, $\tilde{\mathcal{F}}(\chi)$, spanned by symmetrical solutions such as EQ1 cannot all continue to grooved PCoF. Only a subset, $\mathcal{F}_2(\chi)$, can continue to grooved PCoF with one groove per box. While these iterations have not been repeated for cases of multiple grooves per box, we can speculate that continuous families of symmetrical solutions may be confined to their discrete subsets by these geometries too; there is also the possibility that the entire family fails to continue if the symmetries of the solution are not admitted by the geometry.

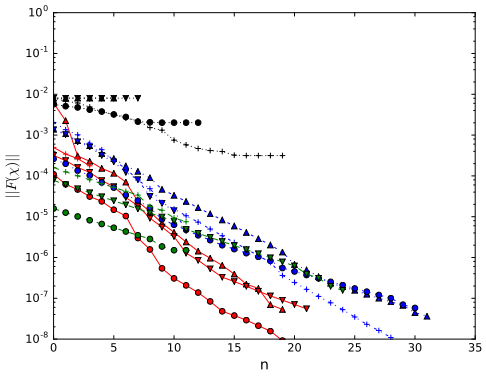

(a) Residual norm for χ^*

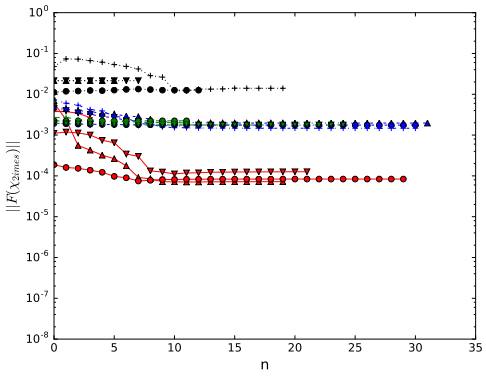

(b) Spatial accuracy for χ^*

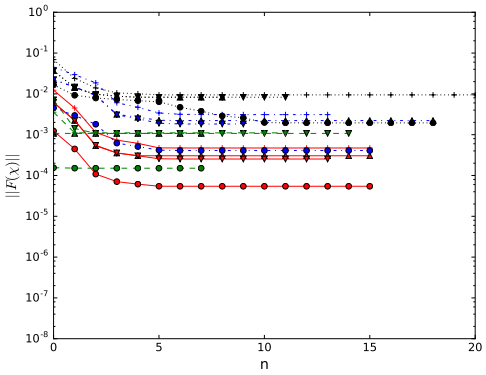

(c) Residual norm for $\mathcal{T}_{0,0.01\pi/\alpha}\chi^*$

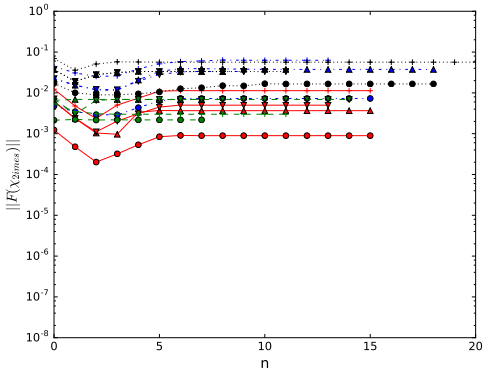

(d) Spatial accuracy for $\mathcal{T}_{0,0.01\pi/\alpha}\chi^*$

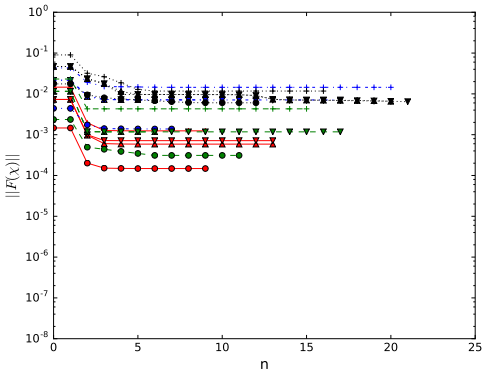

(e) Residual norm for $\mathcal{T}_{0,0.8\pi/\alpha}\chi^*$

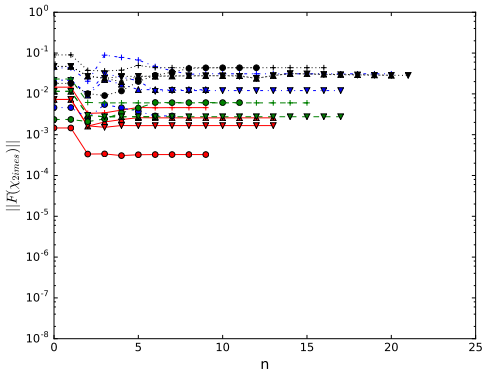

(f) Spatial accuracy for $\mathcal{T}_{0,0.8\pi/\alpha}\chi^*$

Figure 4.7: Convergence of translated versions of EQ1, EQ2, EQ7, and EQ8 in grooved PCoF. Residual norm ($||F(\chi)||$) and spatial accuracy ($||F(\chi_{2x})||$) are plotted against Newton iteration number. —: EQ1; -·-·-: EQ2; - - -: EQ7; ·····: EQ8. △: $A = -0.05$; ◯: $A = 0.01$; □: $A = 0.05$; +: $A = 0.1$.

It is worth noting here that although discrete symmetries are not imposed in the above computations, the solutions from continuation of χ^* remain invariant under s_1, s_2, and s_3. They also reach close to the solutions obtained at finer resolutions by exploiting the symmetries.

Bifurcation

$\mathcal{F}_2$ has two distinct members, χ^* and $\mathcal{T}_{0,L_z/2}(\chi^*)$, denoted χ^+. Their continued solutions at some amplitude A are denoted χ^*_A and χ^+_A respectively. It is found that $\chi^+_A \neq S_{L_z/2}(\chi^*_A)$; the members of $\mathcal{F}_2(\chi^*)$ bifurcate into two distinct families of solutions in grooved PCoF: $\mathcal{F}_1(\chi^*_A)$ and $\mathcal{F}_1(\chi^+_A)$, with distinct values for scalars such as kinetic energy density and bulk dissipation rate. The difference arises because, while grooved PCoF has reflectional symmetry about both $z = 0$ and $z = \pi/\beta$, the walls at $z = 0$ are displaced along $+y$ and the walls at $z = \pi/\beta$ are displaced along $-y$. This bifurcation can also be interpreted in terms of continuing χ^* along positive and negative groove amplitudes.

4.2.1 Significance to turbulence

Willis et al. (2013) argue that the presence of continuous families of solutions could obscure our description of turbulent flow and describe a method of slices to systematically reduce a family of similar solutions to one representative solution; with this approach, travelling wave solutions reduce to equilibria, and relative periodic orbits to periodic orbits. Grooved PCoF achieves this reduction by physically disrupting some of these symmetries. Spatially localized equilibria have also been found in smooth PCoF (Gibson and Brand (2014); Chantry and Kerswell (2015)). Based on our results for global solutions, we can expect that any symmetric localized solutions, when extended to grooved PCoF, would also be phase-restricted by the grooves.

In smooth PCoF turbulence, any of the solutions in a family $\tilde{\mathcal{F}}$ could be visited; no member of a family is special. As a result, turbulence statistics would only show spatial averages over an entire family of solutions. The phase-restriction of solutions

in grooved PCoF, however, implies that turbulence statistics should reflect the spatial structure of the solutions.

Riblets

Certain geometries of riblets in boundary layer flows produce a reduction in drag (Tani (1988); Walsh (1990); Dean and Bhushan (2010)). The drag reduction in such flows is explained as due to streamwise vortices that sit on top of riblets, sustaining low-speed streaks within riblet-valleys which produce lower drag (by $\sim 8\% - 16\%$) than in smooth-walled flows Dean and Bhushan (2010). The reduction of continuous families of solutions to discrete families by grooved PCoF due to symmetry preservation supports this description of riblet-mounted flows. We can reasonably suppose that, in addition to anchoring exact coherent structures spatially, grooves also filter out near-wall coherent structures whose size does not match that of the grooves.

4.3 Wavelength dependence

Figure 4.8 illustrates continuation of EQ1 to three different geometries — one, two, and three grooves per box — at a dominant groove amplitude of 10%. EQ2 is plotted for the same cases in fig. 4.9. The two groove per box geometry does not satisfy the shift-rotate symmetry s_2 or the shift-invert symmetry s_3; these cases were run at a resolution of 20x35x32 grid points ($(L, M, N) = (10, 16, 35)$) to converge to residual norms $\sim 10^{-7}$ and accuracies $\sim 10^{-5}$ for EQ1 and $\sim 10^{-3}$ for EQ2. The three groove per box satisfies s_1, s_2, and s_3, and these cases were run with 32x35x32 grid points ($(L, M, N) = (16, 16, 35)$) like the one groove per box case, and have residual norms similar to the one groove per box case.

The vortex-streak structure remains the same for the two and three grooves per box cases as well. However, the large scale distortion seen in the one groove per box case is not as pronounced in the other two cases. This suggests that the solutions are strongly affected when the wavelength of the grooves is of about the same size as the vortex-streak structure.

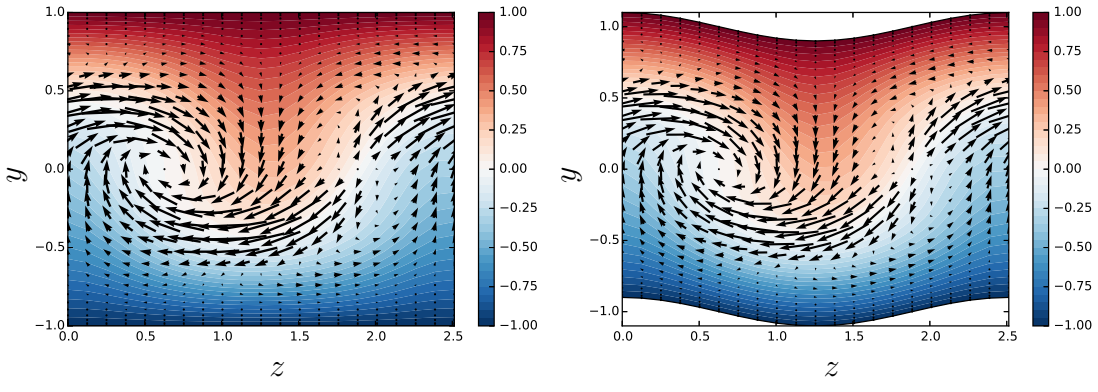

(a) Smooth PCoF

(b) Grooved PCoF with $A_1 = 10\%$

(c) Grooved PCoF with $A_2 = 10\%$

(d) Grooved PCoF with $A_3 = 10\%$

Figure 4.8: Velocity on a cross-stream plane ($x = 0$) for smooth PCoF (a) and grooved PCoF for one, two, and three grooves per box (b-d) for the lower branch solution EQ1. Contours show streamwise velocity and quiver arrows show cross-stream velocities.

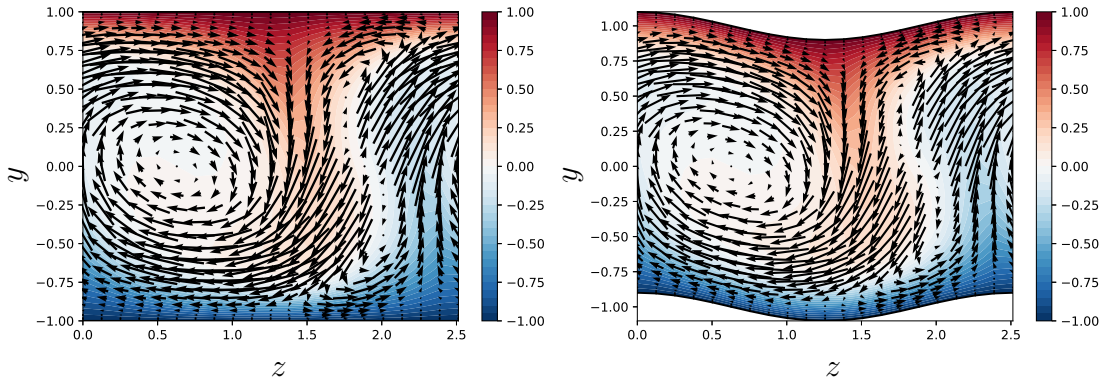

(a) Smooth PCoF

(b) Grooved PCoF with $A_1 = 10\%$

(c) Grooved PCoF with $A_2 = 10\%$

(d) Grooved PCoF with $A_3 = 10\%$

Figure 4.9: Velocity on a cross-stream plane ($x = 0$) for smooth PCoF (a) and grooved PCoF for one, two, and three grooves per box (b-d) for the upper branch solution EQ2. Contours show streamwise velocity and quiver arrows show cross-stream velocities.

4.3.1 Mean velocity

The mean velocity profiles for all three wavenumber cases are shown in fig. 4.10, with the profiles for grooved PCoF shown as a difference from the mean velocity for smooth PCoF. In the profiles of the one groove per box cases, the deficit in the mean velocity (compared to $U = y$) is increased by increasing groove-amplitude. In contrast, the profiles of the two and three groove per box cases bridge the velocity deficit in the mean velocity of both EQ1 and EQ2, and the mean velocity grows closer to the $U = y$ profile as the amplitude increases. The difference in mean velocity for EQ2 for the two groove per box is not zero at the centerline; this is because of the loss of the shift-rotate symmetry s_2 (see § 2.2.3) for the two groove per box case.

The bridging of the velocity deficit is stronger for the EQ2 than EQ1, although the velocity deficit for EQ2 is much higher than that for EQ1 in the first place. This effect is also stronger for the three grooves per box case than it is for the two grooves per box case. This decrease in velocity deficit also leads to the shear stress at the wall for grooved PCoF becoming closer to that for the laminar flow in smooth PCoF. The one groove per box case increases the shear stress at the wall compared to the smooth wall case, while the two and three groves per box cases reduce the shear stress at the wall. While this hints at a drag reducing tendancy for the two and three grooves per box cases, the profiles plotted in fig. 4.10 extend only until the tips of the grooves. They do not show the actual stresses at the wall. An exact quantification of the drag is provided in the next subsection.

4.3.2 Energy density and dissipation rate

We now look at the kinetic energy density (E) and bulk dissipation rate (D) for the three geometries for groove amplitudes of up to 10%. During continuation, the wall speed based Re is held constant.

A drag coefficient is defined as the the force exerted to keep the walls in uniform motion non-dimensionalized by the product of the density of the fluid, square of the

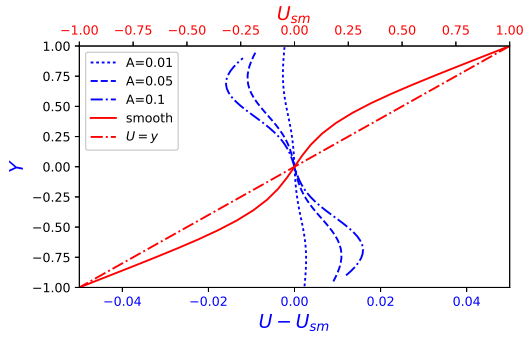

(a) EQ1; one groove per box

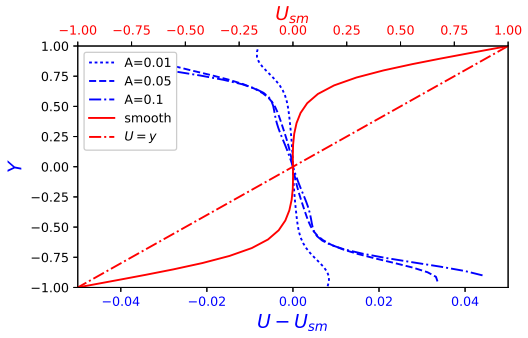

(b) EQ2; one groove per box

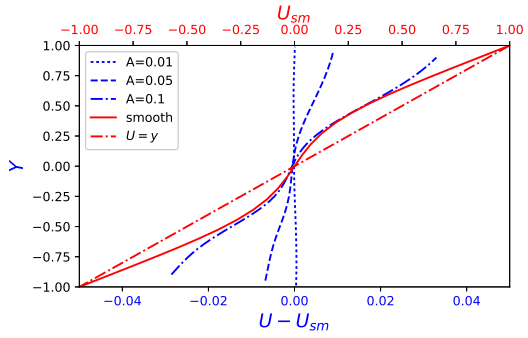

(c) EQ1; two grooves per box

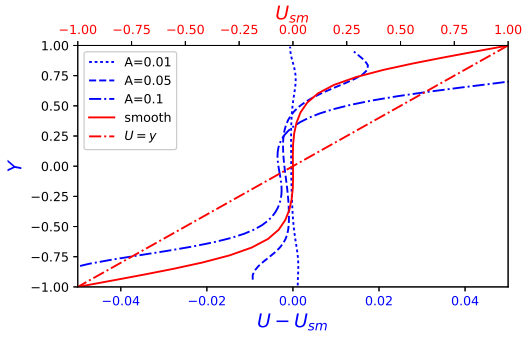

(d) EQ2; two grooves per box

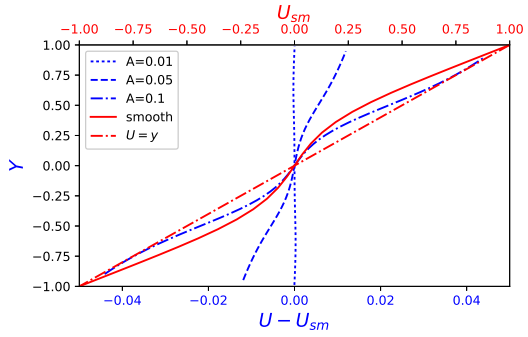

(e) EQ1; three grooves per box

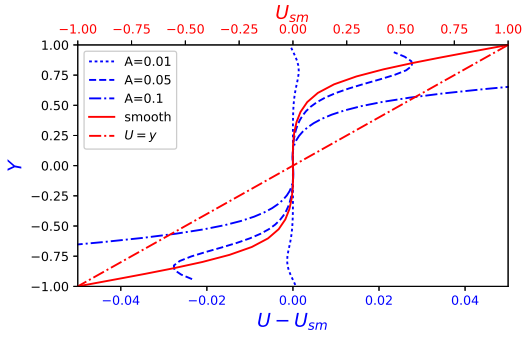

(f) EQ2; three grooves per box

Figure 4.10: Mean velocity profiles for EQ1 and EQ2 in grooved PCoF with one, two, and three grooves per periodic box, shown as differences from the smooth case. The laminar mean velocity, $U = y$, is included for comparison.

wall speed, and the planform area under consideration for the force calculation. The force used in this calculation is due to the streamwise shear stress at the walls, and the magnitudes at the two walls is added since they act in opposite directions at the top and bottom walls. For equilibria, this drag coefficient (C_D) can be related to the bulk dissipation rate (D) as

$$C_D = \frac{\text{Average stress at walls}}{\text{density} \times (\text{wall speed})^2} = \frac{2}{Re} D. \tag{4.3.1}$$

For the constant-Re continuation discussed in this chapter, the drag coefficient differs from the bulk dissipation rate by a constant factor of $2/Re$; so, it is sufficient to plot one of either the drag coefficient or bulk dissipation rate. In keeping with the literature, bulk dissipation rates are shown.

The kinetic energy density and bulk dissipation rate for the three wavenumber cases are shown in fig. 4.11 for the laminar solution and the equilibria, EQ1 and EQ2. The plots for the one groove per box case are reproduced to facilitate comparison.

The curves for the laminar solution are discussed first to serve as a base case. The kinetic energy density and the dissipation rate increase with increasing groove-amplitude, and this increase is stronger for the lower wavelength cases. The increase in kinetic energy is easily understood in terms of the increase in wetted surface area (per unit planform area). The sharper increase in kinetic energy for the three grooves case also follows from the increase in wetted surface area. Bulk dissipation rate, in the laminar case, is mostly due to the wall-normal derivative of the streamwise velocity. Increasing groove amplitude brings high speed regions (of opposite directions) closer, which in turn produces stronger shear and larger dissipation rates.

We now turn our attention to the kinetic energy density for EQ1 and EQ2 for the three geometries. For the two and three groove cases, the energy density increases, and we can expect this to be for the same reason as the laminar case. Indeed, in figs. 4.8 and 4.9, the sizes of the high speed regions (blue at the bottom wall and red at the top wall) do increase as they fill up the area within the grooves.

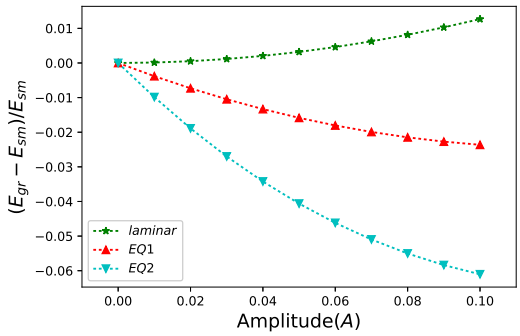

(a) Kinetic energy density; one groove

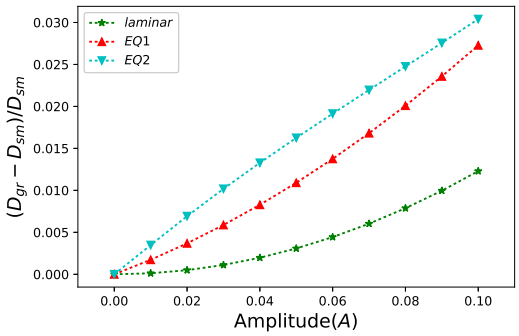

(b) Bulk dissipation rate; one groove

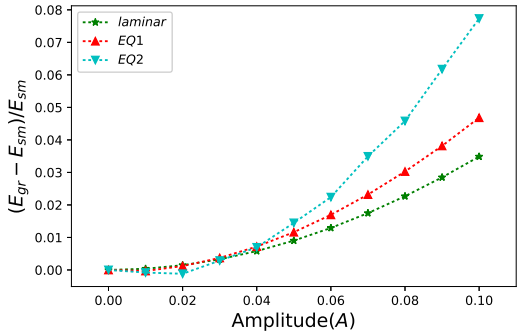

(c) Kinetic energy density; two grooves

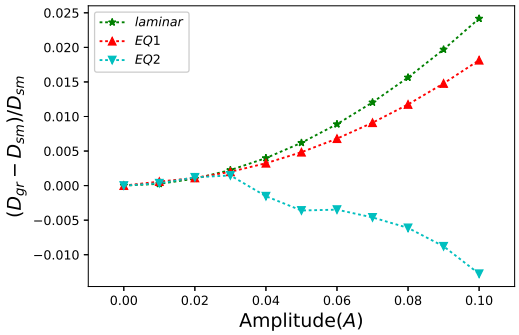

(d) Bulk dissipation rate; two grooves

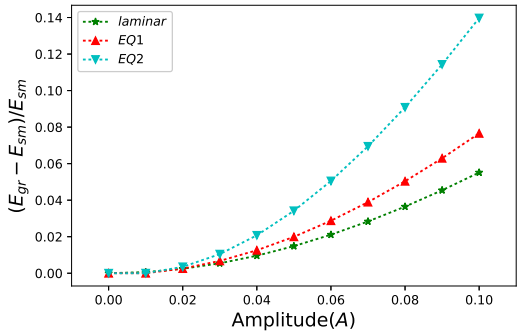

(e) Kinetic energy density; three grooves

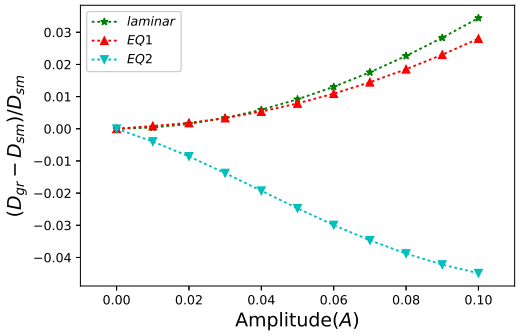

(f) Bulk dissipation rate; three grooves

Figure 4.11: Change in kinetic energy density and bulk dissipation rate in grooved PCoF for laminar flow and upper and lower branch equilibria with one, two, and three grooves per box.

The anamolous case is the one groove case, where the energy density decreases with increasing amplitude. This can be explained in terms of the vortex-streak structure "eating into" the high speed regions near the wall. The vortex-streak structure is based around the $u = 0$ critical layer (it is a critical layer because the equilibria travel with a phase speed of zero). The critical layer moving closer to the wall is accompanied by a shrinkage of the high speed regions, which leads to reduced energy density. It is worth noting that the decrease in energy density for smooth PCoF from laminar to EQ1 to EQ2 is also linked to the critical layer growing closer to the wall.

This mechanism for reduction in energy density is most clearly observed by comparing the smooth PCoF and one groove cases for EQ2 in fig. 4.9. At $z \approx 0$ at the bottom wall and $z \approx 1.25$ at the top wall, the critical layer for the one groove case is much closer to the wall than it is for smooth PCoF. Consequently, there is a significantly smaller high speed region at either locations in the one groove case. In the two and three grooves cases, although the critical layer comes very close to the tips of the grooves, multiple high speed regions exist within the grooves.

We have observed two phenomena that affect kinetic energy density: 1) Increasing wetted surface area leading to increased energy density, and 2) Increased proximity of the critical layer to the walls leading to reduced energy density. Laminar flows in grooved PCoF are dominated by the former effect since the critical layer is far from the walls. The one groove case seems to be dominated by the latter effect as the vortex-streak structure penetrates into the grooves. In the two and three grooves cases, the latter effect is not very pronounced as the structure can only reach up to the tips of the grooves, and the increased wetted surface area leads to an overall increase in energy density.

We also note the increase in kinetic energy density for laminar flows to be significantly smaller than that in EQ1 and EQ2 (for two and three grooves per box). This is an artefact of the plotting; the increase in kinetic energy density is normalized by the kinetic energy density of smooth PCoF, and the kinetic energy density is largest for the laminar case.

The trends in the bulk dissipation rate can also be explained in terms of the two competing phenomena. Their actions are as follows: 1) Increasing wetted surface area leads to an increase in dissipation rate, and 2) Increasing the proximity of the critical layer to the wall increases the dissipation rate. In laminar flow, as with energy density, the trend in dissipation rate is also dominated by the wetted surface area.

For EQ2, the critical layer is very close the walls. We expect the trends in dissipation rate to be dominated by the location of the critical layer. For the one groove per box case, increasing amplitude brings the critical layer closer to the walls, leading to increased dissipation rate (as well as power input and drag coefficient). For the three grooves case, increasing amplitude pushes the critical layer outside the tip of the grooves, leading to reduced dissipation rate. For the two grooves case, with increasing amplitude, the dissipation rate first increases and then decreases. However, the dissipation rate for the two grooves case remains lower than that for the one groove case at all amplitudes. This suggests that for the two grooves case, at low amplitudes, the critical layer might penetrate into the grooves.

For EQ1, the critical layer is far from the walls. The one groove case sees increasing dissipation rate with increasing amplitude as expected. The two and three grooves cases also see an increase in dissipation rate with increasing amplitude, suggesting that the squeezing out of the critical layer from the grooves is either insignificant or absent.

This mechanism for "drag reduction" is consistent with the one discussed in the literature (for instance, see fig. 7 in Lee and Lee (2001)). A Reynolds number dependent optimal spacing of the riblets exists for drag reduction; however, drag reduction is seen for riblet spacing smaller than 25 wall units (Dean and Bhushan (2010)). The near-wall cycle of turbulence also has a spanwise scale of ~ 100 wall-units (for example, Jiménez and Moin (1991); Hamilton et al. (1995)). This suggests that the greatest drag reduction involves riblets whose wavelength is a quarter of the characteristic size of the vortex streak structure.

The present results show a drag decreasing tendency (for EQ2, which is representative of the near-wall cycle of turbulence) for grooves whose wavelength is a half and a third of the characteristic size of the structure. And indeed, the drag reduction is greater when the riblet spacing is a third of the characteristic size than when it is a half. The present solver does not allow computations with smaller wavelengths, but we can reason towards the observed optimal spacing by considering the two competing phenomena described earlier. Decreasing the wavelength (at a fixed amplitude) produces greater drag due to the increase in wetted surface area. So, the decrease in wavelength is only beneficial until the reduction in drag due to the squeezing out of the critical layer offsets the increase in drag due to the increase in wetted surface area. Figure 4.9 shows that the critical layer is already outside the grooves for the three grooves case (i.e., when the wavelength is a third of the characteristic size). Presumably, when the wavelength is reduced beyond a fourth or a fifth of the characteristic size, further decrease in wavelength would not have any significant effect on the critical layer. Beyond this point, reducing the wavelength would only see an increase in drag due to the increase wetted surface area.

We conclude this chapter by looking at the groove spacing (wavelength) in terms of inner units, $\lambda_{grooves}Re_\tau$, where $\lambda_{grooves}$ is the wavelength of the grooves (non-dimensionalized by channel half-height) and Re_τ is the friction Reynolds number. For the one groove per box case, $\lambda_{grooves} = L_z = 0.4$, and for the two and three grooves cases, the groove spacing is 0.2 and 0.13 respectively. The friction Reynolds number may be expressed explicitly in terms of the bulk dissipation rate as follows.

$$\begin{aligned} Re_\tau &= Re\sqrt{\frac{\hat{u}_\tau^2}{\hat{U}_w^2}} \\ &= Re\sqrt{\frac{1}{2Re}\left(\left.\overline{\frac{du}{dy}}\right|_{y=-1} + \left.\overline{\frac{du}{dy}}\right|_{y=1}\right)} \\ &= \sqrt{IRe} \\ &= \sqrt{DRe} \end{aligned} \tag{4.3.2}$$

where $\hat{u}_\tau$ is the dimensinoal friction velocity, $\hat{U}_w$ is the speed of either walls, $\overline{\frac{du}{dy}}\big|_{y=-1}$ is the average (over plan area) of non-dimensional strain-rate at the bottom wall, $\overline{\frac{du}{dy}}\big|_{y=1}$ is the average (over plan area) of non-dimensional strain-rate at the top wall, and I and D are the power input and bulk dissipation rate respectively.

For EQ2, the dissipation rate for the different cases lie roughly between 2.9 and 3.1, with the flat wall case having $D = 3.04$. Using a nominal dissipation rate of 3, and $Re = 400$, the friction Reynolds number is $Re_\tau \approx 35$. Hence, in terms of wall-units, the spacing of the grooves is 14 for the one groove case, 7 for the two groove case, and 4.7 for the ghree groove case. These spacings seem to be inconsistent with the observations in the literature, especially the drag increase at 14 inner units. This apparent disparity is easily reconciled by taking into account the fact that the characteristic spanwise size of the vortex-streak structure itself is 14 inner units, while the characteristic spanwise size of the near-wall cycle in turbulence is about 100 inner units.

Chapter 5

Conclusion and Outlook

> *To expect that the intricacies of science will be pierced by a careless glance, or the eminences of fame ascended without labour, is to expect a peculiar privilege, a power denied to the rest of mankind; but to suppose that the maze is inscrutable to diligence, or the heights inaccessible to perseverance, is to submit tamely to the tyranny of fancy, and enchain the mind in voluntary shackles.*
>
> Samuel Johnson

Equilibria (EQ1 and EQ2) have been successfully continued for PCoF from the smooth wall case to grooved walls. The solver used for this continuation is outlined in chapter 2. Discrete symmetries of these equilibria, s_1, s_2, and s_3, have been exploited to allow computations on a 32x35x32 grid (streamwise, wall-normal, spanwise) for geometries with one and three grooves per spanwise period of 2.51 channel half-heights. The geometry with two grooves per spanwise period (or any even number of grooves per period) does not admit s_2 and s_3, and this case has been run at a lower resolution of 20x35x32 grid points. Geometries with more than three grooves per periodic box have not been investigated since the resolution with each groove becomes worse with increasing number of grooves.

The spanwise inhomogeneity of grooved PCoF makes the relative spanwise positioning of solutions important. Two observations are made regarding this. Solutions that are obtained from zero phase iterates of EQ1 (see § 4.2) produce residual norms $\gtrsim 10^{-3}$ when translated along z, which is interpreted as solutions from iterates with non-zero phase, if they exist, being significantly different from the former. Attempts to compute solutions from iterates of non-zero phase show very slow convergence, suggesting that such solutions may not even exist. Based on these observations, we can speculate that symmetric solutions continued to symmetric geometries tend to get spatially anchored about locations that preserve the discrete symmetries. The fate of symmetric solutions when continued to asymmetric geometries remains an open question.

Grooved PCoF with groove-wavelength of a half or a third of the vortex-streak structure being captured have been found to exhibit a drag reducing tendency for upper branch equilibria (EQ2 in the present work). This drag reduction is a result of the squeezing out of the vortex-streak structure by the grooves. If the wavelength is several times lower than this, we expect the drag to increase as the above effect saturates and the wetted surface area becomes the dominating factor. Both phenomena serve to increase the kinetic energy density.

Using the spacing of streamwise streaks in the near-wall cycle (≈ 100 wall-units) as the relevant characteristic size, the present results are consistent with the observations of an optimal streak spacing ≈ 25 wall units. This provides a strong motivation to extend exact invariant solutions to geometries with greater number of grooves per periodic box to find an optimal size for the grooves. However, the limitation imposed by the present numerical method on the resolution stops us from undertaking such an investigation. This author hopes that future studies involving more efficient numerical scheme for continuation of exact solutions can shed more light on the Reynolds number dependence of optimal riblet spacing.

As a precursor to continuing non-laminar equilibria to grooved PCoF, laminar solutions for grooved channel flows were computed for transverse, longitudinal, and

oblique grooves. In addition to the numerical results, analytical solutions were also derived in the long-wavelength limit. For transverse and oblique grooves, the Stokes-flow approximation was used in the derivation. The in-phase arrangement of the grooved walls allowed derivation of these solutions to be second-order accurate (in the wavenumber). The analytical solutions are found to do well even for wavenumbers approaching unity at Reynolds numbers close to 100. These results complement those of Mohammadi and Floryan (2013), which were obtained for similar geometries, except with one flat wall and one grooved wall, while the present work uses two grooved walls.

The large size of the Jacobian that must be stored and solved imposes serious limitations on the matrix-based domain transformation scheme. A more efficient solver is needed, especially if periodic orbits are to be continued to rough-walled geometries. In spite of the limitations, the present numerical method adequately serves its purpose of computing equilibria and raising interesting questions for future investigations.

5.1 Outlook

We conclude with a brief review of some interesting questions raised in the present work. Symmetrical solutions such as EQ1 and EQ2 bifurcate into two discrete families in grooved PCoF with one groove per box, but the significance of this bifurcation has not been investigated. This bifurcation is a consequence of the geometry (one groove per box) and the solutions (EQ1 and EQ2) each having two planes of reflectional symmetry at $z = (2k)\pi/\alpha$ and $z = (2k+1)\pi/\alpha$ for any integer k.

The spanwise anchoring effect of grooved PCoF (see § 4.2) has been attributed to the preservation of the reflectional symmetry. However, the two groove per box case breaks the shift-rotate symmetry, s_2, and the shift-invert symmetry s_3. EQ1 and EQ2 can still be continued to the two grooves per box PCoF. With the definition of eq. (4.0.2), any geometry with an even number of grooves per box breaks s_2 and s_3. A more detailed study is needed to understand the significance of these discrete symmetries to localization of exact invariant solutions in grooved PCoF.

The geometries explored presently are very limited even for the case of longitudinal grooves in PCoF. The solver developed here does provide the basis for a much richer class of longitudinal grooves to be explored, even approaching "longitudinal roughness" if enough Fourier modes are accommodated in eq. (2.7.8). The relative size of the original smooth PCoF solution to the wavelength of the grooves can also be altered; presently, the spanwise wavelength of the grooves, L_g, has been limited to be L_s/k for $k \in \{1, 2, 3\}$, where L_s is the wavelength of the smooth PCoF solution. If the higher spanwise resolutions are allowed through the use of Jacobian-free methods, then a much larger range of relations between L_g and L_s can be explored to study the size-based filtering of the vortex-streak structure by the grooves.

The drag reduction mechanism for riblet-mounted flows has been successfully identified based on continuation of equilibria for grooved PCoF. It will be interesting to extend this to groove channel flows. For channel flows, travelling wave solutions need to be computed, and these involve one additional variable compared to the PCoF (phase-speed of the travelling wave). One particularly interesting question, which has been raised previously as well, is to see the competing effects of drag reduction and drag increase due to decreasing groove-wavelength. It would also be interesting to see if a simple model can be produced to predict these based on the change in the size of the vortex-streak structure and the laminar solutions for grooved channels.

Appendix A

Convergence properties

A.1 Lipschitz continuity

Super-linear convergence of the Newton method requires that the Jacobian $\boldsymbol{\mathcal{F}}'()$ be Lipschitz continuous, with some Lipschitz constant γ. Lipschitz continuity is proven by requiring that the phase-space for the iterations satisfy eq. (A.2.1) and eq. (A.2.2) for some initial iterate sufficiently close to the solution (see § A.1).

Lipschitz continuity is defined by the existence of a γ such that for all $x, y \in \mathbb{B}(\zeta)$, $\mathbb{B}(\zeta)$ being ball of radius ζ around the exact solution where iterations progress,

$$||\boldsymbol{\mathcal{F}}'(x) - \boldsymbol{\mathcal{F}}'(y)|| \leq \gamma ||x - y||$$

where the matrix norm should be compatible with the vector norm. It can simply be taken as the first singular value under some weight which defines the vector norm.

For the current problem, since $\boldsymbol{\mathcal{F}}'() = \mathcal{L} + \mathcal{G}(\boldsymbol{\chi})$, this condition becomes

$$\begin{aligned} ||\{\mathcal{L} + \mathcal{G}(\boldsymbol{\chi}^1)\} - \{\mathcal{L} + \mathcal{G}(\boldsymbol{\chi}^2)\}|| &\leq \gamma ||\boldsymbol{\chi}^1 - \boldsymbol{\chi}^2|| \\ \implies ||\mathcal{G}(\boldsymbol{\chi}^1) - \mathcal{G}(\boldsymbol{\chi}^2)|| &\leq \gamma ||\boldsymbol{\chi}^1 - \boldsymbol{\chi}^2|| \\ \implies ||\mathcal{G}(\boldsymbol{\chi}^1 - \boldsymbol{\chi}^2)|| &\leq \gamma ||\boldsymbol{\chi}^1 - \boldsymbol{\chi}^2||, \qquad \because \mathcal{G}() \text{ is linear} \end{aligned}$$

(the subscripts 1 and 2 do not necessarily denote the iteration number, but simply identify two state-vectors in some subset X of $\mathbb{R}^{N\times N}$)

$\delta(\boldsymbol{\chi})$ is defined as $\delta\boldsymbol{\chi} = \boldsymbol{\chi}^1 - \boldsymbol{\chi}^2$ so that the above equation simplifies to

$$||\mathcal{G}(\delta\boldsymbol{\chi})|| \leq \gamma||\delta\boldsymbol{\chi}|| \tag{A.1.1}$$

It can be seen that the domain of $\delta\boldsymbol{\chi}$ is a bounded set containing the origin.

To demonstrate Lipschitz continuity, $\delta\boldsymbol{\chi}$ is split as

$$\delta\boldsymbol{\chi} = \begin{bmatrix} \delta\boldsymbol{\chi}_{-n} \\ \delta\boldsymbol{\chi}_{-n+1} \\ \vdots \\ \delta\boldsymbol{\chi}_0 \\ \delta\boldsymbol{\chi}_1 \\ \vdots \\ \delta\boldsymbol{\chi}_n \end{bmatrix} = \begin{bmatrix} \delta\boldsymbol{\chi}_{-n} \\ 0 \\ \vdots \\ 0 \\ 0 \\ \vdots \\ 0 \end{bmatrix} + \begin{bmatrix} 0 \\ \delta\boldsymbol{\chi}_{-n+1} \\ 0 \\ \vdots \\ 0 \\ \vdots \\ 0 \end{bmatrix} + ...$$

Further, each $\delta\boldsymbol{\chi}_k$ is split as

$$\delta\boldsymbol{\chi}_k = \begin{bmatrix} \delta u_k \\ \delta v_k \\ \delta p_k \end{bmatrix}$$

The norm $||\mathcal{G}(\delta\boldsymbol{\chi})||$ then compares as

$$||\mathcal{G}(\delta\boldsymbol{\chi})|| \leq ||\mathcal{G}(\delta u_{-n})|| + ||\mathcal{G}(\delta v_{-n})|| + ||\mathcal{G}(\delta p_{-n})|| + ||\mathcal{G}(\delta u_{-n+1})|| + ||\mathcal{G}(\delta v_{-n+1})|| + ... \tag{A.1.2}$$

where δu_k^i represents either the i^{th} velocity at wavenumber k, or the state-vector $\delta\boldsymbol{\chi}$ whose entries are all zero except for those that correspond to the i^{th} velocity at wavenumber k, depending on the context.

The vector-norm may either be defined as either the kinetic energy, or as the sum of the kinetic energy and the absolute value of the pressure. Either way, the vector norm is defined such that

$$||\delta\boldsymbol{\chi}|| = ||\delta u_{-n}||+||\delta v_{-n}||+||\delta p_{-n}||+||\delta u_{-n+1}||+||\delta v_{-n+1}||+||\delta p_{-n+1}||+..... \quad \text{(A.1.3)}$$

Then, if the following condition is satisfied, $\boldsymbol{\mathcal{F}}'$ is guaranteed to be Lipschitz continuous.

$$||\mathcal{G}(\delta u_k^i)|| \leq \gamma_k^i ||u_k^i||, \qquad \text{where } \{u^1, u^2, u^3\} = \{u, v, p\} \quad \text{(A.1.4)}$$

and the γ for $\mathcal{G}(\boldsymbol{\chi})$ is chosen as $\gamma = max_{i,k}\{\gamma_k^i\}$

The above equation is always satisfied for pressure (δp_k) since pressure does not appear in the advection term- for all k, $\mathcal{G}(\delta p_k) = 0$, resulting in $||\mathcal{G}(\delta p_k)|| = 0 \leq ||p_k||$ for any valid definition of the norm.

The Jacobian $\mathcal{G}(\boldsymbol{\chi})$ contains the partial derivatives of the advection terms in its blocks (Eq. eq. (2.5.12)), the $(k', m')^{th}$ block is given by:

$$\mathcal{G}_{k',m'} = \begin{bmatrix} \frac{\partial \phi_k^1}{\partial u_m} & \frac{\partial \phi_k^1}{\partial v_m} & Z \\ \frac{\partial \phi_k^2}{\partial u_m} & \frac{\partial \phi_k^2}{\partial v_m} & Z \\ Z & Z & Z \end{bmatrix} \quad \text{(A.1.5)}$$

where, $k' = k + n + 1, m' = m + n + 1$, and the wavenumbers considered in the computation go from $-n$ to n (so that when $k = -n$, it corresponds to $k' = 1$. k', m' go from 1 to $2n + 1$), and Z is a zero matrix of the appropriate size.

For an argument δu_l, the non-zero blocks of $\mathcal{G}()$ are:

$$\begin{aligned}
\mathcal{G}_{k',k'-l'-1}(u_l) &= \begin{bmatrix} -ig(U_l' + U_l D) & Z & Z \\ Z & -igU_l D & Z \\ Z & Z & Z \end{bmatrix} \\
\mathcal{G}_{k',k'-l'}(u_l) &= \begin{bmatrix} ik\alpha U_l & U_l' & Z \\ Z & i(k-l)\alpha U_l & Z \\ Z & Z & Z \end{bmatrix} \\
\mathcal{G}_{k',k'-l'+1}(u_l) &= \begin{bmatrix} ig(U_l' + U_l D) & Z & Z \\ Z & igU_l D & Z \\ Z & Z & Z \end{bmatrix} = -\mathcal{G}_{(k+2)',(k+2)'-l'-1}(U_l)
\end{aligned} \tag{A.1.6}$$

where, U_l and U_l' are diagonal matrices with the velocity u_l and the derivative of the velocity u_l' on the principal diagonal respectively.

For an argument δv_l, the non-zero blocks of $\mathcal{G}()$ are:

$$\begin{aligned}
\mathcal{G}_{k',k'-l'-1}(v_l) &= \begin{bmatrix} Z & Z & Z \\ -igV_l' & Z & Z \\ Z & Z & Z \end{bmatrix} \\
\mathcal{G}_{k',k'-l'}(v_l) &= \begin{bmatrix} V_l D & Z & Z \\ il\alpha V_l & (V_l' + V_l D) & Z \\ Z & Z & Z \end{bmatrix} \\
\mathcal{G}_{k',k'-l'+1}(v_l) &= \begin{bmatrix} Z & Z & Z \\ igV_l' & Z & Z \\ Z & Z & Z \end{bmatrix} = -\mathcal{G}_{(k+2)',(k+2)'-l'-1}(v_l)
\end{aligned} \tag{A.1.7}$$

Each of the representative blocks can be further split into three matrices:

$$\mathcal{G}_{k',k'-l'-1}(u_l) = \tilde{U}_l \begin{bmatrix} Z & Z & Z \\ Z & Z & Z \\ Z & Z & Z \end{bmatrix} + \tilde{U}_l' \begin{bmatrix} -igC_{k-2l-1}I & Z & Z \\ Z & Z & Z \\ Z & Z & Z \end{bmatrix} + \tilde{U}_l \begin{bmatrix} -igC_{k-2l-1}I & Z & Z \\ Z & -igI & Z \\ Z & Z & Z \end{bmatrix} \tilde{D}$$

$$\mathcal{G}_{k',k'-l'}(u_l) = \tilde{U}_l \begin{bmatrix} ik\alpha I & Z & Z \\ Z & i(k-l)\alpha I & Z \\ Z & Z & Z \end{bmatrix} + \tilde{U}_l' \begin{bmatrix} Z & I & Z \\ Z & Z & Z \\ Z & Z & Z \end{bmatrix} + \tilde{U}_l \begin{bmatrix} Z & Z & Z \\ Z & Z & Z \\ Z & Z & Z \end{bmatrix} \tilde{D}$$

$$\mathcal{G}_{k',k'-l'+1}(u_l) = \tilde{U}_l \begin{bmatrix} Z & Z & Z \\ Z & Z & Z \\ Z & Z & Z \end{bmatrix} + \tilde{U}_l' \begin{bmatrix} igI & Z & Z \\ Z & Z & Z \\ Z & Z & Z \end{bmatrix} + \tilde{U}_l \begin{bmatrix} igI & Z & Z \\ Z & igI & Z \\ Z & Z & Z \end{bmatrix} \tilde{D}$$

$$\mathcal{G}_{k',k'-l'-1}(v_l) = \tilde{V}_l \begin{bmatrix} Z & Z & Z \\ Z & Z & Z \\ Z & Z & Z \end{bmatrix} + \tilde{V}_l' \begin{bmatrix} Z & Z & Z \\ -igI & Z & Z \\ Z & Z & Z \end{bmatrix} + \tilde{V}_l \begin{bmatrix} Z & Z & Z \\ Z & Z & Z \\ Z & Z & Z \end{bmatrix} \tilde{D}$$

$$\mathcal{G}_{k',k'-l'}(v_l) = \tilde{V}_l \begin{bmatrix} Z & Z & Z \\ il\alpha I & Z & Z \\ Z & Z & Z \end{bmatrix} + \tilde{V}_l' \begin{bmatrix} Z & Z & Z \\ Z & I & Z \\ Z & Z & Z \end{bmatrix} + \tilde{V}_l \begin{bmatrix} I & Z & Z \\ Z & I & Z \\ Z & Z & Z \end{bmatrix} \tilde{D}$$

$$\mathcal{G}_{k',k'-l'+1}(v_l) = \tilde{V}_l \begin{bmatrix} Z & Z & Z \\ Z & Z & Z \\ Z & Z & Z \end{bmatrix} + \tilde{V}_l' \begin{bmatrix} Z & Z & Z \\ igI & Z & Z \\ Z & Z & Z \end{bmatrix} + \tilde{V}_l \begin{bmatrix} Z & Z & Z \\ Z & Z & Z \\ Z & Z & Z \end{bmatrix} \tilde{D}$$

$$\text{where, } \tilde{D} = \begin{bmatrix} D & Z & Z \\ Z & D & Z \\ Z & Z & Z \end{bmatrix}, \tilde{U}_l = \begin{bmatrix} U_l & Z & Z \\ Z & U_l & Z \\ Z & Z & U_l \end{bmatrix}, \tilde{V}_l = \begin{bmatrix} V_l & Z & Z \\ Z & V_l & Z \\ Z & Z & V_l \end{bmatrix}$$

$$\tilde{U}_l' = \begin{bmatrix} U_l' & Z & Z \\ Z & U_l' & Z \\ Z & Z & U_l' \end{bmatrix}, \tilde{V}_l' = \begin{bmatrix} V_l' & Z & Z \\ Z & V_l' & Z \\ Z & Z & V_l' \end{bmatrix} \tag{A.1.8}$$

To make further progress with evaluating the norms, some restrictions are imposed on the set X, the domain of $\delta\boldsymbol{\chi}$, so that the following two conditions on the derivatives

of velocities of any particular wavenumber holds:

$$\begin{aligned} \forall l \in \mathbb{Z}, \forall \delta\boldsymbol{\chi} \in X, \forall y \in (-1,1), \exists q \in \mathbb{R}^+ : \qquad & max_y\{|\frac{d\delta u_l^i}{dy}(y)|\} \leq q(max_y\{|\delta u_l^i(y)|\}) \\ \forall l \in \mathbb{Z}, \forall \delta\boldsymbol{\chi} \in X, \exists r \in \mathbb{R}^+ : \qquad & ||\frac{d\delta u_l^i}{dy}|| \leq r(||\delta u_l^i||) \end{aligned} \tag{A.1.9}$$

The rationale behind applying the above conditions involves the assumption that the exact steady solution evolves smoothly in the boundary-deformation space (as $g = \epsilon\alpha$ goes from 0 to the required value). This assumption is quite reasonable, as it is always possible to choose infinitesimal increments in g so that the difference in the solutions is correspondingly small, and hence satisfies the above conditions.

The above conditions serve to impose upper bounds on the norms of the matrices $\tilde{U}_l', \tilde{V}_l'$, as well as the matrix D. These bounds follow from the properties of diagonal matrices: the p-norm of a diagonal matrix is given by the largest absolute value of its elements (the p-norm is considered here for simplicity, and if a discretization scheme with uniform spacing is used, the L2 norm is an appropriate measure for the norm). First, $||\tilde{U}_l|| = ||U_l||, ||\tilde{V}_l|| = ||V_l||, ||\tilde{U}_l'|| = ||U_l'||, ||\tilde{V}_l'|| = ||V_l'||$. Since U_l' and V_l' are diagonal matrices, their norm is given by the largest absolute value of the derivative of the functions u_l, v_l. From the above condition, the norms are related as (from Eq. eq. (A.1.9)):

$$\begin{aligned} ||U_l||_p = max_y\{u_l\} &\leq ||u_l||_p \\ ||V_l||_p = max_y\{v_l\} &\leq ||v_l||_p \\ ||U_l'||_p = max_y\{u_l'\} \leq r.(max_y\{u_l\}) &\leq r.||u_l||_p \\ ||V_l'||_p = max_y\{v_l'\} \leq r.(max_y\{v_l\}) &\leq r.||v_l||_p \end{aligned} \tag{A.1.10}$$

The p-norm of the matrix $\tilde{D}$ is also bounded, for the following reason:
The norm of $\tilde{D}$ is simply the norm of D, since the set of singular values for block diagonal matrices is simply the union of the sets of singular values for individual blocks. Although the norm of D when defined over $\mathbb{R}^N$ can be arbitrarily large, it becomes bounded when defined over a more restrictive domain. For the vectors $\delta u_l, \delta v_l$

considered here, the norm evaluates as (from Eq. eq. (A.1.9))

$$||D|| = sup\{\frac{||Dv||}{||v||} : v \in \hat{X}, v \neq 0\} \leq r \tag{A.1.11}$$

where $\hat{X}$ is the domain of δu_l^i such that $\delta\boldsymbol{\chi} \in X$. This condition relates to the smoothness of velocity gradients.

Hence, when the conditions in Eq. eq. (A.1.9) are imposed on X, the norms of the matrices evaluate as:

$$\begin{aligned} ||U_l|| &\leq ||u_l|| \\ ||V_l|| &\leq ||v_l|| \\ ||U_l'|| &\leq r.||u_l|| \\ ||V_l'|| &\leq r.||v_l|| \\ ||D|| &\leq r \end{aligned} \tag{A.1.12}$$

With the above relations, the norms of the blocks of $\mathcal{G}()$ compare as

$$\begin{aligned} ||\mathcal{G}_{k',k'-l'-1}(u_l)|| &\leq [0 + qg||u_l|| + rg||u_l||] && = (q+r)g||u_l|| \\ ||\mathcal{G}_{k',k'-l'}(u_l)|| &\leq [max\{|k|, |k-l|\}\alpha||u_l|| + q||u_l|| + 0] && = (q + max\{|k|, |k-l|\}\alpha)||u_l|| \\ ||\mathcal{G}_{k',k'-l'+1}(u_l)|| &\leq [0 + qg||u_l|| + rg||u_l||] && = (q+r)g||u_l|| \\ ||\mathcal{G}_{k',k'-l'-1}(v_l)|| &\leq [0 + qg||v_l|| + 0] && = qg||v_l|| \\ ||\mathcal{G}_{k',k'-l'}(v_l)|| &\leq [l\alpha||v_l|| + q||v_l|| + r||v_l||] && = (l\alpha + q + r)||v_l|| \\ ||\mathcal{G}_{k',k'-l'+1}(v_l)|| &\leq [0 + qg||v_l|| + 0] && = qg||v_l|| \end{aligned} \tag{A.1.13}$$

The matrices $\mathcal{G}(u_l), \mathcal{G}(v_l)$ can be split into sums of three block-diagonal matrices, each with non-zero blocks on one of the three diagonals $\{k', k'-l'-1\}, \{k', k'-l'\}, \{k', k'-l'+1\}$ (not necessarily including the principal diagonal). The norm of each block-diagonal matrix is given by the maximum norm of its non-zero blocks. The norm of the sum of the three diagonal matrices is less than or equal to the sum of the norms of the three diagonal matrices.

Of the coefficients of $||u_l||, ||v_l||$ in Eq. eq. (A.1.13): q, r, g, α (and k, l), g and α are fixed parameters, while q and r can be set through a proper choice of the increment in g, δg, for successive solutions in the boundary-deformation space. Although the equation suggests that the norm increases for higher wavenumbers considered (larger k,l), this is a fictitious result for the following reason: when the largest (absolute value of a) diagonal element of a diagonal matrix is chosen as the norm, it is under the assumption that the vector that corresponds to this singular value is present in the domain. This is illustrated below:

For a diagonal matrix A:

$$A = \text{diag}(\lambda_1, \lambda_2, ..., \lambda_n)$$

supposing that $|\lambda_p|$ is the largest magnitude of its elements,

$$\boldsymbol{v} : v_m = \begin{cases} 1, & \text{if } m = p \\ 0, & \text{otherwise} \end{cases} \qquad \text{gives the largest gain, } \lambda_p$$

In the current case, although higher wavenumbers result in a larger amplification, their amplitudes are significantly lower than the amplitudes of lower wavenumbers. That is, for instance, $||\delta u_3|| \ll ||\delta u_1||$ in $\delta\boldsymbol{\chi}$ that are of interest. Consequently, the norm $||3i\alpha I \delta u_3||$ is much smaller than $||i\alpha I \delta u_1||$, despite the factor 3 multiplying the matrix $i\alpha I$ for $k = 3$. With this understanding, it can now be asserted that it is sufficient to consider $|k|, |k-l|$ to be less than 5 as far as the norm of $\mathcal{G}()$ is considered.

Then, we have:

$$\begin{aligned} ||\mathcal{G}(\delta u_l)|| &\leq \{2(q+r)g + q + 5\alpha\}||\delta u_l|| &&= \alpha\{2\epsilon(q+r) + q/\alpha + 5\}||\delta u_l|| \\ ||\mathcal{G}(\delta v_l)|| &\leq \{2qg + q + r + 5\alpha\}||\delta v_l|| &&= \alpha\{2\epsilon q + (q+r)/\alpha + 5\}||\delta v_l|| \end{aligned} \tag{A.1.14}$$

Supposing that $\epsilon \lll 1$, and that $||\delta u_{k\neq -1,0,1}|| \sim \epsilon^{|k|-1}||\delta u_1||, ||\delta u_1|| \sim ||\delta u_0||$ (with

similar scaling for δv_l), we can write $||\mathcal{G}()||$ as:

$$||\mathcal{G}(\delta\boldsymbol{\chi})|| \leq 6\alpha\{2\epsilon(q+r)+(q+r)/\alpha+5\}||\delta u_0|| \leq 6\alpha\{2\epsilon(q+r)+(q+r)/\alpha+5\}||\delta\boldsymbol{\chi}|| \tag{A.1.15}$$

Hence, when defined on a domain X that satisfies the conditions in Eq. eq. (A.1.9), the Jacobian of $\boldsymbol{\mathcal{F}}(\boldsymbol{\chi})$ is Lipschitz continuous with Lipschitz constant $6\alpha\{2\epsilon(q+r)+(q+r)/\alpha+5\}$. The rate of convergence of Newton's method depends on the Lipschitz constant. Moreover, the convergence itself is conditional on the existence of positive real numbers q and r for the space spanning the error in the iterates. But as can be seen from the above equation, as long as ϵ is small and α is large, q and r are allowed to be correspondingly large. Supposing that a δg is chosen such that $(q+r)\epsilon, (q+r)/\alpha \sim 1$, the Lipschitz constant can be approximated as 50α. The factor multiplying α is only approximate, but the observation to be made is that the convergence becomes slower as α of the surface increases (since the Lipschitz constant increases).

A.2 Assumptions on smoothness

'Closeness to exact solution ($\boldsymbol{\chi}^*$)' is given in terms of the norm of the error ($\boldsymbol{e}$). A 'Ball of radius ζ', $\mathbb{B}(\zeta)$ is defined as follows:

$$\boldsymbol{e} := \boldsymbol{\chi} - \boldsymbol{\chi}^*$$
$$\mathbb{B}(\zeta) := \{\boldsymbol{\chi} : ||\boldsymbol{e}|| < \zeta\}$$

Defining a domain based solely on the norm is not a condition that is relevant to the physical system being represented: for instance, an error $\boldsymbol{e}^1$ having most of its energy in modes of wavenumbers -1,0, and 1 is more likely to correspond to a point in phase space that will be visited than an error $\boldsymbol{e}^2$ that has most of its energy in modes of wavenumbers, say, 10,15, and 20. Hence, another domain $X(\zeta, \epsilon)$, that is expected to span the change in iterates ($\delta\boldsymbol{\chi}$, is defined as follows:

$$\delta\boldsymbol{\chi} \in \{\boldsymbol{\chi}^2 - \boldsymbol{\chi}^1 : \boldsymbol{\chi}^1, \boldsymbol{\chi}^2 \in \mathbb{B}(\zeta)\},$$
$$X := \{\delta\boldsymbol{\chi} : \text{Conditions eq. (A.2.1), eq. (A.2.2) are satisfied}\}$$

The following conditions on substituent vectors of $\delta\boldsymbol{\chi}$- which are the streamwise and wall-normal velocity (and the pressure, which does not show here) at wavenumbers $l\alpha$ - are required to be satisfied $\forall\delta\boldsymbol{\chi} \in X$.

$$\forall|l| > 1, i \in \{1,2\}, ||\delta u_l^i|| \sim \epsilon^{|l|-1}||\delta u_{\pm 1}^i|| \sim \epsilon^{|l|-1}||\delta u_0^i||, \tag{A.2.1}$$

which gives the relative scaling of the velocities at different wavenumbers.

$$\begin{aligned}
&\forall l \in \{-n, .., 0, 1, .., n\}, \forall\delta\boldsymbol{\chi} \in X, \forall y \in (-1, 1), \\
&\qquad \exists q \in \mathbb{R}^+ : max_y\{|\frac{d\delta u_l^i}{dy}(y)|\} \leq q(max_y\{|\delta u_l^i(y)|\}), \\
&\forall l \in \{-n, ..., 0, 1, n\}, \forall\delta\boldsymbol{\chi} \in X, \exists r \in \mathbb{R}^+ : ||\frac{d\delta u_l^i}{dy}|| \leq r(||\delta u_l^i||),
\end{aligned} \tag{A.2.2}$$

which is a weaker form of the stronger conditions in Eq. eq. (A.1.9), resulting from the supposed relative scaling. n needs to be chosen based on ϵ. For very small ϵ ($\sim 10^{-4}$) , n=2 should be sufficient.

At this point, no attempts are made to suggest an iterative scheme that implicitly accounts for the above conditions to be satisfied. Instead, the validity of these conditions will be checked after each iteration to ensure that the iterations proceed in a vector-space that satisfies the conditions.

If iterations proceed such that the change in $\boldsymbol{\chi}$ for successive iterations is restricted

to X, then the Jacobian, $\boldsymbol{\mathcal{F}}'(\boldsymbol{\chi})$, is Lipschitz continuous with Lipschitz constant γ:

$$\gamma \leq 6\alpha\{2\epsilon(q+r) + (q+r)/\alpha + 5\} = M\alpha \tag{A.2.3}$$

A.3 Lemmas used for proof of convergence

The following Lemmas are used in demonstrating the convergence of the iterative scheme Eq. eq. (2.5.3). Their proofs may be found in Kelley (1999).

Lemma A.3.1 *For a function $H(\boldsymbol{x})$ continuously differentiable in a domain D, the following equation holds $\forall \boldsymbol{x}^*, \boldsymbol{x} \in D$:*

$$H(\boldsymbol{x}) - H(\boldsymbol{x}^*) = \int_{t=0}^{t=1} H'(\boldsymbol{x}^* + t(\boldsymbol{x} - \boldsymbol{x}^*))(\boldsymbol{x} - \boldsymbol{x}^*)dt \tag{A.3.1}$$

where $H'(\boldsymbol{x})$ is the Jacobian of $H()$.

This is simply the fundamental theorem of calculus expressed in terms of a parameter t.

Definition $B_{N\times N}$ is an approximate inverse of $A_{N\times N}$ if $||I - BA|| < 1$.

Lemma A.3.2 *If A and B are $N \times N$ matrices and B is an approximate inverse of A, then both A and B are both non-singular and*

$$||B^{-1}|| \leq \frac{||A||}{1 - ||I - BA||}, \qquad ||A^{-1}|| \leq \frac{||B||}{1 - ||I - BA||} \tag{A.3.2}$$

Lemma A.3.3 *There exists $\zeta > 0$ so that $\forall x \in \mathbb{B}(\zeta)$*

$$||F'(\boldsymbol{\chi})^{-1}|| \leq 2||\boldsymbol{\mathcal{F}}'(\boldsymbol{\chi}^*)^{-1}|| \tag{A.3.3}$$

This can be shown as a consequence of Lemma theorem A.3.2 if ζ is chosen such that

$$\zeta < \frac{||\boldsymbol{\mathcal{F}}'(\boldsymbol{\chi}^*)^{-1}||^{-1}}{2\gamma} \tag{A.3.4}$$

A.4 Proof of convergence

Here, it is sought to show that for an initial guess sufficiently close to the exact solution, the error for successive iterations decreases at least linearly.

The iterative scheme is

$$\boldsymbol{\chi}^{m+1} = \boldsymbol{\chi}^m - \boldsymbol{\mathcal{F}}'(\boldsymbol{\chi}^m)^{-1}\boldsymbol{\mathcal{F}}(\boldsymbol{\chi}^m)$$

The invertibility of $\boldsymbol{\mathcal{F}}'(\boldsymbol{\chi}^m)$ follows from Lemma theorem A.3.3 if the initial iterate is sufficiently close to the solution (Eq. eq. (A.3.4)).

Subtracting the exact solution $\boldsymbol{\chi}^*$,

$$\begin{aligned}
&\boldsymbol{e}^{m+1} = \boldsymbol{e}^m - \boldsymbol{\mathcal{F}}'(\boldsymbol{\chi}^m)^{-1}\boldsymbol{\mathcal{F}}(\boldsymbol{\chi}^m) \\
\implies &\boldsymbol{e}^{m+1} = \boldsymbol{\mathcal{F}}'(\boldsymbol{\chi}^m)^{-1}\boldsymbol{\mathcal{F}}'(\boldsymbol{\chi}^m)\boldsymbol{e}^m - \boldsymbol{\mathcal{F}}'(\boldsymbol{\chi}^m)^{-1}\boldsymbol{\mathcal{F}}(\boldsymbol{\chi}^m) \\
\implies &\boldsymbol{e}^{m+1} = \boldsymbol{\mathcal{F}}'(\boldsymbol{\chi}^m)^{-1}\{\boldsymbol{\mathcal{F}}'(\boldsymbol{\chi}^m)\boldsymbol{e}^m - \boldsymbol{\mathcal{F}}(\boldsymbol{\chi}^m)\}
\end{aligned}$$

From Lemma theorem A.3.1,

$$\begin{aligned}
&\boldsymbol{e}^{m+1} = \boldsymbol{\mathcal{F}}'(\boldsymbol{\chi}^m)^{-1}\{\boldsymbol{\mathcal{F}}'(\boldsymbol{\chi}^m)\boldsymbol{e}^m - \int_0^1 \boldsymbol{\mathcal{F}}'(\boldsymbol{\chi}^* + t(\boldsymbol{\chi}^m - \boldsymbol{\chi}^*))(\boldsymbol{\chi}^m - \boldsymbol{\chi}^*)dt\} \\
\implies &\boldsymbol{e}^{m+1} = \boldsymbol{\mathcal{F}}'(\boldsymbol{\chi}^m)^{-1}\{\boldsymbol{\mathcal{F}}'(\boldsymbol{\chi}^m)\boldsymbol{e}^m - \int_0^1 \boldsymbol{\mathcal{F}}'(\boldsymbol{\chi}^* + t\boldsymbol{e}^m)\boldsymbol{e}^m dt\} \\
\implies &\boldsymbol{e}^{m+1} = \boldsymbol{\mathcal{F}}'(\boldsymbol{\chi}^m)^{-1}\int_0^1 \{\boldsymbol{\mathcal{F}}'(\boldsymbol{\chi}^m) - \boldsymbol{\mathcal{F}}'(\boldsymbol{\chi}^* + t\boldsymbol{e}^m)\}\boldsymbol{e}^m dt\}
\end{aligned}$$

If the norm of the error is considered,

$$\begin{aligned}
||\boldsymbol{e}^{m+1}|| &= ||\boldsymbol{\mathcal{F}}'(\boldsymbol{\chi}^m)^{-1}\int_0^1 \{\boldsymbol{\mathcal{F}}'(\boldsymbol{\chi}^m) - \boldsymbol{\mathcal{F}}'(\boldsymbol{\chi}^* + t\boldsymbol{e}^m)\}\boldsymbol{e}^m dt\}|| \\
&\leq ||\boldsymbol{\mathcal{F}}'(\boldsymbol{\chi}^m)^{-1}||| \int_0^1 \{\boldsymbol{\mathcal{F}}'(\boldsymbol{\chi}^m) - \boldsymbol{\mathcal{F}}'(\boldsymbol{\chi}^* + t\boldsymbol{e}^m)\}\boldsymbol{e}^m dt\}|| \\
&\leq ||\boldsymbol{\mathcal{F}}'(\boldsymbol{\chi}^m)^{-1}|| \int_0^1 ||\boldsymbol{\mathcal{F}}'(\boldsymbol{\chi}^m) - \boldsymbol{\mathcal{F}}'(\boldsymbol{\chi}^* + t\boldsymbol{e}^m)|||\boldsymbol{e}^m||dt\} \\
&\leq ||\boldsymbol{\mathcal{F}}'(\boldsymbol{\chi}^m)^{-1}|| \int_0^1 \gamma||\boldsymbol{\chi}^m - \boldsymbol{\chi}^* - t\boldsymbol{e}^m|||\boldsymbol{e}^m||dt\}
\end{aligned}$$

$$
\begin{aligned}
&= \gamma||\boldsymbol{\mathcal{F}}'(\boldsymbol{\chi}^m)^{-1}|| \int_0^1 ||\boldsymbol{e}^m - t\boldsymbol{e}^m||||\boldsymbol{e}^m||dt \\
&= \gamma||\boldsymbol{\mathcal{F}}'(\boldsymbol{\chi}^m)^{-1}||||\boldsymbol{e}^m||^2 \int_0^1 (1-t)dt \\
&= \frac{\gamma}{2}||\boldsymbol{\mathcal{F}}'(\boldsymbol{\chi}^m)^{-1}||||\boldsymbol{e}^m||^2 \\
&\leq \gamma||\boldsymbol{\mathcal{F}}'(\boldsymbol{\chi}^*)^{-1}||||\boldsymbol{e}^m||^2
\end{aligned}
$$

Although the error in the $(m+1)^{th}$ step is quadratic in that in the preceding step, it could still lead to divergence if the coefficient, $K = \gamma||\boldsymbol{\mathcal{F}}'(\boldsymbol{\chi}^*)^{-1}||$ is large (or if $||\boldsymbol{e}^m|| > 1$). However, it is possible to show that the error decreases for successive iterations by choosing an appropriate ζ so that $||\boldsymbol{e}^m||$ is small enough. If the ζ for which Lemma theorem A.3.3 is guaranteed to hold is considered (Eq. eq. (A.3.4)),

$$
\begin{aligned}
||\boldsymbol{e}^{m+1}|| &\leq \gamma||\boldsymbol{\mathcal{F}}'(\boldsymbol{\chi}^*)^{-1}||||\boldsymbol{e}^m||^2 \\
&\leq \gamma||\boldsymbol{\mathcal{F}}'(\boldsymbol{\chi}^*)^{-1}||\zeta||\boldsymbol{e}^m|| \\
&< \frac{1}{2}||\boldsymbol{e}^m||
\end{aligned}
$$

If the initial iterate, $\boldsymbol{\chi}^0$ is chosen such that (it satisfies Eq. eq. (A.2.1) and eq. (A.2.2)) and) the error $\boldsymbol{e}^0$ has a norm

$$
||\boldsymbol{e}^0|| \leq \zeta < \frac{||\boldsymbol{\mathcal{F}}'(\boldsymbol{\chi}^*)^{-1}||^{-1}}{2\gamma} = \frac{||\boldsymbol{\mathcal{F}}'(\boldsymbol{\chi}^*)^{-1}||^{-1}}{2M\alpha} \tag{A.4.1}
$$

then all successive iterates also lie in $\mathbb{B}(\zeta)$. And if these iterates also satisfy conditions Eq. eq. (A.2.1) and eq. (A.2.2), then convergence is guaranteed.

A.5 Increment in g

In this subsection, the approach to choosing increments in g is outlined.

Given the exact solution $\boldsymbol{\chi}^*_{g_0}$ at some g_0, an increment in g, δg needs to be chosen such that Eq. eq. (A.4.1) is satisfied. $\boldsymbol{\mathcal{F}}(g, \boldsymbol{\chi})$ may be expected to be a smooth function of g and $\boldsymbol{\chi}$. Using a Taylor expansion for $\boldsymbol{\mathcal{F}}(g, \boldsymbol{\chi})$ about $(g_0, \boldsymbol{\chi}^*_{g_0})$, and using $\boldsymbol{e}^0 = \boldsymbol{\mathcal{F}}(g_0 + \delta g, \boldsymbol{\chi}^*_{g_0+\delta g}) - \boldsymbol{\mathcal{F}}(g_0, \boldsymbol{\chi}^*_{g_0})$, the norm of the error in the initial iterate can be estimated as

$$\begin{aligned}
\boldsymbol{\mathcal{F}}(g_0 + \delta g, \boldsymbol{\chi}^*_{g_0+\delta g}) &\approx \boldsymbol{\mathcal{F}}(g_0, \boldsymbol{\chi}^*_{g_0}) + \frac{\partial \boldsymbol{\mathcal{F}}()}{\partial g}|_{g_0, \boldsymbol{\chi}^*_{g_0}} \delta g + \boldsymbol{\mathcal{F}}'(g_0, \boldsymbol{\chi}^*_{g_0}) \boldsymbol{e}^0 \\
\implies 0 &\approx 0 + \frac{\partial \boldsymbol{\mathcal{F}}()}{\partial g}|_{g_0, \boldsymbol{\chi}^*_{g_0}} \delta g + \boldsymbol{\mathcal{F}}'(g_0, \boldsymbol{\chi}^*_{g_0}) \boldsymbol{e}^0 \\
\implies \frac{\partial \boldsymbol{\mathcal{F}}()}{\partial g}|_{g_0, \boldsymbol{\chi}^*_{g_0}} \delta g &\approx -\boldsymbol{\mathcal{F}}'(g_0, \boldsymbol{\chi}^*_{g_0}) \boldsymbol{e}^0 \\
\implies \boldsymbol{e}^0 &\approx \{-\boldsymbol{\mathcal{F}}'(g_0, \boldsymbol{\chi}^*_{g_0})\}^{-1} \frac{\partial \boldsymbol{\mathcal{F}}()}{\partial g}|_{g_0, \boldsymbol{\chi}^*_{g_0}} \delta g \\
\implies ||\boldsymbol{e}^0|| &\approx ||\{\boldsymbol{\mathcal{F}}'(g_0, \boldsymbol{\chi}^*_{g_0})\}^{-1} \frac{\partial \boldsymbol{\mathcal{F}}()}{\partial g}|_{g_0, \boldsymbol{\chi}^*_{g_0}}|| |\delta g|
\end{aligned}$$

Eq. eq. (A.4.1) is (approximately) satisfied if the right hand side of the above (approximate) equation is less than the limit upper bound on $||\boldsymbol{e}^0||$ specified in Eq. eq. (A.4.1). Then, an upper limit on $|\delta g|$ that guarantees convergence can be given as

$$|\delta g| \lessapprox \frac{1}{||\{\boldsymbol{\mathcal{F}}'(g_0, \boldsymbol{\chi}^*_{g_0})\}^{-1} \frac{\partial \boldsymbol{\mathcal{F}}()}{\partial g}|_{g_0, \boldsymbol{\chi}^*_{g_0}}||} \frac{||\boldsymbol{\mathcal{F}}'(\boldsymbol{\chi}^*)^{-1}||^{-1}}{2M\alpha} \tag{A.5.1}$$

A.5.1 g-derivative of F

Eq. eq. (A.5.1) suggests an upper bound on the increment in δg for guaranteed convergence (given some conditions). The expression for this upper bound involves the norm of the derivative of $\boldsymbol{\mathcal{F}}()$ with respect to the scalar g. In this subsection, the blocks that make up this derivative matrix are calculated from the definition of $\boldsymbol{\mathcal{F}}()$.

$$\frac{\partial \boldsymbol{\mathcal{F}}}{\partial g} = \frac{\partial}{\partial g}(L(g)\boldsymbol{\chi} + 0.5\mathcal{G}(g, \boldsymbol{\chi})\boldsymbol{\chi} - \boldsymbol{f}) = \frac{\partial \mathcal{L}}{\partial g}\boldsymbol{\chi} + 0.5\frac{\partial \mathcal{G}}{\partial g}\boldsymbol{\chi}$$

The g-derivatives of $\mathcal{L}(g)$ and $\mathcal{G}(g, \boldsymbol{\chi})$ can be obtained from the definition of these

matrix operators, or they can be obtained much more simply by noting that g appears in these matrices only as coefficients g, g^2. So, the matrices can be split as follows:

$$\begin{aligned}\mathcal{L}(g) &=: \tilde{\mathcal{L}}_0 + g\tilde{\mathcal{L}}_1 + g^2\tilde{\mathcal{L}}_2 \\ \mathcal{G}(g,\boldsymbol{\chi}) &=: \tilde{\mathcal{G}}_0(\boldsymbol{\chi}) + g\tilde{\mathcal{G}}_1(\boldsymbol{\chi})\end{aligned}$$

From the definitions, it can be seen that

$$\begin{aligned}\tilde{\mathcal{L}}_0 &= \mathcal{L}(g=0) \\ \tilde{\mathcal{L}}_1 &= \frac{1}{2}\{\mathcal{L}(1) - \mathcal{L}(-1)\} \\ \tilde{\mathcal{L}}_2 &= \frac{1}{2}\{\mathcal{L}(1) + \mathcal{L}(-1) - 2\mathcal{L}(0)\} \\ \tilde{\mathcal{G}}_0(\boldsymbol{\chi}) &= \mathcal{G}(0,\boldsymbol{\chi}) \\ \tilde{\mathcal{G}}_1(\boldsymbol{\chi}) &= \frac{1}{2}\{\mathcal{G}(1,\boldsymbol{\chi}) - \mathcal{G}(-1,\boldsymbol{\chi})\}\end{aligned} \tag{A.5.2}$$

Then, the g-derivatives of $\mathcal{L}$ and $\mathcal{G}$ are given as

$$\begin{aligned}\frac{\partial\mathcal{L}}{\partial g} &= \mathcal{L}(0) + \frac{g}{2}\{\mathcal{L}(1) - \mathcal{L}(-1)\} + \frac{g^2}{2}\{\mathcal{L}(1) + \mathcal{L}(-1) - 2\mathcal{L}(0)\} \\ \frac{\partial\mathcal{G}}{\partial g} &= \mathcal{G}(0,\boldsymbol{\chi}) + \frac{g}{2}\{\mathcal{G}(1,\boldsymbol{\chi}) - \mathcal{G}(-1,\boldsymbol{\chi})\}\end{aligned} \tag{A.5.3}$$

Appendix B

Analytical laminar solutions for long wavelength grooves

B.1 Channel flow with longitudinal grooves

We seek solutions that have zero wall-normal and spanwise velocities, and are homogeneous in the streamwise direction. This simplifies the governing equations to the Poisson equation,

$$\Delta u = -2, \tag{B.1.1}$$

with boundary conditions

$$u(y = \pm 1 + 2\epsilon\cos(\beta z)) = 0, \tag{B.1.2}$$

where $\epsilon = A/2$ is half the amplitude of the groove. The advection term is exactly zero, and so is the streamwise derivative of the fluctuating pressure. The (non-dimensional) solutions are also Re-invariant. The above equation can be written for each Fourier mode in the transformed domain as

$$-\epsilon^2\beta^2 u''_{k-2} + (2k-1)\epsilon\beta^2 u'_{k-1} - k^2\beta^2 u_k + (1+2\epsilon^2\beta^2)u''_k + (-2k-1)\epsilon\beta^2 u'_{k+1} - \epsilon^2\beta^2 u''_{k+2} = -2\delta_{0k}, \tag{B.1.3}$$

The term on the RHS represents the mean pressure gradient that drives the flow, and δ_{0k} is the Kroenecker delta.

We make the following assumptions in the derivation:

$$\begin{aligned} \forall k, \qquad & u_k', u_k'' \sim u_k, \\ \forall k \neq 0, \qquad & u_k \sim \beta^m, \qquad \text{with } m \geq 1. \end{aligned} \tag{B.1.4}$$

These are reasonable assumptions for the smooth velocity profiles of laminar flows in long wavelength grooves. We shall see that the solution enforces the validity of these assumptions.

Solutions such as the present one are often derived to be first-order accurate (i.e., $\mathcal{O}(\beta)$ in this case). However, the in-phase arrangement of the top and bottom walls allows use to derive solutions that are accurate to $\mathcal{O}(\beta^2)$. We ignore all $O(\beta^3)$ terms in the equation. For $k = 0$, this approximation leads to

$$(1 + 2\epsilon^2\beta^2)u_0'' = -2.$$

Integrating along with the boundary conditions produces

$$u_0 = (1 - 2\epsilon^2\beta^2)(1 - Y^2). \tag{B.1.5}$$

For $k = 1$, the approximated equation is

$$u_1'' = -\epsilon\beta^2 u_0' \approx 2\epsilon\beta^2 Y,$$

which, on integration with the boundary conditions, gives

$$u_1 = \frac{\epsilon\beta^2}{3}(Y^3 - Y). \tag{B.1.6}$$

For $k = 2$, the Poisson equation is

$$u_2'' = \epsilon^2\beta^2 u_0'' \approx -2\epsilon^2\beta^2.$$

On integration, we get

$$u_2 = \epsilon^2\beta^2(1 - Y^2). \tag{B.1.7}$$

All higher modes are $O(\beta^3)$ or higher, so we ignore these modes.

The solution is

$$\begin{aligned} u_0 &= (1 - 2\epsilon^2\beta^2)(1 - Y^2), \\ u_1 &= \frac{\epsilon\beta^2}{3}(Y^3 - Y), \\ u_2 &= \epsilon^2\beta^2(1 - Y^2). \end{aligned} \tag{B.1.8}$$

On summation, this gives

$$u(Y, Z) = (1 - 2\epsilon^2\beta^2)(1 - Y^2) + \frac{2\epsilon\beta^2}{3}(Y^3 - Y)\cos(\beta Z) + 2\epsilon^2\beta^2(1 - Y^2)\cos(2\beta Z). \tag{B.1.9}$$

The average shear strain-rate, averaged over spanwise length, on the bottom wall can be calculated as

$$\overline{\frac{\partial u}{\partial n}} = (1 + 2\epsilon^2\beta^2)u_{0,W}' - \epsilon\beta^2\Re(u_{1,W}) - \epsilon^2\beta^2\Re(u_{2,W}'), \tag{B.1.10}$$

where $\Re(f)$ represents the real part of f.

For the current case of small wavenumbers $\beta \ll 1$, this becomes

$$\overline{\frac{\partial u}{\partial n}} = 2(1 - 4\epsilon^4\beta^4) + 2\epsilon^4\beta^4 \approx 2, \tag{B.1.11}$$

which is the same as the average shear stress for a flat channel flow. So, within the accuracy of the solution ($O(\beta^2)$), we see no difference in the average shear strain rate (consequently the shear stress) for flat and grooved channel flows when $\beta \ll 1$. This is to be expected; grooved channels do not produce a pressure drag, so the driving force

due to the mean pressure gradient has to be balanced by only the shear force. Since we hold the mean pressure gradient to be constant for flat channels and grooved channels, the average shear stress at the wall must also be constant for different geometries.

B.2 Channel flow with transverse grooves

We now derive an approximate solution for the case of small wavenumbers, under the restriction of low Re so that the advection term can be neglected. As with the rest of the work in the paper, we use a domain transformation method, and express velocities and pressure as a Fourier series in the transformed domain. x, y are the physical coordinates, and X, Y are the coordinates in the transformed domain. We define $\epsilon = A/2$ to refer the semi-amplitude of the furrows. The walls are given by

$$y_{walls} = \pm 1 + 2\epsilon \cos(\alpha x) = \pm 1 + \epsilon(e^{i\alpha x} + e^{-i\alpha x})$$

The governing equations in the physical system $x - y$ are

$$\begin{aligned} -Re\partial_x p + \Delta u &= -2, \\ -Re\partial_y p + \Delta v &= 0, \\ \partial_x u + \partial_y v &= 0, \end{aligned} \tag{B.2.1}$$

with boundary conditions

$$\begin{aligned} u(y = \pm 1 + 2\epsilon \cos(\alpha x)) &= 0, \\ v(y = \pm 1 + 2\epsilon \cos(\alpha x)) &= 0, \\ (\partial_x u + \partial_y v)(y = \pm 1 + 2\epsilon \cos(\alpha x)) &= 0. \end{aligned} \tag{B.2.2}$$

B.2.1 Flow Symmetry

The governing equations in the transformed domain $X - Y$ are

$$u\partial_X u + uT_x\partial_Y u + v\partial_Y u = -\partial_X p - T_x\partial_Y p + \frac{1}{Re}(\partial_{XX} + 2T_x\partial_{XY} + T_{xx}\partial_Y + T_x^2\partial_{YY} + \partial_{YY})u,$$
$$u\partial_X v + uT_x\partial_Y v + v\partial_Y v = -\partial_Y p + \frac{1}{Re}(\partial_{XX} + 2T_x\partial_{XY} + T_{xx}\partial_Y + T_x^2\partial_{YY} + \partial_{YY})v,$$
$$\partial_X u + T_x\partial_Y u + \partial_Y v = 0,$$

where

$$Y = T(x, y) = y - \epsilon(e^{i\alpha x} + e^{-i\alpha x})$$

is the transformation function of the domain transformation of fig. 2.2, and T_x, T_{xx} are its partial derivatives along x.

We apply a shift along X and a inversion along Y to obtain new coordinates (X', Y') as

$$\begin{aligned} X' = S_{\pi/\alpha}(X) = &\quad X + \frac{\pi}{\alpha}, && \text{(Shift by } \pi/\alpha), \\ Y' = R_0(Y) = &\quad -Y && \text{(Invert across } Y = 0). \end{aligned} \tag{B.2.3}$$

Partial derivatives in the two coordinate systems relate as

$$\partial_X = \partial_{X'},$$
$$\partial_Y = -\partial_{Y'},$$

while derivatives of the transformation function T appearing in the governing equations relate as

$$\partial_x T(X, Y) = -\partial_x T(X', Y'),$$
$$\partial_{xx} T(X, Y) = -\partial_{xx} T(X', Y'),$$
$$(\partial_x T)^2(X, Y) = (\partial_x T)^2(X', Y').$$

It can be seen that the governing equations are invariant under the shift-invert

operation of eq. (B.2.3) when the flow variables u, v, and p relate as

$$\begin{aligned} u(X', Y') &= u(X, Y), \\ v(X', Y') &= -v(X, Y), \\ p(X', Y') &= p(X, Y). \end{aligned} \tag{B.2.4}$$

The boundary conditions in both systems are

$$\begin{aligned} &u(Y = \pm 1) = 0, \qquad v(Y = \pm 1), \qquad \nabla \cdot \boldsymbol{u}(Y = \pm 1) = 0, \\ &u(Y' = \pm 1) = 0, \qquad v(Y' = \pm 1), \qquad \nabla \cdot \boldsymbol{u}(Y' = \pm 1) = 0. \end{aligned}$$

Hence, we expect the equations to admit solutions with the symmetry of eq. (B.2.4). The laminar solution for flat-walled channel flow trivially satisfies this symmetry.

We can see the consequence of this symmetry by reverting to $X - Y$ coordinates,

$$\begin{aligned} u(X, Y) &= u(X + \pi/\alpha, -Y), \\ v(X, Y) &= -v(X + \pi/\alpha, -Y), \\ p(X, Y) &= p(X + \pi/\alpha, -Y), \end{aligned} \tag{B.2.5}$$

and expanding the velocities as Fourier series,

$$\begin{aligned} \sum_{k \in \mathbb{Z}} u_k(Y) e^{ik\alpha X} &= \sum_{k \in \mathbb{Z}} u_k(-Y) e^{ik\alpha(X + \pi/\alpha)} \\ &= \sum_{k \in \mathbb{Z}} (-1)^k u_k(-Y) e^{ik\alpha X}. \end{aligned}$$

The above equation holds for all X, so the coefficients of individual Fourier modes can be matched. The coefficients can be similarly matched for v and p, leading to

$$\begin{aligned} u_k(Y) &= (-1)^k u_k(-Y), \\ v_k(Y) &= (-1)^{k+1} v_k(-Y), \\ p_k(Y) &= (-1)^k p_k(-Y). \end{aligned} \tag{B.2.6}$$

The coefficients $u_{2k}(Y), v_{2k+1}(Y), p_{2k}(Y)$ are even functions in Y, and $u_{2k+1}, v_{2k}(Y), p_{2k+1}(Y)$ are odd. We use this result later to fix the values for pressure modes at the wall.

B.2.2 Exact governing equations for each Fourier mode

The governing equations, for each Fourier mode k, are

Continuity equation:

$$\begin{aligned} -i\epsilon\alpha u'_{k-1} + ik\alpha u_k + i\epsilon\alpha u'_{k+1} + v'_k = 0 \\ \implies i\epsilon\alpha u'_{k-1} - ik\alpha u_k - i\epsilon\alpha u'_{k+1} = v'_k, \end{aligned} \tag{B.2.7}$$

where f'_k denotes the Y-derivative of the k^{th} Fourier mode of the field f.

X-momentum equation:

$$\begin{aligned} -\epsilon^2\alpha^2 u''_{k-2} + \epsilon\alpha^2(2k-1)u'_{k-1} - k^2\alpha^2 u_k + (1+2\epsilon^2\alpha^2)u''_k \\ -\epsilon^2\alpha^2 u''_{k+2} + \epsilon\alpha^2(-2k-1)u'_{k+1} = Re\{-i\epsilon\alpha p'_{k-1} + ik\alpha p_k + i\epsilon\alpha p'_{k+1}\} - 2\delta_{0k}. \end{aligned} \tag{B.2.8}$$

The last term in the RHS, $-2\delta_{0k}$, represents the mean pressure gradient that drives the flow, where δ_{0k} is the Kroenecker delta.

Y-momentum equation:

$$\begin{aligned} -\epsilon^2\alpha^2 v''_{k-2} + \epsilon\alpha^2(2k-1)v'_{k-1} - k^2\alpha^2 v_k + (1+2\epsilon^2\alpha^2)v''_k \\ -\epsilon^2\alpha^2 v''_{k+2} + \epsilon\alpha^2(-2k-1)v'_{k+1} = Rep'_k. \end{aligned} \tag{B.2.9}$$

The derivation shall proceed as follows: First, we express all wall-normal velocity modes in terms of streamwise velocity modes using the continuity equation. We substitute these expressions for v in the wall-normal momentum equations, leading to equations that relate derivatives of pressure to streamwise velocity modes. We then substitute the pressure terms in streamwise momentum equations with the expressions obtained in the previous step. We seek solutions that satisfy the symmetries in eq. (B.2.6); the symmetries allow us to calculate the values of pressure modes

at the wall. Finally, we introduce a few simplifying assumptions that enable us to solve the equations. However, making all these substitutions produces equations that are rather long, so we reduce the equations to approximate forms before making the substitutions.

B.2.3 Approximate equations

We make the following two assumptions:

$$\begin{aligned} \forall k, \qquad & u_k' \sim u_k, \\ \forall k \neq 0, \qquad & u_k \sim \alpha^m, \qquad \text{with } m \geq 1. \end{aligned} \tag{B.2.10}$$

The first assumption can be seen as a consequence of the smoothness of velocity modes that we expect in a laminar flow. This assumption is valid for the wall-normal velocity too, but not for pressure, because pressure modes could have a non-zero value at the walls. The second assumption can be justified by considering all modes $u_{k\neq 0}$ as perturbations about the solution for a flat channel flow. It is reasonable to suppose that these perturbations scale at least linearly (probably super-linearly) with the wavenumber α. In fact, from the streamwise momentum equation, eq. (B.2.8), we can see that all $u_{k\neq 0}$ scale as α^2 or higher.

We shall ignore all terms that are $O(\alpha^3)$ and higher. Following the assumption in eq. (B.2.10), we can ignore all $\alpha^2 u_k, \alpha^2 u_k', \alpha^2 u_k''$ terms for $k \neq 0$. From eq. (B.2.7), we can infer that all v_k, v_k', v_k'' also scale as $\alpha^m, m \geq 1$. All terms except one in the LHS of eqs. (B.2.8) and (B.2.9) have an α^2 factor, so they are ignored except when the terms involve u_0, u_0', or u_0''. With these simplifications, the y-momentum equation eq. (B.2.9) can be approximated as

$$v_k'' = Rep_k'. \tag{B.2.11}$$

We substitute eq. (B.2.7) in eq. (B.2.11) to obtain the (derivatives of) pressure

modes in terms of streamwise velocities as

$$i\epsilon\alpha u''_{k-1} - ik\alpha u'_k - i\epsilon\alpha u''_{k+1} = Rep'_k. \tag{B.2.12}$$

Now, we work through eq. (B.2.8) for each k. All $O(\alpha^3)$ terms are ignored. The approximated equation for $k = 0$ is

$$(1 + 2\epsilon^2\alpha^2)u''_0 = Re\{-i\epsilon\alpha p'_{-1} + i\epsilon\alpha p'_1\} - 2.$$

Substituting eq. (B.2.12), and ignoring $O(\alpha^3)$ terms, we have

$$\begin{aligned}(1 + 2\epsilon^2\alpha^2)u''_0 &= -2 - i\epsilon\alpha\{(i\epsilon\alpha u''_{-2} + i\alpha u'_{-1} - i\epsilon\alpha u''_0) - (i\epsilon\alpha u''_0 - i\alpha u'_1 - i\epsilon\alpha u''_2)\} \\ &\approx -2 - 2\epsilon^2\alpha^2 u''_0.\end{aligned}$$

Integrating the above equation with boundary conditions $u_0(Y = \pm 1) = 0$, produces

$$u_0 = \frac{1}{1 + 4\epsilon^2\alpha^2}(1 - Y^2) \approx (1 - 4\epsilon^2\alpha^2)(1 - Y^2). \tag{B.2.13}$$

For $k = 1$, eq. (B.2.8) is approximated as

$$\begin{aligned}\epsilon\alpha^2 u'_0 + u''_1 &= Re\{-i\epsilon\alpha p'_0 + i\alpha p_1 + i\epsilon\alpha p'_2\} \\ &= i\alpha Rep_1 - i\epsilon\alpha(i\epsilon\alpha u''_{-1} - i\epsilon\alpha u''_1 - i\epsilon\alpha u''_1 + 2i\alpha u'_2 + i\epsilon\alpha u''_3) \\ &\approx i\alpha Rep_1.\end{aligned}$$

We shall write all pressure modes p_k in terms of the pressure at the bottom wall ($Y = -1$) as

$$p_k = p_{k,W} + \int_{\eta=-1}^{Y} p'_k(\eta)d\eta.$$

$p_{k,W}$ is not known. We shall see that this does not pose a problem. Substituting the

express for p_1 in the approximate momentum equation, we get

$$\begin{aligned}
\epsilon\alpha^2 u_0' + u_1'' &\approx i\alpha Rep_{1,W} + i\alpha \int_{\eta=-1}^{Y} Rep_1'(\eta)d\eta \\
&= i\alpha Rep_{1,W} + i\alpha \int_{\eta=-1}^{Y} (i\epsilon\alpha u_0'' - i\alpha u_1' - i\epsilon\alpha u_2'')d\eta \\
&\approx i\alpha Rep_{1,W} - \epsilon\alpha^2(u_0' - u_{0,W}') \\
\implies u_1'' &= i\alpha Rep_{1,W} + 4\epsilon\alpha^2(1 - 4\epsilon^2\alpha^2)Y + 2\epsilon\alpha^2(1 - 4\epsilon^2\alpha^2) \\
&\approx i\alpha Rep_{1,W} + 4\epsilon\alpha^2 Y + 2\epsilon\alpha^2.
\end{aligned}$$

We define $C_1 = i\alpha Rep_{1,W} + 2\epsilon\alpha^2$ to write

$$u_1'' = 4\epsilon\alpha^2 Y + C_1.$$

Integrating the above equation produces

$$u_1 = \frac{2\epsilon\alpha^2}{3}Y^3 + \frac{C_1}{2}Y^2 + C_2 Y + C_3.$$

From eq. (B.2.6), $u_1(Y)$ must be an odd function, implying that C_1 and C_3 should be zero. The boundary conditions fix C_2 to give

$$u_1 = \frac{2\epsilon\alpha^2}{3}(Y^3 - Y). \tag{B.2.14}$$

From C_1 being zero, we also get

$$Rep_{1,W} = 2i\epsilon\alpha. \tag{B.2.15}$$

We shall return to this equation later when calculating the pressure drag.

The approximated streamwise momentum equation for $k = 2$ is

$$-\epsilon^2\alpha^2 u_0'' + u_2'' = Re\{-i\epsilon\alpha p_1' + 2i\alpha p_2 + i\epsilon\alpha p_3'\}.$$

Equation (B.2.12) shows that Rep_2', Rep_3' are $O(\alpha^3)$, while the leading term in p_1' has $\alpha u_0''$. However, the equation above contains p_2 and not p_2'. As before, we write the pressure as a sum of its value at the wall and an integral from the wall as

$$p_2(Y) = p_{2,W} + \int_{\eta=-1}^{Y} p_2'(\eta) d\eta. \tag{B.2.16}$$

The integral is ignored, because $p_2' \sim \alpha^3$. Then, $p_2(Y) \approx p_{2,W}$. Substituting the appropriate expressions for pressure modes,

$$\begin{aligned} -\epsilon^2\alpha^2 u_0'' + u_2'' &= -i\epsilon\alpha(i\epsilon\alpha u_0'' - i\alpha u_1' - i\epsilon\alpha u_2'') + 2i\alpha Rep_{2,W} \\ \implies u_2'' &\approx 2\epsilon^2\alpha^2 u_0'' + 2i\alpha Rep_{2,W} \\ &= (-4\epsilon^2\alpha^2)(1 - 4\epsilon^2\alpha^2) + 2i\alpha Rep_{2,W} \\ &\approx -4\epsilon^2\alpha^2 + 2i\alpha Rep_{2,W}. \end{aligned}$$

We define $C_4 = -4\epsilon^2\alpha^2 + 2i\alpha Rep_{2,W}$, and integrate the equation along with boundary conditions $u_2(Y = \pm 1) = 0$ to get

$$u_2 = \frac{C_4}{2}(1 - Y^2). \tag{B.2.17}$$

To calculate C_4, we consider the divergence-free condition for mode $k = 2$,

$$v_2' = i\epsilon\alpha u_1' - 2i\alpha u_2 - i\epsilon\alpha u_3'.$$

Integrating the equation from the -1 to 1, we get

$$v_2(1) - v_2(-1) = i\epsilon\alpha\{u_1(1) - u_1(-1)\} - i\epsilon\alpha\{u_3(1) - u_3(-1)\} - 2i\alpha \int_{Y=-1}^{1} u_2(Y) dY.$$

All velocity modes are zero at the boundaries, so we have

$$\begin{aligned} \int_{Y=-1}^{1} u_2(Y) &= 0 \\ \implies \frac{C_4}{2}\left[Y - \frac{Y^3}{3}\right]_{-1}^{1} &= 0 \\ \implies \frac{C_4}{2}\frac{4}{3} &= 0 \\ \implies C_4 &= 0. \end{aligned}$$

This leads to

$$u_2 = 0, \tag{B.2.18}$$

and

$$p_{2,W} = \frac{-2i\epsilon^2\alpha}{Re}. \tag{B.2.19}$$

The approximated streamwise momentum equation for $k = 3$ is

$$u_3'' = Re(-i\epsilon\alpha p_2' + 3i\alpha p_3 + i\epsilon\alpha p_4').$$

$\alpha Rep_2', \alpha Rep_3'$, and $\alpha Rep_4'$ are all $O(\alpha^3)$ or higher. So, the only term that needs to be retained in the RHS is $3i\alpha Rep_{3,W}$, producing

$$u_3'' = 3i\alpha Rep_{3,W}.$$

Integrating with the boundary conditions results in

$$u_3 = \frac{3i\alpha Rep_{3,W}}{2}(1 - Y^2).$$

Referring to the symmetries again (eq. (B.2.6)), we see that u_3 must be an odd function in Y. The coefficients of all even powers of Y must be zero. This leads to

$$u_3 = 0, \tag{B.2.20}$$

$$p_{3,W} = 0. \tag{B.2.21}$$

It can be shown that modes u_k for $k > 3$ scale as α^m, where $m \geq 3$, so we ignore all these modes. We have only derived u_k for $k \geq 0$. The negative modes have to be complex conjugates of the positive modes, so that the flowfield remains real-valued.

$$u_k = \text{Conj}(u_{-k}). \tag{B.2.22}$$

The wall-normal velocities are calculated by substituting the streamwise velocities in eq. (B.2.7), producing,

for k=0:

$$\begin{aligned} v_0' &= i\epsilon\alpha u_{-1}' - i\epsilon\alpha u_1' = -i\epsilon\alpha(u_1' - \text{Conj}(u_{-1}')) = 0 \\ \implies v_0 &= 0, \end{aligned}$$

for k=1:

$$\begin{aligned} v_1' &= i\epsilon\alpha u_0' - i\alpha u_1 - i\epsilon\alpha u_2' \\ &= -2i\epsilon\alpha Y - i\alpha\frac{2\epsilon\alpha^2}{3}(Y^3 - Y) - i\epsilon\alpha(2\epsilon^2\alpha^2)(-2Y) \\ &= (-i\alpha\frac{2\epsilon\alpha^2}{3})Y^3 + (-2i\epsilon\alpha - i\alpha\frac{2\epsilon\alpha^2}{3} + 2i\epsilon\alpha(2\epsilon^2\alpha^2))Y \quad \approx -2i\epsilon\alpha Y \\ \implies v_1 &= i\epsilon\alpha(1 - Y^2), \end{aligned}$$

for k=2:

$$\begin{aligned} v_2' &= i\epsilon\alpha u_1' - 2i\alpha u_2 - i\epsilon\alpha u_3' \\ &= i\epsilon\alpha u_1' \\ \implies v_2 &= i\epsilon\alpha u_1 = \frac{2i\epsilon^2\alpha^3}{3}(Y^3 - Y) \approx 0, \end{aligned}$$

and for k=3:

$$\begin{aligned} v_3' &= i\epsilon\alpha u_2' - 3i\alpha u_3 - i\epsilon\alpha u_4' \\ &= 0 \\ \implies v_3 &= 0. \end{aligned}$$

It can be shown that all higher modes $v_{k>3}$ are $O(\alpha^3)$ or higher, so we ignore these modes.

Finally, we retrieve the pressure modes from eq. (B.2.12). For mode $k = 0$, the value at the wall can be arbitrarily chosen; we set this to zero. For modes $k = 1$ and $k = 2$, the values at the wall are given by eqs. (B.2.15) and (B.2.19). Modes for $k > 2$ are zero (up to $O(\alpha^2)$).

Pressure mode $k = 0$:

$$\begin{aligned} p_0(Y) &= p_{0,W} + \int_{\eta=-1}^{Y} p_0'(\eta)d\eta \\ &= 0 - \int_{\eta=-1}^{Y} i\epsilon\alpha(u_1'' - u_{-1}'')d\eta \\ &= 0. \end{aligned}$$

Pressure mode $k = 1$:

$$\begin{aligned} p_1(Y) &= p_1(Y=-1) + \int_{\eta=-1}^{Y} p_1'(\eta)d\eta \\ &= \frac{2i\epsilon\alpha}{Re} + \frac{i\alpha}{Re}\int_{\eta=-1}^{Y}(\epsilon u_0'' - u_1' - \epsilon u_2'')d\eta \\ &= \frac{2i\epsilon\alpha}{Re} + \frac{i\alpha}{Re}\{\epsilon\left[u_0'\right]_{-1}^{Y} - \left[u_1\right]_{-1}^{Y}\} \\ &= \frac{2i\epsilon\alpha}{Re} + \frac{i\alpha}{Re}\{\epsilon(-2Y-2) - \frac{2\epsilon\alpha^3}{3}(Y^3 - Y)\} \\ &\approx \frac{-2i\epsilon\alpha}{Re}Y. \end{aligned}$$

Pressure mode $k = 2$:

$$\begin{aligned} p_2(Y) &= p_2(Y=-1) + \int_{\eta=-1}^{Y} p_2'(\eta)d\eta \\ &= \frac{-2i\epsilon^2\alpha}{Re} + \frac{1}{Re}\int_{\eta=-1}^{Y}(3i\epsilon^2\alpha^3 u_0' + i\epsilon\alpha u_1'' - 2i\alpha u_2' - i\epsilon\alpha u_3'')d\eta \\ &= \frac{-2i\epsilon^2\alpha}{Re} + \frac{3i\epsilon^2\alpha^3}{Re}\int_{\eta=-1}^{Y} u_0' d\eta + \frac{i\epsilon\alpha}{Re}\int_{\eta=-1}^{Y} u_1'' d\eta \\ &\approx \frac{-2i\epsilon^2\alpha}{Re}. \end{aligned}$$

B.2.4 Solution

Finally, the significant modes (up to $O(\alpha^2)$) are

$$\begin{aligned} u_0 &= (1-4\epsilon^2\alpha^2)(1-Y^2), & u_1 &= \frac{2\epsilon\alpha^2}{3}(Y^3-Y), & u_2 &= 0, \\ v_0 &= 0, & v_1 &= i\epsilon\alpha(1-Y^2), & v_2 &= 0, \\ p_0 &= 0, & p_1 &= \frac{-2i\epsilon\alpha}{Re}Y, & p_2 &= \frac{-2i\epsilon^2\alpha}{Re}. \end{aligned} \tag{B.2.23}$$

When the Fourier modes are added, we have

$$\begin{aligned} u(X,Y) &= (1-4\epsilon^2\alpha^2)(1-Y^2) + \frac{4\epsilon\alpha^2}{3}(Y^3-Y)\cos(\alpha X), \\ v(X,Y) &= -2\epsilon\alpha(1-Y^2)\sin(\alpha X), \\ p(X,Y) &= \frac{4\epsilon\alpha}{Re}Y\sin(\alpha X) + \frac{4\epsilon^2\alpha}{Re}\sin(2\alpha X). \end{aligned} \tag{B.2.24}$$

B.2.5 Pressure drag

For the wavy channel geometry considered in the present work, the non-dimensional drag force due to pressure (along the streamwise) per unit planform area acting on one wall can be shown to be

$$\frac{\delta F_{p,x}}{\delta A_{plan}} = -i\epsilon\alpha(p_{1,W} - p_{-1,W}).$$

Appendix B.4 presents the derivation for pressure drag in channels with oblique grooves. The above equation is obtained by setting $\beta = 0$ in the oblique case.

For the the low wavenumber case with $Re \ll 1$, for both walls, this becomes

$$\frac{\delta F_{p,x}}{\delta A_{plan}} = \frac{8\epsilon^2\alpha^2}{Re}. \tag{B.2.25}$$

The pressure drag acts along the x axis on the channel walls, and along $-x$ on the fluid flow. The non-dimensional driving force due to the mean pressure gradient (on

the fluid flow) is

$$\frac{\delta F_{driving}}{\delta A_{plan}} = \frac{4}{Re}.$$

Then, the pressure drag as a fraction of the driving force is

$$\frac{F_{p,x}}{F_{driving}} = 2\epsilon^2\alpha^2. \tag{B.2.26}$$

B.3 Channel flow with oblique grooves

When the Reynolds number is low enough for the advection term to be negligible, the linear problem for oblique waviness can be expressed as a superposition of a streamwise-wavy channel problem and a grooved channel problem; the current section addresses this decomposition. We discuss the problem in the physical domain, the (x, y) coordinates, instead of the transformed domain.

For oblique waviness, we seek solutions that are periodic along the direction defined by the wavenumber vector (α, β), and homogeneous in the direction parallel to it. We obtain a new (Cartesian) coordinate system by rotating along the y-axis,

$$\begin{aligned} \hat{\boldsymbol{e}}_\xi &= \frac{\alpha}{\gamma}\hat{\boldsymbol{e}}_x + \frac{\beta}{\gamma}\hat{\boldsymbol{e}}_z, \\ \hat{\boldsymbol{e}}_\eta &= \frac{-\beta}{\gamma}\hat{\boldsymbol{e}}_x + \frac{\alpha}{\gamma}\hat{\boldsymbol{e}}_z, \end{aligned} \tag{B.3.1}$$

where $\gamma = \sqrt{\alpha^2 + \beta^2}$. In the new coordinate system $\xi - y - \eta$, we seek solutions that are periodic along $\hat{\boldsymbol{e}}_\xi$ with period $2\pi/\gamma$, and homogeneous along $\hat{\boldsymbol{e}}_\eta$. We identify velocity components along ξ, y, η as u_ξ, v, u_η respectively.

The governing equations are

$$\begin{aligned} -Re\boldsymbol{\nabla}p + \Delta\boldsymbol{u} &= -2\hat{\boldsymbol{e}}_x, \\ \boldsymbol{\nabla}\cdot\boldsymbol{u} &= 0, \end{aligned} \tag{B.3.2}$$

with boundary conditions

$$\begin{aligned} \boldsymbol{u}(y = \pm 1 + 2\epsilon\cos(\gamma\xi)) &= 0, \\ \boldsymbol{\nabla}\cdot\boldsymbol{u}(y = \pm 1 + 2\epsilon\cos(\gamma\xi)) &= 0. \end{aligned} \tag{B.3.3}$$

The governing equations in eq. (B.3.2) can be rewritten as

$$-Re\partial_\xi p\hat{\boldsymbol{e}}_\xi - Re\partial_y p\hat{\boldsymbol{e}}_y - Re\partial_\eta p\hat{\boldsymbol{e}}_\eta + \Delta u_\xi\hat{\boldsymbol{e}}_\xi + \Delta v\hat{\boldsymbol{e}}_y + \Delta u_\eta\hat{\boldsymbol{e}}_\eta = -2(\frac{\alpha}{\gamma}\hat{\boldsymbol{e}}_\xi - \frac{\beta}{\gamma}\hat{\boldsymbol{e}}_\eta)$$
$$\partial_\xi u_\xi + \partial_y v + \partial_\eta u_\eta = 0.$$

Since we seek solutions that are homogeneous in η, the ∂_η terms can be ignored and the above equations can be split into two sets of equations as

$$\begin{aligned} -Re\partial_\xi p + \Delta u_\xi &= \frac{-2\alpha}{\gamma}, \\ -Re\partial_y p + \Delta v &= 0, \\ \partial_\xi u_\xi + \partial_y v &= 0, \end{aligned} \tag{B.3.4}$$

and

$$\Delta u_\eta = \frac{2\beta}{\gamma} \tag{B.3.5}$$

The boundary conditions on eq. (B.3.4) are

$$\begin{aligned} u_\xi(y = \pm 1 + 2\epsilon\cos(\gamma\xi)) &= 0, \\ v(y = \pm 1 + 2\epsilon\cos(\gamma\xi)) &= 0, \\ (\partial_\xi u_\xi + \partial_y v)(y = \pm 1 + 2\epsilon\cos(\gamma\xi)) &= 0, \end{aligned} \tag{B.3.6}$$

and the boundary condition on eq. (B.3.5) is

$$u_\eta(y = \pm 1 + 2\epsilon\cos(\gamma\xi)) = 0. \tag{B.3.7}$$

We can see that eqs. (B.3.4) and (B.3.6) are similar to eqs. (B.2.1) and (B.2.2) except with a scaling factor of α/γ and α substituted with γ. That is, a solution

(u, v, p) to the streamwise-wavy problem with the same geometry can be scaled as

$$\begin{aligned} u_\xi &= \frac{\alpha}{\gamma} u_{furrow,\alpha\mapsto\gamma}, \\ v &= \frac{\alpha}{\gamma} v_{furrow,\alpha\mapsto\gamma}, \\ p &= \frac{\alpha}{\gamma} p_{furrow,\alpha\mapsto\gamma}, \end{aligned} \tag{B.3.8}$$

to obtain the solution for the oblique waviness.

Equations (B.3.5) and (B.3.7) are similar to eqs. (B.1.1) and (B.1.2), and the solution can be scaled as

$$u_\eta = \frac{-\beta}{\gamma} u_{groove,\beta\mapsto\gamma} \tag{B.3.9}$$

From the solutions for the streamwise wavy channel and the grooved channel in eqs. (B.1.9) and (B.2.24) respectively, the solution for the oblique-wavy channel is

$$\begin{aligned} u_\xi &= (\frac{\alpha}{\gamma} - 4\epsilon^2\alpha\gamma)(1-Y^2) + \frac{4\epsilon\alpha\gamma}{3}(Y^3 - Y)\cos(\gamma\xi), \\ v &= -2\epsilon\alpha(1-Y^2)\sin(\gamma\xi), \\ u_\eta &= -(\frac{\beta}{\gamma} - 2\epsilon^2\beta\gamma)(1-Y^2) + \frac{-2\epsilon\beta\gamma}{3}(Y^3 - Y)\cos(\gamma\xi) - 2\epsilon^2\beta\gamma(1-Y^2)\cos(2\gamma\xi), \\ p &= \frac{4\epsilon\alpha}{Re} Y\sin(\gamma\xi) + \frac{4\epsilon^2\alpha}{Re}\sin(2\gamma\xi). \end{aligned} \tag{B.3.10}$$

The velocities along the x, z axes can be recovered from the velocities along the ξ, η axes as

$$\begin{aligned} u &= \frac{\alpha}{\gamma} u_\xi - \frac{\beta}{\gamma} u_\eta \\ &= (\frac{\alpha^2}{\gamma^2} - 4\epsilon^2\alpha^2)(1-Y^2) + \frac{4\epsilon\alpha^2}{3}(Y^3 - Y)\cos(\gamma\xi) \\ &\qquad + (\frac{\beta^2}{\gamma^2} - 2\epsilon^2\beta^2)(1-Y^2) + \frac{2\epsilon\beta^2}{3}(Y^3 - Y)\cos(\gamma\xi) + 2\epsilon^2\beta^2(1-Y^2)\cos(2\gamma\xi), \\ w &= \frac{\beta}{\gamma} u_\xi + \frac{\alpha}{\gamma} u_\eta \\ &= (\frac{\alpha\beta}{\gamma^2} - 4\epsilon^2\alpha\beta)(1-Y^2) + \frac{4\epsilon\alpha\beta}{3}(Y^3 - Y)\cos(\gamma\xi) \\ &\qquad - (\frac{\alpha\beta}{\gamma^2} - 2\epsilon^2\alpha\beta)(1-Y^2) - \frac{2\epsilon\alpha\beta}{3}(Y^3 - Y)\cos(\gamma\xi) - 2\epsilon^2\alpha\beta(1-Y^2)\cos(2\gamma\xi) \end{aligned}$$

giving

$$u = (1 - 2\epsilon^2(\alpha^2+\gamma^2))(1-Y^2) + \frac{2\epsilon(\alpha^2+\gamma^2)}{3}(Y^3 - Y)\cos(\gamma\xi) + 2\epsilon^2\beta^2(1-Y^2)\cos(2\gamma\xi),$$
$$w = -2\epsilon^2\alpha\beta(1-Y^2) + \frac{2\epsilon\alpha\beta}{3}(Y^3 - Y)\cos(\gamma\xi) - 2\epsilon^2\alpha\beta(1-Y^2)\cos(2\gamma\xi), \tag{B.3.11}$$

where $\gamma\xi = \alpha x + \beta z$.

The average pressure drag (pressure drag per unit planform area acting on one wall) along x and z for the oblique-wavy channel can be calculated to be

$$\frac{\delta F_{p,x}}{\delta A_{planform}} = -2\epsilon\alpha\Im(p_{-1,W}),$$
$$\frac{\delta F_{p,z}}{\delta A_{planform}} = -2\epsilon\beta\Im(p_{-1,W}),$$

where $\Im(f)$ is the imaginary part of f.

For the present case of $\gamma \ll 1, Re \ll 1$, the average pressure drag along x and z for both walls is

$$\frac{\delta F_{p,x}}{\delta A_{planform}} = -4\epsilon\alpha(\frac{-2\epsilon\alpha}{Re}) = \frac{8\epsilon^2\alpha^2}{Re},$$
$$\frac{\delta F_{p,z}}{\delta A_{planform}} = -4\epsilon\beta(\frac{-2\epsilon\alpha}{Re}) = \frac{8\epsilon^2\alpha\beta}{Re}. \tag{B.3.12}$$

B.4 Pressure drag in terms of Fourier coefficients

An explicit expression for pressure drag in terms of Fourier coefficients of pressure at the wall is now derived for oblique grooves. The pressure drags for longitudinal and transverse grooves are obtained as special cases. We define

$$\gamma\xi = \alpha x + \beta z$$
$$\gamma\eta = \beta x - \alpha z \tag{B.4.1}$$

where $\gamma = \sqrt{\alpha^2+\beta^2}$. The fields (u, v, w, p) are constant along η. The periodic length along ξ is $L_\xi = \frac{2\pi}{\gamma}$.

The total pressure force (within a periodic box of planform area $L_\xi\delta\eta$) is calculated

by integrating only along η. The wall-parallel pressure force is:

$$\frac{\delta F_{p,\xi}}{L_\xi \delta\eta} = \frac{1}{L_\xi}\int_{\xi=0}^{2\pi/\gamma} \hat{\boldsymbol{e}}_\xi \cdot (-\hat{\boldsymbol{n}} p(\xi) ds) \tag{B.4.2}$$

where ds is the arc-length along the surface, and $\hat{\boldsymbol{n}}$ is the unit normal to the wall (pointing into the flow).

The surface (wall) is written as

$$S(\xi, y, \eta) = y + 1 - 2\epsilon\cos(\gamma\xi) \tag{B.4.3}$$

The normal to the surface is

$$\boldsymbol{n} = \begin{bmatrix} \partial_\xi S \\ \partial_y S \\ \partial_\eta S \end{bmatrix} = \begin{bmatrix} 2\epsilon\gamma\sin(\gamma\xi) \\ 1 \\ 0 \end{bmatrix} \tag{B.4.4}$$

The ξ-component of the unit normal is

$$\hat{\boldsymbol{e}}_\xi \cdot \hat{\boldsymbol{n}} = \frac{2\epsilon\gamma\sin(\gamma\xi)}{\sqrt{1 + 4\epsilon^2\gamma^2\sin^2(\gamma\xi)}} \tag{B.4.5}$$

The arc-length ds is

$$ds = \sqrt{1 + (\frac{dy}{d\xi})^2} d\xi = \sqrt{1 + 4\epsilon^2\gamma^2\sin^2(\gamma\xi)} d\xi \tag{B.4.6}$$

So, the expression for the pressure force can be simplified to

$$\frac{\delta F_{p,\xi}}{L_\xi \delta\eta} = \frac{\gamma}{2\pi}\int_{\xi=0}^{2\pi/\gamma} \frac{-2\epsilon\gamma\sin(\gamma\xi)}{\sqrt{1 + 4\epsilon^2\gamma^2\sin^2(\gamma\xi)}} p(\xi)\sqrt{1 + 4\epsilon^2\gamma^2\sin^2(\gamma\xi)} d\xi = \frac{-2\epsilon\gamma^2}{2\pi}\int_{\xi=0}^{2\pi/\gamma} \sin(\gamma\xi) p(\xi) d\xi \tag{B.4.7}$$

It is understood that the pressure $p(\xi)$ represents only the pressure at the bottom wall.

Expanding the pressure as a Fourier series, and using $\int_0^{2\pi/\gamma} e^{ik\gamma\xi}d\xi = 0$ for $k \in \mathbb{Z} - 0$,

$$\begin{aligned}
\frac{\delta F_{p,\xi}}{L_\xi \delta\eta} &= \frac{-2\epsilon\gamma^2}{2i\cdot 2\pi}\int_{\xi=0}^{2\pi/\gamma}(e^{i\gamma\xi} - e^{-i\gamma\xi})\sum_{k\in\mathbb{Z}} p_k e^{ik\gamma\xi}d\xi \\
&= \frac{i\epsilon\gamma^2}{2\pi}\int_{\xi=0}^{L_\xi}\sum_{k\in\mathbb{Z}}(p_{k-1} - p_{k+1})e^{ik\gamma\xi}d\xi \\
&= \frac{i\epsilon\gamma^2}{2\pi}\sum_{k\in\mathbb{Z}}(p_{k-1} - p_{k+1})\int_{\xi=0}^{L_\xi} e^{ik\gamma\xi}d\xi \\
&= \frac{i\epsilon\gamma^2}{2\pi}(p_{-1} - p_1)\frac{2\pi}{\gamma} \\
&= i\epsilon\gamma(p_{-1} - \bar{p}_{-1}) = i\epsilon\gamma\cdot 2i\,\mathrm{Im}(p_{-1}) \\
&= -2\epsilon\gamma\,\mathrm{Im}(p_{-1})
\end{aligned} \tag{B.4.8}$$

This gives the pressure force per unit length along η, and it acts along ξ (because the local normal to the wall is always along ξ). Remember that the pressure p is non-dimensionalized by $\tilde{\rho}\tilde{U}_{ref}^2$. The left hand side in the above equation gives the pressure force per unit area (in the periodic domain). So, the force we calculate above is acutally the drag-coefficient (except without the 0.5 factor), but we'll not call it that.

The coordinate axes relate as

$$\begin{aligned}
\hat{\boldsymbol{e}}_\xi &= \frac{\alpha}{\gamma}\hat{\boldsymbol{e}}_x + \frac{\beta}{\gamma}\hat{\boldsymbol{e}}_z \\
\hat{\boldsymbol{e}}_\eta &= \frac{\beta}{\gamma}\hat{\boldsymbol{e}}_x + \frac{-\alpha}{\gamma}\hat{\boldsymbol{e}}_z
\end{aligned} \tag{B.4.9}$$

So, the (non-dimensional) pressure-force per unit area, which acts along $\hat{\boldsymbol{e}}_\xi$ can be projected along x and z as

$$\begin{aligned}
\frac{\delta F_{p,x}}{L_\xi\delta\eta} &= (\hat{\boldsymbol{e}}_x\cdot\hat{\boldsymbol{e}}_\xi)\frac{\delta F_{p,\xi}}{L_\xi\delta\eta} \\
&= -2\epsilon\alpha\,\mathrm{Im}(p_{-1}) \\
\frac{\delta F_{p,z}}{L_\xi\delta\eta} &= (\hat{\boldsymbol{e}}_z\cdot\hat{\boldsymbol{e}}_\xi)\frac{\delta F_{p,\xi}}{L_\xi\delta\eta} \\
&= -2\epsilon\beta\,\mathrm{Im}(p_{-1})
\end{aligned} \tag{B.4.10}$$

This pressure force only accounts for the bottom wall. By symmetry, the top wall also produces the same force (the difference for deriving the expression for the force at the top wall would be that the pressure force acts along $\hat{\boldsymbol{n}} = [S_\xi, S_y, S_\eta]$ instead of along the negative of this. The pressure force must be positive.

The driving force due to the mean pressure gradient, per unit area in $x-z$ would be

$$\begin{aligned}\frac{\delta F_{driving}}{\delta A_{plan}} &= \frac{1}{\delta A_{plan}}(\delta A_{cross})(|\delta P|) = \frac{1}{\delta A_{plan}}(\delta z \cdot 2)(|P_x|\delta x) = \frac{1}{\delta A_{plan}} 2|P_x|\delta A_{plan} \\ &= \frac{4}{Re}\end{aligned} \tag{B.4.11}$$

The factor 2 shows up because the mean pressure acts on cross-sectional planes, so the relevant area is $\delta z \cdot 2$, where 2 corresponds to the height of the channel.

From eqs. (B.4.10) and (B.4.11), the pressure drag is expressed as a fraction of the total drag (or the driving force) as

$$\begin{aligned}\frac{F_{p,x}}{F_{driving}} &= -\epsilon\alpha\,\mathrm{Im}(p_{-1})Re \\ \frac{F_{p,z}}{F_{driving}} &= -\epsilon\beta\,\mathrm{Im}(p_{-1})Re\end{aligned} \tag{B.4.12}$$

Appendix C

Methodology — Smooth-walled plane shear flows

Matrix-free methods are explored in the context of finding exact invariant solutions of the NSE. A comprehensive review is not the goal of the present work, but an introduction to the methods employed by Gibson (2014) is included because of its relevance to the present work. The modifications to the governing equations (in Cartesian coordinates) produced by this domain transformation, and the numerical method for discretizing and solving these modified equations are the subject of this chapter.

C.0.1 Time-marching

A comprehensive discussion of existing DNS algorithms for plane shear flows is out of the scope of this thesis; the interested reader may refer to standard textbooks, for instance, Versteeg and Malalasekera (2007). A time-marching algorithm using the influence matrix technique to impose the divergence-free condition is now discussed. This scheme follows the ones outlined in the documentation for Gibson (2014) on their website www.channelflow.org, but is reduced to its simplest form for illustration.

The non-linear term in the NSE is treated explicitly in time, while the linear term

is treated implicitly in time. The unsteady NSE are written in the form

$$\frac{\partial \boldsymbol{u}}{\partial t} = \boldsymbol{\mathcal{L}u} - \nabla p - \boldsymbol{\mathcal{N}}(\boldsymbol{u}) + \boldsymbol{f}, \tag{C.0.1}$$

with appropriate boundary conditions. Here, $\boldsymbol{u} = \begin{bmatrix} u, v, w \end{bmatrix}^T$ is the velocity vector, and the constant forcing f is included to account for the mean pressure gradient in channel flow. For any (intermediate) time-step, the time-derivative, linear, and non-linear terms are discretized at an intermediate time $(n+1/2)\Delta t$ as

$$\begin{aligned}
\frac{\partial}{\partial t}\boldsymbol{u}^{n+1/2} &\approx \frac{\boldsymbol{u}^{n+1} - \boldsymbol{u}^{n}}{\Delta t}, \\
(\boldsymbol{\mathcal{L}u})^{n+1/2} &\approx \frac{(\boldsymbol{\mathcal{L}u})^{n+1} + (\boldsymbol{\mathcal{L}u})^{n}}{2}, \\
(\nabla p)^{n+1/2} &\approx \frac{(\nabla p)^{n+1} + (\nabla p)^{n}}{2}, \\
(\boldsymbol{\mathcal{N}}(\boldsymbol{u}))^{n+1/2} &\approx \frac{3}{2}(\boldsymbol{\mathcal{N}}(\boldsymbol{u}))^{n} - \frac{1}{2}(\boldsymbol{\mathcal{N}}(\boldsymbol{u}))^{n-1}.
\end{aligned} \tag{C.0.2}$$

Different integration routines can be built using different number of intermediate time-steps. For the purpose of illustration, we use this simplified scheme without any additional intermediate steps. The unsteady NSE can then be written in a simple form for the time $n\delta t$ as

$$\left[\frac{1}{\delta t} - \frac{1}{2}\boldsymbol{\mathcal{L}}\right]\boldsymbol{u}^{n+1} + \frac{1}{2}\nabla p^{n+1} = \left[\frac{1}{\delta t} + \frac{1}{2}\boldsymbol{\mathcal{L}}\right]\boldsymbol{u}^{n} - \frac{1}{2}\nabla p^{n+1} + \frac{3}{2}\boldsymbol{\mathcal{N}}(\boldsymbol{u}^{n}) - \frac{1}{2}\boldsymbol{\mathcal{N}}(\boldsymbol{u}^{n-1}) + \boldsymbol{f}. \tag{C.0.3}$$

For plane shear flows, the above equation can be discretized in the wall-parallel directions with the Fourier spectral method to obtain decoupled equations for the Fourier coefficients at $t = (n+1)\delta t$ in the form ,

$$\begin{aligned}
c_1 \boldsymbol{u}''^{n+1}_{l,m} + c_2 \boldsymbol{u}^{n+1}_{l,m} + c_3 \nabla p^{n+1}_{l,m} &= \boldsymbol{g}_{l,m}, \\
il\alpha u_{l,m} + v'_{l,m} + im\beta w_{l,m} &= 0, \\
(u_{l,m} - U) = v_{l,m} = w_{l,m} = v'_{l,m} &= 0 \qquad \text{at y} = \pm 1,
\end{aligned} \tag{C.0.4}$$

for some constants c_1, c_2, and c_3 dependent on the wavenumber pair and discretization,

and some easily evaluated vector function $\boldsymbol{g}()$ of the fields at the previous time-step. Here, $\boldsymbol{u}''_{l,m} = \frac{d^2}{dy^2}\boldsymbol{u}_{l,m}$ and $v' = \frac{dv}{dy}$ are wall-normal derivatives. The second equation is the divergence-free condition for velocity, and the set of equations on the third line are the boundary conditions; U is the laminar velocity profile, $U = y$ for Couette flow, and $U = 1 - y^2$ for Poiseuille flow.

These equations are solved using the influence matrix technique as described below.

Influence matrix method

Taking the divergence of eq. (C.0.4) produces a Poisson equation for pressure, which can be used to update the pressure field. This Poisson equation takes the place of the divergence-free condition. The new set of equations along with the boundary conditions is

$$\begin{aligned} p'' - (l^2\alpha^2 + m^2\beta^2)p &= \nabla \cdot \boldsymbol{g}, & v'(\pm 1) &= 0, \\ c_1\boldsymbol{u}'^{n+1} + c_2\boldsymbol{u}^{n+1} + c_3\nabla p^{n+1} &= \boldsymbol{g}, & \boldsymbol{u} - \big[U, 0, 0\big](\pm 1) &= 0, \end{aligned} \tag{C.0.5}$$

where the wavenumbers in the subscripts have been dropped for convenience. The equations for v and p are coupled — v enters the equation for p through the boundary conditions, while p is present in the equation for v. These coupled equations need to be solved together. Once the v and p fields are known, u and w are easily calculated from eq. (C.0.5).

Instead of using $v'(\pm 1) = 0$ as the boundary condition on the pressure Poisson equation, the pressure is assumed to be some (unknown) Q_+ at $y = 1$ and Q_- at $y = \pm 1$ which ensure that the divergence-free condition at the boundary is met (which, in conjunction with the pressure Poisson equation, ensures that the divergence is zero everywhere in the domain). This is done by solving two problems. The first is the A-problem with homogeneous Dirichlet boundary conditions on pressure,

$$\begin{aligned} p''_h - (l^2\alpha^2 + m^2\beta^2)p_h &= \nabla \cdot g_y, & p_h(\pm 1) &= 0, \\ c_1 v''^{n+1}_h + c_2 v^{n+1}_h + c_3\nabla p^{n+1}_h &= g_y, & v_h(\pm 1) &= 0, \end{aligned} \tag{C.0.6}$$

where g_y is the y-component of $\boldsymbol{g}$. The second problem has two sub-problems, B_+ and B_-. The B problems involves finding solutions for a Laplace equation for pressure with a $p = 1$ Dirichlet boundary condition at one wall and $p = 0$ at the other. The B_+ problem is

$$\begin{aligned} p''_+ - (l^2\alpha^2 + m^2\beta^2)p_+ &= 0, \qquad & p_+(1) = 1, \quad p_+(-1) = 0, \\ c_1 v''^{n+1}_+ + c_2 v^{n+1}_+ + c_3 \nabla p^{n+1}_+ &= 0, \qquad & v(\pm 1) = 0, \end{aligned} \tag{C.0.7}$$

and the B_- problem is

$$\begin{aligned} p''_- - (l^2\alpha^2 + m^2\beta^2)p_- &= 0, \qquad & p_-(1) = 0, \quad p_-(-1) = 1, \\ c_1 v''^{n+1}_- + c_2 v^{n+1}_- + c_3 \nabla p^{n+1}_- &= 0, \qquad & v(\pm 1) = 0. \end{aligned} \tag{C.0.8}$$

The solution to the original equation, eq. (C.0.5), is a sum of the solutions to the three sets of equations above,

$$\begin{bmatrix} p \\ v \end{bmatrix} = \begin{bmatrix} p_h \\ v_h \end{bmatrix} + Q_+ \begin{bmatrix} p_+ \\ v_+ \end{bmatrix} + Q_- \begin{bmatrix} p_- \\ v_- \end{bmatrix}. \tag{C.0.9}$$

The boundary conditions on $[p, v]$ for the original equation, eq. (C.0.5), are satisfied if

$$\begin{bmatrix} v'_+(+1) & v'_-(+1) \\ v_+(-1) & v_-(-1) \end{bmatrix} \begin{bmatrix} Q_+ \\ Q_- \end{bmatrix} = - \begin{bmatrix} v_h(+1) \\ v_h(-1) \end{bmatrix}, \tag{C.0.10}$$

which is the *influence-matrix* equation. The equations of the A and B problems are low dimensional with Dirichlet boundary conditions and are easily solved, and so is the influence matrix equation.

C.1 Generating approximate solutions

Non-linearity of the NSE makes it hard to compute exact solutions of the equations. Numerical methods are available for solving non-linear equations, such as Newton's method and "quasi-Newton" methods (Dennis Jr and Schnabel, 1996). These are

iterative methods that start with an initial flow field close to a solution and refine it until the norm of some function of the state-vector is minimized. Typically, these methods have quadratic or super-linear convergence. However, if the approximate solution is not close enough to an exact solution, convergence is not guaranteed. While algorithms that produce global convergence do exist, the number of iterations required might be prohibitively large. The dynamical systems vision of turbulence requires finding a lot of dynamically important, exact invariant solutions, and this requires identifying flow fields that are in sufficiently small neighbourhoods of the exact solutions. Three methods for identifying such approximate solutions are outlined in Kawahara et al. (2012).

C.1.1 Bisection

The bisection method is relevant for finding lower branch solutions that sit on the laminar-turbulent separatrix at low Reynolds number with a stable laminar solution. Two initial flow fields are chosen, one that leads to long-lived turbulence and one that leads to quick laminarization. Bisecting these initial conditions produces orbits that approach lower branch solutions.

C.1.2 Homotopy

Homotopy can be used to continue solutions from one class of flows to other, similar classes of flows. For instance, the early work of Nagata (1990) involved such continuation. The circular Couette system between co-rotating cylinders with a narrow gap produces steady (or travelling) three-dimensional solutions that bifurcate from the two-dimensional Taylor-vortex flow. "Guess" flow fields for plane Couette flow are obtained by computing equilibria for Taylor-Couette flow at asymptotically high cylinder radii.

In the present work, we use homotopy from smooth-walled plane Couette flow (smooth PCoF) to grooved plane Couette flow (grooved PCoF); equilibria for smooth PCoF are used as the approximate solutions in grooved PCoF and iterated to obtain

exact solutions.

C.1.3 Filtering

Recurrence plots are created using turbulent time-series data from DNS to identify appropriate approximate solutions. The approximate solutions obtained this way are usually coarse, and globally convergent methods are needed to get to exact solutions.

C.2 Iterative solvers

The discretized NSE are a high-dimensional non-linear system of equations. Such equations are solved using iterative solvers such as the Newton-Raphson method (often referred to as simply the Newton method), or one of its variations. A large number of such methods are discussed in the literature; see, for instance, Cai et al. (1994); Knoll and Keyes (2004); Viswanath (2007) for methods applicable to partial differential equations (PDE) such as the NSE. This section presents a brief overview of some of these methods that are relevant to the grooved PCoF solver developed in the present work.

C.2.1 The Newton method and its variants

The Newton method is a standard root-finder method for non-linear equations. It is easily extended to systems of non-linear equations by considering Jacobians and matrix-inverses in the place of derivatives and inverses. We write the system of equations to be solved as

$$\mathbf{F}(\mathbf{u}) = 0, \qquad \mathbf{u} \in \mathbb{R}^n, \quad \mathbf{F} : \mathbb{R}^n \to \mathbb{R}^n \tag{C.2.1}$$

The above equation is an abuse of notation with respect to the notation used in eq. (2.1.1), but we use it regardless since the present work is focused on extending equilibria only; however, the time-t map based equations for TWS and periodic orbits may also be cast in the above form for an appropriate definition of the non-linear

operator $\mathbf{F}$. The argument $\mathbf{u}$ is the state-vector (discretized velocity field).

Henceforth, instead of the bold-faced symbol $\mathbf{F}$, plain symbol F is used to refer to the non-linear operator $\mathbf{F}$. Its Jacobian is denoted J. The state-vector, $\mathbf{u}$ in the above equation, is denoted χ.

Given an estimate, χ^0, that is sufficiently close to the exact solution, χ^*, (and under some additional conditions on the Jacobian $\mathbf{F}'$) the Newton method offers quadratic convergence. That is, for successive iterates χ^k and χ^{k+1} for sufficiently large k, the ratio of the errors relates as

$$\lim_{k\to\infty} \frac{||\chi^{k+1} - \chi^*||}{||\chi^k - \chi^*||^q} > 0, \tag{C.2.2}$$

with $q = 2$. A larger q indicates faster convergence to the exact solution χ^*.

The iterations are given by the following step:

$$\chi^{k+1} = \chi^k - \left\{J(\chi^k)\right\}^{-1}\mathbf{F}(\chi^k). \tag{C.2.3}$$

The size of the Jacobian matrix goes as the square of the dimensionality of state-space. For the high-dimensional state-vectors needed to adequately resolve flow features, solving the above matrix equation becomes infeasible. In fact, for a modest resolution of 24×24 non-negative Fourier modes in the wall-parallel directions, and 35 Chebyshev nodes in the wall-normal direction, the Jacobian matrix needs about half a terabyte of storage space for double-float precision. While this can be brought down by exploiting symmetries of the flow, the size of the matrix could still prove too large to be stored on the RAM of most computers. Furthermore, it might not even be possible to explicitly define the Jacobian — for periodic orbits, for instance. This does not take into account the complexity of solving such large matrix equations. Clearly, using dense-matrix methods is infeasible. Matrix-free methods are needed to solve the Newton-iteration of eq. (C.2.3).

C.2.2 Jacobian-free Newton-Krylov methods (JFNK)

Equation (C.2.3) can be rewritten as an equation for the correction in state, $\delta\chi^k$, as

$$J(\chi^k)\delta\chi^k = -F(\chi^k). \tag{C.2.4}$$

For high-dimensional systems where storage and computation becomes prohibitively expensive, matrix-free methods might produce a solution. This section presents a rudimentary introduction to matrix-free methods; a more comprehensive discussion can be found in standard textbooks on matrix algebra, such as Trefethen and Bau (1997).

These methods, called Krylov subspace methods, involve building subspaces of matrix-vector products and finding solutions within acceptable tolerance in low dimensional subspaces. The basis for these methods is in the Cayley-Hamilton theorem; If

$$p(\lambda) = det(\lambda I_n - A) = 0 \tag{C.2.5}$$

is the characteristic equation of the matrix A, then replacing the scalar λ with the matrix A also satisfies the characteristic equation,

$$p(A) = 0. \tag{C.2.6}$$

A consequence of the theorem is that, given that the matrix $A_{n\times n}$ is non-singular, the inverse of the matrix can be expressed in terms of its powers (A^0 through A^{n-1}). In the context of solving sets of linear equations, this leads to the interpretation that a solution χ^* to the linear equation $A\chi = b$ can be found in the subspace spanned by $\{b, Ab, A^2b, A^3b, \ldots, A^{n-1}b\}$. When A is a sparse matrix, it is often the case that the solution χ^* is found to sufficient accuracy in a low-dimensional subspace spanned by $\{b, Ab, A^2b, \ldots, A^{m-1}b\}$ for some m significantly smaller than n.

The set of vectors obtained by multiplying successively higher powers of A with any vector tend to become linearly dependent, because the eigenvectors with the largest

eigenvalues grow faster than the others. To address this, Krylov subspace methods involve some orthogonalization scheme, such as Lanczos iteration or Arnoldi iteration, so that a sufficiently large dimensional subspace can be built to locate a solution.

Another issue often faced in solving high-dimensional linear sets of equations, especially using matrix-free methods, is that of conditioning. A condition number quantifies the sensitivity of the solution $\chi^* = A^{-1}b$ to changes in b, and is often taken to be the ratio of the largest to the smallest singular values of A. Matrices with large condition numbers have slow convergence for a specified tolerance. Convergence rate is often improved by using a preconditioner P (a matrix which approximates A^{-1}) such that the matrix $P^{-1}A$ has a low condition number.

The solver of Gibson (2014) succeeds in finding exact invariant solutions without having to employ a preconditioner.

The linear problem of eq. (C.2.4) has the Jacobian J in the place of the matrix A used in the discussion above. Product of the Jacobian with trial vectors $\delta\chi$ can be computed without explicitly defining the Jacobian. Finite differences over the non-linear function $F(\chi)$,

$$J(\chi^k)\delta\chi \approx \frac{F(\chi^k + \epsilon\delta\chi) - F(\chi^k)}{\epsilon},$$

produce a first order approximation for $J\delta\chi$, accurate to $\mathcal{O}(\epsilon)$. A second order approximation is also straight-forward,

$$J(\chi^k)\delta\chi \approx \frac{F(\chi^k + \epsilon\delta\chi) - F(\chi^k - \epsilon\delta\chi)}{2\epsilon}.$$

However, the second order approximation requires two computations of the non-linear function $F()$ for a given trial vector, and this could significantly slow down the computations; especially for cases where the tolerance required of the solution itself is orders of magnitude greater than ϵ. The choice of ϵ is important. For large ϵ, the Jacobian is not adequately approximated. If it is too small, then truncation errors

due to machine-ϵ may be large enough to distort the approximation. Guidelines on choosing ϵ may be found in works such as Knoll and Keyes (2004); Qin et al. (2000). The value for ϵ is commonly set at $\sim 10^{-7}$ when using double-float precision.

Jacobian-free Newton-Krylov methods are classified into exact and inexact Newton methods depending on how eq. (C.2.4) is solved. Exact Newton methods solve the linear equation to sufficiently low tolerance using methods such as GMRES or L-GMRES, while inexact methods such as L-BFGS do not solve eq. (C.2.4) exactly; instead, they frequently update the guess-vector χ^k and produce a preconditioner for the Jacobian based on the corrections $\delta\chi^k$. The present work employs exact Newton's method following the solver of Gibson (2014).

C.2.3 Global convergence: Line search

Exact Newton's method can fail to converge if the solution of eq. (C.2.4) is used directly to correct the state. As an illustration, consider the application of Newton's method to the scalar function $f(x) = x^3 - 2x + 2$, with the initial guess of 0 as its root. The iterations lead to a stable 2-cycle that goes as 0, 1, 0, 1, ..., while the real root for the equation is ≈ 1.77. This happens because Newton's method constructs a tangent to the curve $y = f(x)$ at x^k to give the root of the tangent as an improved estimate for the root of $f(x)$. For $f(x) = x^3 - 2x + 2$, the tangent at $x = 0$ intersects the x-axis at $x = 1$, and the tangent at $x = 1$ intersects the x-axis at $x = 0$, producing the 2-cycle.

Returning to the multi-dimensional system, the linear approximation to the function $F(\chi)$ produced by eq. (C.2.4) is optimal only if the Newton quadratic model is valid. When this is not the case, the solution to the linear equation can often overshoot the solution to the non-linear function. This can be avoided by using the correction $\delta\chi^k \approx -J^{-1}(\chi^k)F(\chi^k)$ as a direction that can produce a reduction in $F(\chi)$, and using a damping factor d_f so that $F(\chi^k + d_f\delta\chi^k)$ is minimized over all $d_f \in \mathbb{R}$. This method is called the "line search" method, because the actual correction made to χ^k is searched over a single direction. The damping factor, d_f, is often taken to be

between 0 and 1, since a reasonable application of the Newton method should produce a search direction that produces a descent.

C.2.4 Global convergence: Locally constrained optimal hook-step

An alternative approach to address the local validity of the Newton correction step is to look for a correction, $\delta\chi^k$, which minimizes $||J(\chi^k)\delta\chi^k + F(\chi^k)||$ in a region around χ^k where the quadratic Newton model is valid. Such methods are called "trust-region methods", because corrections are made to estimates of the solution in regions in which the model is trusted. An overview of such methods can be found in Dennis Jr and Schnabel (1996). Gibson (2014) uses a trust-region method called the constrained hook-step method, which was introduced by Viswanath (2007) specifically for finding exact invariant solutions of the NSE. This method is outlined below.

Step 1, GMRES and low-rank approximation of the Jacobian.
The method starts with a GMRES to approximately solve the correction step of eq. (C.2.4), but exits after a Krylov subspace basis of an adequate rank is built; the exit condition is set as the relative error, $||J(\chi^k)\delta\chi + F(\chi^k)||/||F(\chi^k)||$, going below a certain tolerance ($\sim 10^{-3}$). GMRES uses Arnoldi iteration to build orthonormal bases (denoted Q) such that

$$J_{n\times n}Q_{n\times d} = Q_{n\times(d+1)}H_{d+1,d}. \tag{C.2.7}$$

$Q_{n\times d}$ and $Q_{n\times(d+1)}$ are referred to as Q_d and Q_{d+1} respectively for convenience. The orthonormal basis matrices, Q_d and Q_{d+1}, and the upper Hessenberg matrix, $H_{d+1,d}$, are used to find an optimal solution within the d-dimensional subspace spanned by Q_d.

If the solution from GMRES lies within the specified trust-region radius, then a constrained hook-step is not necessary and the algorithm goes directly to step 5 given below.

Step 2, Formulating an optimization problem in the low-dimensional subspace.

We seek an approximate solution $\delta\chi = Q_d\sigma_d$ in the subspace spanned by the columns of Q_d, where σ_d is a d-dimensional column vector. Equation (C.2.4) can then be rewritten in the d-dimensional subspace,

$$\begin{aligned} JQ_d\sigma_d &= -F \\ \implies H_{d+1,d}\sigma_d &= -Q_{d+1}^* F, \end{aligned}$$

where Q^* represents the hermitian of the unitary matrix Q. Viswanath (2007); Gibson (2014) indicate that the size of the above problem, d, is typically a number around 30. A constrained optimization problem is easily solved for this size. The constraint used is that the norm of the solution, $||\delta\chi|| = ||\sigma_d||$, is smaller than the radius of the trust-region. It is important that an appropriate norm is chosen; energy norms are often used for their physical significance; the matrices and vectors are weighted using some quadrature according to the discretization scheme so that an L-2 norm of the weighted numerical arrays produces energy norm of the original arrays.

Step 3, Solving the constrained minimization problem.

Performing an SVD of the upper Hessenberg matrix,

$$H = UDV^*,$$

produces the minimization problem

$$\begin{aligned} \text{Minimize} \quad & ||DV^*\sigma_d + U^*Q_{d+1}^*F|| \\ \text{subject to} \quad & ||\sigma_d|| \leq r, \end{aligned}$$

where δ is the radius of the trust-region (not to be confused with the δ in $\delta\chi$, where it is used to denote a correction to the state-vector χ). Note that the only unknown here is the column vector σ_d; the matrices D, V, U, and Q_{d+1}, and the vector F are all known from the GMRES and the SVD. The problem can be further simplified by

defining

$$s = V^* \sigma_d,$$

$$b = -U^* Q^*_{d+1} F,$$

producing the simplified constrained minimization problem,

$$\begin{aligned} &\text{Minimize} \quad \sum (d_i s_i - b_i)^2 \qquad \text{(no Einstein summation)} \\ &\text{subject to} \quad \sum s_i^2 \leq \delta^2, \end{aligned} \tag{C.2.8}$$

where d_i are the singular values of H (the entries on the principal diagonal of D), and are not related to the dimensionality, d, of the problem.

Using the method of Lagrange multipliers, the Lagrangian is

$$L(s_i, \mu) = \sum (d_i s_i - b_i)^2 - \mu(\delta^2 - \sum s_i^2).$$

The equations to be solved are

$$L_{s_i} = 0, \qquad \text{for } i \in \{1, 2, ...\},$$

along with the complementary slackness condition,

$$\mu(s_i^2 - \delta^2) = 0, \qquad \mu \geq 0$$

The Lagrangian equation can be solved in terms of μ as

$$s_i = \frac{b_i d_i}{d_i^2 + \mu}. \tag{C.2.9}$$

Since each s_i is now a function of μ, the complementary slackness equation can also be written as

$$\sum_i s_i(\mu)^2 = \delta^2$$

This is a non-linear equation in one variable, μ, and can be solved using the Newton

method.

Defining

$$\Phi(\mu) := \sum s_i(\mu)^2 - \delta^2, \tag{C.2.10}$$

the function to be solved is

$$\Phi(\mu) = 0. \tag{C.2.11}$$

Gibson (2014) recommends using a modified Newton's method, because $\Phi' \to 0$ as $\mu \to \infty$, and standard Newton's method would have issues inverting Φ'. The modified Newton's method they recommend is the iteration

$$\mu^{k+1} = \mu^k - \frac{||s||_2}{\delta}\frac{\Phi(\mu^k)}{\Phi'(\mu^k)}, \tag{C.2.12}$$

so that, for sufficiently large μ,

$$\begin{aligned} \Phi &= \sum s_i^2 - \delta^2 && \sim \mu^{-2}, \\ \Phi' &= \sum \frac{-2s_i^2}{d_i + \mu} && \sim \mu^{-3}, \text{ and} \\ ||s||_2 &= \sqrt{\sum s_i^2} && \sim \mu^{-1}. \end{aligned}$$

Step 4, Correcting the state-vector.

The correction $\delta\chi$ is recovered by tracing the solution for μ backwards through the above steps,

$$\delta\chi = Q_d\sigma_d = Q_d V s = Q_d V[s_i(\mu)]^T \tag{C.2.13}$$

Step 5, Modifying the trust-region radius

The heuristics of choosing and modifying trust-region radii is fairly involved, and is left out of the current thesis. The interested reader is referred to Dennis Jr and Schnabel (1996). Gibson (2014) uses an initial trust region radius of 0.1, although this is coded as an argument that can be passed to the solver.

Bibliography

Adrian, R. J. (2007). Hairpin vortex organization in wall turbulence a. *Physics of Fluids*, 19(4):041301.

Allen, J., Shockling, M., Kunkel, G., and Smits, A. (2007). Turbulent flow in smooth and rough pipes. *Philosophical Transactions of the Royal Society A: Mathematical, Physical and Engineering Sciences*, 365(1852):699–714.

Bandyopadhyay, P. R. (1987). Rough-wall turbulent boundary layers in the transition regime. *Journal of Fluid Mechanics*, 180:231–266.

Bechert, D. and Bartenwerfer, M. (1989). The viscous flow on surfaces with longitudinal ribs. *Journal of Fluid Mechanics*, 206:105–129.

Blackburn, H., Hall, P., and Sherwin, S. (2013). Lower branch equilibria in couette flow: the emergence of canonical states for arbitrary shear flows. *Journal of Fluid Mechanics*, 726:R2.

Blancher, S., Le Guer, Y., and El Omari, K. (2015). Spatio-temporal structure of the 'fully developed'transitional flow in a symmetric wavy channel. linear and weakly nonlinear stability analysis. *Journal of Fluid Mechanics*, 764:250–276.

Bottin, S., Dauchot, O., Daviaud, F., and Manneville, P. (1998). Experimental evidence of streamwise vortices as finite amplitude solutions in transitional plane couette flow. *Physics of Fluids*, 10(10):2597–2607.

Cai, X.-C., Gropp, W. D., Keyes, D. E., and Tidriri, M. D. (1994). Newton-krylov-

schwarz methods in cfd. In *Numerical methods for the Navier-Stokes equations*, pages 17–30. Springer.

Chandler, G. J. and Kerswell, R. R. (2013). Invariant recurrent solutions embedded in a turbulent two-dimensional kolmogorov flow. *Journal of Fluid Mechanics*, 722:554–595.

Chantry, M. and Kerswell, R. R. (2015). Localization in a spanwise-extended model of plane couette flow. *Physical Review E*, 91(4):043005.

Chantry, M., Willis, A. P., and Kerswell, R. R. (2014). Genesis of streamwise-localized solutions from globally periodic traveling waves in pipe flow. *Physical review letters*, 112(16):164501.

Chen, H., Rao, F., Shang, X., Zhang, D., and Hagiwara, I. (2013). Biomimetic drag reduction study on herringbone riblets of bird feather. *Journal of Bionic Engineering*, 10(3):341–349.

Chen, H., Rao, F., Shang, X., Zhang, D., and Hagiwara, I. (2014). Flow over bio-inspired 3d herringbone wall riblets. *Experiments in fluids*, 55(3):1–7.

Choi, H., Moin, P., and Kim, J. (1993). Direct numerical simulation of turbulent flow over riblets. *Journal of fluid mechanics*, 255:503–539.

Christiansen, F., Cvitanovic, P., and Putkaradze, V. (1997). Spatiotemporal chaos in terms of unstable recurrent patterns. *Nonlinearity*, 10(1):55.

Chu, D. C. and Karniadakis, G. E. (1993). A direct numerical simulation of laminar and turbulent flow over riblet-mounted surfaces. *Journal of Fluid Mechanics*, 250:1–42.

Clever, R. and Busse, F. H. (1997). Tertiary and quaternary solutions for plane couette flow. *Journal of Fluid Mechanics*, 344:137–153.

Colebrook, C. F. (1939). Turbulent flow in pipes, with particular reference to the transition region between the smooth and rough pipe laws. *Journal of the ICE*, 11(4):133–156.

Cossu, C., Pujals, G., and Depardon, S. (2009). Optimal transient growth and very large–scale structures in turbulent boundary layers. *Journal of Fluid Mechanics*, 619:79–94.

Cvitanović, P. (2013). Recurrent flows: the clockwork behind turbulence. *Journal of Fluid Mechanics*, 726:1–4.

Dean, B. and Bhushan, B. (2010). Shark-skin surfaces for fluid-drag reduction in turbulent flow: a review. *Philosophical Transactions of the Royal Society of London A: Mathematical, Physical and Engineering Sciences*, 368(1929):4775–4806.

Deguchi, K. and Hall, P. (2014). The high-reynolds-number asymptotic development of nonlinear equilibrium states in plane couette flow. *Journal of Fluid Mechanics*, 750:99–112.

Deguchi, K. and Hall, P. (2017). The relationship between free-stream coherent structures and near-wall streaks at high reynolds numbers. *Phil. Trans. R. Soc. A*, 375(2089):20160078.

Dempsey, L., Deguchi, K., Hall, P., and Walton, A. (2016). Localized vortex/tollmien–schlichting wave interaction states in plane poiseuille flow. *Journal of Fluid Mechanics*, 791:97–121.

Dennis Jr, J. E. and Schnabel, R. B. (1996). *Numerical methods for unconstrained optimization and nonlinear equations*, volume 16. Siam.

Djenidi, L., Elavarasan, R., and Antonia, R. (1999). The turbulent boundary layer over transverse square cavities. *Journal of Fluid Mechanics*, 395:271–294.

Drazin, P. G. and Reid, W. H. (2004). *Hydrodynamic stability*. Cambridge university press.

Duguet, Y., Schlatter, P., and Henningson, D. S. (2009). Localized edge states in plane couette flow. *Physics of fluids*, 21(11):111701.

Eckhardt, B., Faisst, H., Schmiegel, A., and Schneider, T. M. (2008). Dynamical systems and the transition to turbulence in linearly stable shear flows. *Philosophical Transactions of the Royal Society of London A: Mathematical, Physical and Engineering Sciences*, 366(1868):1297–1315.

Faisst, H. and Eckhardt, B. (2003). Traveling waves in pipe flow. *Physical Review Letters*, 91(22):224502.

Flack, K. A., Schultz, M. P., and Shapiro, T. A. (2005). Experimental support for townsend's reynolds number similarity hypothesis on rough walls. *Physics of Fluids (1994-present)*, 17(3):035102.

Gibson, J. and Brand, E. (2014). Spanwise-localized solutions of planar shear flows. *Journal of Fluid Mechanics*, 745:25–61.

Gibson, J. F. (2014). Channelflow: A spectral Navier-Stokes simulator in C++. Technical report, U. New Hampshire. `Channelflow.org`.

Gibson, J. F., Halcrow, J., and Cvitanović, P. (2008). Visualizing the geometry of state space in plane couette flow. *Journal of Fluid Mechanics*, 611:107–130.

Gibson, J. F., Halcrow, J., and Cvitanović, P. (2009). Equilibrium and travelling-wave solutions of plane couette flow. *Journal of Fluid Mechanics*, 638:243–266.

Gioia, G. and Bombardelli, F. (2001). Scaling and similarity in rough channel flows. *Physical review letters*, 88(1):014501.

Gioia, G. and Chakraborty, P. (2006). Turbulent friction in rough pipes and the energy spectrum of the phenomenological theory. *Physical review letters*, 96(4):044502.

Granville, P. S. (1958). *The frictional resistance and turbulent boundary layer of rough surfaces*. Hydromechanics Laboratory.

Gschwind, P., Regele, A., and Kottke, V. (1995). Sinusoidal wavy channels with taylor-goertler vortices. *Experimental thermal and fluid science*, 11(3):270–275.

Halcrow, J. J. (2008). *Charting the state space of plane Couette flow: equilibria, relative equilibria, and heteroclinic connections*. PhD thesis, Georgia Institute of Technology.

Hall, P. and Sherwin, S. (2010). Streamwise vortices in shear flows: harbingers of transition and the skeleton of coherent structures. *Journal of Fluid Mechanics*, 661:178–205.

Hall, P. and Smith, F. T. (1991). On strongly nonlinear vortex/wave interactions in boundary-layer transition. *Journal of fluid mechanics*, 227:641–666.

Hamed, A., Sadowski, M., Zhang, Z., and Chamorro, L. (2016). Transition to turbulence over 2d and 3d periodic large-scale roughnesses. *Journal of Fluid Mechanics*, 804.

Hamilton, J. M., Kim, J., and Waleffe, F. (1995). Regeneration mechanisms of near-wall turbulence structures. *Journal of Fluid Mechanics*, 287:317–348.

Hutchings, I. M. (1992). *Tribology: friction and wear of engineering materials*. Butterworth-Heinemann Ltd.

Hwang, Y., Willis, A. P., and Cossu, C. (2016). Invariant solutions of minimal large-scale structures in turbulent channel flow for reτ up to 1000. *J. Fluid Mech*, 802:R1.

Islam, N., Bradshaw-Hajek, B., Miklavcic, S., and White, L. (2015). The onset of recirculation flow in periodic capillaries: Geometric effects. *European Journal of Mechanics-B/Fluids*, 53:119–128.

Itano, T. and Toh, S. (2001). The dynamics of bursting process in wall turbulence. *Journal of the Physical Society of Japan*, 70(3):703–716.

Jiménez, J. (2004). Turbulent flows over rough walls. *Annual Review of Fluid Mechanics*, 36:173–196.

Jiménez, J., Kawahara, G., Simens, M. P., Nagata, M., and Shiba, M. (2005). Characterization of near-wall turbulence in terms of equilibrium and "bursting" solutions. *Physics of Fluids*, 17(1):015105.

Jiménez, J. and Moin, P. (1991). The minimal flow unit in near-wall turbulence. *Journal of Fluid Mechanics*, 225:213–240.

Kasliwal, A., Duncan, S., and Papachristodoulou, A. (2012). Modelling channel flow over riblets: Calculating the energy amplification. In *Control (CONTROL), 2012 UKACC International Conference on*, pages 625–630. IEEE.

Kawahara, G., Kida, S., and Nagata, M. (2006). Unstable periodic motion in plane couette system: the skeleton of turbulence. In *IUTAM Symposium on One Hundred Years of Boundary Layer Research*, pages 415–424. Springer.

Kawahara, G., Uhlmann, M., and van Veen, L. (2012). The significance of simple invariant solutions in turbulent flows. *Annual Review of Fluid Mechanics*, 44:203–225.

Kelley, C. T. (1999). *Iterative methods for optimization*, volume 18. Siam.

Khapko, T., Kreilos, T., Schlatter, P., Duguet, Y., Eckhardt, B., and Henningson, D. S. (2016). Edge states as mediators of bypass transition in boundary-layer flows. *Journal of Fluid Mechanics*, 801:R2.

Kline, S., Reynolds, W., Schraub, F., and Runstadler, P. (1967). The structure of turbulent boundary layers. *Journal of Fluid Mechanics*, 30(04):741–773.

Knoll, D. A. and Keyes, D. E. (2004). Jacobian-free newton–krylov methods: a survey of approaches and applications. *Journal of Computational Physics*, 193(2):357–397.

Kreilos, T. and Eckhardt, B. (2012). Periodic orbits near onset of chaos in plane couette flow. *Chaos: An Interdisciplinary Journal of Nonlinear Science*, 22(4):047505.

Kreilos, T., Khapko, T., Schlatter, P., Duguet, Y., Henningson, D. S., and Eckhardt, B. (2016). Bypass transition and spot nucleation in boundary layers. *Physical Review Fluids*, 1(4):043602.

Lee, S.-J. and Lee, S.-H. (2001). Flow field analysis of a turbulent boundary layer over a riblet surface. *Experiments in fluids*, 30(2):153–166.

Ligrani, P. M. and Moffat, R. J. (1986). Structure of transitionally rough and fully rough turbulent boundary layers. *Journal of Fluid Mechanics*, 162:69–98.

Liou, T.-M., Chang, Y., and Hwang, D.-W. (1990). Experimental and computational study of turbulent flows in a channel with two pairs of turbulence promoters in tandem. *Journal of Fluids Engineering*, 112(3):302–310.

Luchini, P. (2013). Linearized no-slip boundary conditions at a rough surface. *Journal of Fluid Mechanics*, 737:349–367.

Luchini, P., Manzo, F., and Pozzi, A. (1991). Resistance of a grooved surface to parallel flow and cross-flow. *Journal of Fluid Mechanics*, 228:87–109.

Marusic, I., Monty, J. P., Hultmark, M., and Smits, A. J. (2013). On the logarithmic region in wall turbulence. *Journal of Fluid Mechanics*, 716:R3.

McKeon, B. and Sharma, A. (2010). A critical-layer framework for turbulent pipe flow. *Journal of Fluid Mechanics*, 658:336–382.

McKeon, B., Zagarola, M., and Smits, A. (2005). A new friction factor relationship for fully developed pipe flow. *Journal of fluid mechanics*, 538:429–443.

Mohammadi, A. and Floryan, J. M. (2013). Pressure losses in grooved channels. *Journal of Fluid Mechanics*, 725:23–54.

Moradi, H. and Floryan, J. (2014). Stability of flow in a channel with longitudinal grooves. *Journal of Fluid Mechanics*, 757:613–648.

Moradi, H. V. and Floryan, J. M. (2013). Maximization of heat transfer across micro-channels. *International Journal of Heat and Mass Transfer*, 66:517–530.

Nagata, M. (1990). Three-dimensional finite-amplitude solutions in plane couette flow: bifurcation from infinity. *Journal of Fluid Mechanics*, 217:519–527.

Nikuradse, J. (1930). Investigation of turbulent flow in tubes of non-circular cross section. *Engineering Archive (Ingen. Arch.)*, 1:306–332.

Nikuradse, J. (1950). *Laws of flow in rough pipes*. National Advisory Committee for Aeronautics Washington.

Nishimura, T., Yano, K., Yoshino, T., and Kawamura, Y. (1990). Occurrence and structure of taylor-goertler vortices induced in two-dimensional wavy channels for steady flow. *Journal of chemical engineering of Japan*, 23(6):697–703.

Park, J. S. and Graham, M. D. (2015). Exact coherent states and connections to turbulent dynamics in minimal channel flow. *Journal of Fluid Mechanics*, 782:430–454.

Perry, A., Henbest, S., and Chong, M. (1986). A theoretical and experimental study of wall turbulence. *Journal of Fluid Mechanics*, 165:163–199.

Perry, A. and Marusic, I. (1995). A wall-wake model for the turbulence structure of boundary layers. part 1. extension of the attached eddy hypothesis. *Journal of Fluid Mechanics*, 298:361–388.

Perry, A. E., Schofield, W. H., and Joubert, P. N. (1969). Rough wall turbulent boundary layers. *Journal of Fluid Mechanics*, 37(02):383–413.

Placidi, M. and Ganapathisubramani, B. (2012). Investigation of wall-bounded turbulence over regularly distributed roughness. *Bulletin of the American Physical Society*, 57.

Pope, S. B. (2000). *Turbulent flows*. Cambridge university press.

Qin, N., Ludlow, D. K., and Shaw, S. T. (2000). A matrix-free preconditioned newton/gmres method for unsteady navier–stokes solutions. *International journal for numerical methods in fluids*, 33(2):223–248.

Roache, P. J. (2002). Code verification by the method of manufactured solutions. *Transactions-American Society of Mechanical Engineers Journal of Fluids Engineering*, 124(1):4–10.

Saric, W. S. (1994). Görtler vortices. *Annual Review of Fluid Mechanics*, 26(1):379–409.

Sarkar, K. and Prosperetti, A. (1996). Effective boundary conditions for stokes flow over a rough surface. *Journal of Fluid Mechanics*, 316:223–240.

Schmid, P. J. and Henningson, D. S. (2001). *Stability and transition in shear flows*, volume 142. Springer.

Schmiegel, A. and Eckhardt, B. (1997). Fractal stability border in plane couette flow. *Physical review letters*, 79(26):5250.

Schneider, T. M., Gibson, J. F., and Burke, J. (2010a). Snakes and ladders: localized solutions of plane couette flow. *Physical review letters*, 104(10):104501.

Schneider, T. M., Marinc, D., and Eckhardt, B. (2010b). Localized edge states nucleate turbulence in extended plane couette cells. *Journal of Fluid Mechanics*, 646:441–451.

Schultz, M. and Flack, K. (2005). Outer layer similarity in fully rough turbulent boundary layers. *Experiments in Fluids*, 38(3):328–340.

Skufca, J. D., Yorke, J. A., and Eckhardt, B. (2006). Edge of chaos in a parallel shear flow. *Physical review letters*, 96(17):174101.

Suri, B., Tithof, J., Grigoriev, R. O., and Schatz, M. F. (2017). Forecasting fluid flows using the geometry of turbulence. *Physical Review Letters*, 118(11):114501.

Taira, K., Brunton, S. L., Dawson, S., Rowley, C. W., Colonius, T., McKeon, B. J., Schmidt, O. T., Gordeyev, S., Theofilis, V., and Ukeiley, L. S. (2017). Modal analysis of fluid flows: An overview. *arXiv preprint arXiv:1702.01453*.

Tani, I. (1988). Drag reduction by riblet viewed as roughness problem. *Proceedings of the Japan Academy. Ser. B: Physical and Biological Sciences*, 64(2):21–24.

Townsend, A. A. (1956). *The structure of turbulent shear flow*. Cambridge university press.

Townsend, A. A. (1976). *The structure of turbulent shear flow*. Cambridge university press.

Townsin, R. and Dey, S. (1990). The correlation of roughness drag with surface characteristics. In *Proceedings of the RINA International Workshop on Marine Roughness and Drag*.

Trefethen, L. N. and Bau, D. (1997). *Numerical linear algebra*, volume 50. Siam.

Versteeg, H. K. and Malalasekera, W. (2007). *An introduction to computational fluid dynamics: the finite volume method*. Pearson Education.

Viswanath, D. (2007). Recurrent motions within plane couette turbulence. *Journal of Fluid Mechanics*, 580:339–358.

Waleffe, F. (1995). Transition in shear flows. nonlinear normality versus non-normal linearity. *Physics of Fluids*, 7(12):3060–3066.

Waleffe, F. (1997). On a self-sustaining process in shear flows. *Physics of Fluids (1994-present)*, 9(4):883–900.

Waleffe, F. (2002). Exact coherent structures and their instabilities: Toward a dynamical-system theory of shear turbulence. In *Proceedings of the International Symposium on "Dynamics and Statistics of Coherent Structures in Turbulence: Roles of Elementary Vortices*, pages 115–128.

Waleffe, F. (2003). Homotopy of exact coherent structures in plane shear flows. *Physics of Fluids (1994-present)*, 15(6):1517–1534.

Walsh, M. J. (1982). Turbulent boundary layer drag reduction using riblets. In *AIAA, Aerospace Sciences Meeting*, volume 1.

Walsh, M. J. (1983). Riblets as a viscous drag reduction technique. *AIAA journal*, 21(4):485–486.

Walsh, M. J. (1990). Effect of detailed surface geometry on riblet drag reduction performance. *Journal of Aircraft*, 27(6):572–573.

Wang, J., Gibson, J., and Waleffe, F. (2007). Lower branch coherent states in shear flows: transition and control. *Physical review letters*, 98(20):204501.

Wedin, H. and Kerswell, R. (2004). Exact coherent structures in pipe flow: travelling wave solutions. *Journal of Fluid Mechanics*, 508:333–371.

Willis, A. P., Cvitanović, P., and Avila, M. (2013). Revealing the state space of turbulent pipe flow by symmetry reduction. *Journal of Fluid Mechanics*, 721:514–540.

Willis, A. P. and Kerswell, R. R. (2008). Coherent structures in localized and global pipe turbulence. *Physical review letters*, 100(12):124501.

Zare, A., Jovanović, M. R., and Georgiou, T. T. (2016). Color of turbulence. *arXiv preprint arXiv:1602.05105*.

Zhou, J., Adrian, R., Balachandar, S., and Kendall, T. (1999). Mechanisms for generating coherent packets of hairpin vortices in channel flow. *Journal of Fluid Mechanics*, 387:353–396.